Control of Optical Properties of Surfaces for Improved Solar Thermophotovoltaic Systems

---

A Ph.D. dissertation

Presented to

the Faculty of the School of Engineering and Applied Science

University of Virginia

In Partial Fulfillment

of the requirements for the Degree

Doctor of Philosophy (Electrical and Computer Engineering)

by

Craig Ungaro

- 2015

Abstract

Alternative energy systems are crucial to meeting the expanding energy needs of the modern world. Unfortunately, the wide spectrum of solar radiation greatly limits the efficiency of photovoltaic systems. Solar thermophotovoltaic (STPV) technology overcomes this problem by tailoring the spectrum of incoming light to better match a photovoltaic cell. This has the potential to greatly increase the efficiency of photovoltaic systems and to help meet future energy demands in an environmentally friendly way.

The main challenge in designing efficient STPV systems is controlling the optical properties of the system's light absorbing and emitting surfaces. Through the use of nanostructures, the level of optical control needed to make highly efficient STPV systems will be realized. This work presents a study of the effects of various microscale and nanoscale structures on the absorption and emission spectra of surfaces, as well as their direct application in STPV systems. Computer modeling is used to determine the absorption spectra of various nanostructured surfaces and to predict the efficiency gains from using these structures in an STPV system. The ability to economically fabricate structures for large-area systems is also discussed.

A design for a full STPV system utilizing nanostructures for improved efficiency is presented, and the losses in such a system are analyzed. The system is then fabricated, and device performance is compared with simulation. A path towards future improvement of STPV systems is discussed. Additionally, a close collaboration was established with the Center for Nanophase Materials (CNM) at Argonne National Laboratory (ANL), leading to several joint research publications and access to modeling computers and fabrication facilities.

Approval Sheet

This Ph.D. dissertation is submitted in partial fulfillment of the requirements for the degree

of

Doctor of Philosophy (Electrical and Computer Engineering)

Craig Ungaro

This Ph.D. dissertation has been read and approved by the Examining Committee:

Professor Mool Gupta, Adviser

Professor Robert Weikle, Committee Chair

Professor Joshua Choi

Professor Lloyd Harriot

Dr Stephen Gray, Argonne National Labs

Accepted for the School of Engineering and Applied Science:

Professor James H. Aylor, Dean, School of Engineering and Applied Science

- 2015

Acknowledgments

First, I would like to thank my advisor professor Mool C. Gupta for his encouragement, advice, and technical knowledge as I pursue my Ph.D. degree. I would also like to thank him for offering me the wonderful opportunity to be a part of the unique graduate program at NASA Langley and the National Institute of Aerospace.

Secondly, Dr. Stephen Gray of Argonne National Labs was an immense help in this research. I appreciate his technical advice on FDTD modeling, as well as his general guidance on my project.

I would also like to thank the NASA Langley Professor program and the NSF IUCRC programs for their support of my research project.

This work was performed, in part, at the Center for Nanoscale Materials, a U.S. Department of Energy, Office of Science, Office of Basic Energy Sciences User Facility under Contract No. DE-AC02-06CH1135.

A portion of this research was conducted at the Center for Nanophase Materials Sciences, which is sponsored at Oak Ridge National Laboratory by the Scientific User Facilities Division, Office of Basic Energy Sciences, U.S. Department of Energy.

Lastly, I would like to thank my family and friends for their help and support throughout my time as a graduate student.

Contents

List of Tables

List of Figures

List of Symbols and Abbreviations

α	Material absorbance
α_{sol}	Solar absorbance
β	Coefficient of thermal expansion
$\Delta\nu$	Frequency-bandwidth
ϵ	Material emittance
ϵ_{1750K}	Thermal emittance at 1750 K
ϵ_A	Relative dielectric constant of material A (for EMT calculations)
ϵ_B	Relative dielectric constant of material B (for EMT calculations)
ϵ_{eff}	Effective dielectric constant
ϵ_r	Relative dielectric constant
$\epsilon_s(\lambda)$	Spectral emittance of emitting surface
ϵ_{sides}	Spectral emittance of sides of structure
ϵ_∞	Dielectric constant of a material at a frequency of infinity
η	Efficiency
η_{abs}	Absorbing surface efficiency
η_{carnot}	Carnot efficiency
η_{conc}	Concentration efficiency
η_{emit}	Emitting surface efficiency
η_{total}	Total system efficiency
γ_j	Damping constant of oscillator j
λ	Wavelength
λ_{bg}	Wavelength of a photon with energy equal to E_{bg}
λ_{cutoff}	Cutoff wavelength for ideal solar absorber
λ_{max}	Peak emission wavelength of a blackbody

μ	Dynamic viscosity
ω	Angular frequency of a wave
ω_j	Frequency of oscillator j
ω_p	Plasma frequency
ϕ_{abs}	Thermal emission from absorbing surface
ϕ_{cav}	Thermal emission from sides of structure
ϕ_{emit}	Thermal emission from emitting surface
σ	Stefan's constant
θ_i	Angle of incidence
θ_r	Angle of reflection
θ_t	Angle of transmission
A_{abs}	Area of absorbing surface
A_C	Cross-sectional area
A_{conc}	Collection area of the solar concentrator
A_{emit}	Area of emitting surface
A_{PV}	The area of the PV cell
A_{ratio}	Ratio of emitting to absorbing surface areas
Al_2O_3	Aluminum oxide (alumina)
AM 1.5	Air mass 1.5
ARC	Anti-reflection coating
$B(\lambda, T)$	Planck's law
c	Speed of light in a medium
c_0	Speed of light in a vacuum
C	Concentration ratio
C_P	Specific heat
Cermet	Ceramic-metal composite
CSP	Concentrated solar power

CVD	Chemical vapor deposition
E_{abs}	Spectral irradiance of the absorbing surface
E_{bg}	Bandgap energy
E_{emit}	Spectral irradiance of the emitting surface
$E_{inc}(\lambda)$	Spectral irradiance incident on the absorbing surface
$E_{sun}(\lambda)$	Spectral irradiance of the sun
E-beam	Electron beam
EMT	Effective medium theory
$E_{photon}(\lambda)$	Photon energy
EQE	External quantum efficiency
Er_2O_3	Erbium oxide (erbia)
f	Percentage of material having $\epsilon = \epsilon_A$ (for EMT calculations)
f_j	Strength of oscillator j
F_{PV}	View-factor between emitting surface and PV cell
FDTD	Finite difference time domain
FF	Fill factor (of a PV cell)
FTIR	Fourier transform infrared spectroscopy
FWHM	Full width at half-maximum
g	Acceleration due to gravity ($9.8\ \frac{m}{s^2}$)
GaSb	Gallium antimonide
Ge	Germanium
GLAD	Glancing angle deposition
Gr	Grashof number
h	Planck's constant
H	Heat transfer coefficient
HfO_2	Hafnium oxide (hafnia)
Ho_2O_3	Holmium oxide (holmium)

I_0	Reverse saturation current
I_{sc}	Short circuit current
InGaAsSb	Indium gallium arsenic antimonide
InGaP	Indium gallium phosphide
J_{emit}	Usable power output per unit area from emitting surface
k	Thermal conductivity
K	Kelvin
k_B	Boltzmann's constant
L_C	Coherence length
MgF_2	Magnesium fluoride
MgO	Magnesium oxide
Mo	Molybdenum
n	Index of refraction
n_{eff}	Effective index of refraction
ND	Neutral density
Ni	Nickel
NIR	Near infrared
Nu	Nusselt number
P	Perimeter length
P_{abs}	Power absorbed by the absorbing surface
P_{conv}	Power lost due to convection
P_{max}	Maximum power output from a PV cell
P_r	Reflected power
P_{sup}	Power lost through conduction
P_t	Transmitted power
PECVD	Plasma-enhanced chemical vapor deposition
Pr	Prandtl number

PV	Photovoltaic
q	Charge of an electron
R_{PV}	Reflectance of the PV cell
Ra	Rayleigh
SEM	Scanning electron microscope
Si	Silicon
Si_3N_4	Silicon nitride
SiO_2	Silicon dioxide
STPV	Solar thermophotovoltaic
T	STPV system temperature
T_{abs}	Temperature of absorbing surface
T_{emit}	Temperature of emitting surface
T_{env}	Temperature of surrounding environment
TMM	Transfer matrix method
V_{coeff}	Additional heat transfer coefficient due to vacuum
V_{mpp}	Voltage at the maximum power point of a PV cell
V_{oc}	Open circuit voltage
W	Tungsten
YSZ	Yttria-stabilized zirconia
ZrB_2	Zirconium diboride

Chapter 1: Introduction

1.1 Solar Thermophotovoltaic System Overview

STPV systems provide increased solar conversion efficiency by using an intermediary material to modify the spectrum of incoming solar radiation to be better matched to a PV cell. To accomplish this, incoming concentrated solar radiation is absorbed by the absorbing surface, or absorber, as heat energy. As the temperature of the device rises, it begins to emit large amounts of thermal radiation (blackbody emission) out of an emitting surface, or emitter. This radiation can be absorbed by a PV cell to create electricity. Modification of the emitting surface to create a narrow-band thermal emission can greatly improve the efficiency of these devices by matching the emitted thermal radiation to the absorption spectrum of the PV cell [1]. This spectral matching allows STPV systems to utilize the full solar spectrum, exceed the Shockley-Queisser limit, and reach high theoretical efficiencies of 85.4% [2]. Energy can also be stored thermally in the intermediary material, allowing power generation after the sun has set. STPV system technology can also be easily adapted to thermophotovoltaic (TPV) systems, which operate similarly to STPV systems but use a burning fuel or waste heat as a thermal source instead of the sun.

While there are a variety of geometric configurations for STPV systems [3], they all have the following parts in common: an absorbing surface (which absorbs incoming sunlight), an emitting surface (which emits thermal radiation), and a PV cell (which converts thermal radiation into electricity) [4]. The absorbing and emitting surfaces are typically located on different areas of an absorber-emitter structure. This spatial separation allows them to have different optical properties. Figure 1.1 shows examples of STPV systems in (a) flat and (b) cylindrical configurations. Additional parts, such as filters, mirrors, and back-reflectors, are also used in some systems to increase efficiency [5, 6].

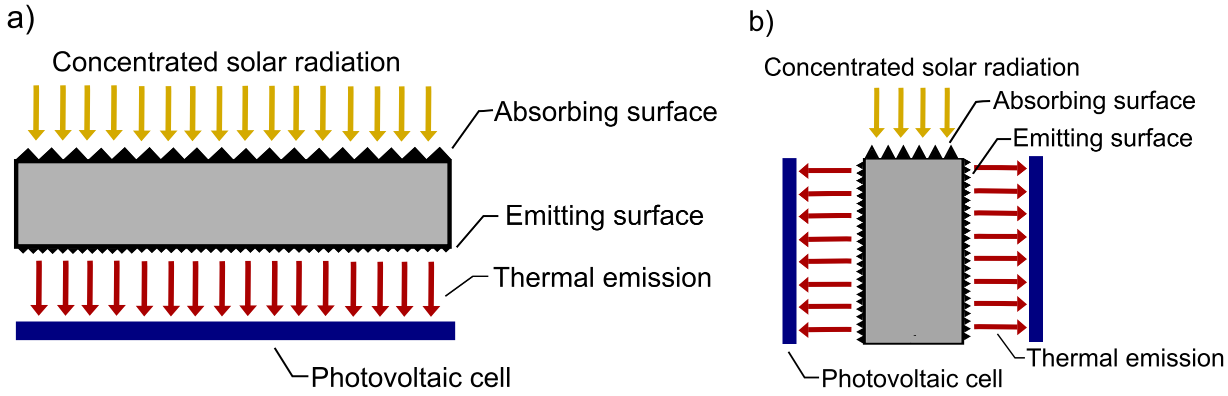

Figure 1.1: Diagram of a) a flat STPV system and b) a cylindrical STPV system, both with solar absorber and thermal emitter.

1.2 Importance of Solar Thermophotovoltaic Systems

Alternative energy systems are crucial to the goal of reducing greenhouse gas generation and reducing dependence on fossil fuels. Energy storage, energy generation efficiency, cost, and consistent power generation are the four primary challenges facing these systems [7]. Solar thermophotovoltaic (STPV) systems promise to provide a solution to these issues via a novel energy generation concept.

Solar energy conversion has been explored through direct conversion via the photovoltaic (PV) effect and through the conversion of sunlight to heat and then to electricity via a heat-engine. Solar cells based on the PV effect have a theoretical maximum efficiency of about 32% (the Shockley-Queisser limit), and a laboratory efficiency of about 25% has been demonstrated [8]. The reason for the low limit on the conversion efficiency of PV cells is that a significant amount of solar light is wasted as heat. This is because excess energy greater than the bandgap of the PV cell (E_{bg}) cannot be utilized, while light with energy below E_{bg} is transmitted and therefore not absorbed.

In the case of STPV systems, broad-spectrum sunlight can be effectively absorbed and converted into heat and then to electrical energy. This allows for a much greater portion of the energy in the solar spectrum to be used, and these systems have a theoretical maximum efficiency of 85.4% based on the Carnot cycle limit [2]. Hence, STPV systems have the potential to be more efficient than PV cells. In addition, the absorbed heat can be directly utilized for solar heaters, and heat can be stored cost-effectively and later converted to electric power [9]. This makes STPV systems attractive for power conversion and for direct-heating applications.

Additionally, STPV systems can be scaled for smaller power applications, such as in-home use. Indeed, thermophotovoltaic systems, which share a large amount of technology with STPV systems, have already been developed for this application [10–12]. STPV systems also contain no heat-exchange fluid or moving parts, making them very reliable.

Because STPV systems operate efficiently at high temperatures, they are commonly used with concentrated solar power (CSP). CSP systems allow large areas of sunlight to be concentrated onto a small PV cell area, opening the door for the use of expensive high-efficiency PV cells [13]. Concentrated light can also result in an increase in PV cell efficiencies; however, high temperatures can reduce PV cell efficiency, and cooling systems are needed to keep PV cell temperatures low [14].

While early STPV systems operated with low (<1%) efficiency, recent advances in 2014 and then 2015 have increased experimental operating efficiency to 3.2% and then 8%, resulting in a renewed interest in the field [15–19]. While difficulties in the fabrication of nanostructures and cell cooling under such high concentrations continue to keep experimental efficiencies well below simulations, the rapid growth in this field promises increased performance in the near future.

In this dissertation, the solar absorption and thermal emission portions of the STPV system will first be addressed separately, and then combined into a complete STPV system. This is viable because the effect of the solar absorbing and emitting surfaces on the overall system efficiency can be decoupled [20]. The thermal stability of the structures will also be addressed; this can be a substantial concern due to the high operating temperatures (>1300 K) common in STPV systems [2].

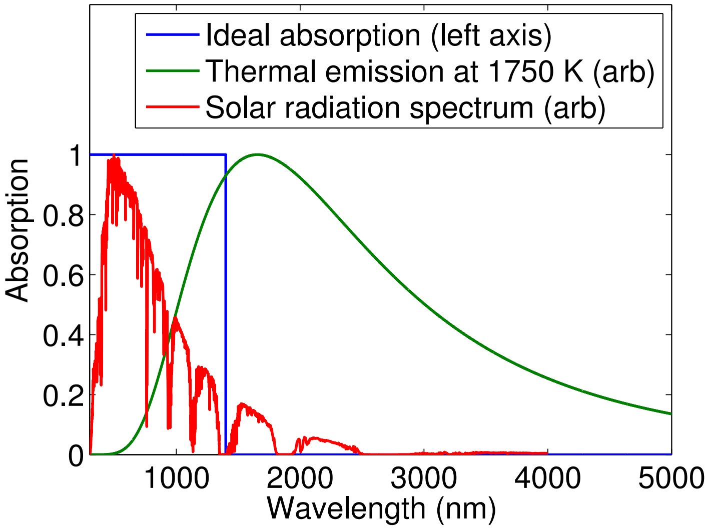

Figure 1.2: Ideal absorption spectra for a solar absorbing surface for an STPV system operating at 1700 K.

1.2.1 Absorbing Surface Figure of Merit

The absorbing surface primarily absorbs incoming concentrated solar radiation, and therefore requires an extremely high solar absorbance (α_{sol}) as well as a good view of the incoming radiation. At the same time, this surface must have a relatively large area due to limitations on the concentration of sunlight. Since this surface will be thermally coupled to the emitting surface, which must reach high temperatures, significant thermal radiation will escape from the absorbing surface, resulting in a loss of efficiency [21]. Therefore, another requirement for an efficient solar absorbing surface is low thermal emittance (ϵ_{1700K}). ϵ_{1700K} is defined as the amount of thermal energy radiated by a surface with emittance ϵ and temperature 1700 K as compared to a blackbody emitter with temperature 1700 K, while α_{sol} is defined as the amount of solar energy absorbed by a surface with absorbance α as compared to a blackbody absorber.

Due to the relation $absorbance = 1 - reflection$, and the assumption that the emittance (ϵ) of a surface is equal to its absorbance due to Kirchhoff's law of thermal radiation, the absorbing surface must have a high absorbance value in the visible region and a low value in the near-infrared (NIR) region. A surface that has high α_{sol} and low ϵ_{1700K} is called a solar selective surface. Figure 1.2 shows an ideal absorbance spectrum for an absorbing surface for an example STPV system operating at 1700 K. It can be seen from the figure that there is some overlap between solar energy and thermal emission from a surface, preventing a perfect absorbing surface ($\alpha_{sol} = 1$, $\epsilon_{1700K} = 0$) from being created.

The ideal surface for a system temperature of 1700 K, as shown in Figure 1.2, would have an α_{sol} of 0.88 and an ϵ_{1700K} of 0.12, resulting in an efficiency of 78% [22]. Lower system temperatures can result in increasingly efficient absorbing surfaces, with an absorption efficiency of 99% being reached at a system temperature of 350 K [2]; however, low system temperatures result in large technical hurdles making them highly impractical, and overall system power output and efficiency will be extremely low for these systems [23].

Using Planck's Law for blackbody radiation, an air mass 1.5 (AM 1.5) solar spectrum [24], and the surface's spectral absorbance, we can find the efficiency of the absorbing surface (η_{abs}) at a certain operating temperature and solar concentration. This is shown by equations 1.1 and 1.2:

$$\eta_{abs}(T) = \frac{\int_0^\infty \{E_{inc,\lambda}(\lambda)\alpha(\lambda) - \epsilon(\lambda)B(\lambda,T)\}\,d\lambda}{\int_0^\infty E_{inc,\lambda}(\lambda)d\lambda} \tag{1.1}$$

$$E_{inc,\lambda}(\lambda) = C\eta_{conc}E_{sun,\lambda}(\lambda) \tag{1.2}$$

where, C is the concentration ratio of incoming sunlight, η_{conc} is the solar concentration efficiency, $E_{sun,\lambda}(\lambda)$ is the spectral irradiance of the sun at the earth's surface, $B(\lambda, T)$ is Planck's Law for the spectral irradiance of a blackbody at temperature T (given in chapter 4 as equation 4.3), and $E_{inc,\lambda}(\lambda)$ is the spectral energy incident per unit area on the absorbing surface.

Equation 1.1 can be used as a figure of merit to compare the performance of various absorbing surfaces. Changes in α_{sol} and ϵ_{1700K} have a complex relationship with η_{abs} due to the fact that they change the concentration ratio required to maintain a temperature, which in turn changes η_{abs}; however, relative comparisons in η_{abs} are possible using realistically assumed values for the concentration ratio and temperature. Incoming sunlight is assumed to be perfectly perpendicular to the absorbing surface in this approximation; the angular dependence of absorbers will be addressed in later chapters.

1.2.2 Emitting Surface Figure of Merit

Two of the largest losses in traditional solar PV systems are thermalization loss and the loss of photons with energy below E_{bg}. These losses are caused by the fact that any excess energy above E_{bg} will be lost, while radiation with energy less than E_{bg} will not be absorbed by the PV material and will also be lost. The magnitude of these losses are directly related to the width of the radiation being absorbed by the PV cell. The broadness of the solar spectrum results in very high losses, giving rise to the Shockley-Queisser limit of about 32% efficiency for single-bandgap solar PV cells.

To reduce these losses and maximize efficiency in STPV systems, a selective emitter is used as the emitting surface. This selective emitter must have low thermal emission for photons with energy below E_{bg}, as well as low thermal emission for photons with energy much higher than E_{bg}. It must also have high thermal emission for photons with energy just above E_{bg}. This narrows the spectrum of emitted thermal radiation to a narrow band just above the E_{bg} of the PV cell, which results in very high theoretical efficiencies for STPV systems [6].

Figure 1.3 shows the ideal emittance spectrum for an emitting surface with no back-reflector for a gallium antimonide (GaSb) PV cell. GaSb is used here because it is a commonly used PV cell in STPV applications due to its small (0.726 eV) bandgap, high efficiency, and the fact that its E_{bg} matches well with many emitters [10]. While an extremely narrow emission spectrum would increase the system efficiency, it would emit a very small amount of power (as seen in equation 1.4). This would cause the temperature of the system to rise, and

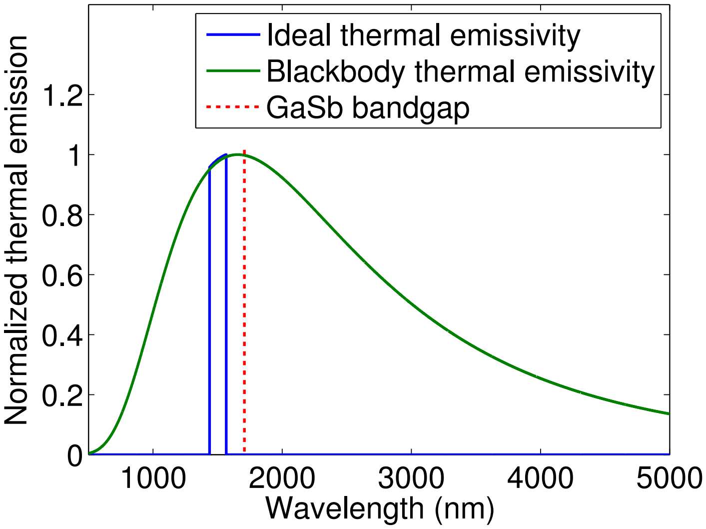

Figure 1.3: Ideal spectra for an emitting surface for an STPV system operating at 1700 K with GaSb PV cells.

an increased amount of energy would be lost through the absorbing surface. Therefore, a balance must be struck between power output and emission bandwidth.

The exact location of the ideal emissivity is at a point close to the PV cell E_{bg} where the cell has high external quantum efficiency (EQE). A PV cell with a small E_{bg} is desirable here because PV cells with large E_{bg} require much higher system temperatures leading to more complex solar concentrators and a reduction of overall system reliability due to thermal stability of materials.

The usable power output per unit area and efficiency of an emitting surface is given by:

$$E_{emit,\lambda}(\lambda, T) = B(\lambda, T)\epsilon_s(\lambda) \tag{1.3}$$

$$J_{emit} = \int_0^{\lambda_{bg}} \frac{E_{bg}}{E_{photon}(\lambda)} E_{emit,\lambda}(\lambda, T) d\lambda \tag{1.4}$$

$$\eta_{emit}(T) = \frac{J_{emit}}{\int_0^{\infty} E_{emit,\lambda}(\lambda, T) d\lambda} \tag{1.5}$$

where T is the temperature of the surface, $E_{emit,\lambda}$ is the spectral irradiance of the emitting surface, $\epsilon_s(\lambda)$ is the emittance of the emitter, $E_{photon}(\lambda)$ is the photon energy as a function of wavelength λ, E_{bg} is the bandgap energy of the PV cell used, and λ_{bg} is the wavelength of a photon with energy equal to E_{bg}.

Emitter efficiency, or η_{emit}, consists of the fraction of thermal energy emitted by the emitting surface that can be used by a PV cell, while J_{emit} is the total usable power emitted by an emitting surface. The total available emitted spectral energy is found by multiplying the spectral emittance of a surface by the blackbody thermal radiation spectrum. A blackbody spectrum representing an emitter temperature of 1700 K is used for matching with GaSb PV cells since they are commonly used in STPV systems [6, 25].

These equations can also be used as a figure of merit to compare emitting surfaces. The relationship between the system efficiency, η_{abs}, η_{emit}, and J_{emit} is complex and will be explored later in this report. While η_{emit} takes into account only the efficiency of the emitting surface, and does not represent an overall system efficiency, it can be used in conjunction with J_{emit} to compare various emitting surfaces.

1.3 Problem Statement

There is a need for highly efficient alternative energy solutions as well as solutions that lend themselves to easy power storage. STPV systems have the potential to convert sunlight into electricity with an extremely high conversion efficiency [21]. They are also able to store energy thermally, and can be easily modified to operate with an alternate heat source, such as burning natural gas, when there is no sunlight available. STPV systems are scalable as well, allowing them to be used for both distributed and central power generation. With no moving parts or heat exchange fluids, STPV systems have the potential to be extremely reliable. This research examines existing STPV systems and identifies avenues for improving performance.

For efficient operation, the absorbing and emitting surfaces must meet the following requirements: a) sunlight must be efficiently absorbed by the absorbing surface, b) the emission of thermal radiation by the absorbing surface must be minimized, c) a large amount of power must be emitted by the emitting surface, and d) the emitting surface must emit primarily above the E_{bg} of the PV cell. To meet these requirements, precise control over the absorbance and reflectance of the light absorbing and emitting surfaces is required. The use of nanostructured surfaces to achieve this goal can result in highly efficient STPV systems.

Additionally, while many studies have simulated the use of nanostructures in STPV devices, this work will focus on the incorporation of modeled nanostructures into an experimental system. For this reason, focus is placed on the practicality of the fabrication of different nanostructures.

1.4 Objective

This dissertation examines nanostructured absorbing and emitting surfaces and STPV system designs that allow for improved efficiency in STPV devices. Through the use of computer simulation of the interaction between light as an electromagnetic wave and materials, the reflectance spectrum of materials with arbitrary dielectric profiles can be determined [26, 27]. In addition to this, a thermodynamic model for a full STPV system has been developed to investigate the overall efficiency of a device incorporating these surfaces. By combining these simulation methods, the surface properties required for high efficiency STPV operation are identified.

An experimental system has been designed and fabricated to demonstrate high efficiency using this system, as well as to verify the accuracy of the simulations. By combining simulated and experimental data, the effect of system parameters such as absorbing/emitting surface reflectance, PV cell choice, concentration factor, and the emitter/absorber aspect ratio on overall device efficiency is determined. Using these results, a path forward towards highly efficient STPV devices is examined.

Chapter 2: Literature Review

Here, a literature review of the primary components of STPV devices will be performed. These include the PV cell, absorbing surface, and emitting surface. While experimental studies of complete STPV systems are rare, there has been much research into their individual components. This is partially due to the various additional applications for each of these surfaces, and partially due to the fact that whole STPV systems are very complex. In order to study each component on an individual level, figures of merit have been developed. These allow relative comparisons between components, although they do not accurately reflect exactly how a given component will behave in a complete system.

Because STPV devices operate at high temperatures (a system operating at 1700 K is examined in this dissertation), thermal stability is a large concern when looking at absorbing and emitting surfaces. Many papers that focus on other applications or discuss only simulated surfaces do not take this into account, resulting in many surfaces examined here being unsuitable for use in an STPV device.

2.1 Photovoltaic Cells for Solar Thermophotovoltaic Systems

The choice of PV cells in STPV systems is limited by the maximum achievable temperature of the system. Due to the fact that a monochromatic emitter is not realistically achievable, the maximum efficiency for an STPV system occurs when the blackbody peak is near the E_{bg} of the PV cell used [28]. The wavelength of peak emission of a blackbody with temperature T is given by Wien's displacement law:

$$\lambda_{max} = \frac{2.898 \times 10^{-3}[\mathrm{m} \cdot \mathrm{K}]}{T[\mathrm{K}]} \tag{2.1}$$

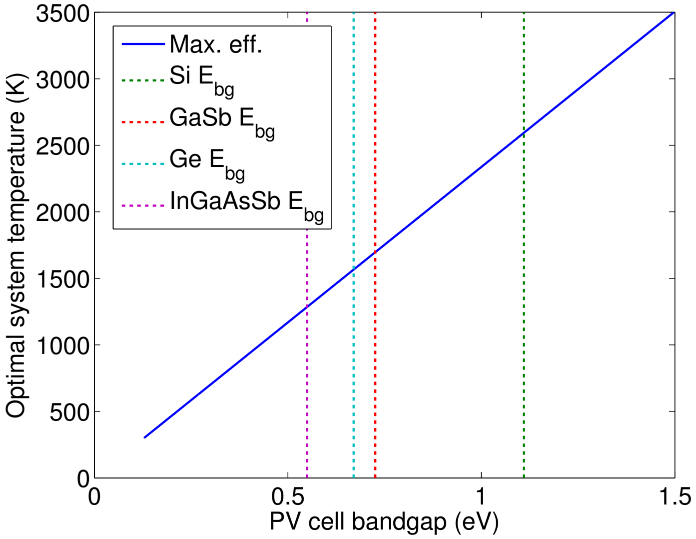

Figure 2.1: The optimal temperature for an STPV system at different PV cell bandgaps, with selected PV cells shown for reference.

Figure 2.1 shows the optimal temperature for an STPV system at different PV cell bandgaps. Due to limitations on the concentration of sunlight and material stability, temperatures above 2000 K are not easily achievable in STPV systems [3]. An STPV system using a silicon (Si) PV cell with a bandgap of 1.1 eV would require an operating temperature of about 2600 K to be efficient; other common solar PV cells require even higher temperatures [8]. Due to these difficulties, there are three PV cells most commonly used in STPV systems: GaSb cells [10, 16, 17, 19], germanium (Ge) cells [15], and indium gallium arsenic antimonide (InGaAsSb) cells [18].

Research into additional PV cells for STPV research has included III-V binary compounds and alloys, Si-based cells, and II-VI binary compounds [29]. GaSb PV cells have been studied for use in thermophotovoltaic and STPV systems as well as in cascade solar cells [10, 30]. Their bandgap of 0.75 eV corresponds to an STPV system operating temperature of 1700 K for maximum efficiency. GaSb PV cells also have high efficiency, with recent cells having an external quantum efficiency (EQE) of over 0.8 and a fill factor (FF) of over 0.65 [31–33]. InGaAsSb quaternary compounds with bandgaps of 0.55 eV have also been developed [25, 34].

These allow for even lower temperature operation than GaSb-based STPV systems; however, the EQE is lower at about 0.5. Ge PV cells, while having high FF, EQE, and photocurrent values, tend to have very low open circuit voltages (V_{oc}s) that result in low efficiencies; however, surface passivation can greatly improve the V_{oc} of Ge PV cells [35, 36]. Indeed, an increase in V_{oc} from 0.17 V to 0.24 V has been observed using an indium gallium phosphide (InGaP) passivating window layer [37].

In a comparative study, Khvostikov et al. found that for an STPV system with a bare tungsten (W) emitter at 2000 K, GaSb PV cells were able to convert 18.5% of emitted power to electricity, while Ge PV cells could convert only 11.5% [36]. An additional advantage of GaSb PV cells is their relatively simple fabrication process using diffusion from the gas phase directly into the GaSb substrate [10, 33, 36]. This dissertation will focus on the use of GaSb PV cells in experiment due to their availability and high efficiency; however, the effects of Ge and InGaAsSb PV cells on efficiency will also be addressed via simulation.

2.2 Absorbing Surfaces

Absorbing surfaces are important components in STPV systems. It can be seen from equations 1.1 and 1.2 that an increase in the concentration ratio, C, results in the α_{sol} term having a larger impact on system efficiency compared to the ϵ_{1700K} term. Due to the high levels of concentration typically used in STPV systems, an absorbing surface with a high α_{sol} is essential for an efficient STPV system. There are a variety of existing designs for solar selective surfaces for STPV systems, such as ceramic-metal composites (cermets), rare earth materials, photonic crystals, nanotube arrays, and 2-D or 3-D periodic nanostructures on W substrates [18, 38, 39].

A common theme among selective solar absorbers is nanometer-scale feature sizes. This is due to the fact that selective properties rely on interference due to the wave-like nature of photons, which is strong when structures are close to photonic wavelengths in size.

Unfortunately, the thermal stability of nanostructures is much lower than that of bulk materials. This is due to melting point depression, and an increased surface area to volume ratio leading to high rates of oxidation and surface diffusion [40–42]. Many solar selective absorbers are studied for solar thermal applications, which typically operate at temperatures below 750 K [43]. While many different absorbing surface designs are explored here, the only experimentally demonstrated STPV system using selective absorbers to date used a 1-D photonic crystal [9, 18, 19]. This research focuses on nanostructured tungsten because it is one of the few selective absorber materials that has been experimentally demonstrated to be stable at temperatures over 1650 K and has good intrinsic absorption and emission properties [44].

2.2.1 Bulk Materials

Selective absorbers based on bulk materials absorb incoming radiation because of the intrinsic properties of the materials used. These include rare-earth materials, cavities made from solid metals, and doped semiconductor materials. While these have the advantage of being simple systems, they generally have a lower α_{sol} than some of the more complex systems and can exhibit thermal stability issues at higher operating temperatures [38].

Geometric shapes such as cavities provide increased absorption via multiple reflections that increase relative to the ratio of the cavity depth and diameter [45, 46]. A commonly used material for cavity-type absorbers in STPV systems is tungsten, due to its intrinsic α_{sol} of 0.41, which is very high for a polished metal, and high temperature stability [2, 16, 47–49]. Tungsten cavities with an aperture diameter of 12 mm and a depth of 45 mm were experimentally shown to have an α_{sol} of 0.7 - 0.8 and an ϵ_{1700K} of 0.5 - 0.6 [16].

Many material combinations exist that can have an intrinsic α_{sol} that is higher than tungsten [38, 47]. Chemical vapor deposition (CVD) of zirconium diboride (ZrB_2) has been shown to achieve an α_{sol} of 0.77 and ϵ_{1700K} of 0.3, and shows high temperature stability [50]. Black nickel, produced by the electro-deposition of a complex of nickel and zinc sulfide, has an α_{sol} of 0.9, but an ϵ_{1700K} of 0.6 [51]. Black chrome [52] and many other thick coatings deposited by CVD and electro-deposition have been developed for use in solar thermal systems; however, most lack the high-temperature stability necessary for incorporation into an STPV system [53].

2.2.2 Nanostructures

Photonic crystals work to reduce the reflection of photons in certain bandwidths through interference effects. Typically, 1-D photonic crystals consist of alternating layers of metal or dissimilar dielectrics with precise thicknesses. These layered structures frequently have low thermal stability due to the low melting temperatures of many dielectrics and thermal expansion mismatch between layers [54]. Aperiodic metal and dielectric stacks (1-D photonic crystals) were simulated to have α_{sol} >0.9 while maintaining ϵ_{1700K} <0.16 at 1700 K using alternating layers of magnesium oxide (MgO) and W [22]. A simpler stack consisting of two layers of yttra-stabilized zirconia and a single layer of W was experimentally shown to have an α_{sol} equal to 0.74 with a very low ϵ_{1700K} [19].

2-D photonic crystals with α_{sol} >0.9 and ϵ_{1700K} <0.1 have been reported as well [55]. These structures consist of a two-dimensional array of W blocks on top of a dielectric spacer and a metallic substrate. These are high melting point materials, although the thermal stability of these structures has not been directly reported. Both 1-D and 2-D photonic crystals suffer from melting point depression and surface diffusion that can result in low thermal stability [41].

Nanostructures achieve high α_{sol} via multiple reflections and interference effects. Very small nanostructures can also exhibit a low ϵ_{1700K} provided their feature sizes are on the order of the wavelength of visible light. Pyramidal structures in particular can have extremely high α_{sol} due to multiple reflections [56]. Again, tungsten is typically used as a substrate because of its thermal stability and high α_{sol}; however, the thermal stability of nanostructured tungsten can be much lower than bulk tungsten due to oxidation, surface diffusion, and recrystallization effects [41, 44]. Protective oxides and thermal annealing can improve the thermal stability of W structures in air, and the use of a vacuum or protective gas can further increase stability [41].

Experimental results for periodic grating structures consisting of a pattern of micron-sized square shaped holes on W substrates achieve α_{sol} >0.8 combined with ϵ_{1700K} <0.2 at 1400 K [57]. Periodic pyramidal or conical nanostructures on W substrates were simulated to have an α_{sol} of 0.95 and ϵ_{1700K} <0.5 but have not been successfully fabricated [56].

In addition to ordered structures, chaotic structures can have very high α_{sol}. Carbon nanotubes are experimentally shown to have α_{sol} >0.99, but also exhibit ϵ_{1700K} >0.9 [18, 58, 59]. Glancing angle deposition (GLAD) of W nanostructures has also been proposed for use as a selective solar absorber which will be discussed later in this work [60]. Pseudo-random arrays of cones can have α_{sol} >0.99 while maintaining ϵ_{1700K}<0.5 and can be fabricated via laser processes; however, control of structure size during laser processing is difficult [61, 62]. These structures will also be considered later in this work.

2.2.3 Composite Materials

High α_{sol} combined with low ϵ_{1700K} can be achieved by coating a NIR reflector with a material that selectively absorbs visible light. Typically, a metallic reflector is coated with a ceramic layer impregnated with metallic nanoparticles (a cermet layer) [63]. If the nanoparticles have diameters on the order of 10 nm, then photons with a wavelength below 1 μm will be absorbed while longer wavelength photons will be transmitted through the cermet layer and reflected by the substrate [64–66].

Nickel-alumina (Ni-Al_2O_3) cermet coatings with an α_{sol} of 0.93 and ϵ_{1700K} of 0.6 have been reported; however, they are thermally stable in air only up to 600 K [67]. Replacing the nickel nanoparticles with molybdenum (Mo) can result in stability to 1100 K in vacuum, but results in an increase in ϵ_{1700K} to 0.8 [68]. Molybdenum nanoparticles in silicon dioxide (SiO_2) are also stable up to 1100 K in vacuum, and have an α_{sol} of 0.95 while maintaining

Table 2.1: Efficiency, relative solar absorption, and relative thermal emission at a temperature of 1700 K of selected absorbing surfaces.

Absorber type	Absorber efficiency (η_{abs})	α_{sol}	ϵ_{1700K}
Ideal solar absorber for 1700 K STPV	0.83	0.87	0.04
Pseudo random nano-cones	0.80	0.97	0.16 (this work) [61]
W pyramidal nanostructures	0.79	0.92	0.13 [56]
Mo-SiO_2 cermet	0.77	0.93	0.16 [69]
Carbon nanotubes	0.74	0.99	0.95 [18]
1-D photonic crystal on W	0.74	0.8	0.06 [19]
Black nickel	0.74	0.85	0.11 [51]
Blackbody absorber	0.73	1	1
Anti-reflection coating on W	0.67	0.73	0.05 [19]
GLAD of W	0.64	0.81	0.18 (this work) [60]
ZrB_2 coating	0.60	0.74	0.14 [50]
W cavities	0.59	0.74	0.15 [16]
Surface-relief grating on W	0.49	0.53	0.05[57]
Bare W	0.41	0.44	0.04 [47]

an ϵ_{1700K} of 0.5 [69]. Despite this recent progress, further research is needed to enhance the thermal stability of cermets for use in STPV systems [63].

2.2.4 Comparison of Absorbing Surfaces

Absorbing surface performance is compared by calculating the absorbing surface efficiency (η_{abs}) for various material systems presented in literature using equation 1.1. These calculations are performed assuming an operating temperature of 1700 K and a concentration ratio of 2500. These values are chosen for their prevalence in STPV systems [15–19, 28, 30]. Table 2.1 shows the efficiency of the considered absorbing surfaces under these conditions. These efficiencies take into account only the losses due to reflection and thermal emission of the absorbing surface of an STPV system. It should also be noted that these numbers are calculated using equation 1.1 based on reported reflectance, α, and ϵ data, and are not directly reported in literature.

Table 2.1 illustrates the high efficiency of many reported structures. Nanostructured W and Mo-SiO_2 cermets were both able to achieve very good efficiencies; however, this dissertation will focus on nanostructured W because of its proven thermal stability at high temperatures using protective oxide coatings [44]. It is also of interest that a high α_{sol} is more important than a low ϵ_{1700K} for STPV systems due to their high solar concentration levels; indeed, blackbody surfaces show quite high efficiencies while ideal solar absorbers show a relatively minor improvement. It should also be noted that the ideal solar absorber here is optimized for an operating temperature of 1700 K, and that the ideal characteristics change with system temperature.

2.3 Emitting Surfaces

In order to achieve a high-efficiency STPV system, the blackbody thermal emission spectrum must be narrowed. Because most STPV systems operate in the 1200 to 2000 K temperature range, a large amount of the radiation emitted from a blackbody will be below the E_{bg} of the PV cell and therefore unusable [9]. A selective emitter can greatly reduce the amount of energy emitted below E_{bg} and increase system efficiency. The efficiency can be further increased by decreasing the thermalization loss within the PV cell by reducing emission with energy far above E_{bg}.

Many designs for selective emitters have been studied for use in STPV systems, including bare W substrates, micro-structures on W substrates, nanofibers, rare-earth films, doped MgO films, and photonic crystals [3, 20, 70–72]. Thermal stability is again an important point when discussing emitters. While solar thermal systems do not use emitters, thermophotovoltaic systems do, and many of these systems operate in the 700–1100 K temperature range [28].

2.3.1 Bulk Materials

Flat tungsten has a relatively high efficiency as a selective emitter due to the rise in its reflectance at a wavelength of 1.5 μm, although it has a low power output due to its low emissivity at visible wavelengths [47]. Its simplicity has led many experimental systems to utilize flat tungsten emitters [15, 16]; however, improvements to flat tungsten can be made and will lead to higher operating efficiencies. Tungsten is also used as a substrate for many STPV emitters due to both its intrinsic reflectance spectrum and high melting point.

Rare earth materials are frequently used as emitters in STPV systems due to their naturally narrow emittance spectra [70]. Erbium is particularly interesting due to its emittance at a wavelength of 1.5 μm that matches very well with GaSb PV cells [73]. Unfortunately, the emittance band of pure rare-earth materials is too narrow, resulting in a very small amount of power in the output band [74]. To remedy this issue, rare earth elements are incorporated into ceramic matrices, causing a broadening of the emission band [75, 76]. Incorporating multiple rare-earth elements into the same matrix further broadens the emission band [77].

Yugami et al. report eutectic composites of aluminum oxides ($Al_2O_3/Er_3Al_5O_{12}$) that have spectral selectivity due to the presence of europium ions [17]. These structures also exhibit high mechanical strength and a melting point of 2130 K. Experiments showed low power density due to the configuration used, resulting in poor system efficiencies [17].

An alternative to rare earth materials for bulk selective emitters is transition element doped ceramics [74]. The inclusion of transition elements in a ceramic matrix can lead to narrow emission bands [78], and transition element doped ceramics are frequently used as emitters in lasers [79]. Compared to rare earth elements, transition elements allow for a broader emission band thus increasing the amount of power received by the STPV cell [71]. Experiments on a NiO doped MgO emitter show spectral selectivity of the emission and a high thermal stability [71, 80].

2.3.2 Nanostructures

Selective emission can also be accomplished through the use of photonic crystals. As with absorbing structures, photonic crystal emitters work via interference effects and can be 1-D, 2-D, or 3-D. While 1-D photonic crystal selective emitters can have very high efficiencies, they typically involve many layers of material with stringent thickness requirements, which make them difficult to fabricate [20, 54]. Another issue with 1-D photonic crystals is that they frequently use materials, such as Si or magnesium fluoride (MgF_2), that have low melting points, which make them unsuitable for use in high-temperature STPV systems. Systems consisting of a metal/dielectric stack on a tungsten substrate were simulated to achieve a η_{emit} of 0.68; however, these utilized silver as a metallic material and are not suitable for high temperature STPV applications [81]. Replacing the silver with a tungsten layer reduces the spectral efficiency to 0.56, but improves the thermal stability of the structures and allows high temperature operation.

One strategy to address this is to use PV cells with a lower bandgap, such as InGaAsSb cells with $E_{bg} = 0.5$ eV, allowing the STPV system to operate at a lower temperature [18, 25]. Unfortunately, as previously mentioned, low-bandgap PV cells suffer from high non-radiative recombination rates and typically have efficiencies below GaSb PV cells [82]. Another strategy is to use high-temperature materials with few layers; however, this sacrifices some efficiency [19]. 2-D and 3-D photonic crystals have the advantage of being made from a single material, although 3-D photonic crystals can require very complex fabrication methods [55, 72]. Many designs for 2-D photonic crystal emitters with high spectral selectivity exist, and they can be fabricated with lithographic methods [83–85].

Square type diffraction gratings have also been examined in previous works; however, they suffer from low NIR emittance due to their rapid change in index of refraction compared to conical structures as well as narrow absorption peaks [57, 83]. Emittance peaks can be broadened by combining multiple periods of gratings, but these structures still lack high emission in the visible and NIR regions [86]. Blazed gratings can have a higher emittance due to their graded index type behavior at wavelengths that are small compared to the grating period, and can maintain spectral selectivity through control of feature size [87, 88].

As with nanostructured W absorbing surfaces, the thermal stability of W nanostructured emitters can be low; however, protective hafnia (HfO_2) coatings and thermal annealing can help to alleviate this problem [41, 44]. The stability of these structures in both air and vacuum is promising and is another focus of this research.

2.3.3 Multi-band Emitters

Multi-band emitters are emitting structures that have two or more separated emission bands combined with multi-junction PV cells [82]. Although an STPV system with a perfect emitter would not benefit from multiple PV cell bandgaps because they are already spectrally matched, gains can be realized from multiple bandgaps in systems with broadband emitters. Utilizing multi-junction PV cells can also increase J_{emit} while maintaining high system efficiencies; however, the addition of a multi-junction PV cell also adds a significant amount of complexity to the STPV system [82, 89].

Multi-band emitters using several rare earth elements have been investigated by Wong et al. [90]. A combination of erbium and holmium oxides (Er_2O_3/Ho_2O_3) was used to create an emitting structure with two emission bands centered at 1550 and 2000 nm. GaSb and GaInAsSb PV cells with E_{bg}s of 0.73 and 0.5 eV were fabricated on separate cells to test the emitter. Wong et al. found that the emission band splitting would allow for higher device efficiencies if multi-junction GaSb PV cells could be produced [90].

Horner et al. proposed a Ga_2AsSb PV cell with separate ordered and disordered layers to produce a multi-junction PV cell for STPV devices [91]. They found that multi-junction PV cells could increase the efficiency of an STPV system with a blackbody emitter at 1700 K from 26% to 30% for a 2 junction PV cell; however, multi-junction devices require very low bandgaps for the lower PV cell junction and low bandgap PV cells have poor efficiencies due to high non-radiative recombination rates [34, 82, 92].

2.3.4 Comparison of Emitting Surfaces

Equation 1.5 was used to calculate η_{emit} for various emitting surfaces [88]. η_{emit} does not represent an overall system efficiency, and takes into account only the efficiency of the emitting surfaces. This consists of the fraction of emitted energy that can be used by a PV cell. The total available emitted spectral energy is found by multiplying the spectral emittance of a surface by the blackbody thermal radiation spectrum. A blackbody spectrum at 1700 K is used for matching with GaSb PV cells since they are commonly used in STPV systems [6, 25]. Table 2.2 shows η_{emit} and J_{emit} for various types of emitting surfaces. Note that these were calculated via equations 1.3, 1.4, and 1.5 using reflectance spectra reported by the various authors, and were not directly reported in literature.

For multi-band emitters, equation 1.4 must be modified with a separate absorption for each PV cell. Equation 2.2 shows the modifications for a dual-junction system:

$$J_{emit} = \int_{0}^{\lambda_{bg,bot}} \frac{E_{bg,bot}}{E_{photon}(\lambda)} E_{emit,\lambda}(\lambda,T)d\lambda + \int_{\lambda_{bg,bot}}^{\lambda_{bg,top}} \frac{E_{bg,top}}{E_{photon}(\lambda)} E_{emit,\lambda}(\lambda,T)d\lambda \tag{2.2}$$

where $E_{bg,bot}$ and $\lambda_{bg,bot}$ are the energy and photon wavelength at the bandgap of the bottom layer PV cell (with a larger E_{bg}), $E_{bg,top}$ and $\lambda_{bg,top}$ are the energy and photon wavelength at the bandgap of the top layer PV cell (with a lower E_{bg}), $E_{emit,\lambda}$ is the spectral irradiance of the emitting surface, and $E_{photon}(\lambda)$ is the energy of a photon of wavelength λ. Equations 1.3 and 1.5 remain unchanged.

Table 2.2 illustrates the high efficiency of the structures reported here. The periodic hole array on tungsten, NiO-doped MgO film, and the blazed grating on tungsten have a high J_{emit} coupled with efficient radiation. The NiO-doped MgO films have a high thermal stability, as do nanostructures on tungsten with the use of a protective oxide coating [42, 71]. High J_{emit} is important to maintain high efficiency in a complete STPV system. This effect will be discussed later in this work.

Table 2.2: Efficiency of selected emitting surfaces.

Emitter type	J_{emit} (W/cm^2)	η_{emit}
Ideal emitting surface for 1700 K STPV	53.3	0.84 (figure 1.3)
Periodic hole array on W	68.1	0.64 (this work)
NiO-doped MgO films	66.8	0.61 [71]
Blazed grating on tungsten	67.6	0.59 (this work) [88]
Anti-reflection coating on W	57.1	0.59 (this work)
Polished tungsten	27.3	0.56 [47]
Complex square grating on tungsten	63.8	0.53 [86]
1-D photonic crystal on W	45.5	0.53 [19]
Er doped titania nanofibers	37.5	0.53 [76]
Rare earth (Er) in aluminum garnet	30.6	0.52 [75]
Er_2O_3/Ho_2O_3 emitter (dual-junction)	38.4	0.52 [90]
Micro-cavity in tungsten	69.3	0.51 [3]
Blackbody emitter (dual-junction)	83.7	0.48 [91]
$Al_2O_3/Er_3Al_5O_{12}$ eutectic composite	37.2	0.41 [17]
Blackbody emitter	83.7	0.29

2.4 Combined Solar Thermophotovoltaic Systems

Thermodynamic models of combined STPV systems using the previously reported absorbing and emitting structures show efficiencies around 40% [3, 20, 39, 55, 85], with the non-ideal absorption of practical absorbing and emitting surfaces being the largest loss. Experimental efficiencies, however, have not yet reached these levels [15–19]. An experimental system efficiency of 0.02% was achieved using a graphite cavity as an absorbing surface and a Er_2O_3/Al_2O_3 eutectic emitter with GaSb PV cells. Sunlight was concentrated onto the system using a parabolic concentrator with ∼25000 sun concentration and 60% concentrator efficiency [17]. Efficiencies of 0.8% were obtained using blackbody absorbing surfaces with W emitters and Ge PV cells with ∼3200 sun concentration [15], while efficiencies of 1% were achieved using a similar system with GaSb PV cells and ∼4600 sun concentration [16].

An experimental STPV system with an efficiency of 3.2% was achieved using a carbon nanotube absorbing surface (α_{sol} and ϵ_{1700K} >99%) with a 1-D photonic crystal comprised of alternating Si and SiO_2 layers as the selective emitter [18]. This system used an InGaAsSb

PV cell with a small bandgap to allow efficient operation at lower temperatures compared to systems using Ge or GaSb PV cells. This lower temperature of operation allowed the photonic crystal to remain stable, as well as reducing the concentration required to reach operating temperatures. The concentration used in this system was ~750 suns; this was achieved using a xenon lamp with optical concentrators to simulate concentrated solar energy.

The highest experimental efficiency to date was 8% using a 1-D photonic crystal with layers of yttria-stabilized zirconia (YSZ) and tungsten for both the absorbing and emitting surfaces [19]. These surfaces had an η_{abs} of 0.74, an η_{emit} of 0.53, and a J_{emit} of 45.5 W/cm^2. This setup also used a planar geometry, and operated at 1640 K using GaSb PV cells with a concentration ratio of 450 suns, achieved with a solar simulator setup. Due to the use of a solar simulator, losses due to the solar concentrator system are not accounted for in this research. A water cooling system was used to keep the PV cells cool; however, its energy requirements were not included in the efficiency data. A passive cooling system could potentially be used to remedy this issue.

While many promising absorbing/emitting surfaces have been examined for use in STPV systems, more research is needed to enhance their efficiency and thermal stability. Additionally, many surfaces and STPV devices have been simulated but never experimentally demonstrated, creating a need for further exploration of fabrication methods and verification of modeled data. The data in this chapter has been submitted for publication as part of an invited review article for the journal Optics Express [93].

Chapter 3: STPV System Fundamentals and Modeling

In order to investigate the use of new materials in STPV systems, the effect of material properties on system performance is determined. First, a thermodynamic model of an entire STPV system was developed. This allows the overall efficiency and individual losses in the system to be calculated based on system parameters and the spectral emission of the absorbing and emitting surfaces. Ideal surface properties are identified, and system parameters are optimized. Once an understanding of the ideal emission spectrum is obtained, the emission spectra of various material systems can be determined.

In general, techniques to model the reflectance, and therefore emissivity, of a surface fall into two categories: wave-regime techniques which take interference effects between electromagnetic waves into account, and particle-regime techniques that ignore them. In order to determine which regime must be used, the coherence length of incoming radiation is taken into account. The coherence length of radiation is given by $L_C = \frac{c}{\Delta\nu}$ where L_C is the coherence length, c_0 is the speed of light in a vacuum, and $\Delta\nu$ is the frequency-bandwidth of the radiation [94]. For blackbody radiation, such as radiation from the sun, the coherence length is on the order of the wavelength of highest emission given by Planck's law (501 nm for solar radiation) [95, 96].

In cases where the feature size of a surface is much larger than the coherence length of incoming radiation, interference and diffractive effects can be ignored and a ray-tracing model (a classical-regime technique) will give accurate results [97, 98]. For flat (1-D) structures with feature sizes on the order of or smaller than the coherence length, surface reflectance can be found by solving the Fresnel equations via the transfer matrix method (TMM), which is a wave-regime technique [99]. For textured (2-D or 3-D) structures, TMM modeling can only be used with effective medium theory (EMT) when the feature sizes of the surface are smaller than the wavelength of incoming radiation [100]. When the feature sizes of a textured surface are on the order of a wavelength, a finite difference time domain (FDTD) model must be used [26]. While FDTD modeling can determine the reflectance of surfaces with arbitrary shape and dielectric constants, it is extremely computationally intensive and can be difficult to run on larger sample sizes with fine resolution [27]. This chapter will cover the application of the previously mentioned modeling techniques for STPV systems.

3.1 STPV System Model

A thermodynamic model for an STPV system was developed. The STPV system can be broken down into a series of components with individual efficiencies that are multiplied together to obtain an overall efficiency [101]. While these losses are affected by the system temperature, each loss can be looked at as an individual function of temperature, unrelated to other losses. In the model, incoming solar energy is simulated with an air-mass 1.5 (AM 1.5) solar spectrum [24]. Diffuse energy is not included in this simulation since it is not captured by solar concentrators. This energy is concentrated and absorbed by the absorbing surface with efficiency dependent upon α_{sol}. The system is operated under a vacuum, as this reduces thermal losses due to convection and protects the nanostructures from oxidation [4, 102].

The temperature of the absorber-emitter structure, pictured in Figure 1.1, rises until thermal equilibrium is reached, with the assumption that temperature is constant at every point within the structure. This is accurate for the thin planar systems primarily modeled here but may be less accurate for thick cylindrical systems. Energy escapes this structure via heat conducted through the mechanical supports, convection, thermal energy radiated out of the top and sides, and thermal energy emitted from the emitter. The area ratio of absorber to emitter, the distance from the emitter to the PV cell, and the height of the absorber-emitter structure are important geometrical factors in this model. The inside of the vacuum chamber

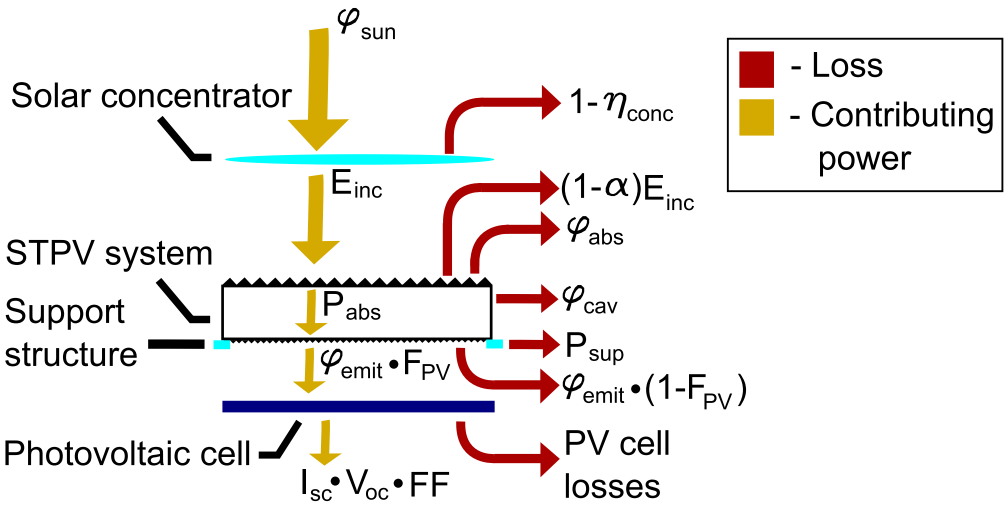

Figure 3.1: The flow of power through an STPV system, showing each system component and the power remaining after each loss. η_{total} is given by $I_{sc} \times V_{oc} \times FF$ divided by the input power, ϕ_{sun}. Each loss is discussed in further detail in this chapter.

is covered in a reflective material to minimize radiative losses from the top and sides of the structure. Figure 3.1 shows the flow of power through this system.

The overall efficiency of the STPV system, η_{total}, is given by the efficiency of the PV cell output, and can be expressed as:

$$\eta_{total} = \frac{I_{sc} \times V_{oc} \times FF}{\phi_{sun}} \tag{3.1}$$

where ϕ_{sun} is the radiant flux incident on the solar concentrator, I_{sc} is the short circuit current of the cell, FF is the fill factor of the cell, and V_{oc} is the open circuit voltage of the cell. Here, it is assumed that 1000 W/m^2 of solar energy is available to be captured by the solar concentrator [24], so that $\phi_{sun} = 1000A_{conc}$ where A_{conc} is the collection area of the solar concentrator in square meters.

Emitted radiation that falls on the PV cell will generate photocurrent:

$$I_{sc} = qA_{PV}\int_0^{\infty} \frac{\lambda}{hc} F_{PV}(1 - R_{PV})\phi_{emit,\lambda}(\lambda, T) \cdot EQE(\lambda)d\lambda \tag{3.2}$$

where q is the charge of an electron, A_{PV} is the area of the cell, $\frac{hc}{\lambda}$ is the energy of a photon, h is Planck's constant, F_{PV} is the view-factor between the emitter and PV cell, R_{PV} is the reflectance of the PV cell, and $EQE(\lambda)$ is the spectral external quantum efficiency of the cell. $\phi_{emit,\lambda}(\lambda, T)$ is the spectral radiant flux from the emitting surface and is given as follows:

$$\phi_{emit,\lambda}(\lambda, T) = E_{emit,\lambda}(\lambda, T) \times A_{emit} \tag{3.3}$$

where $E_{emit,\lambda}(\lambda, T)$ is the spectral irradiance of the emitting surface given in equation 1.3 and A_{emit} is the area of the emitting surface.

Assuming an isothermal structure, the steady-state temperature of this system is determined by:

$$P_{abs} - \phi_{abs}(T) - \phi_{cav}(T) - P_{sup}(T) - P_{conv}(T) - \phi_{emit}(T) = 0 \tag{3.4}$$

where P_{abs} is the power absorbed by the absorbing surface, $\phi_{abs}(T)$ is the radiant flux emitted by the absorbing surface and lost, $\phi_{cav}(T)$ is the radiant flux lost from the sides of the STPV system, $P_{sup}(T)$ is the power lost through conduction via the supporting structure, $P_{conv}(T)$ is the power lost through convection, and $\phi_{emit}(T)$ is the total radiant flux from the emitting surface, equal to $\int_0^\infty \phi_{emit,\lambda}(\lambda, T) d\lambda$. This equation is solved iteratively using Newton's method, and this temperature is then used to find the overall efficiency of the STPV system.

P_{abs} and $\phi_{abs}(T)$ are given by:

$$P_{abs} = \int_0^\infty A_{abs} E_{inc,\lambda}(\lambda) \alpha(\lambda) d\lambda \tag{3.5}$$

$$\phi_{abs}(T) = \int_0^\infty A_{abs} \epsilon(\lambda) B(\lambda, T) d\lambda \tag{3.6}$$

where A_{abs} is the area of the absorbing surface.

Note that $(P_{abs} - \phi_{abs}(T))$ divided by the power incident on the absorbing surface is equal to η_{abs} found in equation 1.1.

ϕ_{cav} can be found by simply multiplying the surface area of the sides of the STPV system by their radiant flux per unit area:

$$\phi_{cav} = B(\lambda, T)\epsilon_{sides}A_{sides} \tag{3.7}$$

$P_{sup}(T)$ is found via a fin approximation, valid here due to the support's small Biot number [18, 103]. The Biot number is given by:

$$Bi = H(A_c/P)/k \tag{3.8}$$

where H is the heat transfer coefficient, P is the perimeter length, k is the thermal conductivity of the support, and A_c is the cross-sectional area of the support. $P_{sup}(T)$ is then found from:

$$P_{sup}(T) = (T_{env} - T)\sqrt{HPkA_c}\tanh(mL) \tag{3.9}$$

$$mL = \sqrt{\frac{PH}{kA_c}}L \tag{3.10}$$

where T_{env} is the temperature of the surrounding environment, assumed here to be 300 K, L is its length, and mL is a dimensionless quantity given by equation 3.10.

The convective loss, P_{conv}, is found via equations for natural convection from a horizontal plate with an additional adjustment for the system pressure: [102, 104]:

$$Pr = \frac{\mu C_p}{k} \tag{3.11}$$

$$Gr = \frac{L^3P^2\beta \cdot g(T_{env} - T)k}{\mu^2} \tag{3.12}$$

$$Ra = Pr \cdot Gr \tag{3.13}$$

$$Nu = .54Ra^{(1/4)} \tag{3.14}$$

$$P_{conv} = \frac{V_{coeff}Nu \cdot kTA_{emit}}{L} \tag{3.15}$$

where C_p is the specific heat of the convective gas, μ is the dynamic viscosity, β is the coefficient of thermal expansion, g is the acceleration due to gravity, V_{coeff} is the additional coefficient due to the presence of a vacuum (extrapolated from literature to be 0.05 [102]), Pr is the Prandtl number, Gr is the Grashof number, Ra is the Rayleigh number, and Nu is the Nusselt number.

3.1.1 The Ray Tracing Method

The ray tracing method is used in conjunction with the thermodynamic model to find values for F_{PV}, R_{PV}, and η_{conc}. In this method, asymptotic solutions to the wave equations are found when the wavelength goes to 0 [105]. This leads to the derivation of Fermat's principle, from which Snell's law of refraction and the law of reflection can be found [94]. The Fresnel equations are used with the dielectric constants of materials to determine reflected intensity, and the combination of reflection and refraction is used to trace rays through the system [106].

Snell's law of refraction, the law of reflection, and the Fresnel equations for S and P polarized light are as follows:

$$n_1 \sin\theta_i = n_2 \sin\theta_t \tag{3.16}$$

$$\theta_i = \theta_r \tag{3.17}$$

$$R_S = \left|\frac{n_1 \cos\theta_i - n_2 \cos\theta_t}{n_1 \cos\theta_i + n_2 \cos\theta_t}\right|^2 \tag{3.18}$$

$$R_P = \left|\frac{n_1 \cos\theta_t - n_2 \cos\theta_i}{n_1 \cos\theta_t + n_2 \cos\theta_i}\right|^2 \tag{3.19}$$

where θ_r is the angle of reflectance, θ_t is the angle of transmittance, θ_i is the angle of incidence, n_1 is the initial index of refraction, and n_2 is the index of refraction of the material the photon is entering.

η_{conc} is determined by the percentage of rays incident on the solar concentrator that reach the substrate, found by tracing incoming rays through the concentrator system. Ideal optical

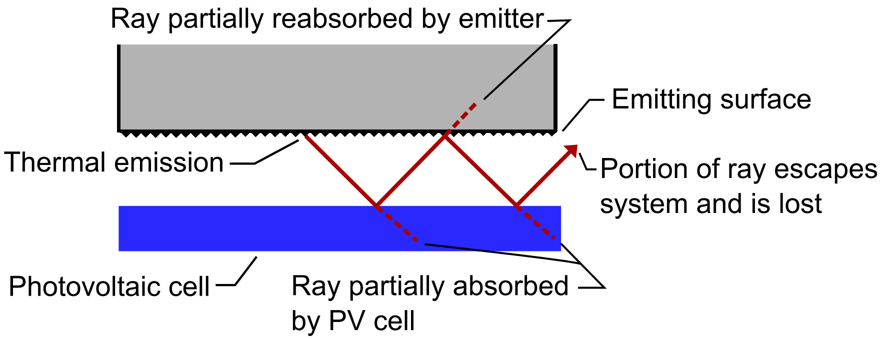

Figure 3.2: The path of an emitted ray through a simple STPV system. The emitted ray will be partially absorbed by the PV cell, partially re-absorbed by the emitting surface, and partially lost. The addition of mirrors on the side of the system can reduce this loss. A ray tracing model is used to determine the power of these rays.

elements are assumed for theoretical calculations; however, measured spot size, efficiency, and focal length are used for calculations of real-world lenses. The power and uniformity of light focused by the concentrator can be found via this method, and η_{conc} is given by integrating across the absorber area.

To find F_{PV} and R_{PV}, rays are traced from the emitting surface to the PV cell. Rays are emitted from the emitting surface according to the angular emittance and Lambert's cosine law. The ray is followed through the system, and the portion of the ray's power that is absorbed by the PV cell and substrate is recorded. The Fresnel equations are used to find the reflectance of the PV cell at various angles of incidence. Figure 3.2 shows the path of a ray through the system for a simple linear geometry. Inputs into this portion of the model include the angular emittance of the emitter, the PV cell index as a function of wavelength, PV cell size, emitter size, and the distance from the emitter to the PV cell.

3.2 Surface Emissivity

3.2.1 The Transfer Matrix Method (TMM)

The TMM, derived from Maxwell's equations, allows the reflectance, transmittance, and absorption of 1-D structures made from the addition of many homogeneous and isotropic layers of arbitrary refractive indices and thicknesses to be calculated. Each layer of a system is represented as a 2×2 transfer matrix, and these matrices are multiplied together to find the system transfer matrix, from which the overall reflection and transmission coefficients can be found [107]. The 2×2 transfer matrix for each optical element can be found by multiplying a transmission matrix, given by the Fresnel coefficients (equations 3.18 and 3.19), and a propagation matrix which contains the phase information of the elements [108].

Thin layers with thickness on the order of the wavelength of incident radiation cause interference effects while thicker layers are treated with an incoherent approximation to prevent high-frequency oscillations. This results in a stable solution for any layer thickness [109]. Thick layers do not cause interference effects due to surface roughness and the coherence length of the radiation [99]. The TMM is primarily used here to find the reflectance of absorbing and emitting surfaces consisting of dielectric stacks (1-D photonic crystals). The reflectivity of PV cells with anti-reflection coatings are also found using this method.

Effective Medium Theory (EMT)

EMT can also be used with the TMM to find the reflectance of surfaces with 2-D or 3-D surface textures. In EMT, a structure made from multiple materials is represented as a single material with an effective refractive index that is calculated from the dielectric constant and filling factor of the constituent materials. Since only a single effective refractive index is used, the resulting material is homogeneous and information about the scattering properties of the material is lost. Therefore, this method is only accurate for sub-wavelength sized textures that do not exhibit significant high-order ($m>0$) diffraction [110].

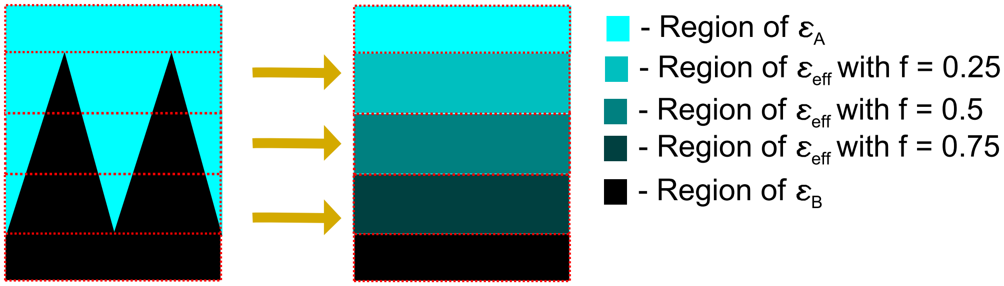

Figure 3.3: A nano-cone array is broken down into a sum of layers of varying n$_{eff}$. Many layers (∼100) were interpolated in the EMT model; only 5 are shown here for clarity.

Common methods to describe the effective medium of arbitrary structures include the Maxwell Garnett, Lorentz-Lorentz, and Bruggeman theories. The Bruggeman theory is primarily used here due to the fact that it is accurate for a wide range of material ratios and is symmetric, so that the choice of which material is specified as the inclusion and which is specified as the matrix does not effect the results [100, 110, 111]. This is important when working with dual-material systems where either material might be considered the inclusion. The effective dielectric constant, originally derived by Bruggeman in his 1935 paper [112], is given by [100]:

$$f\frac{\epsilon_A - \epsilon_{eff}}{\epsilon_A + 2\epsilon_{eff}} + (1-f)\frac{\epsilon_B - \epsilon_{eff}}{\epsilon_B + 2\epsilon_{eff}} = 0 \tag{3.20}$$

where ϵ_{eff} is the effective dielectric constant, ϵ_A is the dielectric constant of material A, ϵ_B is the dielectric constant of material B, and f is the percentage of material having $\epsilon = \epsilon_A$. The effective refractive index of the material, n$_{eff}$, is then simply $\sqrt{\epsilon_{eff}}$.

The EMT with the Bruggeman method is used here to find the reflectance of moth-eye type structures consisting of arrays of nano-cones, which is a common application of this theory [113, 114]. These structures provide broadband absorption for textures with height greater than 0.4λ and an inter-cone spacing less than $\lambda/2n$, where n is the refractive index of the matrix material [110, 115]. To apply the EMT to a nano-cone structure, f is varied as a function of height in the structure, and the structure is broken down into many (∼100) thin-film layers, as seen in Figure 3.3 [110]. The reflectance can then be calculated using the

TMM.

3.2.2 The Finite Difference Time Domain (FDTD) Method

This work also uses the FDTD method to simulate the effect of various nanotextures on the reflectance spectrum of metal substrates. In an FDTD simulation, a solution is found by iteratively solving Maxwell's equations on a grid [26, 27]. The time-dependent Maxwell's equations are discretized via a central-difference approximation. A leapfrog method is then used to solve the discretized equations on a spatial grid called a Yee lattice: first the electric field vector components at each point in the lattice are solved, then the magnetic field vector components are solved for neighboring grid points for the next time-step, and so on [116]. This method has been further refined and applied for a large variety of applications [26], and FDTD simulations for this work were run using an open-source implementation called the MIT Electromagnetic Equation Propagation (MEEP) package [117].

An inherent advantage of the FDTD method is the ability to simulate the properties of a material over a wide range of frequencies in a single run using a Gaussian source. This greatly reduces the computation time needed to run a simulation at multiple frequencies and allows smooth reflectance curves to be generated. The FDTD method also takes into account scattering and resonant phenomena, allowing it to be accurate for feature sizes that are on the order of a wavelength.

One disadvantage of the FDTD method (and numerical methods in general) is that errors can be introduced because of the discretization of phenomena. In the FDTD method, pixelization of objects, and staircasing of diagonal interfaces in particular, is an issue due to computational restraints on the resolution of the spatial grid used. This error can be greatly reduced by the use of subpixel smoothing; this has been implemented in the simulations used here [117, 118].

Because Maxwell's equations are solved in the time domain, inputs into the simulation must be given in the time domain. This can be a problem when searching for material dispersion parameters, as most research on optical material properties is conducted in the frequency domain. Accurate Fourier transforms require optical data spanning large frequency ranges which are not typically measured, so to accurately model dispersive materials in the time domain, functions for which analytical Fourier transforms are known are used. The most common functions for describing the relative dielectric function (ϵ_r) of materials in FDTD simulations are based off the Lorentz and Drude models [26].

The Lorentz-Drude Model

A Lorentz-Drude (LD) oscillator model was used to simulate the relative dielectric function of metals in the wavelength range 0.2 to 10 μm. Since only non-magnetic materials are simulated in this report, permeability is assumed to be 1. The LD model here consists of the sum of a Drude term plus multiple Lorentzian terms.

The Drude term is calculated via the Drude model, or free electron model, which describes the intraband (bound-electron) effects within a metal [119, 120]. This can be used to calculate the complex relative dielectric function of the metal for regions where interband contributions are small (typically mid-infrared and lower photon energies). The relative dielectric function of a metal as given by the Drude model is given by:

$$\epsilon(\omega) = 1 - \frac{f_0 \omega_p^2}{\omega^2 + i\Gamma_0 \omega} \tag{3.21}$$

where ω is the angular frequency of the electromagnetic wave, ω_p is the plasma frequency, f_0 is the oscillator strength, and Γ_0 is the damping constant of the oscillator.

In higher energy regions, the correct relative dielectric function can be obtained via the addition of multiple Lorentzian oscillators to account for interband transitions [121]. The approximate dielectric function for a metal using one Drude and four Lorentzian terms is:

$$\epsilon(\omega) = \epsilon_\infty - \frac{f_0 \omega_p^2}{\omega^2 + i\Gamma_0 \omega} - \sum_{j=1}^{4} \frac{f_j \omega_p^2}{\omega_j^2 - i\omega\Gamma_j - \omega^2} \tag{3.22}$$

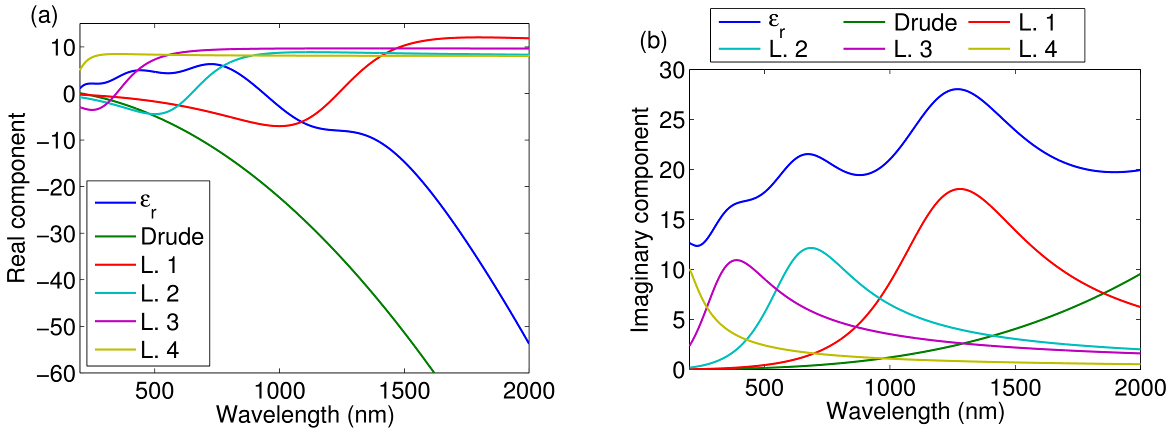

Figure 3.4: a) real part and b) imaginary part of the Drude plus four Lorentzian operators and ϵ_r for tungsten found via experiment and the Kramers-Kronig relation [122]. The sum of the Drude and four Lorentzian operators is equal to ϵ_r, as shown in Figure 3.5. L. terms in the legends refer to Lorentzian components.

where ω_j is the frequency of oscillator j, f_j is the strength of oscillator j, ϵ_∞ is the dielectric constant of the material at a frequency of infinity, and Γ_j is the damping constant of oscillator j.

Specific constants for tungsten are given by Rakic et al. [122]. These constants were found by fitting LD parameters to a relative dielectric function found by applying the Kramers-Kronig relation to experimental reflectance data obtained for polished tungsten substrates [123]. The inclusion of four Lorentzian terms is sufficient to accurately describe the refractive index of tungsten in the visible and near-IR bands.

Equation 3.22 is solved with the values given by Rakic et al. for tungsten, and the individual contributions of each Drude and Lorentzian term to the relative permittivity (ϵ_r) are shown in Figure 3.4. This illustrates the significant contribution of Lorentzian oscillators in the visible band, and the increasing accuracy of the Drude term alone as photon energy decreases.

Figure 3.5 shows a comparison between reflectance data found in literature and the simulated absorbance for a flat tungsten substrate [47, 122]. Good agreement was found,

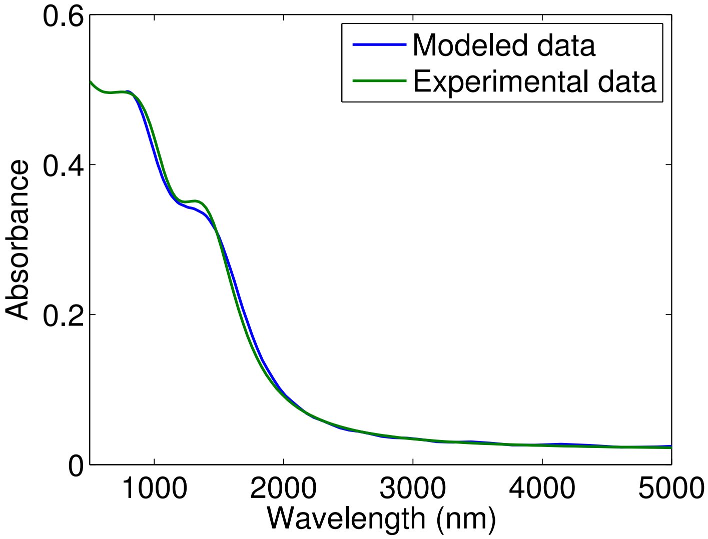

Figure 3.5: A comparison between simulation and data found in literature for the absorbance of flat tungsten, showing good agreement [122].

showing the accuracy of the Drude and Lorentzian constants used in this research. The small discrepancy between modeled and experimental data is due to the use of only 4 Lorentzian oscillators. The addition of more oscillators, or of modified Lorentzian operators can improve matching; however, the surfaces differ by less than 1% and modified Lorentzian values are not readily available for tungsten in literature [124].

Finite Difference Time Domain Simulation Setup

Computation time on the Carbon cluster at Argonne National Labs (ANL) was awarded via a no-cost user proposal, and this was used to run the MEEP model. Coding for this project was done in two separate portions, one using C++ and one using MATLAB, which were linked together and run on the Carbon cluster. Dr. Stephen Gray of ANL provided collaboration and guidance on this portion of the research.

In the simulation, a Gaussian source is used to excite electrical and magnetic fields traveling in the negative Z (vertical) direction, and an object is specified by setting the dielectric constants of a 3D grid at each point. Two simulations are run, one with S-polarization and

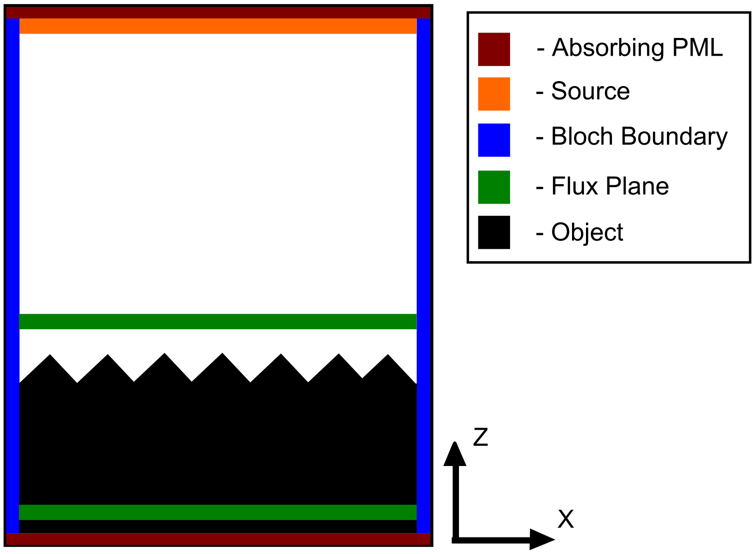

Figure 3.6: The FDTD simulation setup, showing locations and types of boundary conditions, flux planes, a Gaussian source, and the object.

one with P-polarization, and they are averaged to obtain polarization independent reflectance. Absorbing perfectly matched layer (PML) boundary conditions in the XY plane were used at the ends of the Z axis, while Bloch periodic boundary conditions in the XZ and YX planes were used at the ends of the X and Y axes, allowing infinitely large structures to be simulated.

The surfaces described in this report were simulated with a 1 µm substrate beneath the nanotextures to ensure that the substrate thicknesses exceed their skin depths. Transmission was simulated to be negligible through this substrate. The electromagnetic flux through two different flux planes was used to calculate reflectance, absorbance, and emittance from the structures. A diagram of the simulation setup can be seen in Figure 3.6.

MATLAB was used to create 3D surface files that specify the height (in the Z direction) of the surface of an object at each point on a 2D grid in the XY plane. The object is assumed to be solid down to the 1 µm thick substrate. The surface locations are specified either through a geometrical function or from data obtained with a scanning electron microscope (SEM) image. The resolution of the surface is specified in the MATLAB program, and varies from 1 to 50 nm depending on the smallest feature size and wavelength range simulated.

The C++ portion of the code specifies the parameters used in the simulation as well as the type and location of the electromagnetic source. All simulations set the source wave in the far-field at a 1 µm stand-off distance to ensure proper plane wave propagation. The resolution of the FDTD simulation is taken to be the same as the resolution of the surface file to avoid errors due to the interpolation of the surface file by MEEP. The simulation is run for 10 times longer than necessary for the shortest wavelength light beam to propagate through the entire grid to ensure that resonant or plasmonic modes have had enough time to propagate before the simulation is ended.

To calculate the reflected power, a simulation is first run with no object to obtain the incident wave power through flux planes 1 and 2 ($P_{01,02}$). Next, the simulation is run with the object present, and the power through flux plane 1 and 2 is again recorded ($P_{s1,s2}$). Then, the percent of power reflected (P_r) and transmitted (P_t) can be found through the following equations 3.23 and 3.24:

$$P_r = \frac{P_{s1} - P_{01}}{P_{01}} \tag{3.23}$$

$$P_t = \frac{P_{s2}}{P_{02}} \tag{3.24}$$

To test the stability of the simulation, the resolution, grid size, and simulation time were varied one at a time. The simulation was deemed stable when changing these parameters had an effect of less than 0.1% on the reflectance or transmission of the structure. An example of the change in integrated reflectance and transmission due to simulation time on a flat tungsten substrate is illustrated in Figure 3.7.

Bloch periodic boundary conditions with a Bloch wave-vector of e^{ikx}, where x is the position along the X-axis, and k is the Bloch wave-vector, were used to allow incoming waves to propagate at an angle [125]. k is defined here by $\frac{\omega}{c_0}\sin\theta$ where ω is the angular frequency of the propagating light, c_0 is the speed of light in a vacuum, and θ is the angle of incidence.

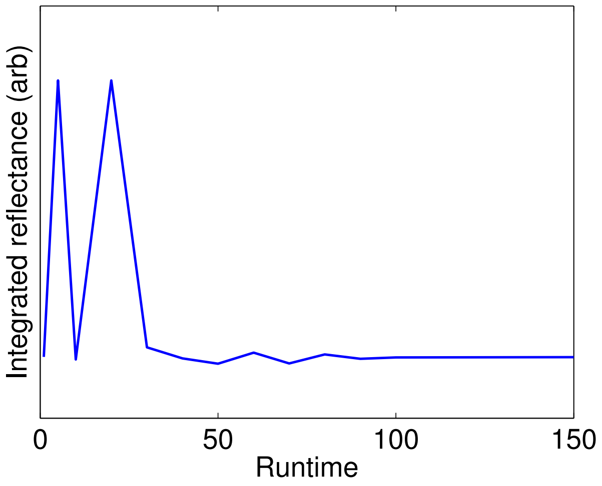

Figure 3.7: Change in integrated reflectance due to simulation time, showing convergence for long runtimes.

To specify a tilted Gaussian source in MEEP, the amplitude function of the source is set to $e^{2\pi iky}$, where y is the position along the Y axis (for a beam tilted in the Y direction). Since the amplitude function of the source depends on the frequency of the light being simulated, angular simulations must be done in a very narrow bandwidth. Due to this, the angular dependence of the reflection spectra must be found at a single frequency for each simulation, with multiple simulations being required for an angle-dependent absorption spectra.

Pseudo-Random Surfaces

Random surface elements were added to the simulations of some absorbing surfaces to explore their effect on light absorption. The MATLAB portion of the FDTD program was modified to place multiple features on a large unit cell to allow variance in the properties of each feature. The height and radius were varied according to a Gaussian distribution with the center and standard deviation specified. A Gaussian function was used to simulate the distribution of structure shapes under experimental conditions. To place the features within the grid, the program looked at the total overlap between new and existing features at each possible placement and chose a location with overlap $<10\%$. This is similar to a dart-throwing

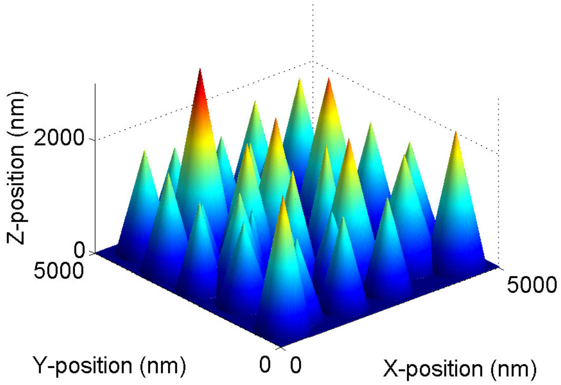

Figure 3.8: Surface plot of nano-cones with randomized placement, height (variance = 1000 nm, average = 1000 nm), and radius (variance = 500 nm, average = 500 nm) on a 5000 nm^2 grid [61].

algorithm with a Poisson distribution [126]. Figure 3.8 shows an example of pseudo-random nano-cones in a 5000 × 5000 nm grid [61].

This model was also used to predict the location of resonant absorption peaks in a sample fabricated by Ankit Shah et al. in a paper published in *Solar Energy Materials and Solar Cells* [127]. Good agreement between modeled and experimental data was seen, although the limited resolution on scanning electron microscope images of the surface prevented a perfect match.

3.3 Conclusion

A thermodynamic simulation of an STPV system was developed and combined with various electromagnetic simulations to create a simulation of a complete STPV system. By using a combination of FDTD, Fresnel, EMT, and raytracing models, the interactions of light with a broad range of wavelengths is able to be simulated, allowing the reflectance and absorbance of a wide array of surfaces to be determined. The completed model takes into account many loss vectors in STPV systems, and allows the system design to be optimized over a variety of parameters. In the next chapters, this model will be applied to design an experimental system and then used to pinpoint the losses in this system.

Chapter 4: Modeled Solar Thermophotovoltaic System Design Results

This chapter uses the models laid out in chapter 3 to simulate the performance of various STPV systems. First, an ideal system is looked at to get an idea of the fundamental limits in STPV operation. Next, some practical considerations for the ideal system are examined, and the power output per PV cell area of the system is examined. After this examination, the potentials of different absorbing and emitting surfaces are considered, and their feasibility for fabrication is discussed. A practical STPV system with very high efficiency is simulated, and the losses in such a system are examined.

4.1 Ideal Solar Thermophotovoltaic System

Here, the requirements and performance of an ideal STPV system are examined with the goal of gaining a fundamental understanding of STPV system operation. The STPV system can be seen as a heat engine with the emitting surface as the hot side and the PV cell as the cold side. Here, we assume an ideal emitting surface that emits photons monochromatically at the E_{bg} of a PV cell, with all emitted radiation reaching the cell, and an ideal PV cell operating at the radiative limit, $\eta_{emit} = 1$. The only losses in the STPV system are then the Carnot efficiency and absorbing surface efficiency [128]. In this ideal system, radiative recombination in the PV cell will be re-absorbed by the emitting surface and will not contribute to a loss in efficiency.

The Carnot efficiency (η_{carnot}) of such an engine is given in equation 4.1:

$$\eta_{carnot} = 1 - T_{env}/T \tag{4.1}$$

where T is the temperature of the heat engine and T_{env} is the temperature of the surrounding environment. Assuming an ideal solar concentrator with $\eta_{conc} = 1$ and C $\cong$ 46000 (the maximum achievable solar concentration [129]), combined with an absorbing surface with $\alpha = 0$ above a cutoff wavelength (λ_{cutoff}) and $\alpha = 1$ below λ_{cutoff}, equation 1.1 can be reduced to:

$$\eta_{abs}(T) = \frac{\int_0^{\lambda_{cutoff}} \{C \cdot E_{sun}(\lambda) - B(\lambda, T)\}\, d\lambda}{\int_0^{\infty} C \cdot E_{sun}(\lambda) d\lambda} \tag{4.2}$$

$$B(\lambda, T) = \frac{2\pi hc^2}{\lambda^5} \frac{1}{e^{\frac{hc}{\lambda k_B T}} - 1} \tag{4.3}$$

where k_B is the Boltzmann constant, and c is the speed of light in a vacuum.

The efficiency of an ideal STPV system at various temperatures can be found by multiplying equation 4.1 by 4.2. Since the Carnot efficiency increases with increasing T, and η_{abs} decreases with increasing T, finding the ideal efficiency for an STPV system can be considered a maximization of $\eta_{carnot} \cdot \eta_{abs}$, with T and λ_{cutoff} as input variables. The results of this maximization are shown in Figure 4.1. The highest efficiency was 84% at a temperature of 2300 K and a λ_{cutoff} of infinity. This compares extremely favorably to the Shockley-Queisser limit of about 32% on the efficiency of PV cells. The primary reasons for such a high efficiency limit are the broadband absorption of the absorbing surface combined with the monochromatic radiation received by the PV cell. Interestingly, this monochromatic radiation also means that system efficiency does not depend on PV cell bandgap in the ideal case.

Note that at maximum concentration, the ideal absorbing surface is a blackbody; however, spectrally selective absorbing surfaces will begin to play a larger role when concentrations below the theoretical maximum are considered.

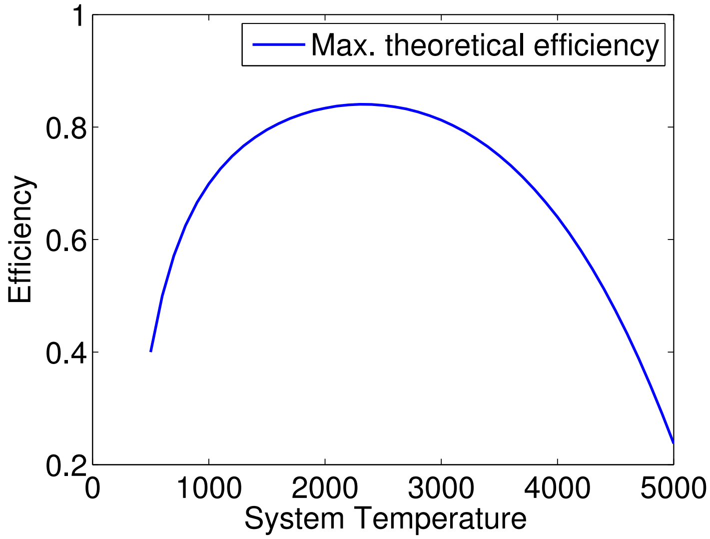

Figure 4.1: The maximum efficiency of an ideal STPV system at various temperatures given by multiplying equations 4.1 and 4.2.

4.1.1 Practical Considerations

The ideal system described here will have a P$_{emit}$ of 0 according to equation 1.4 because $\epsilon_s(\lambda)$ is an impulse function with a height of 1, so the integral of $\epsilon_s(\lambda)$ over λ is equal to 0. This results in the requirement of an infinitely large emitting area for useful power to be harvested from the device.

System temperature is found from the balance of energy given in equation 3.4. In order for an equilibrium temperature of 2300 K to be reached, P_{abs} must equal $\phi_{abs}(2300) + \phi_{emit}(2300)$ (ϕ_{cav}, P_{conv}, and P_{sup} are equal to 0 for an ideal system). At maximum concentration (46000), the irradiance of the sun is equivalent to the irradiance at the surface of a blackbody with temperature 5778 K [129]. Assuming blackbody emission for the absorbing surface ($\epsilon = 1$), and using the Stefan-Boltzmann law for the irradiance of a blackbody, given in equation 4.4, the required ratio between emitter and absorber area to reach an operating temperature of 2300 K is expressed as A$_{ratio}$ in equations 4.5 and 4.6 as a function of the emitted radiant

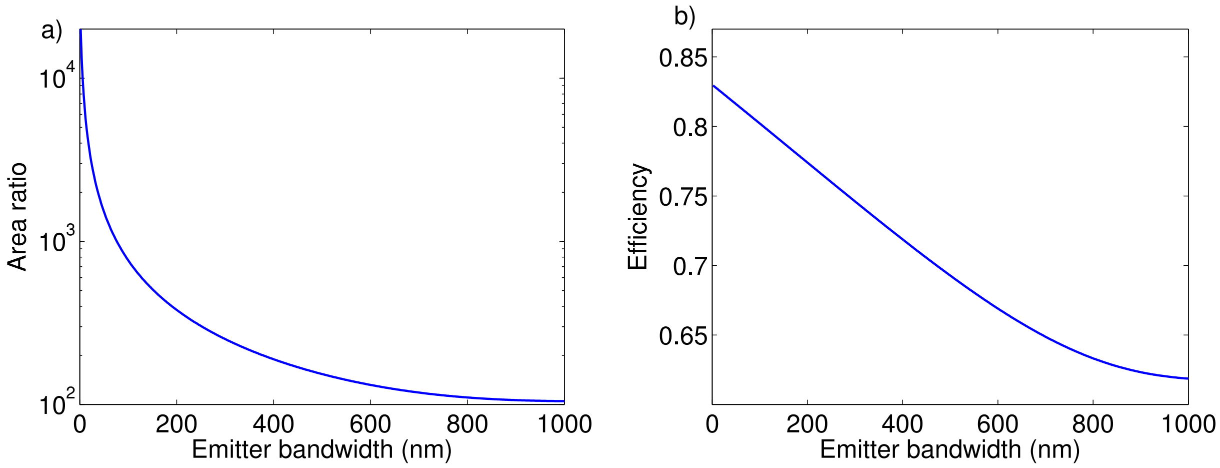

Figure 4.2: Graph of a) emitter-absorber area ratio vs. emitter bandwidth, and b) system efficiency vs. emitter bandwidth of an ideal STPV system at an operating temperature of 2300 K.

power per unit area, J_{emit} (from equation 1.4):

$$J = \sigma T^4 \tag{4.4}$$

$$A_{ratio} = \frac{A_{emit}}{A_{abs}} = \frac{J_{emit}}{E_{sun} - E_{abs}} \tag{4.5}$$

$$= \frac{J_{emit}}{1.09 \times 10^{15} \sigma} \tag{4.6}$$

where σ is Stefan's constant, and the factor 1.09×10^{15} is the difference between the temperature of the absorbing surface to the fourth power (T_{abs}^4) and the temperature of the emitting surface to the fourth power (T_{emit}^4).

Increasing the bandwidth of the emitting surface, as shown in Figure 1.3, will increase the emitted power and reduce the area ratio required for maximum efficiency, but will also reduce the overall system efficiency from the ideal. Figure 4.2a shows the A$_{ratio}$ required for various emitter bandwidths, while Figure 4.2b shows the system efficiency at each emitter bandwidth.

While adding a small bandwidth to the emitting surface will result in a finite emitter area requirement, Figure 4.2a shows us that this area remains extremely large while Figure 4.2b shows that a large drop in efficiency is associated with large emitter bandwidths. While designs such as cylindrical STPV systems (shown in Figure 1.1b) can increase A_{ratio}, extremely high ratios are not practical to achieve. Additionally, A_{PV} must be greater than or equal to A_{emit} for efficient operation, so an extremely large A_{emit} is impractical from an economic standpoint. The STPV system must be operated at a lower concentration and temperature to reduce the emitter area requirement; this also has the advantage of increasing material stability.

Besides these issues, perfect PV cells operating at the radiative limit, perfect absorbing and emitting structures, and perfect solar concentrators operating at a concentration of 46000 are not currently achievable. The following sections will examine an STPV system part by part from a practical standpoint to determine optimal operating points for an experimental system.

4.2 Practical System Design

4.2.1 Solar Concentrators

Solar concentrators are important aspects of solar thermal, concentrated photovoltaic, and STPV systems. In practice, a higher concentration will always result in a more efficient system because η_{abs} will always increase with concentration; however, extremely high solar concentrations can result in a high A_{emit} being required for high efficiency operation, as mentioned earlier.

While 46000 is the ultimate limit of the solar concentration ratio, systems that attempt extremely high concentration ratios are typically not practical [129]. Parabolic type solar concentrators can provide for up to 3000 suns, while Fresnel lenses have been shown to achieve over 1000 suns [3, 30, 130]. The combination of a Fresnel lens with a secondary meniscus lens can allow higher concentrations to be achieved, increasing the potential concentration ratio to 2500 [30].

Fresnel lens systems can have an efficiency of up to 80%, while the addition of a secondary lens reduces this efficiency to 75% [18, 30]. For the purpose of optimizing the system, a maximum concentration of 2500 suns is used, which comes from ease of use considerations provided by Fresnel lenses as well as system efficiency scaling with increased concentration levels [15–18, 130].

4.2.2 System Temperature

The thermal stability of tungsten nanostructures limits the operating temperature of the system to about 1700 K [41, 44]. Even though the ideal system efficiency is at 2300 K, diminishing returns in system efficiency per increase in degree Kelvin above 1000 K show that a 1700 K will prove to be both practical and efficient. The change in efficiency with change in system temperature will be further explored in section 4.2.7.

4.2.3 Emitter to Absorber Area Ratio

Once the concentration ratio is fixed at 2500 and the temperature at 1700 K, the optimum A_{ratio} may be determined. While cylindrical systems allow for easy control over A_{ratio} and a relatively large A_{emit}, in planar systems the size of the absorbing and emitting surfaces must remain the same. To increase A_{ratio} in a planar system, a mirror must be placed over part of the absorber; however, this will not prevent all radiation emitted by this part of the absorber from escaping. Leaving the covered portion of the absorbing surface without a coating or texture will help reduce the amount of radiation that escapes. Coating this area with a highly reflective coating can further reduce escaping radiation, but these materials must be able to withstand the high temperature of the emitting surface. These additional optical losses result in a lower optimum A_{ratio} for planar systems as compared to cylindrical systems. The

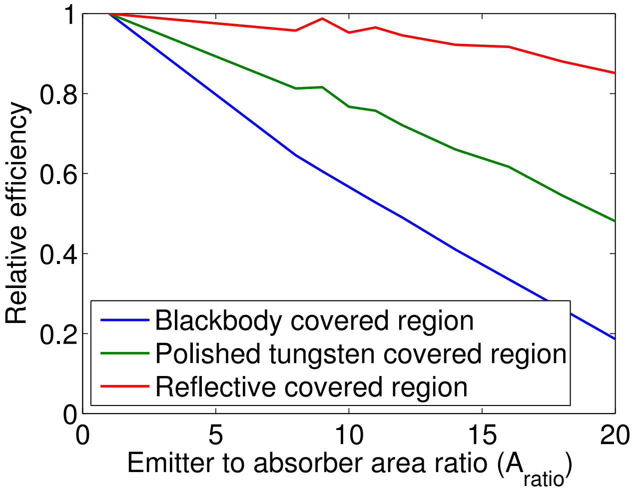

Figure 4.3: Relative efficiency of the absorbing surface for a planar STPV system with various A_{ratio}'s compared to the absorbing surface efficiency for a system with $A_{ratio} = 1$. The STPV system is operating at 1700 K, with an absorber area of 1 cm^2 and 1 mm distance between the absorber and mirror. The reflective covered region is assumed to have a reflectivity of 0.98.

experimental section of this paper will focus on planar systems due to their simplicity and considerations of fabrication methods for flat and curved surfaces.

The ray tracing method was used to find the relative efficiency of absorbing surfaces with a portion of the surface area covered by a mirror, with the results shown in Figure 4.3. A large drop in absorbing surface efficiency can be seen for a large A_{ratio} due to radiation escaping from the edge of the absorber. While polished tungsten reduces this loss, it is still substantial. Adding a mirrored coating to the covered portion of the absorbing surface can greatly reduce this loss; however, temperature stability and delamination issues make this challenging. A polished tungsten covered region is therefore the more practical solution and is used for further system efficiency calculations. It should be noted that cylindrical systems eliminate the need for a portion of the absorbing surface to be covered by a mirror allowing for a greater range of A_{ratio} while maintaining efficient operation. However, large cylindrical systems also tend to form temperature gradients along their length, reducing system efficiency

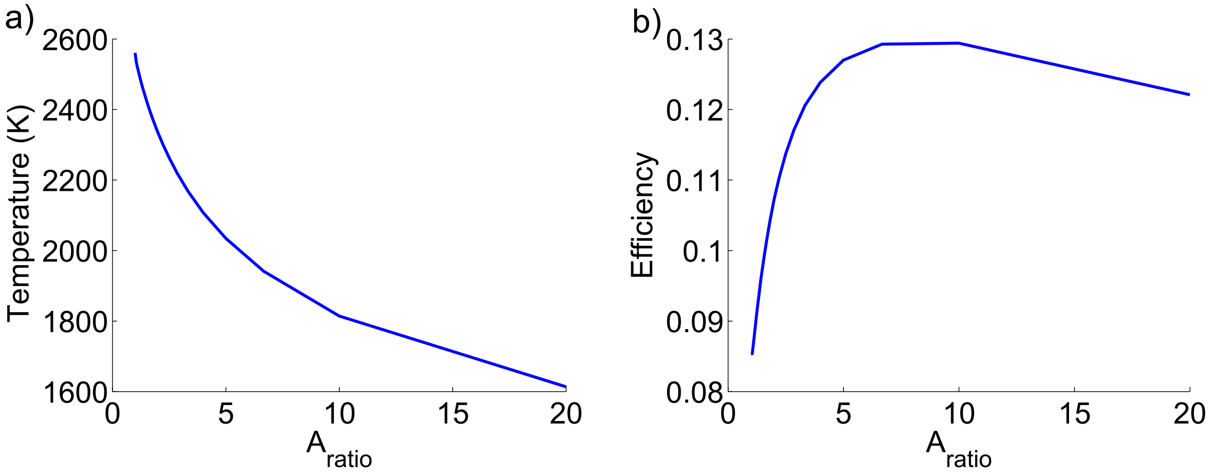

Figure 4.4: Graphs of a) the change in system temperature and b) efficiency with A$_{ratio}$ for an STPV system with the parameters listed in Table 4.3.

and requiring a large PV cell area.

In systems where the power input is kept constant, efficiency will increase continuously with A$_{ratio}$ due to the corresponding increases in solar concentration; however, as previously mentioned, extremely high solar concentrations may be difficult to reach. If the solar concentration is fixed, then there will be an A$_{ratio}$ where the device efficiency reaches a maximum. This is because the amount of radiation lost from the absorbing surface decreases with A$_{ratio}$, but the total energy into the system does too. This reduced energy input results in a lower operating temperature, which results in a lowered efficiency. Figure 4.4a shows the change in temperature as A$_{ratio}$ is varied, while Figure 4.4b shows the change in efficiency. A maximum efficiency at an A$_{ratio}$ of 10 can be seen for this system, but the optimum A$_{ratio}$ varies for each device modeled here.

4.2.4 Absorbing Surfaces

Here, two absorbing surfaces are considered for use in STPV systems. Both consist of nanostructured tungsten with pseudo-random element placement and sizing to simulate random processes in fabrication techniques. FDTD, TMM, and EMT calculations were used to simulate the reflectance of these surfaces, from which η_{abs} can be calculated. Tungsten substrates were used due to their naturally high α and low ϵ due to the combination of many interband electronic transitions that occur in the visible and near-IR regimes [131, 132].

Pseudo-random Nanocone Arrays

Simulations were used to explore the use of non-periodic nanotextures on tungsten substrates to create absorbing surfaces for use in STPV systems. Nanotextures offer the advantage of being a single-layer without any coating, leading to increased reliability under high temperature operation and long term reliability due to lack of a thermal expansion mismatch [133].

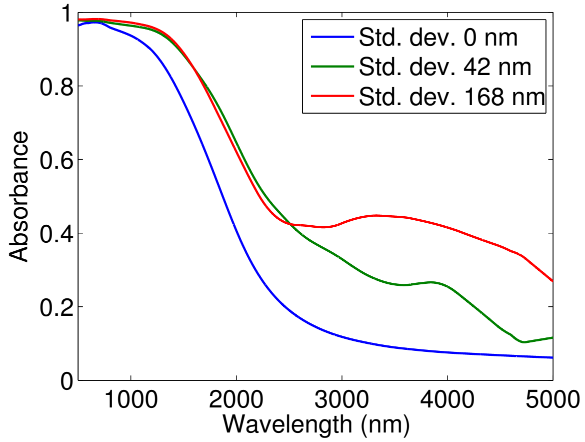

Figure 4.5: Absorbance of tungsten nanocones with increasingly large standard deviations for radius and height distributions. Average radius is 400 nm and average height is 800 nm, with 90% of the substrate filled with cones [61].

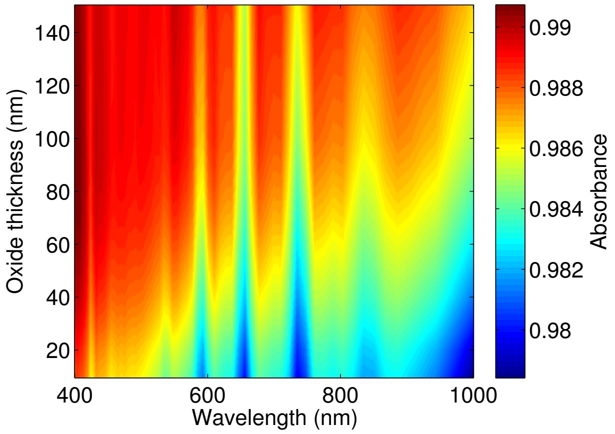

Figure 4.6: Simulated absorbance for various oxide thicknesses on tungsten nanocones [61].

Non-periodic structures offer relaxed geometrical requirements with higher error tolerances, making them good candidates for fabrication via self-assembly. They also broaden the absorption spectrum and reduce the effect of Bragg peaks, allowing large structures to remain highly absorptive [56]. FDTD simulations show cones to be the most efficient shape for broadband absorption due to their graded-index type behavior. Absorbance plots for 400 nm radius cones with increasingly large standard deviations for radius and height distributions are shown in Figure 4.5. It can be seen that the solar absorbance of the nanotexture increases with increasing randomness, reaching an absorptivity >99% across the majority of the solar spectrum, with emissivity at longer wavelengths being reduced by increasing reflectance. Work on this structure led to a publication in Applied Physics Letters [61].

To ensure the survival of these nano-structures at high temperatures, they must be coated with a protective oxide [44]. The effect of oxide coatings of various thicknesses on the absorption of these structures is illustrated in Figure 4.6. A constant refractive index of 1.46 is used in this simulation due to the lack of significant dispersion for oxides in the visible regime. The addition of an oxide layer to the surface increases α due to its index-matching properties. This makes the addition of a protective oxide layer a viable method for protection of the substrate during high temperature operation.

Figure 4.7a shows the dependency of η_{abs} on average cone radius assuming a height equal to 2 times the radius and variances of 20% for both height and radius. η_{abs} reaches a maximum at a radius of 800 nm and height of 1600 nm, because an absorbing surface with structures of this size has a high α_{sol} and a low ϵ_{1700K}. As the radius gets larger, there is a slight increase in α_{sol} and a larger increase in ϵ_{1700K}, leading to reduced efficiency. As the cones get very large compared to the wavelength, the surface starts to have characteristics similar to a blackbody, and its efficiency levels off at $\eta_{abs} = 0.73$ (the efficiency of a blackbody absorber). This shows that while increased efficiency is possible with small nano-cones, high efficiencies can still be reached with larger cones. FDTD simulations were used where feasible, but TMM modeling with EMT was used to extend the range of the simulation due to the large computing requirements of FDTD simulations.

The effect of the temperature dependence of the optical constants of tungsten on its absorption can be taken into account by modifying the γ term in the Drude model to account for the increased path length for conduction-band electrons at high temperatures [134].

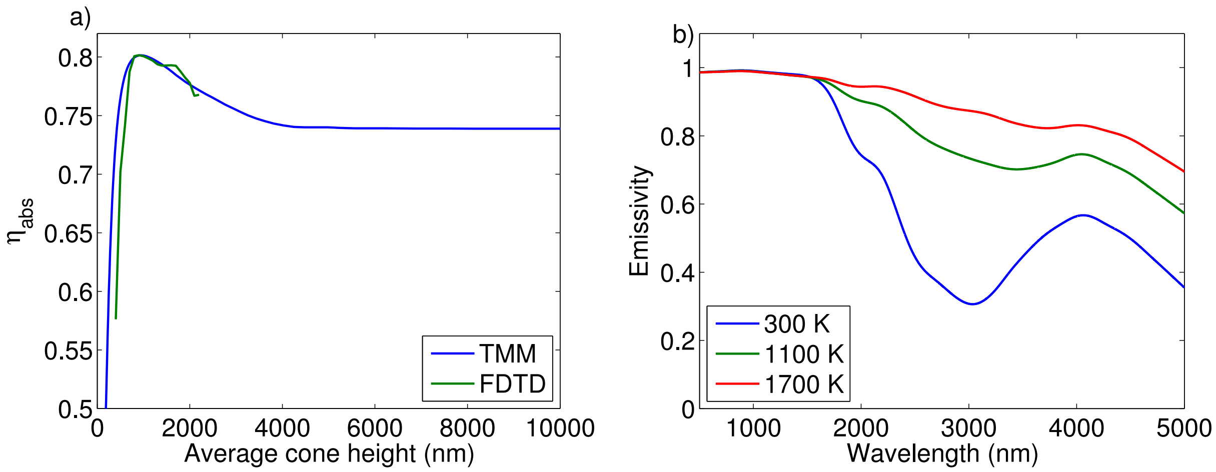

Figure 4.7: Graph of a) the dependence of η_{abs} on cone size (with radius equal to 1/2 the cone height and variances of 20% for both height and radius), and b) the dependence of the nanostructure's emissivity on temperature. The FDTD model shows more accurate results for shorter cones; however, its accuracy begins to fall off for larger structures due to increased computation requirements requiring a decreased simulation resolution.

Figure 4.7b shows that increasing temperature causes increased α at the cost of increasing ϵ. This causes a slight decrease in the spectral efficiency of the surface.

Glancing Angle Deposition

In addition to nano-cones, experimental data from tungsten nanostructures deposited via glancing angle deposition (GLAD) were compared to simulations of similar structures. GLAD is a technique that allows a self-assembled, nanostructured thin film to be deposited on a substrate by vapor deposition or sputtering [135]. During GLAD, a substrate is placed at a large (∼85°) angle relative to the deposition source. This causes incoming atoms to form mounds on the substrate. If the substrate is rotated during this process, nano-pillars or nano-screws can be formed. The parameters of deposition, including angle, spin speed, and deposition rate and time can be used to control the morphology of the resulting surface [136]. In the past, GLAD has been used for various applications, including the fabrication of

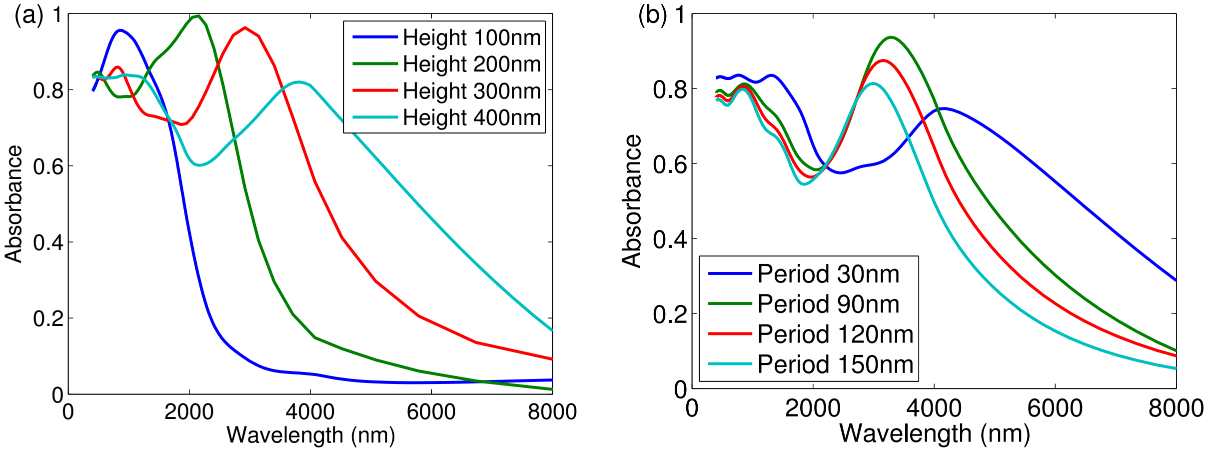

Figure 4.8: FDTD simulation of the absorbance of GLAD nano-structures with varying a) height and b) periodicity [60]. This shows good control over absorbance peak locations, resulting in the potential to create a highly efficient absorbing surface with high solar absorption and low thermal emissivity.

photonic crystals, super hydrophobic coatings, PV cell absorption layers, and more [137]. GLAD of tungsten has also been used for various applications [138].

To accurately model the GLAD surfaces, simple image recognition was used with the top-view SEM images shown in Figure 5.2b to trace the outline of the nano-pillars; this data was used as an input for the simulation, as seen in Figure 4.9 [139]. Figure 4.8 contains the results of changing the periodicity and height of the nano-structures in the model. It can be seen from this data that good control over the absorption of the nano-structured tungsten can be exercised via changing the properties of the deposited film.

The α of this surface was found to be 82.3%, with an ϵ of 0.75 at 1700 K. The surface was found to be stable at 400°C in air for one hour. Due to its relatively low α and high ϵ at high temperatures, this surface as fabricated proved to be better suited to solar thermal systems than STPV systems since solar thermal systems operate at a lower temperature and lower solar concentrations make them less dependent on an extremely high α [140]. Modeling, however, shows this surface's high potential for STPV applications should its height and

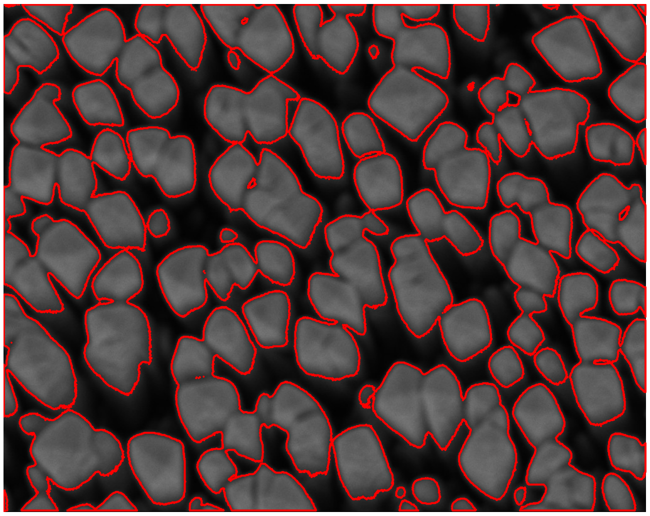

Figure 4.9: Tracing of islands in an SEM of a GLAD substrate.

periodicity be optimized for that purpose.

4.2.5 Emitting Surfaces

Periodic Gratings in Tungsten

The first emitter structure looked at in detail in this research was a periodic blazed grating on a tungsten substrate. When the grating's period is smaller than the wavelength of incoming light, the grating will act as a sub-wavelength grating and will not have any propagating diffractive modes [141]. This allows for light absorption due to the grating acting as a graded index structure for zero-order modes [87, 142]. Figure 4.10a illustrates how η_{emit} changes with grating properties, while Figure 4.10b displays the absorbance spectrum at the maximum efficiency with a 285 nm height, 200 nm periodicity, and blaze angle of 55°. Due to the fact that it is operating in the zero-order condition, there is no strong angular dependence of its emission [143].

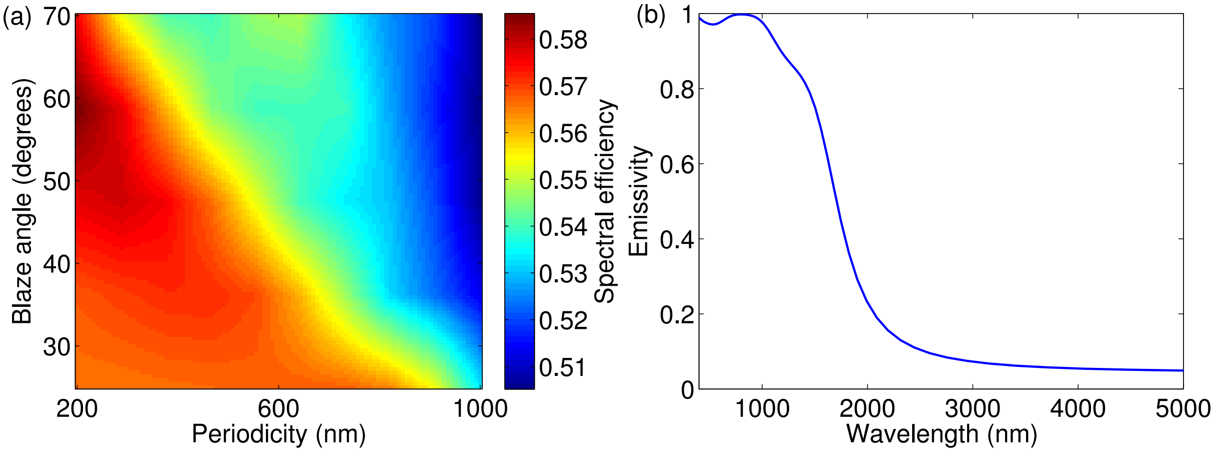

Figure 4.10: a) Efficiency (η_{emit}) vs. periodicity and blaze angle for a blazed grating on tungsten and b) emissivity of an optimized grating with a 285 nm height, a 200 nm periodicity, and a blaze angle 55° [88].

Periodic Nanohole Arrays

In the interest of finding a surface that lent itself to large area fabrication, periodic arrays of nano-holes on tungsten substrates were investigated. These structures can be fabricated using interference lithography, which is a technique that can be applied to large-area substrates [144]. Figure 4.11a is a plot of η_{emit} vs. periodicity and depth that shows a maximum at a periodicity of 1200 nm and a depth of 200 nm. The fill factor of holes on this surface is 0.5. This plot shows a range of parameters that perform well in this application, implying a high tolerance of manufacturing defects in the finished surface. An image of this surface can be seen in figure 4.12a. The emittance spectrum of this nanostructure is shown in Figure 4.11b, showing an emissivity peak at 1500 nm, matching well with GaSb PV cells.

As shown in Figure 4.11b, this nanostructure shows very good selectivity for use with a GaSb PV cell with a bandgap at 1707 nm. The η_{emit} of this surface is 0.65, which compares favorably with other emittance spectra reported in literature, as shown previously in Table 2.2. Blackbody radiation of wavelengths longer than the bandgap is suppressed while radiation at wavelengths much shorter than the bandgap is also suppressed. This narrowing of the

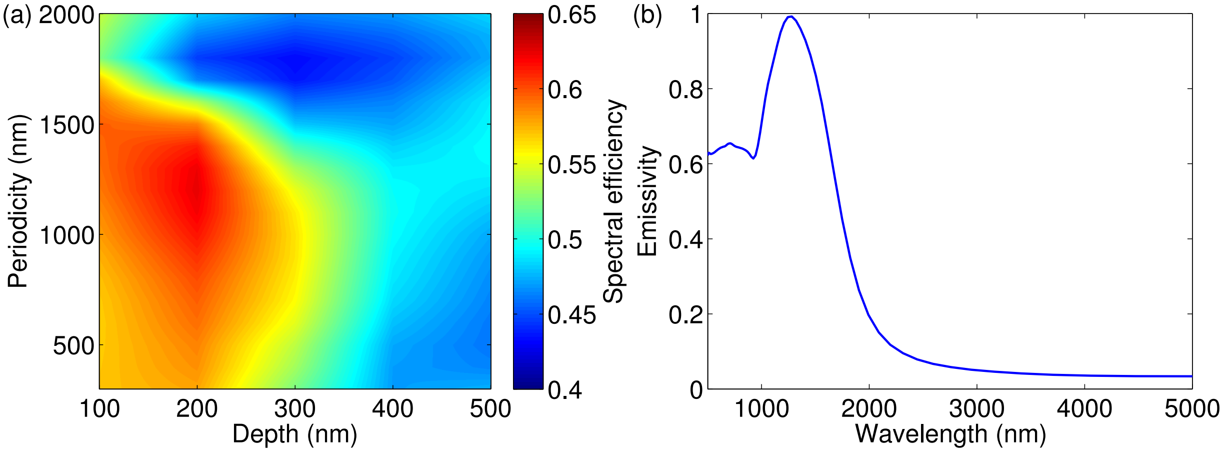

Figure 4.11: a) Spectral efficiency (η_{emit}) of the surface vs. periodicity and depth for a periodic array of holes in tungsten and b) emissivity of optimized array with a periodicity of 1200 nm, a depth of 200 nm, and a fill factor of 0.5.

blackbody emission will greatly improve the efficiency of the STPV systems.

Dielectric/Metal Stacks

Modeling was done in conjunction with a collaborator, Jay Foley of ANL, on a structure utilizing alternating layers of metal and dielectric. It was found that by adding a thin metal layer in between two dielectric layers on a metallic substrate a sharp absorption peak could be created at a specific wavelength. This peak is known as a perfectly-absorbing mode. These modes occur due to an interference effect between light reflected off the first metal surface and light reflected off the metallic substrate. This effect is similar to the interference effect seen in a Fabry-Perot interferometer. The top dielectric surface acts to reduce initial reflection off the surface. Figure 4.13 illustrates the spectral emittance of this surface, while Figure 4.12b shows its structure.

This structure, using a 126 nm YSZ layer, followed by a 19 nm Ag layer, an additional 283 nm YSZ layer, and a tungsten substrate, has an η_{emit} of 0.68, making it a very good candidate emitter for STPV systems, although its power output is lower than the other emitting surfaces analyzed here. YSZ is used over Si_3N_4 or HfO_2 due to the higher index of

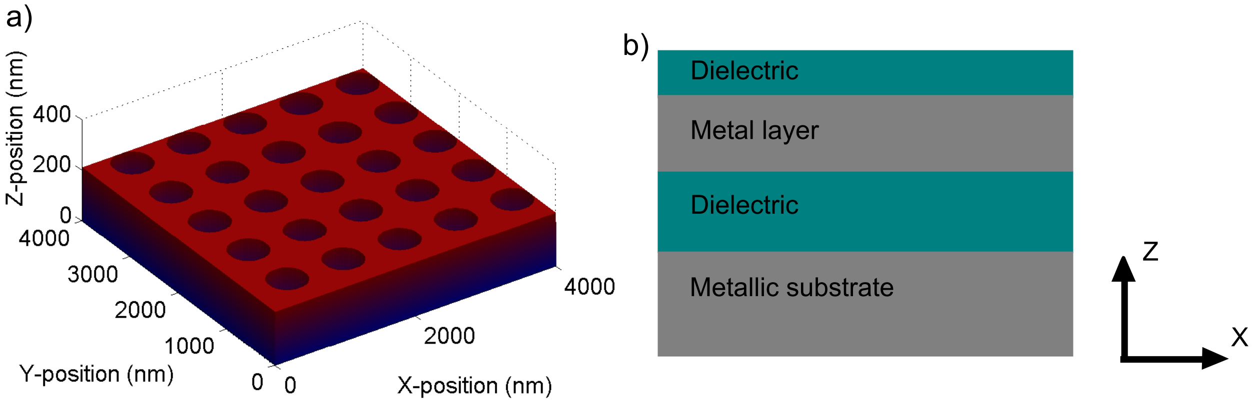

Figure 4.12: a) Nano-hole array on tungsten substrate and b) metal-dielectric stack emitter. Thermal radiation is emitted in the positive Z direction.

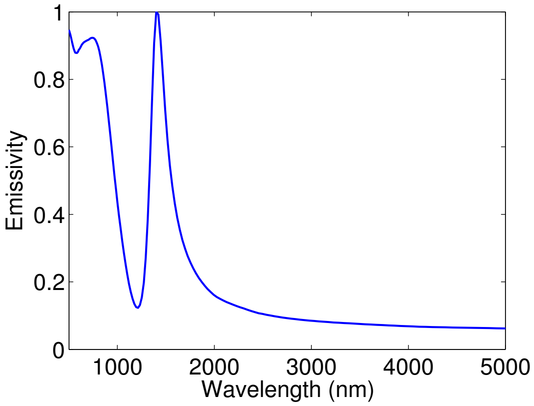

Figure 4.13: Emissivity of an optimized dielectric/metal stack consisting of a tungsten substrate, Ag metal layer, and YSZ dielectric layers. This structure has a η_{emit} of 0.68.

refraction that is achievable with YSZ. Unfortunately, the low thermal stability of Ag limits the use of this structure in high-temperature applications, although it may be useful for lower temperature STPV systems [81].

Replacing the Ag layer with a tungsten layer (resulting in a YSZ/W/YSZ structure on a tungsten substrate) reduces η_{emit} to 0.56; however, it was noticed that the tungsten metallic layer was optically thick for optimized structures, so that a simpler structure of a single YSZ layer on tungsten was able to achieve the same η_{emit} as the more complex YSZ/W/YSZ structure.

4.2.6 Photovoltaic Cells

GaSb, Ge, and InGaAsSb PV cells are modeled here. The spectral EQE of a GaSb PV cell was taken from a paper by Sundaram et al. [145], while the V_{oc} of the cell as a function of temperature was found with equations 4.7 - 4.9 taken from literature [146, 147] (with I_{sc} given in equation 3.2):

$$I_0 = 1.84 \times 10^{-3} T^3 e^{\frac{-E_{bg}}{kT}} \tag{4.7}$$

$$E_{bg} = 0.813 - 6 \times 10^{-4} \frac{T^2}{T + 265} \tag{4.8}$$

$$V_{oc} = \frac{kT}{q} \ln\left(\frac{I_{sc}}{I_0} + 1\right) \tag{4.9}$$

where I_0 is the reverse saturation current of the cell.

The FF can be found by first solving the transcendental equation 4.10 for V_{mpp}, and then finding the FF from equations 4.11 and 4.12:

$$V_{oc} = \frac{kT}{q} \ln\left(1 + \frac{qV_{mpp}}{kT}\right) + V_{mpp} \tag{4.10}$$

$$P_{max} = \frac{qI_{sc}(V_{mpp})^2}{kT + qV_{mpp}} \tag{4.11}$$

$$FF = \frac{P_{max}}{I_{sc}V_{oc}} \tag{4.12}$$

where P_{max} is the power at the maximum power point of the PV cell and V_{mpp} is the voltage at the maximum power point. Figure 4.14 shows the change in P_{max}, V_{oc}, and I_{sc} with T for the modeled GaSb PV cell. The I_{sc} increases with temperature due to a decrease in E_{bg} that allows the PV cell to absorb more photons, while V_{oc} and P_{max} decrease with temperature. This illustrates the need to keep PV cells cool during operation, which can be a challenge in STPV systems due to the PV cell typically being kept in a vacuum.

The E_{bg}, V_{oc}, FF, and EQE of InGaAsSb and Ge PV cells were directly taken from literature [25, 33, 148]. Table 4.1 summarizes these values for GaSb, InGaAsSb, and Ge PV

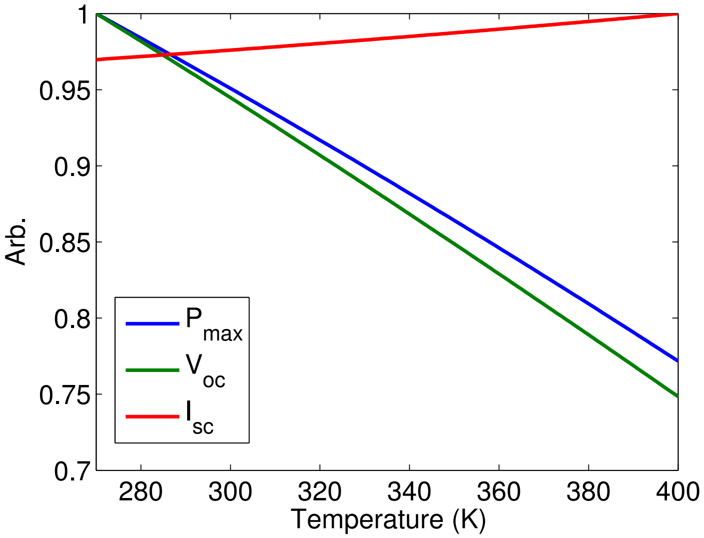

Figure 4.14: Temperature dependence of P_{max}, V_{oc}, and I_{sc} in GaSb PV cells under 1 sun illumination.

Table 4.1: E_{bg}, V_{oc}, FF, and EQE of PV cells

Cell Type	E_{bg} (eV)	V_{oc} (mV)	FF	EQE at 1500 nm
GaSb	0.726	586	0.82	0.72 [33, 146]
Ge	0.67	264.1	0.69	0.87 [148]
InGaAsSb	0.55	320	0.62	0.56 [25]

cells.

This chart shows that GaSb PV cells are the most efficient for use in STPV systems, as previously stated in Chapter 2. The simulations here will focus on GaSb PV cells, but will include operating efficiencies with Ge and InGaAsSb cells for comparison.

4.2.7 Complete System

The overall system efficiency was simulated using an absorber made of pseudo-random nanocones on tungsten and a periodic hole array on tungsten as the emitter. The results of this simulation can be seen in Figure 4.15a, while the corresponding system temperatures can be

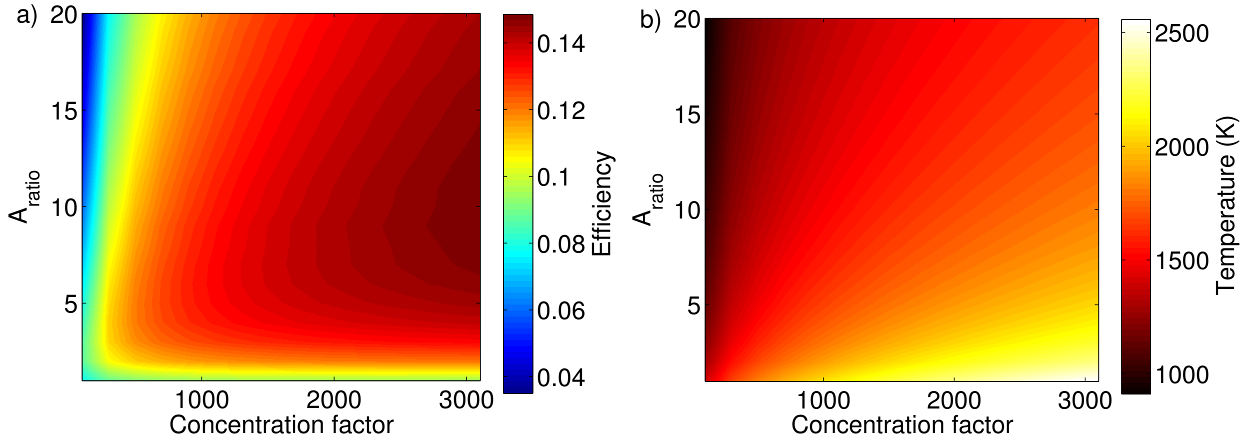

Figure 4.15: a) System efficiency vs. A_{ratio} and concentration ratio and b) temperature vs. A_{ratio} and concentration ratio for a GaSb PV cell.

seen in Figure 4.15b. Table 4.2 lists the losses that occur for this system with absorber area 1 cm^2, A_{ratio} 9.7, emitter area 12.2 cm^2, concentration ratio of 2500, and a GaSb PV cell. The system has an overall power conversion efficiency of 14.4% and an internal temperature of 1703 K under these conditions.

Table 4.3 shows the default values for the system simulated here, along with the sensitivity of the overall efficiency to each parameter. The sensitivity was calculated by varying each parameter by 1% and re-running the simulation to find the resulting change in overall efficiency, as shown in equation 4.13:

$$\text{Sensitivity} = \frac{\partial \eta_{total}}{\partial \chi} = \frac{\eta_{total}(\chi * 0.01)\eta_{total}(\chi)}{\eta_{total}(\chi) * 0.01} \tag{4.13}$$

where χ is the parameter to be varied. Negative sensitivity values indicate that an increase in the value of the parameter will decrease the overall system efficiency. This results in a sensitivity of 1 for parameters that directly affect the entire system's efficiency: the solar concentrator efficiency, the solar absorption of the system, the emitting surface efficiency, and the efficiency of the PV cell. The emissivity of the absorbing surface and power of the emitting surface are both important parameters, but less so than the other surface parameters,

Table 4.2: List of losses in the simulated STPV system with parameters listed in Table 4.3 (losses shown in Figure 3.1)

.

Loss type	Formula	Percent of input power lost
Concentrator loss	$1 - \eta_{conc}$	25.0%
Reflection off of absorbing surface	$1 - \alpha E_{inc}$	2.5%
Emittance from absorbing surface	ϕ_{abs}	8.0%
Emittance from sides of structure	ϕ_{cav}	0.99%
Thermal conductivity through supports	P_{sup}	0.17%
Convective losses	P_{conv}	0.78%
Emittance from emitter that does not reach PV cell	$\phi_{emit} \times (1 - F_{PV})$	4.6%
Thermal emission below E_{bg}	PV cell loss	16.0%
Thermalization loss in PV cell	PV cell loss	9.2%
Loss due to PV cell efficiency	FF & EQE	18.0%
Power conversion efficiency	η_{total}	14.4%

as expected.

Surprisingly, increasing the system temperature had a large effect on the efficiency. This is due to the fact that increasing temperatures shift the peak of the blackbody emission spectrum to shorter wavelengths, increasing the amount of emitted radiation usable by the PV cell, and also require higher concentrations that result in a lower percentage of radiation being lost as emission from the absorbing surface. The temperature is limited to 1700 K here due to material stability concerns; however, increasing this limit will result in higher efficiency operation. The tungsten substrate itself is stable to higher temperatures in vacuum but delamination issues with the protective oxide coating limit the high temperature stability of the nanostructures. Finding new methods of protecting these structures at high temperatures could increase system efficiency beyond current levels without requiring new absorbing and emitting surface structures.

To examine the various absorbing and emitting surfaces described in this chapter as a whole, Figure 4.16 shows the efficiency vs. concentration factor for systems utilizing different

Table 4.3: List of default values for system simulations, and the sensitivity of these values.

Parameter	Default value	Sensitivity
Concentrator efficiency	75%	1
α_{sol} (Pseudo-random cones)	0.95	1
η_{emit} (Nanoholes on W)	0.64	1
PV cell FF	0.82	1
System temperature	1700 K	0.4273
ϵ_{1700K} (Pseudo-random cones)	0.16	0.278
Distance from absorber to reflective mirror	1 mm	-0.188
J_{emit} (Nanoholes on W)	68.1 W/cm^2	0.15
Solar concentration (C)	2500	0.13
Distance from emitter to PV cell	1 mm	-0.099
A_{abs}	1 cm^2	-0.0425
Absorber/emitter thickness	1 mm	-0.032
A_{emit}	9.7 cm^2	-0.012
Support thermal conductivity	1.38 W/mK	-0.007
System pressure	10 mTorr	negligible
PV cell type	GaSb	-
System type	Flat	-

Table 4.4: Optimized efficiency of different system types.

System type	PV cell	Temperature	Efficiency
Flat	GaSb	1700 K	14.4%
	Ge	1700 K	6.5%
	InGaAsSb	1450 K	5.8%
Cylindrical	GaSb	1700 K	15.1%
	Ge	1700 K	6.9%
	InGaAsSb	1430 K	7.2%

surfaces. In all cases, the nanoholes in tungsten was the best-performing emitting surface. In the case of a blackbody absorbing surface, the use of a single-layer dielectric or blazed grating type emitting surface provided a clear advantage over bare tungsten.

Table 4.4 shows the efficiency of different STPV system types. The operating temperature was limited to a max of 1700 K, and each system was optimized for maximum efficiency. Cylindrical systems result in increased efficiency because emission from the side of the

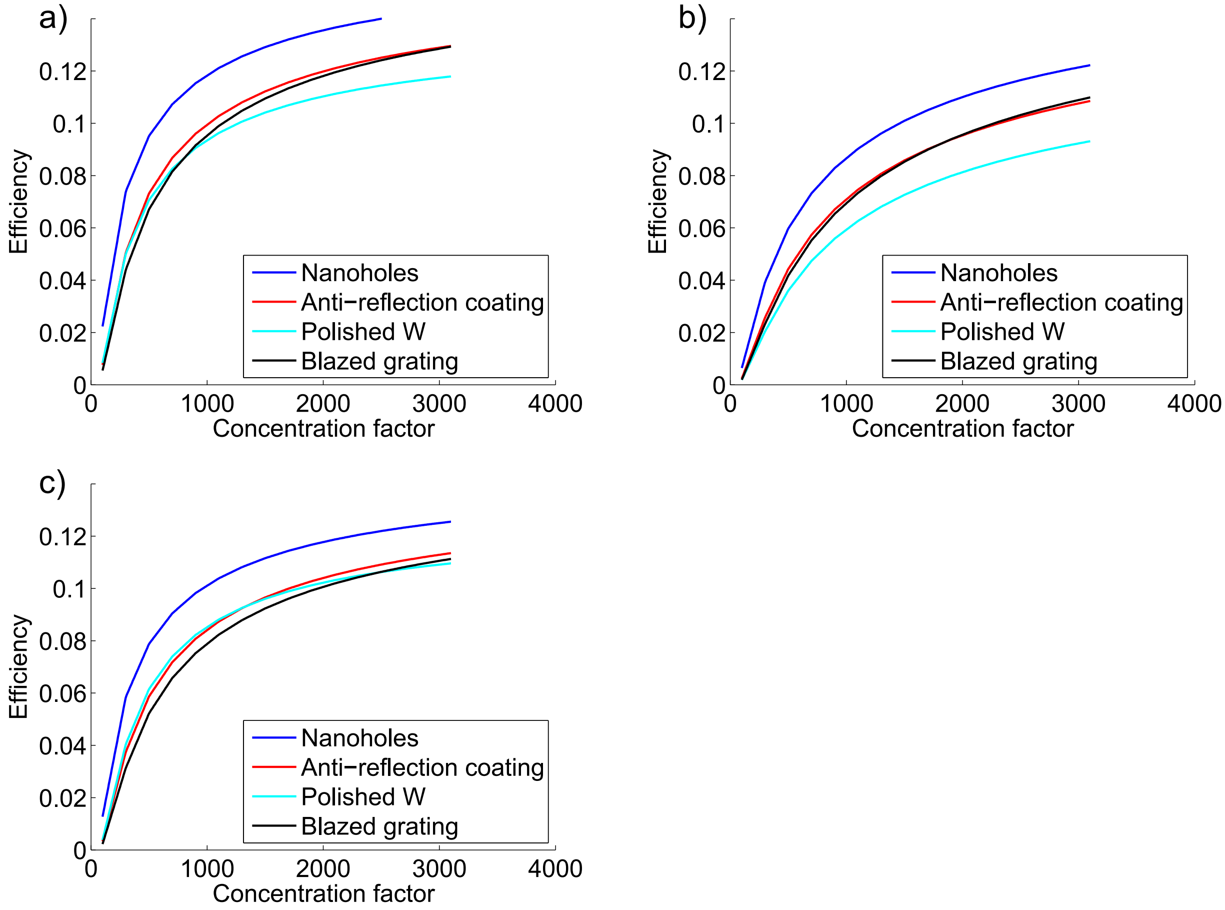

Figure 4.16: The effect of different absorbing and emitting surfaces on system efficiency. The legend specifies emitting structures, and each chart uses a different absorbing surface: a) a nano-cone absorbing surface, b) a blackbody absorbing surface, and c) a single layer dielectric absorbing surface.

structure can be captured by the PV cells, and a large A_{ratio} can be achieved without additional losses such as those shown in Figure 4.3.

Systems using Ge PV cells have lower efficiencies due to their low V_{oc}, while InGaAsSb PV cells have lower efficiencies due to their low EQEs. It is interesting to note that the systems using InGaAsSb cells have lower operating temperatures due to their low E_{bg}. This allows a greater range of materials to be used in InGaAsSb systems, and also allows them to retain high efficiency at lower solar concentrations, lowering the fabrication cost of the system. InGaAsSb systems also benefit more from the switch from flat to cylindrical system architecture due to their lower operating temperatures, allowing efficient operation with a very high A_{ratio}.

Chapter 5: Experimental

An experimental STPV system setup was built using GaSb PV cells and nanostructured absorbing/emitting surfaces inside a vacuum chamber. The A_{ratio} was controlled by placing a heat mirror over unused portions of the top absorbing surface, and by leaving the covered portions of the top surface untextured. A copper heat sink was used to keep the PV cell cool, and the supporting structure was made from insulating materials to minimize conductive losses. A Fresnel lens was used to focus sunlight, and a laser was used for solar simulation under laboratory conditions. Methods to measure temperature and system efficiency are described.

5.1 Photovoltaic Cells

Four 1.48 cm^2 GaSb PV cells were purchased from JX Crystals. The V_{oc}, I_{sc}, FF, and P_{max} of the cells were measured using a Xenon lamp, voltage source, and multimeter. The total power of the lamp was set to 1 sun using a Si cell of known efficiency. The results of these measurements are shown in Table 5.1. The I-V curve for cell number 1 can also be seen in Figure 5.1a. While the FF and $V_{oc}$of these cells was lower than those reported in literature, this is expected for commercial-grade cells.

Table 5.1: Measured V_{oc}, I_{sc}, FF, and P_{max} of 1.48 cm^2 GaSb PV cells purchased from JX Crystals.

Cell Number	V_{oc} (mV)	I_{sc} (mA)	FF	P_{max} (mW/cm^2)
1	413	50.8	0.61	9.1
2	419	51.2	0.61	9.4
3	416	51.1	0.59	9.0
4	417	50.9	0.62	9.5

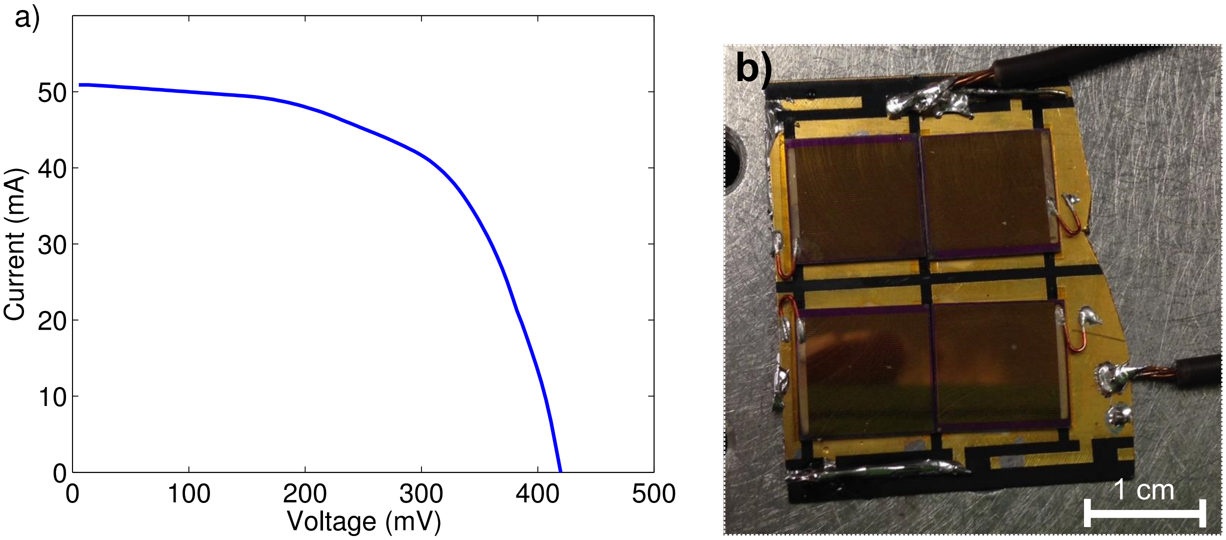

Figure 5.1: Graph of a) the I-V curve of a GaSb PV cell used in experiment, and b) a photo of the mounted cells.

These cells were soldered to a copper substrate via reflow soldering. The PV cells were connected in series to reduce the current passing through the cells. Figure 5.1b shows a photo of the PV cell setup.

5.2 Absorbing Surface

5.2.1 Pseudo-random Nanocone Arrays

Pseudo-random nano-cone arrays were fabricated via laser texturing. In the past, similar techniques using ultrafast lasers have been used to create self-assembled microtextures on silicon and titanium substrates [62, 149]. A nanosecond 1064 nm laser (IPG Photonics, GLP-10) operating with a pulse width of 50 ns, focused to a spot with a power of 24 W and 30 kHz frequency was scanned across the substrate by means of a Galvo. The 6.5 cm^2 tungsten substrates purchased from MTI corporation were cleaned with acetone and then methanol, and then were used as substrates in this experiment. Due to the relatively large size of these textures, this surface will act as a gray body, as shown in Figure 4.7a. To make

Table 5.2: Average reflectivity of microtextured tungsten substrates at 405 nm, 532 nm, 633 nm, 790 nm, 980 nm, and 1064 nm wavelengths.

Coating	Anneal	Reflectivity
None	Unannealed	0.85
None	1700 K	0.72
160 nm Si_3N_4	Unannealed	0.92
160 nm Si_3N_4	1700 K	0.9

samples with a texture on only a small portion of the top surface, a similar technique was used, except the laser was scanned only across a smaller area.

Measurements of the reflectivity of this surface were performed using lasers with 405 nm, 532 nm, 633 nm, 790 nm, 980 nm, and 1064 nm wavelengths with a Labsphere RTC-060-SF integrating sphere with a Spectraflect barium sulfate reflecting surface. The sample was angled so that direct reflection would be captured by the sphere, allowing for measurement of total (direct + scattered) reflectivity. Table 5.2 shows the reflectance of these surfaces before and after coating and heating to 1700 K. Surface reflectivity was invariant across the wavelengths measured, indicating broadband absorbance.

The increase in surface reflection upon heating of the untreated sample was most likely due to oxidation or changes in surface morphology due to migration of atoms across the tungsten surface, resulting in a flatter structure. An Si_3N_4 layer was deposited on the tungsten microtexture via plasma-enhanced chemical vapor deposition (PECVD) at a deposition temperature of 100°C. Si_3N_4 is a dielectric coating that is stable at temperatures up to 1673 K in air [150]. The addition of this coating increased the thermal stability of the microtexture while simultaneously acting as an anti-reflection coating (ARC) and decreasing the reflectance of the surface.

These structures show very high broadband absorbance and good thermal stability with the addition of a protective Si_3N_4 coating. η_{abs} can be increased via the use of nanostructures, as shown in Figure 4.7a; however, fabrication using ultrafast laser methods is fast and easily

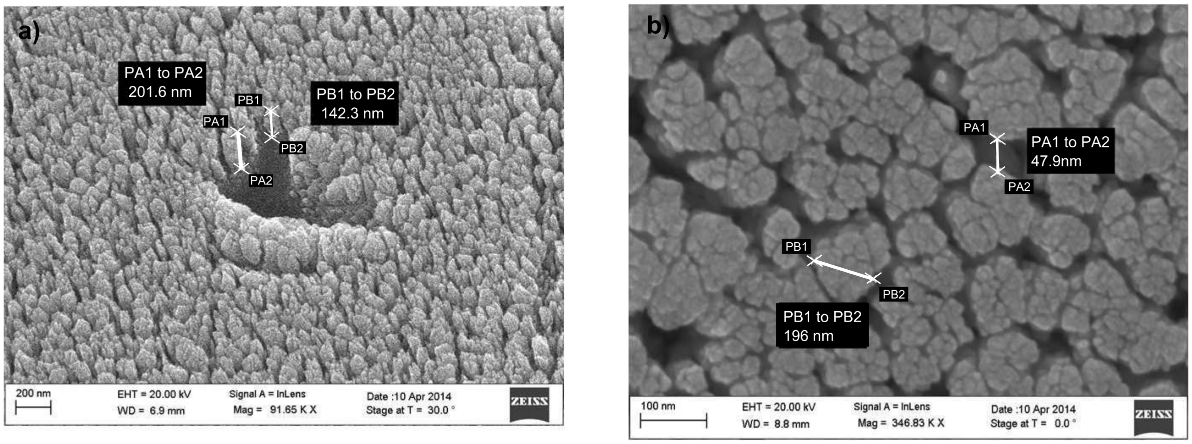

Figure 5.2: SEM images of GLAD nano-structures on tungsten a) tilted and b) top view [60].

scalable, which is an important advantage for STPV systems.

Additionally, a second sample was created in the same way as the first, except with a texture on only a small (0.6 cm^2) section of the surface. This sample will be used to test an STPV system with a high A$_{ratio}$, as discussed in section 4.2.3. This sample was also coated with a 160 nm Si_3N_4 layer to increase its thermal stability.

5.2.2 Glancing Angle Deposition

GLAD of tungsten nanostructures was performed on a stainless steel substrate at Oak Ridge National Labs (ORNL) by staff members Ivan Kravchenko and Dale Hensley. The deposition angle used was 85 degrees from the normal of the surface, the sample rotation speed was 20 rpm, and the sample was kept at room temperature. The vacuum during deposition was 4x10^{-3} Pa.

A thin ($\sim$80 nm) HfO_2 coating was grown via atomic layer deposition as a protective layer on top of the W GLAD film. A full description of the deposition process is described by Balke *et al.* [151]. Measurements of α, ϵ, thermal stability, and energy dispersive X-ray spectroscopy (EDS) were performed by Ankit Shah, a colleague of the author of this dissertation. α measurements were performed using the Labsphere integrating sphere and lasers with wavelengths 405 nm, 532 nm, 633 nm, 790 nm, 980 nm, and 1064 nm. The ϵ

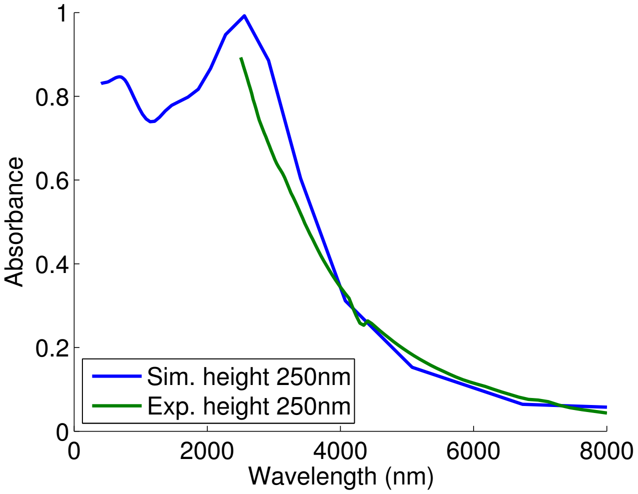

Figure 5.3: Comparison between simulated and experimental data for GLAD nano-structures on tungsten [60].

was found by measuring the IR reflectance using a Fourier transform infrared spectroscopy (FTIR) system manufactured by Thermo Fisher Scientific, Inc. Samples were illuminated with IR radiation, and the power of the reflected beam was measured. The acceptance angle of the collector was a cone angle of 35° from the normal.

Figure 5.2 shows an SEM image of the deposited nano-structures. The nano-structures have a height varying from 130 to 200 nm and a diameter varying from 40 to 100 nm. EDS data shows 25 % tungsten, 49 % iron, 13 % chromium, 5 % nickel, 4 % carbon, 3 % oxygen, and 1 % manganese. The iron, chromium, nickel, and manganese are attributable to the stainless steel substrate.

Figure 5.3 shows a comparison between modeled and experimental data for these structures showing good correlation. Discrepancies between the modeled and experimental data are due to the size of the area simulated and the resolution limits of the SEM. Despite good results for modeled GLAD structures, further improvements of fabricated structures is needed before they are suitable for high-temperature STPV systems. This work has been published in the journal of Optics Letters [60].

5.3 Emitting Surface

5.3.1 Periodic Nanohole Arrays

A no-cost user proposal was approved by the Center for Nanoscale Materials (CNM) at Argonne National Laboratory (ANL) to fabricate an emitter structure. Two types of emitter structures were fabricated: periodic nano-holes on a tungsten substrate and a 1D metal/dielectric photonic crystal on a tantalum substrate. These structures were chosen due to their high efficiencies exhibited by modeling, their stability, and their ease of fabrication. Tungsten and tantalum were chosen due to their high melting points and naturally high α combined with low ϵ.

Araghchini et al. attempted the fabrication of nano-holes on tungsten using an interference lithography technique [144]. Their work used a chrome hard mask on a tungsten substrate with an anti-reflection coating and photoresist layer on top. The photoresist was exposed to an interference pattern from a laser, then chemically developed, and the anti-reflection coating was etched via reactive ion etching. Finally, the chrome mask was etched using a wet enchant and the tungsten was etched via reactive ion etching with a CF_4 and oxygen mixture. Tungsten nano-holes of depth 1 μm and radius ∼0.6 μm were fabricated by Araghchini et al. using this method.

For this work, an attempt was made to fabricate nano-hole arrays on tungsten using a similar method. A polished 6.5 cm^2 tungsten substrate was used. This substrate has surface roughness Ra <30 Å and a purity >99 %. An interference lithography setup at ANL was used to attempt this fabrication. Unfortunately, as-fabricated substrates contained defects that prevented them from being used as efficient emitting surfaces. This was due to the substrates used, as samples fabricated from thin tungsten layers deposited on silicon wafers did not have these defects.

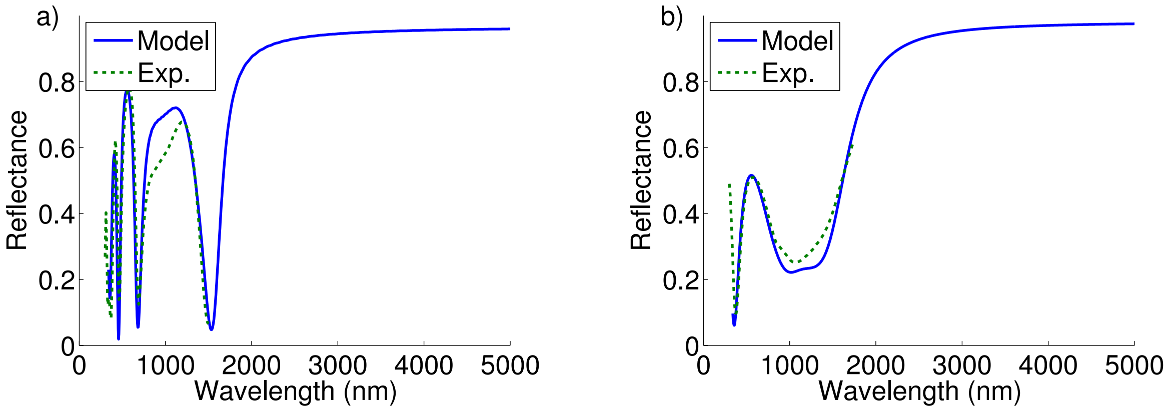

Figure 5.4: Graph of reflectivity vs. wavelength for a structure consisting of a) 120 nm Si_3N_4/13.5 nm Ag/345 nm Si_3N_4/W substrate and b) a 160 nm Si_3N_4 layer on a tungsten substrate.

5.3.2 Dielectric/Metal Stacks

Polished 6.5 cm^2 tungsten substrates were purchased from MTI corporation, and were cleaned sequentially by acetone and methanol. Si_3N_4 was deposited onto the substrate via plasma-enhanced chemical vapor deposition (PECVD). An Ag layer was then deposited by e-beam evaporation, followed by an additional Si_3N_4 layer. The temperature of deposition was kept to 100°C for this experiment. This resulted in a structure consisting of a 120 nm Si_3N_4 layer, followed by a 13.5 nm Ag layer, then a 345 nm Si_3N_4 layer, and finally a tungsten substrate. This is similar to the structure depicted in Figure 4.12b.

The reflectance of this structure was measured with a UV/VIS spectrometer manufactured by Perkin Elmer. Figure 5.4a shows a comparison of modeled simulated and experimental results for this structure. Good agreement was found, with the discrepancy at 1000 nm being due to a lamp change in the spectrometer. The spectral efficiency of this structure was 0.56. Further work on precise control of layer thickness is needed to increase the spectral efficiency of this surface to the predicted maximum of 0.68. This work was submitted to the journal Optics Express [152].

Due to concerns over the thermal stability of Ag at high temperatures, a second substrate was fabricated for experimental use, consisting of a tungsten substrate with a 160 nm Si_3N_4 coating. This structure had an $\eta_{spectral}$ of 0.59, and a high thermal stability. A comparison of simulated and measured reflectance for this surface is displayed in Figure 5.4b. Again, good agreement between experiment and modeling were found with the exception of the region around 1000 nm.

5.4 Solar Concentration and Simulation

5.4.1 Solar Concentrator System

STPV systems require high (>2000 suns) solar concentrations that are typically achieved via Fresnel lens systems, sometimes with an additional optical lens to further focus the light [15–17]. A 0.94 m^2 Fresnel lens with a 114 cm focal length was purchased from Green Power Science for use as a primary concentrating lens in the STPV system.

A table with a lens holder on the end of two long arms was built to allow the Fresnel lens to be properly aligned. A photo of this setup can be found in Figures 5.5a and 5.5b. A linear actuator is used to change the angle of the lens, with counterweights placed to reduce the load on the actuator. The wheeled base of the system allowed it to be twisted to follow the sun, and features wheel locks to hold it in alignment. Two sets of aluminum bars with sliders were used to allow the primary and secondary lenses to be raised and lowered, and clips held it in place once focused. The vacuum chamber was then placed on the table under the solar concentrator. Since the absorbing surface of the STPV system was parallel to the top face of the vacuum chamber, a wooden frame was built to hold the vacuum chamber at an angle such that the normal from the absorbing surface is parallel to the sun's rays.

To test the solar concentrator, an attenuator was fashioned to reduce the amount of light captured by the system to avoid damaging the power meter. While a neutral density (ND) filter can work to reduce the power focused by the lens, most ND filters are not able to attenuate light evenly over a wavelength range as broadband as solar energy [23]. Due to the

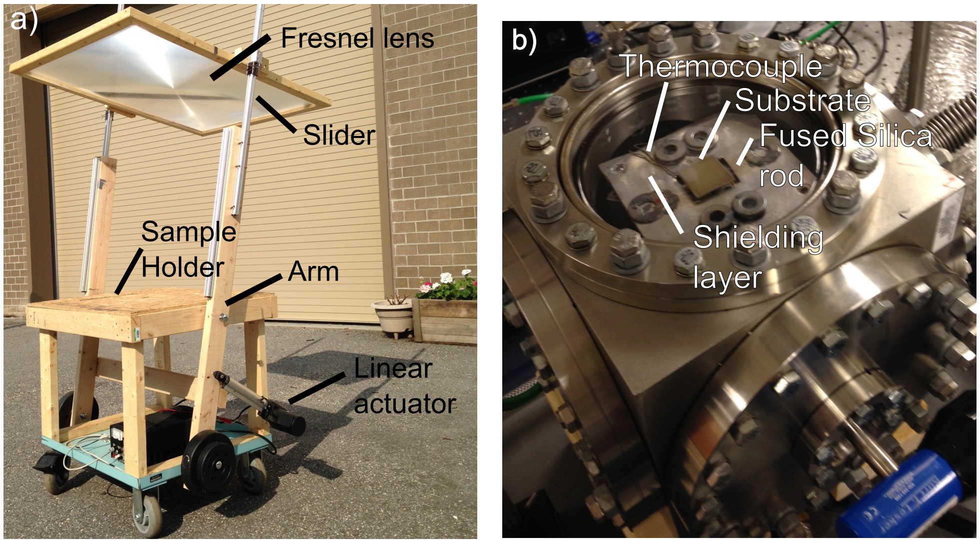

Figure 5.5: Photo of a) the solar concentrator setup and b) the vacuum chamber setup.

fact that chromatic aberrations are common in Fresnel lenses, reducing the effective width of the solar spectrum by attenuating certain wavelengths more than others will increase the perceived focusing efficiency of the lens.

This problem can be solved by using a cardboard or metal mask as an attenuator [23]. A series of small holes or lines are cut into the mask material, and the mask is then placed on top of the Fresnel lens. This reduces the amount of light received by the power meter without altering its spectrum. By evenly spacing the lines or holes across the entire lens surface, light hitting each part of the lens will be focused.

With the attenuating mask in place, a 3.14 cm^2 thermopile detector manufactured by Melles Griot was placed at the focus of the Fresnel lens. The detector was then moved in .5 cm increments, and the power at each spot was recorded. The results of these measurements are plotted in Figure 5.6. These results show a good focus, with 93% of the energy focused by the lens contained in a spot with a 2.5 cm diameter. Spherical and chromatic aberrations in the lens prevented the light from being focused further.

Although the lens focus was good, only 28% of the light reaching the lens was focused; the rest was reflected, scattered, or transmitted through the lens without focusing. Low lensing

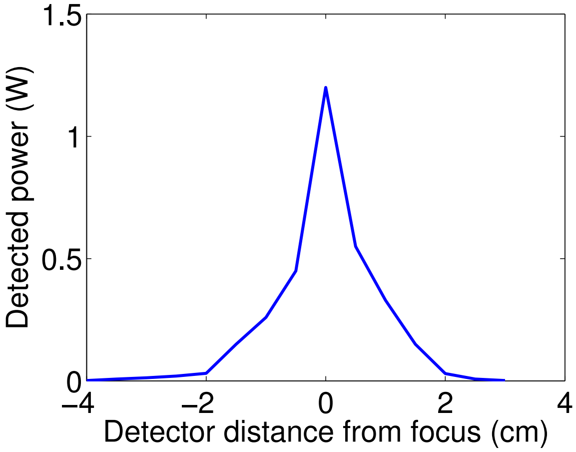

Figure 5.6: Detected power vs. distance from the focal spot for the Fresnel lens used for solar concentration using a 3.14 cm^2 thermopile detector.

efficiencies are common in such large Fresnel lenses. The use of a secondary meniscus lens can help to reduce the spot size of the focus, but would result in a lower lensing efficiency [15]. Despite this, a solar concentration of 391 was achieved within the 2.5 cm diameter spot, due to the large size of the lens.

5.4.2 Solar Simulation

In addition to the solar concentrator setup, a solar simulator setup was used to allow more precise control over the optical power input to the STPV system. A 808 nm, 300 W continuous wave (CW) laser was purchased from Sino Laser. This laser can be focused to a 0.25 cm^2 spot. Although lasers emit light at a single wavelength, the use of a blackbody absorbing surface in this case makes the wavelength of radiation irrelevant, and makes the laser a good approximation of solar energy.

To test the system efficiency, the laser was focused onto the textured area on the absorbing surface, and the relative solar concentration was calculated assuming an incident solar power of $0.1\frac{W}{cm^2}$ and a concentration factor ranging from 1 to 2500. 2500 was chosen as the upper concentration limit due to its being achievable with Fresnel lens systems, and to avoid unrealistic solar tracking requirements [130]. For the sample with a 0.6 cm^2 textured area on the top surface, a concentration factor of 2500 was achieved for a laser power output of 150 W.

5.5 STPV System

Many different configurations for STPV systems exist, including planar, spherical, cylindrical and conical geometries [3]. While cylindrical geometries can typically achieve higher efficiencies than planar geometries, cylindrical STPV systems have increased complexity and typically require a large cylindrical area to be tiled with small area PV cells [4]. This dissertation focuses on the use of a planar geometry for the experimental system, as seen in Figure 1.1, due to its simplicity and relaxed constraints on PV cell size and area. The loss in efficiency in differing geometries can be mitigated by increasing A_{ratio} [18].

The system was held under vacuum during high temperature operation to ensure the thermal stability of the tungsten nanostructures and to reduce the loss of heat due to thermal convection [41]. A 1 square foot vacuum chamber from Kurt J. Lesker with 8-inch ConFlat flanges housed the STPV system. A Fisher Scientific Maxima vacuum pump was used to reduce the pressure inside the chamber to 10 mTorr. The vacuum was measured with a 275i series convection vacuum gauge made by Kurt J. Lesker. The chamber was back-filled with nitrogen gas during operation to ensure the thermal stability of the Si_3N_4 coatings. This would not be necessary if a high vacuum was achieved, or if a hafnia coating was used in place of the silicon nitride. The absorber-emitter structure was held in place inside the vacuum chamber via two 0.5 mm diameter fused silica rods. Fused silica was used due to its high melting point, low thermal conductivity, and optical clarity. The GaSb PV cells were attached to a water-cooled copper heat sink Arctic Silver 5 thermal compound used to reduce thermal resistance between the substrate and heat sink and prevent air pockets from forming. A thin aluminum cover plate was then placed between the PV cell and the

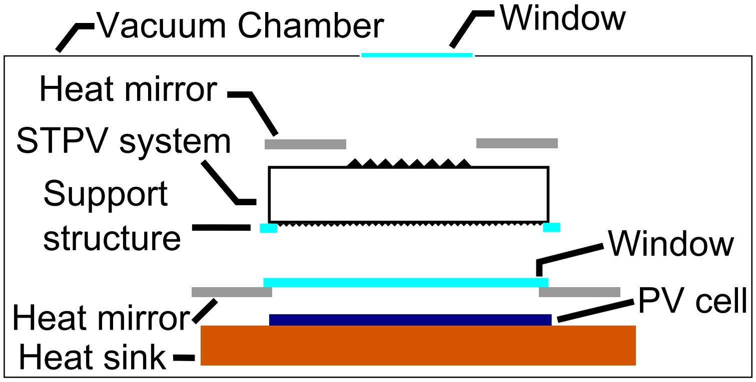

Figure 5.7: A diagram of the STPV system setup inside the vacuum chamber.

emitting surface to prevent excess radiation from the emitting surface from reaching the heat sink and PV cell frame. A hole was cut in this plate over the active area of the PV cell to allow radiation from the emitting surface to reach the PV cell, and a thin glass slide was placed over this hole to reduce convective losses and the amount of IR radiation reaching the cell. Additionally, a heat mirror was placed over the untextured portion of the absorbing surface to reflect back thermal radiation from the untextured portion of the top surface. A diagram of this setup is shown in Figure 5.7, with a top-down photo in Figure 5.5b.

System power output was recorded directly from the PV cells. The open circuit voltage (V_{oc}) and short circuit current (I_{sc}) of the cells were recorded with a multimeter at each input power. The efficiency was then determined by $\frac{V_{oc} \times I_{sc} \times FF}{P_{in}}$ where P_{in} is the total power input to the system either from a Fresnel lens or a laser.

5.5.1 Emitter/Absorber Area Ratio (A_{ratio})

To test the effect of A_{ratio} on system efficiency, an STPV system with a texture on the entire absorbing surface was used. The A_{ratio} was then varied by changing the size of the heat mirror placed on top of the absorbing surface. For this experiment, an equivalent solar concentration ratio of 1500 was maintained, allowing the absorbing surface area to be varied from 0.25 cm^2 to 2 cm^2. This resulted in a possible A_{ratio} from 3.2 to 26.

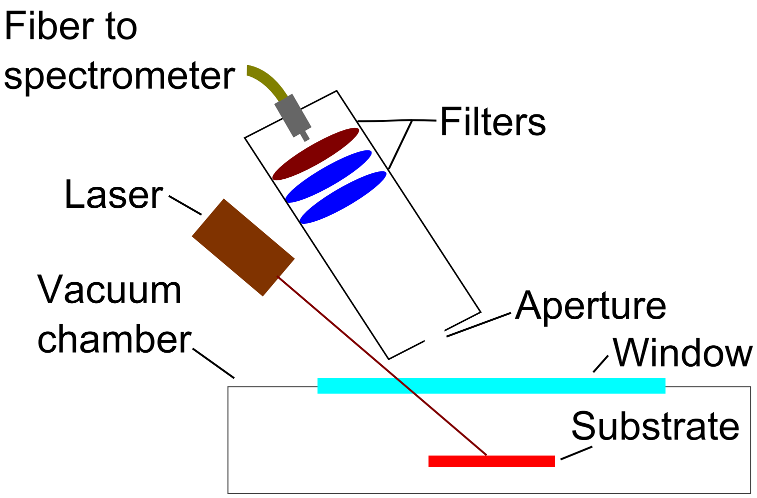

Figure 5.8: A diagram of the temperature measurement setup.

Due to the fact that the heat mirror must be suspended slightly above the absorber/emitter structure to avoid damage to the mirror, and the fact that concentrated sunlight will approach the STPV system at an angle, the gap in the heat mirror above the top surface must be slightly larger than the absorbing portion of this surface. Although this issue can be avoided when using a laser as input power, the gap is widened in these experiments to simulate the conditions of the system under concentrated solar energy.

5.5.2 Temperature Measurements

Temperature measurements were taken with a type R thermocouple purchased from Nordic Sensors, Inc. This thermocouple was bonded to the tungsten surface with a high-temperature thermally-conductive cement purchased from Sigma-Aldrich. Temperature measurements were reliably taken at temperatures up to 1400 K. Temperature measurements for the PV cell were taken in the same way as measurements for the substrate. Because the PV cell did not reach temperatures over 400 K, this method was sufficient. Temperatures beyond 1400 K were calculated using thermal emission data from the blackbody absorbing surface. A StellarNet EPP2000CXR-SR-200 spectrometer with a glass fiber was used to capture the thermal emission, with two Edmund Optics 808 nm OD 4 notch filters, one ThorLabs

FEL0850 850 nm cutoff longpass filter, and a 3 cm aperture in-line with the fiber to reduce the amount of scattered laser radiation reaching the spectrometer. A diagram of this setup is shown in Figure 5.8.

The range of the spectrometer used was 400-1100 nm, which is not a long enough wavelength to determine the peak of the blackbody curve for the temperatures encountered in this experiment. To remedy this situation, blackbody curves were fit to the tail end of the curve that was captured by the spectrometer. Thermocouple data from low temperatures was used as a calibration. Using this method, temperatures up to 1700 K were recorded.

Chapter 6: System Characterization and Results

The experimental STPV system was tested in a laboratory and solar setting, and experimental and simulated results were compared. The efficiencies and operational temperatures of the system under different operating conditions were recorded and compared. Reasons for lowered efficiency values and a path forward to higher efficiencies are discussed.

6.1 High-efficiency System

First, an STPV system with a fixed A_{ratio} of 11 was tested with a laser under laboratory conditions. A 0.6 cm^2 portion of the absorbing surface was textured, and the remaining portion was covered with a mirror. This is an optimal A_{ratio} for this system, according to simulations. The input power was varied to change the effective solar concentration of the system, and the temperature and efficiency were recorded at each point. Figures 6.1 a and b show the measured and simulated temperature and efficiency of this system. This was the most efficient system tested due to the large untextured portion of the absorbing surface. Good agreement was found between experimental and simulated data, showing that the basic premise of the simulation is sound. There was also good agreement between temperatures measured with a thermocouple and via curve-fitting of spectral blackbody emission data. The highest efficiency recorded for this system was 6.2% at a laser power of 149 W, corresponding to a solar concentration factor of 2483. PV cell temperature data was also taken during this experiment, and is shown in Figure 6.2. The cell reached a maximum temperature of 345 K with a solar concentration factor of 2483. At this temperature, the V_{oc} of the cell was lowered, lowering overall cell efficiency, as shown in Figure 4.14. The system efficiency

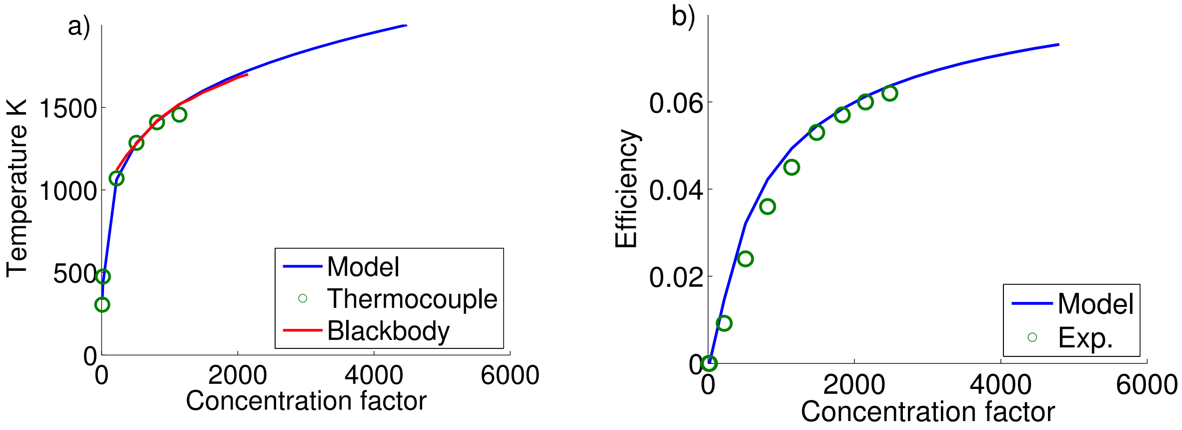

Figure 6.1: Graph of a) temperature vs. solar concentration and b) efficiency vs. solar concentration for an experimental system with a fixed A_{ratio} of 11.

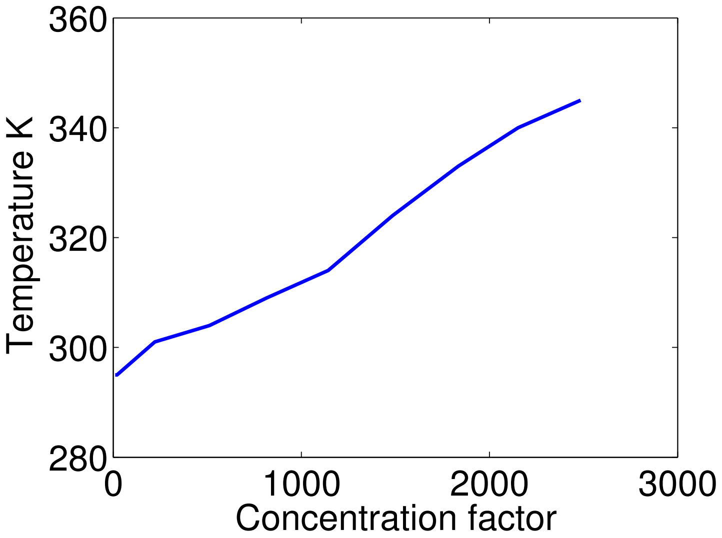

Figure 6.2: Temperature of the PV cell vs. solar concentration factor, measured with a thermocouple.

could be significantly improved if the PV cell was kept at room temperature during this measurement [146]. Table 6.1 shows major sources of PV cell heating, according to the simulation. Note that there is negligible convective transfer of heat due to the glass plate between the emitter and PV cell.

Efficiency losses within the PV cell are the single greatest source of cell heating, and also

Table 6.1: Simulated sources of PV cell heating.

Source	Percentage of heating
Radiation with energy <E_{bg}	27%
Thermalization in cell	23%
EQE and FF loss in cell	50%

a large efficiency loss in the system as a whole. Improved GaSb PV cells could help to greatly increase system efficiency by tackling both problems at once. Higher efficiency cells have been reported in literature, and should be obtainable for this purpose.

Additional dielectric layers to the glass sheet between the emitting surface and PV cell can be used to create a filter that would reflect some radiation with energy <E_{bg} back to the emitter. While an ideal filter could greatly improve efficiency by functioning similarly to a selective emitter, simulations using realistic filters failed to show such an improvement due to the broadband regions of high transmittance required. Despite this, filters could be used to decrease the thermal load on the PV cell without adversely affecting system efficiency.

Lastly, although the cell was cooled with a copper heat sink and chiller, an improved thermal compound or PV cell substrate could help to decrease the thermal resistance between the PV cell and heat sink, resulting in a cooler cell. Table 6.2 shows the values of the parameters used in the experimental system, and Table 6.3 shows the origin of the losses. Compared with the simulated results in Table 4.2, major sources of additional efficiency loss include emittance from the absorbing surface, thermal emission from the emitting surface that has energy <E_{bg}, thermalization loss in the PV cell, and the efficiency loss due to the PV cell itself. These losses are due primarily to three changes in the experimental system from the simulated setup: 1) the change from a selective (nano-cone) absorbing surface to a blackbody (micro-cones), 2) the change in emitting surfaces from nano-holes in W to an anti-reflective coating on W, and 3) the low-quality commercial grade PV cell as compared to experimental cells reported in literature.

Table 6.2: List of values for experimental system.

Parameter	Default value
α_{sol} (Blackbody)	0.9
η_{emit} (Anti-reflection coating on W)	0.59
PV cell FF	0.61
System temperature	1777 K
ϵ_{1700K} (Blackbody)	0.9
Distance from absorber to reflective mirror	1 mm
J_{emit} (Anti-reflection coating on W)	57.1 W/cm^2
Solar concentration (C)	2483
Distance from emitter to PV cell	3 mm
A_{abs}	0.6 cm^2
Absorber/emitter thickness	1 mm
A_{emit}	6.25 cm^2
Support thermal conductivity	1.38 W/mK
System pressure	10 mTorr
PV cell type	GaSb
System type	Flat

Table 6.3: List of losses in a simulation of the experimental STPV system with parameters listed in Table 6.2.

Loss type	Percent of input power lost
Reflection off of absorbing surface	10.0%
Emittance from absorbing surface	23.6%
Emittance from sides of structure	1.2%
Thermal conductivity through supports	0.1%
Convective losses	2.1%
Emittance from emitter that does not reach PV cell	11.0%
Thermal emission below E_{bg}	12.1%
Thermalization loss in PV cell	10.3%
Loss due to PV cell efficiency	22.4%
Loss due to PV cell temperature	0.8%
Power conversion efficiency	6.4%

Despite these reductions in efficiency, an experimental efficiency of 6.2% is high for an STPV system. This is the highest reported efficiency for a system using micro or nanostructured surfaces, and the second highest efficiency achieved to date. By demonstrating the accuracy of the simulations used in this dissertation, the potential for extremely high efficiency STPV devices using the nanostructures described here is displayed. This work has been submitted to the journal of Optics Express for publication [153].

6.1.1 High Efficiency System Improvements

Absorbing Surface

Using the pseudo-random nanocone surface described in section 4.2.4, the modeled efficiency of the device rose to 8.1%. This was largely due to a reduction in energy emitted from the absorbing surface from 23.6% to 14.0% of the total energy, which allowed the system temperature to rise from 1777 K to 1857 K.

This primarily results from the reduced ϵ_{1700K} (from 0.9 to 0.16) of this surface due to the presence of nanostructures. This is a large improvement because emission from the absorbing surface is the largest loss in the experimental STPV system, and the change from an emissivity of 0.9 to 0.16 is very significant.

Emitting Surface

Replacing the anti-reflective coating used as an emitting surface in the experimental system with the periodic array of nanoholes described in section 4.2.5 increases both J_{emit} (from 57.1 to 68.1 W/cm^2) and η_{emit} (from 0.59 to 0.64). This caused a rise from 6.2% to 6.9% in the modeled device efficiency.

The portion of power emitted from the emitting surface (as opposed to lost through the top and side surfaces or supports) rose due to the increase in J_{emit}, while the increase in η_{emit} caused both the thermalization loss and loss from thermal emission below the E_{bg} of the PV cell to fall. This resulted in a significant improvement in system efficiency, although it was less than the gain from improving the absorbing surface because the relative change in J_{emit} and η_{emit} was small.

PV Cell

Both the PV cell cooling and the quality of the cell itself could be improved to increase system efficiency. By keeping the cell at room temperature, either by having better thermal coupling between the cell and heat sink or by using a heat-reflecting filter between the cell and emitting surface (as described in section 6.1), the V_{oc} of the cell during the experiment can be improved. This resulted in the modeled efficiency of the system rising from 6.2% to 7.0%.

Further improvements in the PV cell would be to increase its FF and room-temperature V_{oc}. An increase in cell V_{oc} from the 413 mV found in the experimental system (in Table 5.1) to the 586 mV reported in literature, combined with an increase in the filling factor from 0.6 (as measured in Table 5.1), to 0.82, as found in literature [33, 146], would result in the system efficiency rising to 11.8%.

Additionally, a multi-junction PV cell could be used to increase system efficiency by reducing thermalization loss; however, this will result in a more complicated fabrication process for the PV cell, and may result in lower PV cell efficiency.

System Architecture

Changing from a planar to cylindrical system architecture helps reduce both the power emitted from the absorbing surface, by minimizing its area, and the power emitted from the sides of the structure (because power emitted from the side of a cylindrical system is collected, and not lost). This results in the system efficiency increasing from 6.2% to 7.4%. Again, this is a large increase because it results in a reduction in energy emitted from the absorbing surface from 23.6% to 16.3%, and this is the largest loss in the system.

Combination of Improvements

The combination of all these improvements would increase the system efficiency of a planar system to 19.1%, and a cylindrical system to 21.6%. Adding in a solar concentrator with a

75% loss would bring the results for a planar system back down to the 14.4% seen in Table 4.2, and the results for a cylindrical system to 16.5%. While this combination of improvements may be difficult to achieve, 16.5% is an extremely high efficiency for an STPV system, and partial implementation of these improvements would still result in a very efficient device.

6.2 Solar System

The system was also tested under solar conditions using a Fresnel lens. The lens used was able to focus light to a 6.25 cm^2 spot, which required the A_{ratio} of the device to be fixed at 1 for the absorbing surface to be large enough to receive all the incoming light. With a concentration factor of 391 and a lens efficiency of 28%, a system efficiency of 0.8% was found. This decrease is due to the low solar concentration, which leads to low system temperatures, and low concentration efficiency of the lens.

6.2.1 Solar System Improvements

The primary way to improve the efficiency of the solar system is to improve the solar concentrator setup. Since the same setup was used for the solar and high-efficiency systems, an efficiency of 6.2% is achievable by improving the solar concentration. If the lensing efficiency was raised to 80%, which is a reasonably achievable value for a single Fresnel lens, the system efficiency would rise to 2.1%, according to the model. Increasing the solar concentration factor to 2500 using a secondary lens, and dropping the efficiency to 75% to account for the addition of a second lens would result in the efficiency rising to 4.5%.

Using a parabolic type concentrator, allowing solar concentrations of 3000 with an efficiency of 90%, would increase the efficiency of this device to 6.1%. With the addition of the increased efficiency PV cells, improved cell cooling, and improved absorbing and emitting surfaces mentioned in section 6.1.1, the system could reach a solar conversion efficiency of 10.6%.

These numbers show a very promising system with many avenues in both the short and long term to increase efficiency.

Chapter 7: Conclusions and Future Work

7.1 Conclusions

In this work, nanostructures were examined for use in STPV systems due to their use in precisely controlling the spectral properties of surfaces. First, figures of merit were developed to compare the performance of various architectures for the absorbing and emitting surfaces in STPV systems. These figures provided a good relative comparison of efficiency between various surfaces, although they were not found to be an accurate measurement of total system efficiency.

A combination of FDTD, raytracing, and Fresnel simulations with EMT were used to investigate theoretical absorbing and emitting structures. These modeling techniques allowed the reflectance, absorbance, and emittance of arbitrary structures to be determined. These were used to explore the potential of surfaces with various materials, shapes, and coatings. Additionally, modeled data was fit to experimental reflectance data for fabricated surfaces such as GLAD coatings, laser-textured tungsten layers, and metal and dielectric stacks on tungsten substrates. A focus was placed on the use of nanostructures that would be easy and inexpensive to fabricate, and that would also be thermally stable at STPV operating temperatures. A variety of nanostructured surfaces with very high potential were found, with a periodic array of nano-holes on a tungsten substrate being very good for the emitting surface, and a pseudo-random array of nanocones on tungsten making an excellent absorbing surface.

To better understand the viability of these surfaces, the mechanisms of power loss in STPV systems were explored, and a thorough theoretical analysis of these losses was provided.

It was found that although there is a large amount of interplay between losses, they can generally be decoupled for analysis over short ranges. This was instrumental in forming an understanding of how each loss played into the system efficiency as a whole, and in pinpointing the most important areas for improvement.

A thermodynamic model of a complete STPV system was developed. This model featured two primary device architectures: planar and cylindrical, as well as various parameters listed in Table 4.3 as variables. The spectral reflection and absorption of surfaces calculated in previous simulations were also entered as inputs into the model. The model used Newton's method to find the temperature of the system and then the efficiency. The output from the model included a breakdown of the primary losses in the STPV system, as shown in Table 4.2.

The data generated from these models showed that control of the spectral reflectance and emittance of the absorbing and emitting surfaces were of primary importance in STPV system efficiency, but it also showed that changes in the absorbing surface have a larger effect on efficiency. The quality of PV cells was also a large factor for the device efficiency, and there are papers published in literature showing routes to increased GaSb cell efficiency.

It is interesting to note that the change to the absorbing surface and the change from planar to cylindrical geometry (both of which primarily decrease ϵ_{1700K}) have a larger effect than the changes to the emitting surface. This is because the values of ϵ_{1700K} vary a large amount for various absorbing surface types, and also constitute one of the largest losses in the system. A simple anti-reflective coating on a tungsten substrate can achieve an η_{emit} of 0.59, which is about 1.4 times the loss from an ideal emitting surface with an η_{emit} of 0.84. In contrast to this, a blackbody absorbing surface has an ϵ_{1700K} of 0.9, which is about 5.6 times the loss from an absorbing surface using pseudo-random nanocones. While using an anti-reflective coating on tungsten as an absorbing surface can reduce ϵ_{1700K}, the corresponding reduction in η_{abs} nullifies the gain from this for the systems tested.

To test the simulation, an experimental STPV system was developed. This system included a laser-textured blackbody absorbing surface and anti-reflective coated emitting surface in a planar setup. Si_3N_4 was used for both the anti-reflective coating and as a protective layer on the blackbody absorber. GaSb PV cells were used, and the system was kept under vacuum during operation. This system was tested under both laboratory conditions using a laser as a light source, and outside under solar radiation.

The system had an efficiency of 6.2% under laboratory conditions, which is very high for an STPV system. Furthermore, both efficiency and temperature measurements compared well with simulated data across a wide range of input powers. Under solar conditions, low power input due to a low-quality Fresnel lens hampered performance, resulting in an efficiency of 0.8%. This matched well with modeled data, however, and could be greatly improved with greater concentration of incoming sunlight.

The accuracy of the model helps to show the great potential for STPV systems. Devices simulated under reasonable assumptions reached efficiencies of 16.5% under solar concentration, and 21.6% under laboratory conditions. Future improvements can improve this further, and will eventually allow STPV systems to break the Shockley-Queisser limit on PV cell efficiency.

7.2 Future Work

In order to realize highly efficient STPV systems, the following issues need to be addressed: 1) An absorbing surface with high η_{abs} and low ϵ_{1700K} needs to be fabricated, 2) an emitting surface with high η_{emit} must be fabricated, 3) a high efficiency GaSb PV cell must be used, 4) the PV cell must be kept cool during device operation (possibly by use of a spectral filter between the PV cell and emitting surface), 5) a solar concentrator capable of reaching a concentration factor of 2500 with reasonable (>75%) efficiency must be used, and 6) these components must all be incorporated into a cylindrical STPV system.

If these changes are taken into account, the simulations in this dissertation show that an STPV device with efficiency >15% can be realized. To take STPV systems beyond 20%

efficiency, more advanced control of the reflectance and emittance of surfaces will be required, and these surfaces will need to be stable to higher operating temperatures.

Bibliography

[1] R. M. Swanson. A proposed thermophotovoltaic solar energy conversion system. *Proceedings of the IEEE*, 67:446–447, 1979.

[2] P. A. Davies and A. Luque. Solar thermophotovoltaics: brief review and a new look. *Solar Energy Materials and Solar Cells*, 33:11–22, 1994.

[3] Y. Xuan, X. Chen, and Y. Han. Design and analysis of thermophotovoltaic systems. *Renewable Energy*, 36:374–387, 2011.

[4] A. Datas and C. Algora. Global optimization of solar thermophotovoltaic systems. *Progress in Photovoltaics: Research and Applications*, 21:1040–1055, 2013.

[5] H. Hofler, H. J. Paul, W. Ruppel, and P. Wurfel. Interference filters for thermophotovoltaic solar energy conversion. *Solar Cells*, 10:273–286, 1983.

[6] V. M. Andreev, V. P. Khvostikov, O. A. Khvostikova, A. S. Vlasov, P. Y. Gazaryan, N. A. Sadchikov, and V. D. Rumyantsev. Solar thermophotovoltaic system with high temperature tungsten emitter. *IEEE Photovoltaic Specialists Conference*, pages 671–674, 2005.

[7] H. Lund, E. Schaltz, D. Tonini, L.-L. P. Hansen, F. Hvelplund, J. R. Pillay, T. Astrup, H. Wenzel, B. V. Mathiesen, M. P. Nielsen, K. Heussen, L. Hamelin, P. A. Ostergaard, C. Felby, P. E. Morthorst, J. Munksgaard, P. Christensen, N. S. Bentsen, F. M. Andersen, P. Karnoe, D. Connolly, N. I. Meyer, M. Munster, and M. Lind. Coherent energy and environmental system analysis (CEESA). *The Danish Council for Strategic Research Programme Commission on Sustainable Energy and Environment*, 2011.

[8] M. A. Green, K. Emery, Y. Hishikawa, W. Warta, and E. D. Dunlop. Solar cell efficiency tables (Version 45). *Progress in Photovoltaics: Research and Applications*, 23:1–9, 2014.

[9] S. Fan. Photovoltaics: An alternative 'sun' for solar cells. *Nature Nanotechnology*, 9:92–93, 2014.

[10] L. M. Fraas, J. E. Avery, and H. X. Huang. Thermophotovoltaic furnace-generator for the home using low bandgap GaSb cells. *Semiconductor Science and Technology*, 18:S247, 2003.

[11] W. Durisch, B. Bitnar, J.-C. Mayor, Fritz von Roth, H. Sigg, H.R. Tschudi, and G. Palfinger. Small self-powered grid-connected thermophotovoltaic prototype system. *Applied Energy*, 74:149 – 157, 2003. Energex 2002 - New and Renewable Sources of Energy - Topic I.

[12] T. A. Butcher, J. S. Hammonds, E. Horne, B. Kamath, J. Carpenter, and D. R. Woods. Heat transfer and thermophotovoltaic power generation in oil-fired heating systems. *Applied Energy*, 88(5):1543–1548, 2011.

[13] P. J. Sonneveld, G. L. A. M. Swinkels, B. A. J. van Tuikl, H. J. J. Janssen, J. Campen, and G. P. A. Bot. Performance of a concentrated photovoltaic energy system with static linear Fresnel lenses. *Solar Energy*, 85:432–442, 2011.

[14] B. Du, E. Hu, and M. Kolhe. Performance analysis of water cooled concentrated photovoltaic (CPV) system. *Renewable and Sustainable Energy Reviews*, 16:6732–6736, 2012.

[15] A. Datas and C. Algora. Development and experimental evaluation of a complete solar thermophotovoltaic system. *Progress in Photovoltaics: Research and Applications*, 890:327–334, 2012.

[16] A. S. Vlasov, V. P. Khvostikov, O. A. Khvostikova, P. Y. Gazaryan, S. V. Sorokina, and V. M. Andreev. TPV systems with solar powered tungsten emitters. *AIP Conference Proceedings*, 890:327–334, 2007.

[17] H. Yugami, H. Sai, K. Nakamura, H. Nakagawa, and H. Ohtsubo. Solar thermophotovoltaic using $Al_2O_3/Er_3Al_5O_{12}$ eutectic composite selective emitter. *IEEE Photovoltaic Specialists Conference*, 28:1214–1217, 2000.

[18] A. Lenert, D. M. Bierman, Y. Nam, W. R. Chan, I. Celanovic, M. Soljacic, and E. N. Wang. A nanophotonic solar thermophotovoltaic device. *Nature Nanotechnology*, 9:126–130, 2014.

[19] M. Shimizu, A. Kohiyama, and H. Yugami. High-efficiency solar thermophotovoltaic system equipped with a monolithic planar selective absorber/emitter. *Journal of Photonics for Energy*, 5:053099, 2015.

[20] E. Rephaeli and S. Fan. Absorber and emitter for solar thermophotovoltaic systems to achieve efficiency exceeding the Shockley-Queisser limit. *Optics Express*, 17:15145–15159, 2009.

[21] N. P. Harder and P. Wurfel. Theoretical limits of thermophotovoltaic solar energy conversion. *Semiconductor Science and Technology*, 18:151–157, 2003.

[22] N. P. Sergeant, O. Pincon, M. Agrawal, and P. Peumans. Design of wide-angle solar-selective absorbers using aperiodic metal-dielectric stacks. *Optics Express*, 17:22800–22812, 2009.

[23] A. Datas. *Development of solar thermophotovoltaic systems*. Phd thesis, University Politecnica de Madrid, 2011.

[24] Reference solar spectral irradiance: Astm g-173. http://rredc.nrel.gov/solar/spectra/am1.5/ASTMG173/ASTMG173.html, 2012. Accessed: 2014-09-20.

[25] C. A. Wang, H. K. Choi, S. L. Ransom, G. W. Charache, L. R. Danielson, and D. M. DePoy. High-quantum-efficiency 0.5 eV GaInAsSb/GaSb thermophotovoltaic devices. *Applied Physics Letters*, 75:1305–1307, 1999.

[26] A. Taflove and S. C. Hagness. *Computational Electrodynamics: The Finite-Difference Time-Domain Method, Third Edition.* Artech House, Norwood, MA, 2005.

[27] D. M. Sullivan. *Electromagnetic simulation using the FDTD method.* IEEE Press, Piscataway, NJ, 2000.

[28] D. L. Chubb. *Fundamentals of Thermophotovoltaic Energy Conversion.* Elsevier, 2007.

[29] M. G. Mauk. *Survey of Thermophotovoltaic (TPV) Devices*, volume 118 of *Springer Series in Optical Sciences.* Springer London, 2006.

[30] V. M. Andreev, V. A. Grilikhes, V. P. Khvostikov, O. A. Khvostikova, V. D. Rumyantsev, N. A. Sadchikov, and M. Z. Shvarts. Concentrator PV modules and solar cells for TPV systems. *Solar Energy Materials and Solar Cells*, 84:3–17, 2004.

[31] V. P. Khvostikov, S. V. Sorokina, O. A. Khvostikova, N. Kh. Timoshina, N. S. Potapovich, B. Ya. Ber, D. Yu. Kazantsev, and V. M. Andreev. High-efficiency GaSb photocells. *Physics of Semiconductor Devices*, 47:307–313, 2013.

[32] Gasb cells and circuits. http://jxcrystals.com/GaSb/4sale5.pdf. Accessed: 2014-09-20.

[33] W. Chan, R. Huang, C. Wang, J. Kassakian, J. Joannopoulos, and I. Celanovic. Modeling low-bandgap thermophotovoltaic diodes for high-efficiency portable power generators. *Solar Energy Materials and Solar Cells*, 94:509–514, 2010.

[34] M. W. Dashiell, J. F. Beausang, H. Ehsani, G. J. Nichols, D. M. Depoy, L. R. Danielson, P. Talamo, K. D. Rahner, E. J. Brown, S. R. Burger, P. M. Fourspring, W. F. Topper, P. F. Baldasaro, C. A. Wang, R. K. Huang, M. K. Connors, G. W. Turner, Z. A. Shellenbarger, G. Taylor, Jizhong Li, R. Martinelli, D. Donetski, S. Anikeev, G. L. Belenky, and S. Luryi. Quaternary InGaAsSb thermophotovoltaic diodes. *IEEE Transactions on Electron Devices*, 53:2879–2891, 2006.

[35] J. Fernandez. *Quaternary InGaAsSb thermophotovoltaic1 diodes.* Phd thesis, University Konstanz, 2010.

[36] V. P. Khvostikov, O. A. Khvostikova, P. Y. Gazaryan, S. V. Sorokina, N. S. Potapovich, A. V. Malevskaya, N. A. Kaluzhiny, M. Z. Shvarts, and V. M. Andreev. Photovoltaic cells based on GaSb and Ge for solar and thermophotovoltaic applications. *Journal of Solar Energy Engineering*, 129:291–297, 2006.

[37] D. J. Friedman, J. M. Olson, S. Ward, T. Moriarty, K. Emery, S. Kurtz, and A. Duda. Ge concentrator cells for III-V multijunction devices. *Proceedings of the 28th IEEE Photovoltaic Specialists Conference*, pages 965–967, 2000.

[38] C. E. Kennedy. Review of mid-to-high temperature solar selective absorber materials. Technical report NREL/TP-520-31267. page 58, 2002.

[39] P. Bermel, M. Ghebrebrhan, W. Chan, Y. X. Yeng, M. Araghchini, R. Hamam, C. H. Marton, K. F. Jensen, M. Soljacic, J. D. Joannopoulos, S. G. Johnson, and I. Celanovic. Design and global optimization of high-efficiency thermophotovoltaic systems. *Optics Express*, 18:A314–A334, 2010.

[40] M. Zhang, M. Y. Efremov, F. Schiettekatte, E. A. Olson, A. T. Kwan, S. L. Lai, T. Wisleder, J. E. Greene, and L. H. Allen. Size-dependent melting point depression of nanostructures: Nanocalorimetric measurements. *Physical Review B*, 62:10548–10557, 2000.

[41] C. Schlemmer, J. Aschaber, V. Boerner, and J. Luther. Thermal stability of micro-structured selective tungsten emitters. *Thermophotovoltaic Generation of Electricity: 5th Conference, CP653 - American Institute of Physics*, 2003.

[42] T. Chookajorn, H. A. Murdoch, and C. A. Schuh. Design of stable nanocrystalline alloys. *Science*, 337:951–954, 2012.

[43] O. Behar, A. Khellaf, and K. Mohammedi. A review of studies on central receiver solar thermal power plants. *Renewable and Sustainable Energy Reviews*, 23:12–39, 2013.

[44] K. A. Arpin, M. D. Losego, and P. V. Braun. Electrodeposited 3D tungsten photonic crystals with enhanced thermal stability. *Chemistry of Materials*, 23:4783–4788, 2011.

[45] E. M. Sparrow, L. U. Albers, and E. R. G. Eckert. Thermal radiation characteristics of cylindrical enclosures. *Journal of Heat Transfer*, 84:73–79, 1962.

[46] V. M. Andreev, V. P. Khvostikov, V. D. Rumyantsev, O. A. Khvostikova, P. Y. Gazaryan, A. S. Vaslov, N. A. Sadchikov, S. V. Sorokina, Y. M. Zadiranov, and M. Z. Sharts. Thermophotovoltaic converters with solar powered high temperature emitters. *Proceedings of the 20th European Photovoltaic Solar Energy Conference*, pages 8–13, 2005.

[47] E. D. Palik. *Handbook of Optical Constants of Solids*. Academic Press, Boston, MA, 1985.

[48] T. K. Chaudhuri. A solar thermophotovoltaic converter using Pbs photovoltaic cells. *International Journal of Energy Research*, 16:481–487, 1992.

[49] F. Demichelis and E. Minetti-Mezzetti. A solar thermophotovoltaic converter. *Solar Cells*, 1:395–403, 1980.

[50] E. Randich and D. D. Allred. Chemical vapor-deposited ZrB_2 as a selective solar absorber. *Thin Solid Films*, 83:393–398, 1981.

[51] H. Tabor. Solar collectors, selective surfaces, and heat engines. *Proceedings of the National Academy of Sciences of the United States of America*, 47:1271–1278, 1961.

[52] G. B. Smith and A. Ignatiev. Black chromium-molybdenum: a new stable solar absorber. *Solar Energy Materials*, 4:119–113, 1981.

[53] N. Selvakumar and H. C. Barshilia. Review of physical vapor deposited (PVD) spectrally selective coatings for mid- and high-temperature solar thermal applications. *Solar Energy Materials and Solar Cells*, 98:1–23, 2012.

[54] R. N. Schmidt and K. C. Park. High-temperature space-stable selective solar absorber coatings. *Applied Optics*, 4:917–925, 1965.

[55] C. Wu, B. Neuner III, J. John, A. Milder, B. Zollars, S. Savoy, and G. Shvets. Metamaterial-based integrated plasmonic absorber/emitter for solar thermophotovoltaic systems. *Journal of Optics*, 14:24005–24008, 2012.

[56] E. Rephaeli and S. Fan. Tungsten black absorber for solar light with wide angular operation range. *Applied Physics Letters*, 92:211107, 2008.

[57] H. Sai and H. Yugami. Thermophotovoltaic generation with selective radiators based on tungsten surface gratings. *Applied Physics Letters*, 85:3399–3401, 2004.

[58] H. Shi, J. G. Ok, H. W. Baac, and L. J. Guo. Low density carbon nanotube forest as an index-matched and near perfect absorption coating. *Applied Physics Letters*, 99:211103, 2011.

[59] Z. P. Yang, L. Ci, J. A. Bur, S. Y. Lin, and P. M. Ajayan. Experimental observation of an extremely dark material made by a low-density nanotube array. *Nano Letters*, 8:446–451, 2008.

[60] C. Ungaro, A. Shah, I. Kravchenko, D. K. Hensley, S. K. Gray, and M. C. Gupta. Optical and infrared properties of glancing angle deposited nanostructured tungsten films. *Optics Letters*, 40:506–509, 2015.

[61] C. Ungaro, S. K. Gray, and M. C. Gupta. Black tungsten for solar power generation. *Applied Physics Letters*, 103(7):071105–071105–3, 2013.

[62] B. K. Nayak, M. C. Gupta, and K. W. Kolasinski. Formation of nano-textured conical microstructures in titanium metal surface by femtosecond laser irradiation. *Applied Physics A*, 90:399–402, 2008.

[63] F. Cao, K. McEnaney, G. Chen, and Z. Ren. A review of cermet-based spectrally selective solar absorbers. *Energy and Environmental Science*, 7:1615–1627, 2014.

[64] T. Bostrom, E. Wackelgard, and G. Westin. Solution-chemical derived nickelalumina coatings for thermal solar absorbers. *Solar Energy*, 74:497–503, 2003.

[65] T. Bostrom, S. Valizadeh, J. Lu, J. Jensen, G. Westin, and E. Wackelgard. Structure and morphology of nickel-alumina/silica solar thermal selective absorbers. *Nature Nanotechnology*, 9:92–93, 2014.

[66] Z. Y. Nuru, C. J. Arendse, T. F. G. Muller, and M. Mazza. Structural and optical properties of $Al_xO_y/Pt/Al_xO_y$ multilayer absorber. *Materials Science and Engineering: B*, 177:1194–1199, 2012.

[67] T. S. Sathiaraj, R. Thangaraj, H. A. Sharbaty, M. Bhatnager, and O. P. Agnihotri. Ni-Al_2O_3 selective cermet coatings for photothermal conversion up to 500 C. *Thin Solid Films*, 190:241–254, 1990.

[68] J. Cheng, C. Wang, W. Wang, X. Du, Y. Liu, Y. Xue, T. Wang, and B. Chen. Improvement of thermal stability in the solar selective absorbing Mo-Al_2O_3 coating. *Solar Energy Materials and Solar Cells*, 109:204–208, 2013.

[69] J. Wang, B. Wei, Q. Wei, and D. Li. Optical property and thermal stability of Mo/Mo-SiO_2/SiO_2 solar-selective coating prepared by magnetron sputtering. *Physica Status Solidi A*, 208:664–667, 2011.

[70] B. Bitnar, W. Durisch, J. C. Mayor, H. Sigg, and H. R. Tschudi. Characterisation of rare earth selective emitters for thermophotovoltaic applications. *Solar Energy and Materials Solar Cells*, 73:221–234, 2002.

[71] L. G. Ferguson and F. Dogan. A highly efficient NiO-Doped MgO matched emitter for thermophotovoltaic energy conversion. *Material Science and Engineering B*, 83:35–41, 2001.

[72] S. Lin, J. Moreno, and J. G. Fleming. Three-dimensional photonic-crystal emitter for thermal photovoltaic power generation. *Applied Physics Letters*, 83:380–382, 2003.

[73] D. L. Chubb, A. T. Pal, M. O. Patton, and P. P. Jenkins. Rare earth doped high temperature ceramic selective emitters. *Journal of the European Ceramic Society*, 19:2551–2562, 1999.

[74] A. Licciulli, D. Diso, G. Torsello, S. Tundo, A. Maffezzoli, M. Lomascolo, and M. Mazzer. The challenge of high-performance selective emitters for thermophotovoltaic applications. *Semiconductor Science and Technology*, 18:S174–S183, 2003.

[75] A. Licciulli, A. Maffezzoli, D. Diso, S. Tundo, M. Rella, G. Torsello, and M. Mazzer. Sol-gel preparation of selective emitters for thermophotovoltaic conversion. *Journal of Sol-Gel Science and Technology*, 26:1119–1123, 2003.

[76] V. Tomer, R. Teye-Mensah, J. C. Tokash, N. Stojilovic, W. Kataphinan, E. A. Evans, G. G. Chase, R. D. Ramsier, D. J. Smith, and D. H. Reneker. Selective emitters for thermophotovoltaics: erbia-modified electrospun titania nanofibers. *Solar Energy Materials and Solar Cells*, pages 477–488, 2005.

[77] D. Diso, A. Licciulli, A. Bianco, G. Leo, G. Torsello, S. Tundo, A. De Risi, and M. Mazzer. Selective emitters for high efficiency TPV conversion: materials preparation and characterization. *AIP Conference Proceedings*, 653:132–141, 2002.

[78] T. Suzuki, G. S. Murugan, and Y. Ohishi. Optical properties of transparent Li_2O-Ga_2O_3-SiO_2 glass-ceramics embedding Ni-doped nanocrystals. *Applied Physics Letters*, 86:131903, 2005.

[79] A. Ikesue, Y. L. Aung, T. Taira, T. Kamimura, K. Yoshida, and G. L. Messing. Progress in ceramic lasers. *Annual Review of Materials Research*, 36:397–429, 2006.

[80] L. G. Ferguson and F. Dogan. Spectral analysis of transition metal-doped MgO matched emitters for thermophotovoltaic energy conversion. *Journal of Materials Science*, 37:1301–1308, 2002.

[81] H. C. Kim, T. L. Alford, and D. R. Allee. Thickness dependence on the thermal stability of silver thin films. *Applied Physics Letters*, 81:4287–4289, 2002.

[82] A. Datas. Optimum semiconductor bandgaps in single junction and multijunction thermophotovoltaic converters. *Solar Energy Materials and Solar Cells*, 134:275–290, 2015.

[83] H. Sai, Y. Kanamori, K. Hane, H. Yugami, and M. Yamaguchi. Numerical study on tungsten selective radiators with various micro/nano structures. *Photovoltaic Specialists Conference*, pages 762–765, 2005.

[84] V. Rinnerbauer, S. Ndao, Y. X. Yeng, J. J. Senkevich, K. F. Jensen, J. D. Joannopoulos, M. Soljacic, I. Celanovic, and R. D. Geil. Large-area fabrication of high aspect ratio tantalum photonic crystals for high-temperature selective emitters. *Journal of Vacuum Science and Technology B*, 31:011802, 2013.

[85] Y. Nam, A. Lenert, Y. X. Yeng, P. Bermel, M. Soljacic, and E. N. Wang. Solar thermophotovoltaic energy conversion systems with tantalum photonic crystal absorbers and emitters. *Transducers and Eurosensors CCVII: The 17th International Conference*, pages 1372–1375, 2013.

[86] Y. B. Chen and Z. M. Zhang. Design of tungsten complex gratings for thermophotovoltaic radiators. *Optics Communication*, 269:411–417, 2007.

[87] E. B. Grann and M. G. Moharam. Comparison between continuous and discrete subwavelength grating structures for antireflection surfaces. *Journal of the Optical Society of America A*, 13:988–992, 1996.

[88] C. Ungaro, S. K. Gray, and M. C. Gupta. Graded-index structures for high-efficiency solar thermophotovoltaic emitting surfaces. *Optics Letters*, 39(18):5259–5262, 2014.

[89] V. M. Andreev, V. P. Khostikov, V. R. Larionov, V. D. Rumyantsev, S. V. Sorokina, M. Z. Shvarts, V. I. Vasilev, and A. S. Vaslov. Tandem GaSb/InGaAsSb thermophotovoltaic cells. *Photovoltaic Specialists Conference*, pages 935–938, 1997.

[90] E. M. Wong, J. P. Hickey, G. A. Holmquist, P. N. Uppal, and C. H. Waldman. Multiband spectral emitters matched to MBE grown photovoltaic cells. *AIP Conference Proceedings*, 358:278–289, 1996.

[91] G. S. Horner, T. J. Coutts, and M. W. Wanlass. Proposal for a second-generation, lattice matched, multiple junction Ga_2AsSb TPV converter. *AIP Conference Proceedings*, 321:390–403, 1995.

[92] O. V. Sulima, A. W. Bett, P. S. Dutta, M. G. Mauk, and R. L. Mueller. GaSb-, InGaAsSb-, InGaSb-, InAsSbP- and Ge- TPV cells with diffused emitters, in: Photovoltaic Specialists Conference, 2002. *Conference Record of the Twenty-Ninth IEEE*, pages 892–895, 2002.

[93] M. C. Gupta, C. Ungaro, J. J. Foley, and S. K. Gray. Optical nanostructures design, fabrication and applications for solar/thermal energy conversion. *Optics Express*. (Submitted).

[94] F. A. Jenkins and H. E. White. *Fundamentals of Optics*. McGraw-Hill, Inc., NY, 1965.

[95] C. L. Mehta. Coherence-time and effective bandwidth of blackbody radiation. *Il Nuovo Cimento*, 28:401–408, 1963.

[96] A. Donges. The coherence length of black-body radiation. *European Journal of Physics*, 19:245–249, 1998.

[97] P. Y. Wong, C. K. Hess, and I. N. Miaoulis. Thermal radiation modeling in multilayer thin film structures. *International Journal of Heat and Mass Transfer*, 35:3313–3321, 1992.

[98] Y. Qin, A. Michalowski, R. Weber, S. Yang, T. Graf, and Z. Ni. Comparison between ray-tracing and physical optics for the computation of light absorption in capillaries - the influence of diffraction and interference. *Optics Express*, 20:26606–26617, 2012.

[99] C. C. Katsidis and D. I. Siapkas. General transfer-matrix method for optical multilayer systems with coherent, partially coherent, and incoherent interface. *Applied Optics*, 41:3978–3987, 2002.

[100] G. A Nikalsson, C. G. Granqvist, and O. Hunderi. Effective medium models for the optical properties of inhomogeneous materials. *Applied Optics*, 20:26–30, 1981.

[101] Y. Nam, Y. X. Yeng, A. Lenert, P. Bermel, I. Celanovic, M. Soljacic, and E. N. Wang. Solar thermophotovoltaic energy conversion systems with two-dimensional tantalum photonic crystal absorbers and emitters. *Solar Energy Materials and Solar Cells*, 122:287–296, 2014.

[102] M. Saidi and R. H. Abardeh. Air pressure dependence of natural-convection heat transfer. *Proceedings of the World Congress on Engineering 2010*, II, 2010.

[103] M. Levitsky. The criterion for validity of the fin approximation. *International Journal of Heat and Mass Transfer*, 15:1960–1963, 1972.

[104] Z. Rotem and L. Classen. Natural convection above unconfined horizontal surfaces. *Journal of Fluid Mechanics*, 38:173–192, 1969.

[105] F. G. Friedlander. Geometrical optic and Maxwell's equations. *Mathematical Proceedings of the Cambridge Philosophical Society*, 43:284–286, 1947.

[106] G. A. Deschamps. Ray techniques in electromagnetics. *Proceedings of the IEEE*, 60:1022–1035, 1972.

[107] A. Goetzberger, J. Knobloch, and B. Voss. *Crystalline silicon solar cells.* John Wiley and Sons Ltd., West Sussex, England, 1998.

[108] G. Lubberts, B. C. Burkey, F. Moser, and E. A. Trabka. Optical properties of phosphorus-doped polycrystalline silicon layers. *Journal of Applied Physics*, 52:6870–6878, 1981.

[109] C. L. Mitsas and D. I. Siapkas. Generalized matrix method for analysis of coherent and incoherent reflectance and transmittance of multilayer structures with rough surfaces, interfaces, and finite substrates. *Applied Optics*, 34:1678–1683, 1996.

[110] A. Rahman, A. Ashraf, H. Xin, X. Tong, P. Sutter, M. D. Eisaman, and C. T. Black. Sub-50-nm self-assembled nanotextures for enhanced broadband antireflection in silicon solar cells. *Nature Communications*, 6:5963, 2015.

[111] D. E. Aspnes and J. B. Theeten. Investigation of effective-medium models of microscopic surface roughness by spectroscopic ellipsometry. *Physical Review B*, 8:3292–3302, 1979.

[112] D. A. G. Bruggeman. Berechnung verschiedener physikalischer Konstanten von heterogenen Substanzen. I. Dielektrizittskonstanten und Leitfhigkeiten der Mischkrper aus isotropen. *Annalen der Physik*, 416:636–664, 1935.

[113] D. G. Stavenga, S. Foletti, G. Palasantzas, and K. Arikawa. Light on the moth-eye corneal nipple array of butterflies. *Proceedings of the Royal Society B*, 273:661–667, 2006.

[114] C.-H. Sun, P. Jiang, and B. Jiang. Broadband moth-eye antireflection coatings on silicon. *Applied Physics Letters*, 92:061112, 2008.

[115] H. Sai, Y. Kanamori, K. Arafune, Y. Oshita, and M. Yamaguchi. Light trapping effect of submicron surface textures in crystalline Si solar cells. *Progress in Photovoltaics: Research and Applications*, 15:415–423, 2007.

[116] K. S. Yee. Numerical solution of initial boundary value problems involving Maxwell's equations in isotropic media. *IEEE Transactions on Antennas and Propagation*, 14:302–307, 1966.

[117] A. F. Oskooi, D. Roundy, M. Ibanescu, P. Bermel, J. D. Joannopoulos, and S. G. Johnson. MEEP: A flexible free-software package for electromagnetic simulations by the FDTD method. *Computer Physics Communications*, 181:687–702, 2010.

[118] A. Farjadpour, D. Roundy, A. Rodriguez, M. Ibanescu, P. Bermel, J. D. Joannopoulos, S. G. Johnson, and G. W. Burr. Improving accuracy by subpixel smoothing in the finite-difference time-domain. *Optics Letters*, 31:2972–2974, 2006.

[119] H. Ehrenreich, H. R. Philip, and B. Segall. Optical properties of aluminum. *Physical Review*, 132:1918–1928, 1963.

[120] M. I. Markovic and A. D. Rakic. Determination of the reflection coefficient of laser light of wavelengths $\lambda = (0.22\ \mu\text{m}, 200\ \mu\text{m})$ from the surface of aluminum using the Lorentz-Drude model. *Applied Optics*, 29:3479–3483, 1990.

[121] C. J. Powell. Analysis of optical- and inelastic-electron-scattering data. II. Application to Al. *Journal of the Optical Society of America*, 60:78–93, 1970.

[122] A. D. Rakic, A. B. Djurisic, J. M. Elazar, and M. L. Majewski. Optical properties of metallic films for vertical-cavity optoelectronic devices. *Applied Optics*, 37:5271–5283, 1998.

[123] H. Ehrenreich, H. R. Philip, and B. Segall. Optical properties of crystalline tungsten. *Physical Review B*, 12:1293–1297, 1975.

[124] A. B. Djurisic and E. H. Li. Modeling the index of refraction of insulating solids with a modified lorentz oscillator model. *Applied Optics*, 37:5291–5297, 1998.

[125] J. D. Joannopoulos, S. G. Johnson, R. D. Meade, and J. N. Winn. *Photonic Crystals: Molding the Flow of Light.* (2nd ed.) Princeton University Press, 2008.

[126] A. Lagae and P. Dutre. A comparison of methods for generating Poisson disk distributions. *Computer Graphics Forum*, 27:114–129, 2008.

[127] A. A. Shah, C. Ungaro, and M. C. Gupta. High temperature spectral selective coatings for solar thermal systems by laser sintering. *Solar Energy Materials and Solar Cells*, 134:209–214, 2015.

[128] A. Luque. Solar thermophotovoltaics: combining solar thermal and photovoltaics. *AIP Conference Proceedings*, 3:3–16, 2007.

[129] P. Gleckman, J. O'Gallagher, and R. Winston. Concentration of sunlight to solar-surface levels using non-imaging optics. *Nature*, 339:198–200, 1989.

[130] K. Ryu, J.-G. Rhee, K.-M. Park, and J. Kim. Concept and design of modular Fresnel lenses for concentration solar PV system. *Solar Energy*, 80:1580–1587, 2006.

[131] L. V. Nomerovannaya, M. M. Kirillova, and M. M. Noskov. Optical properties of tungsten monocrystals. *Soviet Journal of Experimental and Theoretical Physics*, 33:405–409, 1971.

[132] L. Fraas, J. Samaras, J. Avery, and L. Minkin. Antireflection coated refractory metal matched emitters for use with GaSb thermophotovoltaic generators. *Photovoltaic Specialists Conference*, pages 1020–1023, 2000.

[133] V. Rinnerbauer, S. Ndao, Y. X. Yeng, W. R. Chan, J. J. Senkevich, J. D. Joannopoulos, M. Soljacic, and I. Celanovic. Recent developments in high-temperature photonic crystals for energy conversion. *Energy & Environmental Science*, 5:8815–8823, 2012.

[134] H.-P. Chiang, P. T. Leung, and W. S. Tse. The surface plasmon enhancement effect on adsorbed molecules at elevated temperatures. *Journal of Chemical Physics*, 108:2659–2660, 1998.

[135] J. C. Sit, D. Vick, K. Robbie, and M. J. Brett. Thin film microstructure control using glancing angle deposition by sputtering. *Journal of Materials Research*, 14:1197–1199, 1999.

[136] P. M. Martin (Ed.), M. T. Taschuk, M. M. Hawkeye, and M. J. Brett. *Handbook of Deposition Technologies for Films and Coatings, 3rd Ed.* Oxford, UK, 2010.

[137] K. R. Khedir, G. K. Kannarpady, H. Ishihara, J. Woo, C. Ryerson, and A. S. Biris. Morphology control of tungsten nanorods grown by glancing angle RF magnetron sputtering under variable argon pressure and flow rate. *Physics Letters A*, 374:4430–4437, 2010.

[138] D. Deniz, D. J. Frankel, and R. J. Lad. Nanostructured tungsten and tungsten trioxide films prepared by position. *Thin Solid Films*, 518:4095–4099, 2010.

[139] J. C. Fiala. Reconstruct: a free editor for serial section microscopy. *Journal of Microscopy*, 218:52–61, 2005.

[140] A. Ambrosini, T. N. Lambert, M. Bencomo, A. Hall, K. vanEvery, N. P. Siegel, and C. K. Ho. Improved high temperature solar absorbers for use in concentrating solar power central receiver applications. *Proceedings of ASME*, 5:587–594, 2011.

[141] W. Stork, N. Streibl, H. Haidner, and P. Kipfer. Artificial distributed-index media fabricated by zero-order gratings. *Optics Letters*, 16:1921–1923, 1991.

[142] K.-H. Kim and Q.-H. Park. Perfect anti-reflection from first principles. *Scientific Reports*, 3:1062 – 1062–14, 2013.

[143] C. Palmer. *Diffraction Grating Handbook 6th edition.* Newport Corporation, Rochester, NY, 2005.

[144] M. Araghchini, Y. X. Yang, N. Jovanovic, P. Bermel, L. A. Kolodziejski, M. Soljacic, I. Celanovic, and J. D. Joannopoulos. Fabrication of two-dimensional tungsten photonic crystals for high-temperature applications. *Journal of Vacuum Science and Technology B*, 29:061402–061402–4, 2011.

[145] V. S. Sundaram and P. E. Gruenbaum. Zinc diffusion in GaSb. *Journal of Applied Physics*, 73:3787–3789, 1993.

[146] L. G. Ferguson and L. M. Fraas. Theoretical study of GaSv PV cell efficiency as a function of temperature. *Solar Energy Materials and Solar Cells*, 39:11–18, 1995.

[147] L. M. Fraas, J. E. Avery, P. E. Gruenbaum, V. S. Sundaram, K. Emery, and R. Matson. Fundamental characterization studies of gasb solar cells. *Photovoltaic Specialists Conference, Conference Record of the Twenty Second IEEE*, pages 80–84, Oct 1991.

[148] J. van der Heide, N. E. Posthuma, G. Flamand, W. Geens, and J. Poortmans. Cost-efficient thermophotovoltaic cells based on germanium substrates. *Solar Energy Materials and Solar Cells*, 93:1810–1816, 2009.

[149] B. K. Nayak, V. V. Iyengar, and M. C. Gupta. Efficient light trapping in silicon solar cells by ultrafast-laser-induced self-assembled micro/nano structures. *Progress in Photovoltaics: Research and Applications*, 19:631–639, 2011.

[150] J. Z. Jiang, F. Kragh, D. J. Frost, K. Stahl, and H. Lindelov. Hardness and thermal stability of cubic silicon nitride. *Journal of Physics: Condensed Matter*, 13:L515–L520, 2001.

[151] N. Balke, P. Maksymovych, S. Jesse, I. I. Kravchenko, Q. Li, and S. V. Kalinin. Exploring local electrostatic effects with scanning probe microscopy: Implications for piezoresponse force microscopy and triboelectricity. *ACS Nano*, 8:10229–10236, 2014.

[152] J. J. Foley, C. Ungaro, K. Sun, M. C. Gupta, and S. K. Gray. Design of emitter structures based on resonant perfect absorption for thermophotovoltaic applications. *Optics Express*. (Submitted).

[153] C. Ungaro, S. K. Gray, and M. C. Gupta. A solar thermophotovoltaic system using nanostructures. *Optics Express*. (Submitted).

Appendix A: List of Publications

1. C. Ungaro, S. K. Gray, and M. C. Gupta. “Black tungsten for solar power generation,” *Applied Physics Letters*, **103**, 071105, 2013
2. C. Ungaro, S. K. Gray, and M. C. Gupta. “Graded-index structures for high-efficiency solar thermophotovoltaic emitting surfaces,” *Optics Letters*, **39**, 5259, 2014
3. C. Ungaro, A. Shah, I. Kravchenko, D. K. Hensley, S. K. Gray, and M. C. Gupta. “Optical and infrared properties of glancing angle deposited nanostructured tungsten films,” *Optics Letters*, **40**, 506, 2015
4. C. Ungaro, S. K. Gray, and M. C. Gupta. “A solar thermophotovoltaic system using nanostructures” (submitted to *Optics Express*)
5. A. A. Shah, C. Ungaro, and M. C. Gupta. “High temperature spectral selective coatings for solar thermal systems by laser sintering,” *Solar Energy Materials and Solar Cells*, **134**, 209, 2015
6. J. Foley, C. Ungaro, K. Sun, M. C. Gupta, and S. K. Gray. “Design of emitter structures based on resonant perfect absorption for thermophotovoltaic applications” (submitted to *Optics Express*)
7. M. C. Gupta, C. Ungaro, J. Foley, and S. K. Gray. “Optical nanostructures design, fabrication, and applications for solar/thermal energy conversion” (submitted to *Optics Express*)

Appendix B: Published Works

Black Tungsten for Solar Power Generation

Craig Ungaro,[1] Stephen K. Gray,[2] and Mool C. Gupta[1, a)]
[1)] *Department of Electrical & Computer Engineering, University of Virginia, Charlottesville, Virginia, 22901, USA*
[2)] *Center for Nanoscale Materials, Argonne National Laboratory, 9700 South Cass Avenue, Argonne, IL, 60439, USA*

(Dated: 30 June 2015)

The viability of micro/nano textured tungsten as an efficient solar absorber is explored via computational electrodynamics simulations. Pseudo-random structures are investigated, along with the effects of protective oxide coatings. These structures show extremely high absorption across the solar spectrum along with relaxed requirements for manufacturing, allowing them to be applied for power generation.

Highly absorbing materials that can operate under high temperature conditions are vital to the solar thermal and solar thermophotovoltaic industry. These materials must be able to absorb a majority of the solar spectrum and withstand temperatures of over 1500 °C for thermophotovoltaic applications and temperatures over 600 °C for solar thermal applications.[1]

Many designs for these materials exist, including dielectric stacks, photonic crystals, and 2D or 3D periodic textures.[2,3] Periodic textures on tungsten have been predicted via simulation to have high (>99%) absorption over a wide angular range; however, the stability of textured tungsten at high temperatures can be low due to oxidation effects.[4,5] Experimental results using grating structures on tungsten show absorption of over 90% in the solar range.[6] Dielectric stacks can absorb over 94% of incident solar light while suppressing emissivity to be below 16% at 1750 K.[7]

This paper explores the use of micro/nano non-periodic textures on tungsten substrates for solar thermal applications. Non-periodic structures allow for increased ease of manufacturing and a broadening of the absorption spectrum. The lack of periodic textures also reduces the effect of Bragg peaks on the absorption spectrum of the structure.[4] This allows for larger structures to retain their highly absorptive properties. The behavior of these systems under high temperatures is also explored, along with an analysis of the effect on system performance when a protective oxide layer is applied.

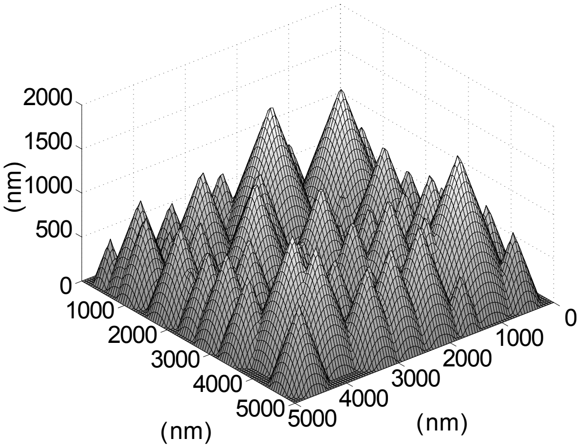

FIG. 1. Cone-based surface with Gaussian-based distributions for width, height, and placement.

Black tungsten may find applications in solar thermophotovoltaic (STPV) and solar thermal areas. STPV systems have been simulated to have efficiencies exceeding 40% using absorbing surfaces with zero reflectance.[8] This is achieved with a concentration of 1000 suns and a spectrally selective emitter. Theoretically, STPV systems can achieve efficiencies of up to 86.8% using only a single junction photovoltaic cell, far exceeding the Shockley-Queisser limit of 32.1% for silicon cells.[9] Currently, experimental STPV systems have shown efficiencies of over 10% using bare tungsten as the absorbing surface.[10] Black tungsten also has applications in solar thermal systems utilizing solar towers. The high concentration factor required in these systems will make black tungsten ideal for use as a solar absorber.[11]

While tungsten is a good absorber in the visible range, the large real component of its dielectric constant results in a large portion of incident power being reflected from the surface. This results in flat films exhibiting an absorptivity of less than 60%.[12] In order to improve absorption, the tungsten can be textured with cone-shaped micro/nano structures that provide a graded index at the tungsten-air interface.

Periodic structures require advanced manufacturing techniques capable of accurately reproducing a structure with a periodicity that is smaller than the wavelength of absorbed light. In the case of a solar absorber, this requires structures on the order of 250 nm to avoid absorption peaks due to Bragg effects.[4] The non-periodic structures detailed in this paper are able to achieve high absorptivity with structure sizes on the order of a micron. The relaxed requirement for precision in processing, combined with larger structure sizes, results in simplified manufacturing techniques.[13]

The structures in this paper are simulated via the finite-difference time-domain (FDTD) method that al-

---

[a)] mgupta@virginia.edu

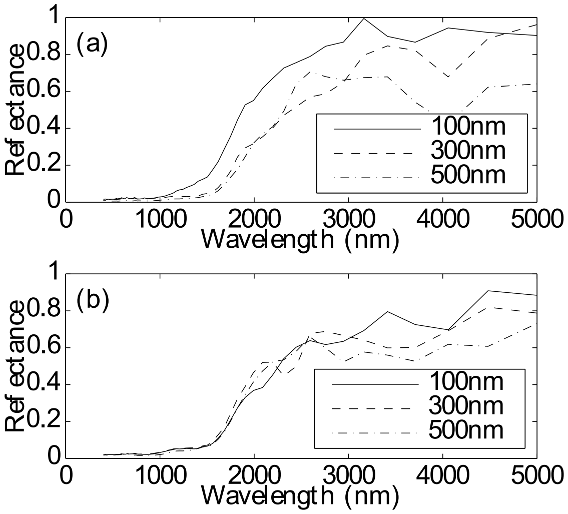

FIG. 2. (a) Reflectance for textured tungsten with different average radii. FWHM of these cones is 300 nm with 95% of the substrate being filled with cones. (b) Simulated reflectance for various distributions of cone periods. Cone average radius is 500 nm, with 95% of the substrate being filled with cones.

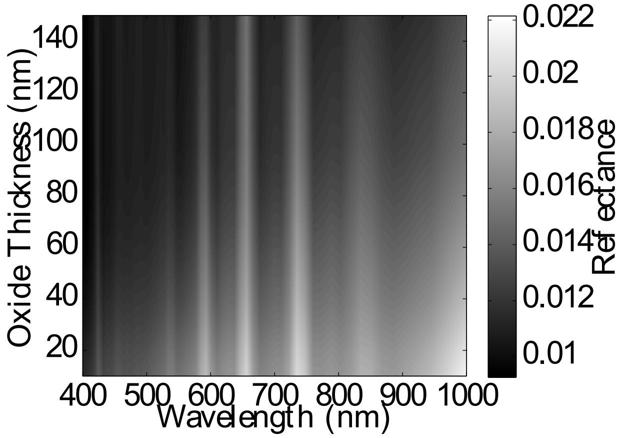

FIG. 3. Simulated reflectance for different thicknesses of oxides on a textured tungsten substrate. Cone average radius is 500 nm with a FWHM of 300 nm and 95% of the substrate being filled with cones.

lows the absorbance of textured tungsten surfaces to be calculated across the solar spectrum.[14] An open-source implementation of the FDTD algorithm, MIT Electromagnetic Equation Propagation (MEEP), was used for the simulations performed in this paper.[15] An accurate model with Drude plus multiple Lorentzian terms for tungsten was used to describe its dielectric constant in the simulated wavelength range.[12]

Figure 1 shows a 3D image of one of the textures studied here. Absorbing perfectly matched layers (PMLs) were used on the edges of the cell to ensure that no periodic effects due to the lattice size played a role in the simulation. An algorithm was developed to place cones on a 3D substrate while minimizing the spacing between cones. The degree of overlap between a potential new cone and existing cones is caluclated for each spot that a new cone can be placed in, and the new cone is then placed in a spot that minimizes this overlap. The cone radius and height follow a Gaussian distribution with the full width at half maximum (FWHM) and average value as variables in the simulation. The cone shapes are on a tungsten substrate that is 500 nm thick.

The reflectance of such structures is plotted in Figure 2. As the FWHM of the structures is increased, the reflectance peak widens. The results show very good (greater than 99%) absorption across the majority of the solar spectrum for textures with large feature sizes. As the average height increases, the absorbance of the surface increases due to a more gradual matching between air and tungsten at the interface. Absorbance is calculated from the transmittance and reflectance values that are computed by the simulation. Transmittance is very small in the case of this simulation due to the thickness of the tungsten substrate.

Another important aspect of textured tungsten structures for solar thermal applications to consider is their high temperature performance. Tungsten structures can degrade due to oxidation and thermal expansion, which can lead to cracking. The use of protective oxide coatings on the tungsten layer can prevent this damage.[5] The effects of various thicknesses of protective oxide layers on the overall performance of textured tungsten substrates were also examined using the FDTD method. Oxide layers were modeled with a constant refractive index of $n = 1.46$ due to their small dispersion throughout the visible range.

Figure 3 shows the simulation results for various oxides. The addition of an oxide layer increased the absorptivity of the structure by acting as an additional index-matching layer on the tungsten-air interface. This makes a protective layer of oxide a viable method of protecting the substrate during high temperature operation.

The temperature dependence of the optical constants of tungsten must also be taken into account for high temperature operation. To simulate the change in the properties of tungsten at high tempertaures, the gamma term in the Drude model is increased to reflect the increased path length for conduction band electrons at elevated temperatures.[16] Figure 4 shows the absorbance of the texture at different temperatures. It can be seen that an increase in temperature results in an increase in the absorptivity of tungsten, resulting in an increase in the performance of the texture under high temperature operation.

In conclusion, this paper provides a viable design for a surface capable of absorbing a large portion of the solar spectrum (>99%). The surface does not require precise manufacturing techniques or sub-micron feature sizes. We have also taken into account high operating

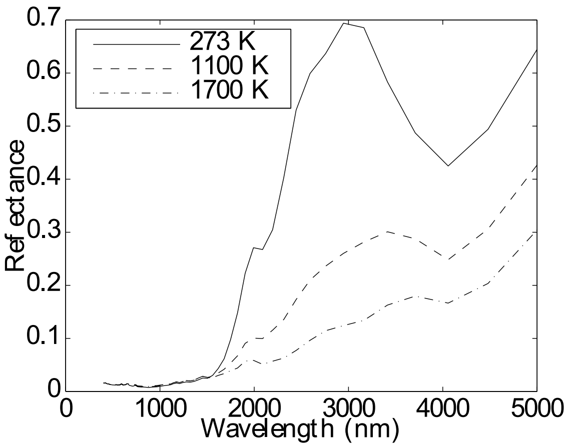

FIG. 4. (a) Reflectance for textured tungsten at various temperatures. Cone average radius is 500nm with an average height of 2um, with a 100nm oxide layer on the cones. Cone FWHM is 300nm.

temperatures, and provided a solution for the thermal behavior of the surface at these temperatures. The availability of an easy to manufacture surface with high solar absorption and high temperature stability could have a significant impact on the solar thermal and solar thermophotovoltaic applications.

ACKNOWLEDGMENTS

We thank the NASA Langley Professor Program for their support of this project. This work was performed, in part, at the Center for Nanoscale Materials, a U.S. Department of Energy, Office of Science, Office of Basic Energy Sciences User Facility under Contract No. DE-AC02-06CH11357.

[1] P. A. Davies and A. Luque, Sol. Energ. Mat. Sol. Cells **33**, 11 (1994).

[2] C. E. Kennedy, NREL/TP- 520-31267 (2002).

[3] P. Bermel, M. Ghebrebrhan, W. Chan, Y. X. Yeng, M. Araghchini, R. Hamam, C. H. Marton, K. F. Jensen, M. Soljacic, J. D. Joannopoulos, S. G. Johnson, and I. Celanovic, Opt. Express **18**, A314 (2010).

[4] E. Rephaeli and S. Fan, Appl. Phys. Lett. **92**, 211107 (2008).

[5] K. A. Arpin, M. D. Losego, and P. V. Braun, Chem. Mater. **23**, 4783 (2011).

[6] H. Sai and H. Yugami, Appl. Phys. Lett. **85**, 3399 (2004).

[7] N. P. Sergeant, O. Pincon, M. Agrawal, and P. Peumans, Opt. Express **17**, 22800 (2009).

[8] E. Rephaeli and S. Fan, Opt. Express **17**, 15145 (2009).

[9] W. Shockley and H. J. Queisser, J. Appl. Phys **32**, 510 (1961).

[10] A. Datas and C. Algora, Sol. Energ. Mat. Sol. Cells **94**, 2137 (2010).

[11] A. Ambrosini, T. N. Lambert, C. L. Staiger, A. C. Hall, M. Bencomo, and E. B. Stechel, Report SAND2010-7080 (Sandia National Laboratories, 2010).

[12] A. D. Rakic, A. B. Djurisic, J. M. Elazar, and M. L. Majewski, Appl. Opt. **37**, 5271 (1998).

[13] S. Chattopadhyay, Y. F. Huang, Y. J. Jen, A. Ganguly, K. H. Chen, and L. C. Chen, Mater. Sci. Eng. Rev. **69**, 1 (2010).

[14] A. Taflove and S. C. Hagness, *Computational Electrodynamics: The Finite-Difference Time-Domain Method, Third Edition* (Artech House, Norwood, MA, 2005).

[15] A. F. Oskooi, D. Roundy, M. Ibanescu, P. Barmel, J. D. Joannopoulos, and S. G. Johnson, Comput. Phys. Commun. **181**, 687 (2010).

[16] H. P. Chiang, P. T. Leung, and W. S. Tse, J. Chem. Phys **108**, 2659 (1997).

Graded-index structures for high efficiency solar thermophotovoltaic emitting surfaces

Craig Ungaro,[1] Stephen K. Gray,[2] and Mool C. Gupta[1,*]
[1]*Department of Electrical & Computer Engineering,*
University of Virginia, Charlottesville, Virginia, 22901, USA
[2]*Center for Nanoscale Materials, Argonne National Laboratory,*
9700 South Cass Avenue, Argonne, IL, 60439, USA

(Dated: April 6, 2014)

compiled: April 6, 2014

This paper presents a highly efficient emitter structure for solar thermophotovoltaic systems. The structure consists of a graded-index on tungsten, and shows a spectral efficiency of 59%, or 70% with the use of a back reflector, and is compared to other state of the art emitter structures. The effects of different structures and periodicities on the efficiency of the emitter are explored, as well as the effect of a protective oxide coating. The causes of the antireflection properties of these structures are also explored.

OCIS codes: 350.6050
http://dx.doi.org/10.1364/XX.99.099999

Solar thermophotovoltaic (STPV) systems provide increased efficiency for solar power conversion by using an intermediary material to absorb incoming sunlight, convert it to heat, and then re-emit it in a narrow band as thermal radiation where it is absorbed by a photovoltaic (PV) cell. This is shown in Figure 1. This increases efficiency since the narrow-band emission is better matched to a PV cell [1]. Spectral matching allows STPV systems to bypass the Shockley-Queisser limit and reach extremely high theoretical efficiencies of 85.4% [2].

Previous work by the authors has focused on efficient solar absorbing surfaces for STPV systems [3]. This work focuses on a separate component of the STPV system that emits the absorbed solar energy as thermal radiation. These absorbing and emitting surfaces play a critical role in the efficiency of STPV systems, and the combination of the two surfaces presented in this and the previous work will result in a highly efficient STPV system.

In order to improve spectral matching between thermally emitted radiation and the PV cell bandgap, the spectrum of emitted radiation must be narrowed. Narrowing of the emitted radiation spectrum can cause a large increase in efficiency [4]. This can be accomplished by using a selective emitter or by placing a filter in front of the PV cell; however, filters placed in front of the PV cell can reduce efficiency and must operate on a diverging beam in high temperatures [5]. Sub-bandgap photons that transmit through the PV cell can also be reflected back to the emitter by a mirror placed behind the cell, called a back reflector [4]. This paper combines the use of graded-index type selective emitter structures with a back reflector to create a highly efficient STPV system.

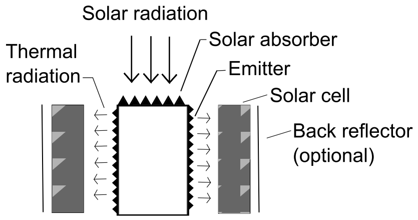

Fig. 1. Diagram of a STPV system with solar absorber and thermal emitter.

There are a variety of selective emitters that have been studied for use in STPV systems, such as micro-cavities in tungsten, NiO-doped MgO films, titania nanofibers, rare-earth emitters, and photonic crystals [6–10]. While photonic crystals can provide a high efficiency selective emitter, they are high cost and difficult to manufacture. Many photonic crystal-based selective emitters also utilize materials such as Si and MgF_2 that have melting points in the range of STPV operating temperatures, as well as nanometer scale geometry that has problems related to long-term stability at high operating temperatures [8, 11].

Square gratings have also been explored in past work, but suffer from relatively low absorption in the near in-

---

[*] Corresponding author: mgupta@virginia.edu

frared region due to their sudden change in index of refraction [12, 13]. The absorption spectrum can be broadened via combining multiple periods of gratings; however, these structures still lack broadband absorption in the visible and near infrared region [14]. Blazed gratings can show higher absorption due to their graded index type behavior at certain wavelengths [15]. Pyramidal and cone type structures also show similar high absorption due to graded index behavior.

This work presents a periodic micro-texture on a tungsten surface that can provide selective emission with the use of only a protective coating. This coating is a single layer, and varied layer thickness can be tolerated. The elimination of multi-layer coatings is advantageous for high temperature operation and long-term stability [16]. The protective material can be chosen to have a high melting point to protect the tungsten surface from oxidation. The optical properties of the system are controlled by the textured tungsten and not by the oxide layer. This is achieved via the use of a blazed grating on tungsten with a thin layer for protection. This paper also investigates the use of pyramid and cone type graded-index structures. These structures have lower maximum efficiencies than blazed gratings within the parameters of this paper; however, they can tolerate larger feature sizes and may be simpler to manufacture.

To describe the relative performance of various types of selective emitters, equation 1 was used to calculate the spectral efficiency. This equation takes into account only the effect of the emitting surface, and does not represent an overall efficiency. The micro-textures proposed in this paper are analyzed along with structures from other papers in the STPV field to demonstrate the viability of this texture for STPV applications.

The spectral efficiency consists of the fraction of the absorbed energy emitted by the selective emitter that the PV cell is able to use. The total available emitted spectral energy is found by multiplying the emittance of an emitter by the blackbody thermal radiation spectrum. This assumes that the STPV system temperature is at 1750 K. The actual absorption of solar energy is not considered here because this paper focuses on the emitting surface only, and the absorbing and emitting surfaces are in different locations. The amount of energy available for solar power conversion is then found by multiplying the number of photons available, as determined by the cell's bandgap energy. A bandgap energy of $E_{bg} = 0.726$ eV (corresponding to a wavelength of $\lambda_{bg} = 1707$ nm) was used since GaSb is a commonly used PV cell in STPV applications [4]. Emitter temperature ranges from 1700 to 2200 K are common in STPV systems; however, a temperature of 1750 K is used in this simulation due to its prevalence [5, 8]. Temperatures in this range have been used previously under experimental conditions [4].

The spectral efficiency is given by:

$$Eff = \frac{\int_0^{\lambda_{bg}} \frac{E_{bg}}{E_{photon}(\lambda)} B(\lambda, T) * \epsilon_s(\lambda) d\lambda}{\int_0^{\infty} B(\lambda, T) * \epsilon_s(\lambda) d\lambda} \tag{1}$$

where $B(\lambda, T)$ is Planck's law for the spectral radiance of a blackbody at temperature T, $\epsilon_s(\lambda)$ is the emittance of the emitter which is equal to absorbance or $1-$ reflectance, $E_{photon}(\lambda)$ is the energy of a photon of wavelength λ, E_{bg} is the bandgap energy of the PV cell used, and λ_{bg} is the wavelength of a photon with the bandgap energy.

To maximize conversion efficiency, the emitter must minimize emitted radiation with energy below and far above the bandgap. The focus of this paper is to illustrate that the performance of existing emitter structures can be enhanced with a simple graded-index structure on tungsten.

Bare tungsten has a very high (greater than 90%) reflection in the 2 to 10 μm wavelength range, and a lower (40% to 90%) reflection in the visible to 2 μm wavelength range [17]. This reflection spectrum combined with its high melting point of 3695 K makes tungsten a good candidate for an emitter material for a STPV system.

This paper uses Finite Difference Time Domain (FDTD) modeling to examine the effect of various micro-textures on the reflectance spectrum of tungsten with the goal of finding an easy to manufacture texture that can increase the spectral efficiency of tungsten for STPV applications [18]. An open-source implementation of the FDTD algorithm, MIT Electromagnetic Equation Propagation (MEEP), was used for the simulations performed in this paper [19]. In an FDTD simulation, a solution is found by iteratively solving Maxwell's equations on a grid. A Gaussian source was used to excite electrical and magnetic fields, and structures were specified via the dielectric constants of the grid at each location. Perfectly matched layer (PML) boundary conditions were used in the direction of the light propagation, while Bloch periodic boundary conditions were used in the lateral directions. This allows an infinitely large surface to be simulated. The surfaces described in this paper were modeled with a 1 μm thick tungsten substrate beneath the graded structures. Transmission was recorded to be less than .01 %. An accurate Drude plus multiple Lorentzian model for tungsten was used to describe its dielectric constant in the simulated wavelength range [20]. While room temperature optical constants were used, the expected change in the emissivity of tungsten from room temperature to 1900 K is only 3.3% [21]. This simulation used an unpolarized light source to simulate the conditions of emission.

The structure used to control the emission spectrum is a blazed grating. When the grating period is smaller than the wavelength of incoming radiation, the grating will operate as a sub-wavelength grating. Sub-wavelength gratings do not have any propagating diffractive modes (only zero-order modes are allowed in this

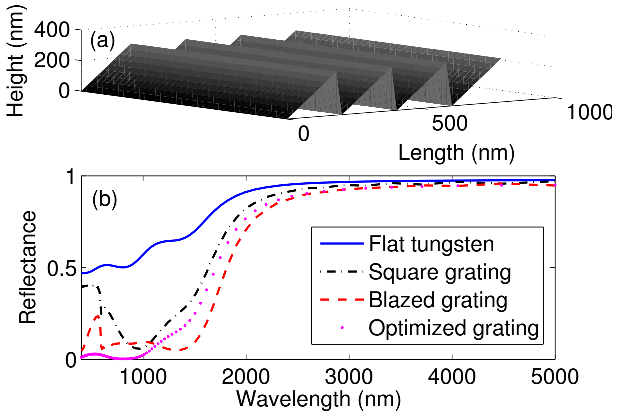

Fig. 2. (a) - The surface of a blazed grating with periodicity 200 nm and a blaze angle of 55 degrees (b) - FDTD calculation of the reflectance of square and blazed grating, both with 600 nm periodicity, and an optimized structure with 200 nm periodicity.

condition), and they demonstrate broadband antireflection properties at wavelengths larger than the first order of diffraction due to their graded index characteristics [22, 23]. Blazed gratings in particular provide a more gradual index gradient when compared to square gratings, increasing their antireflection properties [15].

Figure 2a shows the blazed grating on a tungsten surface that was found to have the highest spectral efficiency. It has a height of 285 nm and a period of 200 nm. First order diffraction will occur at a wavelength of 188 nm for this grating according to the grating equation. For wavelengths longer than 188 nm, this grating will act as a zero-order grating.

Figure 2b uses a FDTD model to compare the reflection of a square and blazed grating with a 600 nm period and height of 450 nm. While the square grating provides an intermediary change in the effective index of refraction between the metal and air, this is less effective than the gradual index change provided by a blazed grating. Surface plasmons and the microcavity effect cause absorption peaks in the case of the square grating; however, these peaks are narrow and do not provide broad absorption of solar radiation [24]. The blazed grating shows a broader band of low reflection than the square grating in the visible region while maintaining a high reflectance in the infrared region. This results in higher efficiency due to enhanced solar absorption.

At the zero-order condition, gratings exhibit specular reflection properties and no diffraction. [25] The emission of light at wavelengths longer than 188 nm is not expected to have an angular dependency beyond that of Lambert's cosine law. FDTD simulations show a change in spectral efficiency from 0.59 to 0.58 when equation 1 is integrated from -85 to 85 degrees. Equation 1 is used without angular dependence due to a lack of data in many references.

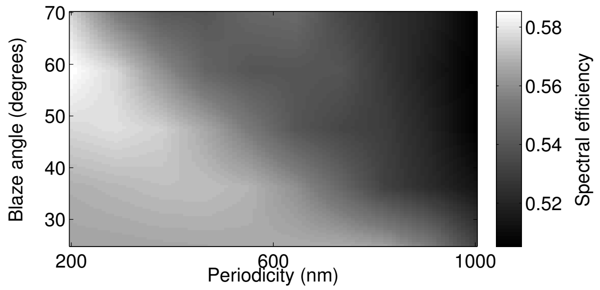

Fig. 3. Spectral efficiency vs. periodicity and angle of blazed grating on tungsten. The angle is the angle of the blazing, with 0 degrees meaning a flat surface.

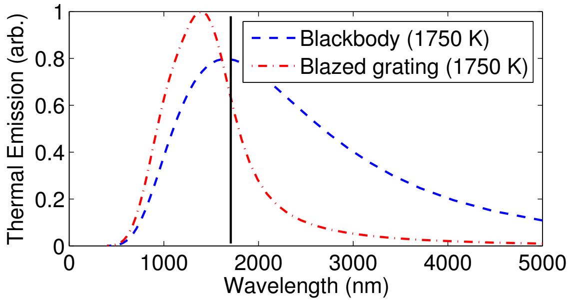

Fig. 4. Thermal emission of a blackbody and blazed grating on a tungsten substrate with periodicity 200 nm and angle 55 degrees. The vertical line is the absorption edge of a GaSb PV cell.

The height and periodicity of this grating were varied, and the spectral efficiency was calculated at each point, as shown in Figure 3. While decreasing the periodicity farther below 200nm resulted in a small (<1%) increase in efficiency, this data was not included in this paper due to concerns about the viability of manufacturing such a structure. While the maximum spectral efficiency of 0.59 can be seen at a period of 200 nm and blaze angle of 55 degrees, other periods and angles show promise as well. At a period of 600 nm and a blaze angle of 35 degrees, the spectral efficiency is 0.57. Cone or pyramid type structures also maintain high spectral efficiencies of over 0.56 at a 900 nm periodicity and an angle of 25 degrees, and can be fabricated using standard optical lithography [26]. Larger feature sizes may be desirable due to increased manufacturability and thermal stability.

Figure 4 shows the thermal emission of a blazed grating on tungsten with a period of 200 nm and blaze angle of 55 degrees as compared to the blackbody spectrum at a temperature of 1750 K. The blazed grating results in a much larger portion of the emitted radiation occurring at wavelengths that are usable by a GaSb PV cell. The spectral efficiency of a blackbody radiator is only 0.23 while it is 0.59 for a blazed grating, making the surface structure presented in this paper highly efficient

Table 1. Spectral Efficiency Calculations

Emitter type	Spectral efficiency
Blazed grating on tungsten	0.59 (this work)
Micro-cavity in tungsten	0.49 [6]
NiO-doped MgO films	0.61 [9]
Titania nanofibers	0.49 [6]
Rare earth (Yb_2O_3)	0.54 [6]
Photonic crystals on tungsten	0.63 [8]
Complex square grating on tungsten	0.53 [14]

in comparison.

The effect of a protective oxide film on the spectral efficiency was also examined. A protective oxide will allow the textured tungsten to operate at high temperatures without oxidation on the surface [27]. An oxide of Al_2O_3 was chosen for simulation in this paper due to its high temperature stability and melting point of 2345 K. It was found that there is a small (less than 1%) loss in spectral efficiency at an oxide thickness of up to 100 nm. This allows for the use of a protective oxide layer on the emitter while maintaining high spectral efficiency.

Table 1 shows the spectral efficiency of the blazed grating on tungsten compared to other emitters found in literature. The results shown in Table 1 were obtained by applying equation 1 to the emission spectra presented in each reference.

This work presents a solution for a high efficiency, temperature stable, and manufacturable graded-index emitter for use in STPV systems. It also investigates structures that allow for larger periods while maintaining a high spectral efficiency. The availability of such a structure combined with the absorbing structure for high temperature STPV systems presented in our previous work could have a large impact on the STPV field [3].

Acknowledgments

We thank the NASA Langley Professor and NSF IU-CRC Programs for their support of this project. This work was performed, in part, at the Center for Nanoscale Materials, a U.S. Department of Energy, Office of Science, Office of Basic Energy Sciences User Facility under Contract No. DE-AC02-06CH11357.

References

[1] R. M. Swanson, Proc. IEEE **67**, 446 (1979).

[2] P. A. Davies and A. Luque, Sol. Energ. Mat. Sol. Cells **33**, 11 (1994).

[3] C. Ungaro, S. K. Gray, and M. C. Gupta, Appl. Phys. Lett. **103**, 071105 (2013).

[4] V. M. Andreev, V. P. Khvostikov, O. A. Khvostikova, A. S. Vlasov, P. Y. Gazaryan, N. A. Sadchikov, and V. D. Rumyantsev, IEEE Photovoltaic Specialists Conference , 671 (2005).

[5] H. Hofler, H. J. Paul, W. Ruppel, and P. Wurfel, Solar Cells **10**, 273 (1983).

[6] Y. Xuan, X. Chen, and Y. Han, Renew. Energ. **36**, 374 (2011).

[7] B. Bitnar, W. Durisch, J. C. Mayor, H. Sigg, and H. R. Tschudi, Sol. Energ. Mat. Sol. Cells **73**, 221 (2002).

[8] E. Rephaeli and S. Fan, Opt. Express **17**, 15145 (2009).

[9] L. G. Ferguson and F. Dogan, Mat. Sci. Eng. B **83**, 35 (2001).

[10] S.-Y. Lin, J. Moreno, and J. G. Fleming, Appl. Phys. Lett **83**, 380 (2003).

[11] N. P. Sergeant, O. Pincon, M. Agrawal, and P. Peumans, Opt. Express **17**, 22800 (2009).

[12] H. Sai and H. Yugami, Appl. Phys. Lett. **85**, 3399 (2004).

[13] H. Sai, Y. Kanamori, K. Hane, H. Yugami, and M. Yamaguchi, Photovoltaic Specialists Conference , 762 (2005).

[14] Y. B. Chen and Z. M. Zhang, Opt. Commun. **269**, 411 (2007).

[15] E. B. Grann and M. G. Moharam, J. Opt. Soc. Am. A **13**, 988 (1996).

[16] V. Rinnerbauer, S. Ndao, Y. X. Yeng, W. R. Chan, J. J. Senkevich, J. D. Joannopoulos, M. Soljacic, and I. Celanovic, Energy Environ. Sci. **5**, 8815 (2012).

[17] E. D. Palik, *Handbook of Optical Constants of Solids* (Academic Press, Boston, MA, 1985).

[18] A. Taflove and S. C. Hagness, *Computational Electrodynamics: The Finite-Difference Time-Domain Method, Third Edition* (Artech House, Norwood, MA, 2005).

[19] A. F. Oskooi, D. Roundy, M. Ibanescu, P. Bermel, J. D. Joannopoulos, and S. G. Johnson, Comput. Phys. Commun. **181**, 687 (2010).

[20] H. P. Chiang, P. T. Leung, and W. S. Tse, J. Chem. Phys. **108**, 2659 (1998).

[21] A. G. Worthing, J. Opt. Soc. Am. Rev. Sci. Inst. **13**, 635 (1926).

[22] W. Stork, N. Streibl, H. Haidner, and P. Kipfer, Opt. Lett **16**, 1921 (1991).

[23] K.-H. Kim and Q.-H. Park, Scientific Reports **3** (2013).

[24] H. Sai, Y. Kanamori, K. Hane, and H. Yugami, J. Opt. Soc. Am. A **22**, 1805 (2005).

[25] C. Palmer, *Diffraction Grating Handbook* (Newport Corporation, 2005).

[26] G. Owen, R. Pease, D. Markle, A. Grenville, R. Hsieh, R. von Bunau, and N. Maluf, J. Vac. Sci. Technol. B **10**, 3032 (1992).

[27] K. A. Arpin, M. D. Losego, and P. V. Braun, Chem. Mater. **23**, 4783 (2011).

References

[1] Richard M. Swanson, “A proposed thermophotovoltaic solar energy conversion system,” Proc. IEEE **67**, 446–447 (1979).

[2] P. A. Davies and A. Luque, “Solar thermophotovoltaics: brief review and a new look,” Sol. Energ. Mat. Sol. Cells **33**, 11–22 (1994).

[3] Craig Ungaro, Stephen K. Gray, and Mool C. Gupta, “Black tungsten for solar power generation,” Appl. Phys. Lett. **103**, 071105 (2013).

[4] V. M. Andreev, V. P. Khvostikov, O. A. Khvostikova, A. S. Vlasov, P. Y. Gazaryan, N. A. Sadchikov, and V. D. Rumyantsev, “Solar thermophotovoltaic system with high temperature tungsten emitter,” IEEE Photovoltaic Specialists Conference , 671–674 (2005).

[5] H. Hofler, H. J. Paul, W. Ruppel, and P. Wurfel, “Interference filters for thermophotovoltaic solar energy conversion,” Solar Cells **10**, 273–286 (1983).

[6] Yimin Xuan, Xue Chen, and Yuge Han, “Design and analysis of thermophotovoltaic systems,” Renew. Energ. **36**, 374–387 (2011).

[7] B. Bitnar, W. Durisch, J. C. Mayor, H. Sigg, and H. R. Tschudi, “Characterisation of rare earth selective emitters for thermophotovoltaic applications,” Sol. Energ. Mat. Sol. Cells **73**, 221–234 (2002).

[8] Eden Rephaeli and Shanhui Fan, “Absorber and emitter for solar thermophotovoltaic systems to achieve efficiency exceeding the shockley-queisser limit,” Opt. Express **17**, 15145–15159 (2009).

[9] Lucian G. Ferguson and Fatih Dogan, “A highly efficient nio-doped mgo matched emitter for thermophotovoltaic energy conversion,” Mat. Sci. Eng. B **83**, 35–41 (2001).

[10] Shawn-Yu Lin, J. Moreno, and J. G. Fleming, “Three-dimensional photonic-crystal emitter for thermal photovoltaic power generation,” Appl. Phys. Lett **83**, 380–382 (2003).

[11] Nicholas P. Sergeant, Olivier Pincon, Mukul Agrawal, and Peter Peumans, “Design of wide-angle solar-selective absorbers using aperiodic metal-dielectric stacks,” Opt. Express **17**, 22800–22812 (2009).

[12] Hitoshi Sai and Hiroo Yugami, “Thermophotovoltaic generation with selective radiators based on tungsten surface gratings,” Appl. Phys. Lett. **85**, 3399–3401 (2004).

[13] H. Sai, Y. Kanamori, K. Hane, H. Yugami, and M. Yamaguchi, “Numerical study on tungsten selective radiators with various surface micro/nano structures,” Photovoltaic Specialists Conference , 762–765 (2005).

[14] Y. B. Chen and Z. M. Zhang, “Design of tungsten complex gratings for thermophotovoltaic radiators,” Opt. Commun. **269**, 411–417 (2007).

[15] Eric B. Grann and M. G. Moharam, “Comparison between continuous and discrete subwavelength grating structures for antireflection surfaces,” J. Opt. Soc. Am. A **13**, 988–992 (1996).

[16] Veronika Rinnerbauer, Sidy Ndao, Yi Xiang Yeng, Walker R. Chan, Jay J. Senkevich, John D. Joannopoulos, Marin Soljacic, and Ivan Celanovic, “Recent developments in high-temperature photonic crystals for energy conversion,” Energy Environ. Sci. **5**, 8815–8823 (2012).

[17] Edward D. Palik, *Handbook of Optical Constants of Solids* (Academic Press, Boston, MA, 1985).

[18] Allen Taflove and Susan C. Hagness, *Computational Electrodynamics: The Finite-Difference Time-Domain Method, Third Edition* (Artech House, Norwood, MA, 2005).

[19] A. F. Oskooi, D. Roundy, M. Ibanescu, P. Bermel, J. D. Joannopoulos, and S. G. Johnson, “Meep: A flexible free-software package for electromagnetic simulations by the fdtd method,” Comput. Phys. Commun. **181**, 687–702 (2010).

[20] H. P. Chiang, P. T. Leung, and W. S. Tse, “The surface plasmon enhancement effect on adsorbed molecules at elevated temperatures,” J. Chem. Phys. **108**, 2659–2660 (1998).

[21] A. G. Worthing, “Deviation from lambert’s law and polarization of light emitted by incandescent tungsten, tantalum and molybdenum and changes in the optical constants of tungsten with temperature,” J. Opt. Soc. Am. Rev. Sci. Inst. **13**, 635–647 (1926).

[22] W. Stork, N. Streibl, H. Haidner, and P. Kipfer, “Artificial distributed-index media fabricated by zero-order gratings,” Opt. Lett **16**, 1921–1923 (1991).

[23] Kyoung-Ho Kim and Q-Han Park, “Perfect antireflection from first principles,” Scientific Reports **3** (2013).

[24] Hitoshi Sai, Yoshiaki Kanamori, Kazuhiro Hane, and Hiroo Yugami, “Numerical study on spectral properties of tungsten one-dimensional surface-relief gratings for spectrally selective devices,” J. Opt. Soc. Am. A **22**, 1805–1813 (2005).

[25] Christopher Palmer, *Diffraction Grating Handbook* (Newport Corporation, 2005).

[26] G. Owen, R.F.W. Pease, D.A. Markle, A. Grenville, R.L. Hsieh, R. von Bunau, and N.I. Maluf, “1/8 um optical lithography,” J. Vac. Sci. Technol. B **10**, 3032–3035 (1992).

[27] K. A. Arpin, M. D. Losego, and P. V. Braun, “Electrodeposited 3d tungsten photonic crystals with enhanced thermal stability,” Chem. Mater. **23**, 4783–4788 (2011).

Optical and infrared properties of glancing angle deposited nanostructured tungsten films

Craig Ungaro,[1] Ankit Shah,[1] Ivan Kravchenko,[2] Dale K. Hensley,[2] Stephen K. Gray,[3] and Mool C. Gupta[1,*]
[1] *Department of Electrical & Computer Engineering,*
University of Virginia, Charlottesville, Virginia, 22901, USA
[2] *Center for Nanophase Materials Sciences, Oak Ridge National Laboratory, Oak Ridge, TN, 37831, USA*
[3] *Center for Nanoscale Materials, Argonne National Laboratory,*
9700 South Cass Avenue, Argonne, IL, 60439, USA

(Dated: November 3, 2014)

Nanotextured tungsten thin films were obtained on a stainless steel (SS) substrate using the glancing angle deposition (GLAD) method. It was found that the optical absorption and thermal emittance of the SS substrate can be controlled by varying the parameters used during deposition. Finite difference time domain (FDTD) simulations were used to predict the optical absorption and infrared reflectance spectra of the fabricated samples, and good agreement was found between simulated and measured data. FDTD simulations were also used to predict the effect of changes in the height and periodicity of the nanotextures. These simulations show that good control over the absorption can be achieved by altering the height and periodicity of the nanostructure. These nanostructures were shown to be temperature stable up to 500 °C with the addition of a protective HfO_2 layer. Applications for this structure are explored, including a promising application for solar thermal energy systems.

Glancing angle deposition (GLAD) is a technique which allows a nanostructured thin film to be deposited on a substrate via vapor deposition or sputtering. The features of this deposited film can be controlled by varying the substrate spin speed, angle of deposition, and deposition rate and time [1]. GLAD has been used to form tungsten nanostructures [2, 3] for different applications. Here we report the control of optical and infrared properties of nanostructured tungsten (W) thin films using the GLAD method. A hafnium oxide (HfO_2) layer was deposited on top of the nanostructures to act as an anti-reflection coating and provide protection against oxidation [4]. We also present data on optical and infrared properties simulated using the finite difference time domain (FDTD) method. Simulations and experiments show that the optical absorbance and infrared emittance of the surfaces can be controlled by altering the features of the nanostructures. These surfaces can be used for a variety of applications, including control of hydrophobicity, sensing, infrared sources, and solar energy harvesting.

One of the applications of spectral selective surfaces is in concentrated solar power (CSP) using solar thermal tower systems. Solar thermal tower systems are capable of providing >300 MW of power and are highly important for utility scale power generation [5]. Mirrors on the ground concentrate sunlight onto a central receiver and concentrations of 600-fold can be achieved [6]. As a result of this high concentration, receivers in the tower systems reach extremely high temperatures, with temperatures >600°C desired to meet an electricity cost target of $\$0.06/kWh$ [7]. Receivers for tower systems require solar absorbance (α) >0.95 and thermal emittance (ϵ) <0.3 and must be able to operate in air at high temperatures [6]. To achieve these requirements, receivers are coated with a material that has low reflectance in the solar spectrum and high reflectance in the IR and this behavior is called spectral selectivity [8].

Multilayers of ceramic-metal composites (cermets) have been used to form spectral selective coatings but their performance degrades due to oxidation, cracking, and delamination at high temperatures [9]. Cermets have only been stable up to 500 °C in air [10] and as mentioned earlier there is a need to go to higher temperatures. Surface texturing has also been used to obtain spectral selectivity that can achieve relatively high solar absorbance but having low emittance is a challenge [11, 12]. Submicron periodic tungsten structures have been fabricated on tungsten substrate that achieved solar absorption (α) of 82% and thermal emittance (ϵ) of 15.9% at 1200 K; however, the heat treatment was carried out only in vacuum [12]. Chromium surface was textured to achieve an α of 94% and an ϵ of 30% at 100 °C after being oxidized in air at 500 °C and it can be seen that surface textures are either stable under vacuum at high temperatures or in air up to 500 °C [13].

GLAD structures offer a way to achieve the high level of control over the optical properties of a surface that is needed for solar applications without the need for periodic nanostructures. GLAD using sputtering can be applied to a wide area without the need for lithography techniques, and the aperiodicity of the GLAD structures also makes them more tolerant of small changes in surface morphology due to high temperature operation.

Spectral selective surfaces can also be used as infrared sources since they are needed for infrared based analytic systems [14]. Specifically, carbon dioxide gas sensor systems employ IR sources and detectors. Most IR sources are very broadband, therefore narrow band emission is

---

[*] mgupta@virginia.edu

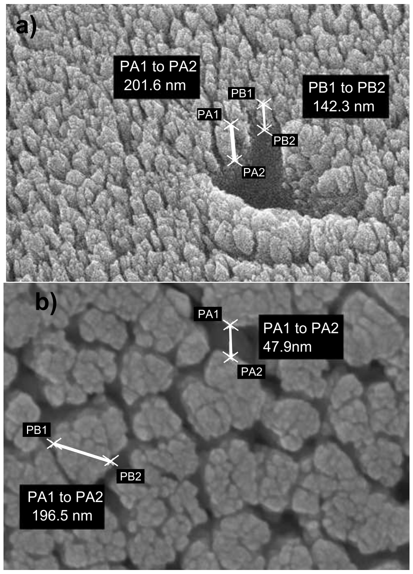

FIG. 1. SEM image of tungsten nanostructures on SS substrate a) tilted view and b) top view.

needed that corresponds to particular gas concentration and detection. In the paper by Lai et. al., the design of a MEMS based IR emitter and detector as a gas sensor system was considered and the IR emission was centered at a wavelength of 4.25 microns [15].

In this work, the authors show that fabricated GLAD tungsten nanostructures have an emission at 5 microns and are thermally stable. The IR emission center wavelength can be controlled by changing the height of the structures thus GLAD structures would be very useful as IR emitters in gas sensor systems. Another application of spectral selective surfaces is in filters. The surface can be used as a mirror which reflects infrared radiation and absorbs visible radiation with a cutoff that is tunable via the GLAD deposition parameters.

GLAD of tungsten nanostructures was carried out on a stainless steel (SS) substrate. The deposition angle used was 85 degrees from the normal of the surface and the sample rotation speed was 20 rpm. The sample was kept at room temperature. The electron beam evaporator chamber vacuum was 4x10^{-3} Pa.

HfO_2 layers were grown via atomic layer deposition at a substrate temperature of 563 K, with the full deposition process as described by Balke et al. [16]. Significant oxidation of the substrate is unlikely at a deposition temperature of 563 K; however, a native oxide of unknown thickness will be present on the tungsten substrate at room temperature. Solar absorbance measurements were performed using an integrating sphere supplied by Labsphere Inc. and using individual lasers having wavelengths 405 nm, 532 nm, 633 nm, 790 nm, 980 nm, and 1064 nm.

IR reflectance measurements were performed using a continuum microscope that was purchased from Thermo Fischer Scientific, Inc. The sample was illuminated with IR radiation and the reflected beam was collected with a $+/-35\,^{\circ}$ acceptance angle from the normal. In order to study high temperature performance of the nanostructures, the sample was heated to 400 °C and then to 500 °C for one hour in air. Emittance at high temperatures was calculated from experimental reflectance data measured for heat-treated samples using blackbody irradiance at 500 °C.

Energy dispersive X-ray spectroscopy (EDS) measurements were carried out for GLAD tungsten nanostructures without a HfO_2 coating. The samples were tilted towards the detector during the EDS measurement to avoid X-ray attenuation by the sample itself. The resulting angle between the samples and the detector is 5 °. The spot size of the electron beam in the EDS measurement was 1 nm in diameter; however, X-rays are excited and collected from a much larger area. The EDS data is as follows: 25% Tungsten, 49% Iron, 13% Chromium, 5% Nickel,1% Manganese,4% Carbon, and 3% Oxygen. Iron, chromium, nickel, and manganese are in EDS data due to stainless steel composition.

Simulations of these nanostructures were performed with the FDTD method using the MIT Electromagnetic Equation Propagation (MEEP) [17, 18]. The FDTD method finds a solution to a system by iteratively solving Maxwell's equations over a grid. A Gaussian source was used to excite electric and magnetic fields, and structures were specified via the dielectric constants of the grid at each location. Perfectly matched layer (PML) boundary conditions were used in the direction of light propagation, while Bloch periodic boundary conditions were used in the lateral directions. Discretization errors were avoided by using a small (1 nm) resolution and subpixel averaging [19]. To calculate the reflected power, a simulation is first run with no object, to obtain the incident wave power, then another simulation is run with the object present. The electromagnetic flux from the first simulation is then subtracted from the second to obtain the reflected wave. Unpolarized light was approximated by averaging the reflectance spectra for S and P polarized light. The dimensions of the structure were determined by the scanning electron microscope (SEM) images shown in Figure 1.

A Drude-Lorentz model was used to simulate dielectric constants in the wavelength range. In this model, intraband, or free-electron effects, are described by a Drude term, while inter-band, or bound-electron effects, are described by the addition of multiple Lorentzian terms. Specific constants for tungsten are given by Rakic et al. [20].

Figure 1 shows the SEM image of tungsten nanostructures on SS substrate. The nanostructures are randomly arranged and the height of the nanostructures varies from 130 to 202 nm as seen in Fig. 1a. As seen in Fig. 1b, the diameter of the nanostructures varies from 40 to 100 nm and the spacing between them varies from 10 to 50 nm. Small-scale surface roughness is seen on the tops of the nanostructures.

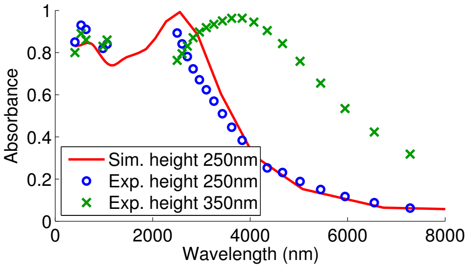

FIG. 2. Comparison between experiment and FDTD modeling of absorption spectra.

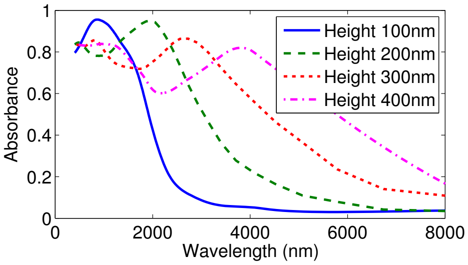

FIG. 3. FDTD simulation results for absorbance by tungsten nanostructures with various heights.

Experimental studies of GLAD structures of similar dimensions show a RMS roughness of 5.8 [21] and 4.3 nm [22]. It was found that surface roughness of Rms <5.8 nm had little effect on the absorbance of the surfaces at the wavelengths investigated in this paper. Nanoscale crystalinity of the tungsten nanostructure is not taken into account in this paper. While it is an important factor in calculating the absorbance spectra of many nanostructures, it is unlikely to have a large effect on this research due to the short electron mean free path (19.1 nm) combined with the typically large grain size in GLAD deposited tungsten and the lack of significant edge effects due to the size of the structures considered [3, 23, 24]. The randomness of nanostructures helps to achieve high solar absorbance and spectral selectivity important for solar thermal application. This occurs due to a widening of the absorption peak as the radii of the nanostructures become more random [25, 26].

Figure 2 shows a comparison of the absorption spectra for simulated and experimental results. The nanostructure was simulated by tracing the nanostructure edges in a top view SEM image to create a 2D model of the surface in a 5 by 5 micron area using a common imaging tracing technique [27]. The 2D image was then extended into 3 dimensions by adding the height and small ∼5 nm surface roughness obtained from an angled SEM image. This information was used to define the tungsten structure used by the FDTD simulations. Internal reflection between the tungsten layer and the SS substrate is taken into account in this simulation. It can be seen from this data that there is a good correlation between simulated and experimental results at different heights for the tungsten nanostructure. Discrepancies between experimental and simulated data are due to SEM resolution limits and the size of the area simulated.

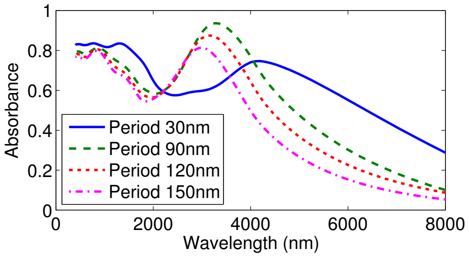

FIG. 4. FDTD simulation results for absorbance by tungsten nanostructures with various periods. Note that periodicity here refers to the average distance between nanostructure centers.

In Figure 3, similar nanostructures of tungsten are simulated with various heights. It can be seen from the graph that increasing the nanostructure's height shifts the absorbance peak to longer wavelengths, and decreases the height of the peak. In Figure 4, it can be seen that the height of the absorbance peak can be controlled via the average distance between the centers of adjacent structures. In this way, we can control the position and height of the absorbance peak in GLAD structures. This control allows tuning of the spectrally selective surface to be used for a variety of applications.

The W nanostructures discussed in this paper are subwavelength compared to the wavelengths in the solar and IR spectrum as seen earlier in the SEM images. Increased absorption occurs due to Fabry-Perot resonances occurring in the nanostructured area formed by GLAD. In addition to this, the HfO_2 layer acts as an anti-reflection coating thus reducing front surface reflection. The combined effect of the Fabry-Perot type behavior and the anti-reflection from the coating leads to a very high solar absorbance of 87.4%.

Figure 5 shows an IR absorbance plot of the W nanostructures with HfO_2 coating before and after heat treatment. The peak in absorbance between 4 and 6 microns occurs due to the Fabry-Perot resonances that occur in the GLAD structure. Maxwell-Garnett effective medium theory can be used to predict the locations of the resonances and their shift with height [28]. Beyond wavelength of 5.5 microns, the absorbance starts falling and approaching that of bulk tungsten as the structure dimensions are much smaller than the wavelength.

A slight shift to the right can be seen in the IR absorbance after heating the sample at 500 °C in air for one hour and this could be due to a change in the large-scale surface morphology of the GLAD film due to diffusion or recrystallization at high temperatures [4, 29]. Flat tungsten substrates have been shown to grow 3.5 nm of oxide under similar experimental conditions [30]. However, the structures still maintain their performance as beyond 6.5

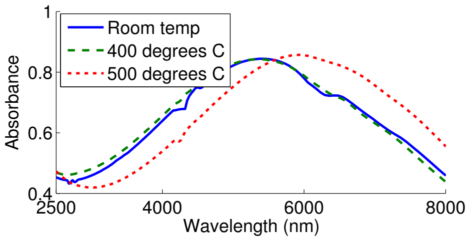

FIG. 5. Change in absorbance after heat treatment.

microns the absorbance approaches that of bulk tungsten and also the solar absorbance remains unchanged.

This paper demonstrates the use of the GLAD method to achieve a surface with high optical absorption and low thermal emittance. Solar absorbance and thermal emittance data are presented as well. Thermal stability of the structure is shown up to 500 °C in air with a protective HfO_2 layer. Electrodynamics simulation results also show a path forward towards increased efficiency by using shorter tungsten nanostructures. This research is very promising for solar thermal applications, and to the authors' knowledge is the first demonstration of the GLAD method for these systems.

ACKNOWLEDGMENTS

We thank the NASA Langley Professor and NSF IUCRC Programs for their support of this project. This work was performed, in part, at the Center for Nanoscale Materials, a U.S. Department of Energy, Office of Science, Office of Basic Energy Sciences User Facility under Contract No. DE-AC02-06CH1135. A portion of this research was conducted at the Center for Nanophase Materials Sciences, which is sponsored at Oak Ridge National Laboratory by the Scientific User Facilities Division, Office of Basic Energy Sciences, U.S. Department of Energy.

[1] J. C. Sit, D. Vick, K. Robbie, and M. J. Brett, J. Mater. Res. **14**, 1197 (1998).
[2] K. R. Khedir, G. K. Kannarpady, H. Ishihara, J. Woo, C. Ryerson, and A. S. Biris, Phys. Lett. A **374**, 4430 (2010).
[3] D. Deniz, D. J. Frankel, and R. J. Lad, Thin Solid Films **518**, 4095 (2010).
[4] L. A. Arpin, M. D. Losego, and P. V. Braun, Chem. Mater. **23**, 4783 (2011).
[5] NREL: Concentrating Solar Power, "Ivanpah solar electric generating system," `http://www.nrel.gov/csp/solarpaces/project_detail.cfm/projectID=62`, accessed: 2014-07-31.
[6] A. Ambrosini, T. N. Lambert, M. Bencomo, A. Hall, K. vanEvery, N. P. Siegel, and C. K. Ho, Proc. ASME **5**, 1 (2011).
[7] A. Hall, A. Ambrosini, and C. Ho, Adv. Mater. Processes **170**, 28 (2012).
[8] S. Fan, Nat. Nanotechnol. **9**, 92 (2014).
[9] R. N. Schmidt and K. C. Park, Appl. Opt. **4**, 917 (1965).
[10] F. Cao, K. McEnaney, G. Chen, and Z. Ren, Energ. Environ. Sci. **7**, 1615 1627 (2014).
[11] A.Y.Vorobyev and G.Chunlei, Proc. IEEE **7**, 135 (2010).
[12] H. Sai, H.Yugamia, Y.Kanamorib, and K.Hane, Sol. Energy Mater. Sol. Cells **79**, 35 (2003).
[13] S. Kunc, Sol. Wind Technol. **4**, 473 (1987).
[14] J. Hodgkinson and R. P. Tatam, Meas. Sci. Technol. **24**, 1 (2013).
[15] J. J. Lai, H. F. Liang, Z. L. Peng, X. Yi, and X. F. Zhai, Journal of Physics: Conference Series **276**, 1 (2011).
[16] N. Balke, P. Maksymovych, S. Jesse, I. I. Kravchenko, Q. Li, and S. V. Kalinin, ACS Nano **8**, 10229 (2014).
[17] A. Taflove and S. C. Hagness, *Computational Electrodynamics: The Finite-Difference Time-Domain Method, Third Edition* (Artech House, Norwood, MA, 2005).
[18] A. F. Oskooi, D. Roundy, M. Ibanescu, P. Bermel, J. D. Joannopoulos, and S. G. Johnson, Comput. Phys. Commun. **181**, 687 (2010).
[19] A. Deinega and I. Valuev, Comp. Phys.s Commun. **182**, 149 (2011).
[20] A. D. Rakic, A. B. Djurisic, J. M. Elazar, and M. L. Majewski, Appl. Opt. **37**, 5271 (1998).
[21] S. Wang, X. Fu, G. Xia, J. Wang, J. Shao, and Z. Fan, Appl. Surf.Sci. **252**, 8734 (2005).
[22] J. Lintymer, N. Martin, J.-M. Chappe, P. Delobelle, and J. Takadoum, Surf. and Coat. Technol. **180-181**, 26 (2004).
[23] R. Atkinson, W. R. Hendren, G. A. Wurtz, W. Dickson, A. V. Zayats, P. Evans, and R. J. Pollard, Phys. Rev. B **73**, 235402 (2006).
[24] D. Choi, C. S. Kim, D. Naveh, S. Chung, A. P. Warren, N. T. Nuhfer, M. F. Toney, K. R. Coffey, and K. Barmak, Phys. Rev. B **86**, 045432 (2012).
[25] T. Jun, L. Yong-Hua, Z. Rong-Sheng, L. Kai-Qun, X. Zhi-Guo, L. Zhao-Feng, L. Sheng-li, W. Pei, and M. Hai, Chin. Phys. Lett. **25**, 4459 (2008).
[26] C. Ungaro, S. K. Gray, and M. C. Gupta, Appl. Phys. Lett. **103**, 071105 (2013).
[27] J. C. Fiala, J. Microsc. **218**, 52 (2005).
[28] L. Hu and G. Chen, Nano Lett. **7**, 3249 (2007).
[29] C. Schlemmer, J. Aschaber, V. Boerner, and J. Luther, AIP Conference Proceedings **653**, 164 (2003).
[30] J. Habainy and C. Nilsson, "Oxidation of pure tungsten in the temperature interval 400 to 900 C," (2013), Lund University, Sweden. Master's thesis.

[1] J. C. Sit, D. Vick, K. Robbie, and M. J. Brett, "Thin film microstructure control using glancing angle deposition by sputtering," J. Mater. Res. **14**, 1197–1199 (1998).

[2] K. R. Khedir, G. K. Kannarpady, H. Ishihara, J. Woo, C. Ryerson, and A. S. Biris, "Morphology control of tungsten nanorods grown by glancing angle rf magnetron sputtering under variable argon pressure and flow rate," Phys. Lett. A **374**, 4430–4437 (2010).

[3] D. Deniz, D. J. Frankel, and R. J. Lad, "Nanostructured tungsten and tungsten trioxide films prepared by glancing angle deposition," Thin Solid Films **518**, 4095–4099 (2010).

[4] L. A. Arpin, M. D. Losego, and P. V. Braun, "Electrodeposited 3D tungsten photonic crystals with enhanced thermal stability," Chem. Mater. **23**, 4783–4788 (2011).

[5] NREL: Concentrating Solar Power, "Ivanpah solar electric generating system," `http://www.nrel.gov/csp/solarpaces/project_detail.cfm/projectID=62`, accessed: 2014-07-31.

[6] A. Ambrosini, T. N. Lambert, M. Bencomo, A. Hall, K. vanEvery, N. P. Siegel, and C. K. Ho, "Improved high temperature solar absorbers for use in concentrating solar power central receiver application," Proc. ASME **5**, 1–8 (2011).

[7] A. Hall, A. Ambrosini, and C. Ho, "Solar selective coatings for concentrating solar power central receivers," Adv. Mater. Processes **170**, 28–32 (2012).

[8] S. Fan, "Photovoltaics: An alternative 'Sun' for solar cells," Nat. Nanotechnol. **9**, 92–93 (2014).

[9] R. N. Schmidt and K. C. Park, "High-temperature space-stable selective solar absorber coatings," Appl. Opt. **4**, 917–925 (1965).

[10] F. Cao, K. McEnaney, G. Chen, and Z. Ren, "A review of cermet-based spectrally selective solar absorbers," Energ. Environ. Sci. **7**, 1615 1627 (2014).

[11] A.Y.Vorobyev and G.Chunlei, "Solar absorber surfaces treated by femtosecond laser," Proc. IEEE **7**, 135–138 (2010).

[12] H. Sai, H.Yugamia, Y.Kanamorib, and K.Hane, "Solar selective absorbers based on two-dimensional w surface gratings with submicron periods for high-temperature photothermal conversion," Sol. Energy Mater. Sol. Cells **79**, 35–49 (2003).

[13] S. Kunc, "Thermo-optical properties of some solar absorbers," Sol. Wind Technol. **4**, 473–481 (1987).

[14] J. Hodgkinson and R. P. Tatam, "Optical gas sensing: a review," Meas. Sci. Technol. **24**, 1–59 (2013).

[15] J. J. Lai, H. F. Liang, Z. L. Peng, X. Yi, and X. F. Zhai, "Mems integrated narrow band infrared emitter and detector for infrared gas sensor," Journal of Physics: Conference Series **276**, 1–4 (2011).

[16] N. Balke, P. Maksymovych, S. Jesse, I. I. Kravchenko, Q. Li, and S. V. Kalinin, "Exploring local electrostatic effects with scanning probe microscopy: Implications for piezoresponse force microscopy and triboelectricity," ACS Nano **8**, 10229–10236 (2014).

[17] Allen Taflove and Susan C. Hagness, *Computational Electrodynamics: The Finite-Difference Time-Domain Method, Third Edition* (Artech House, Norwood, MA, 2005).

[18] A. F. Oskooi, D. Roundy, M. Ibanescu, P. Bermel, J. D. Joannopoulos, and S. G. Johnson, "Meep: A flexible free-software package for electromagnetic simulations by the fdtd method," Comput. Phys. Commun. **181**, 687–702 (2010).

[19] A. Deinega and I. Valuev, "Long-time behavior of PML absorbing boundaries for layered periodic structures," Comp. Phys.s Commun. **182**, 149–151 (2011).

[20] A. D. Rakic, A. B. Djurisic, J. M. Elazar, and M. L. Majewski, "Optical properties of metallic films for vertical-cavity optoelectronic devices," Appl. Opt. **37**, 5271–5283 (1998).

[21] S. Wang, X. Fu, G. Xia, J. Wang, J. Shao, and Z. Fan, "Structure and optical properties of zns thin films grown by glancing angle deposition," Appl. Surf.Sci. **252**, 8734–8737 (2005).

[22] J. Lintymer, N. Martin, J.-M. Chappe, P. Delobelle, and J. Takadoum, "Influence of zigzag microstructure on mechanical and electrical properties of chromium multilayered thin films," Surf. and Coat. Technol. **180-181**, 26–32 (2004).

[23] R. Atkinson, W. R. Hendren, G. A. Wurtz, W. Dickson, A. V. Zayats, P. Evans, and R. J. Pollard, "Anisotropic optical properties of arrays of gold nanorods embedded in alumina," Phys. Rev. B **73**, 235402 (2006).

[24] D. Choi, C. S. Kim, D. Naveh, S. Chung, A. P. Warren, N. T. Nuhfer, M. F. Toney, K. R. Coffey, and K. Barmak, "Electron mean free path of tungsten and the electrical resistivity of epitaxial (110) tungsten films," Phys. Rev. B **86**, 045432 (2012).

[25] T. Jun, L. Yong-Hua, Z. Rong-Sheng, L. Kai-Qun, X. Zhi-Guo, L. Zhao-Feng, L. Sheng-li, W. Pei, and M. Hai, "Effect of aspect ratio distribution on localized surface plasmon resonance extinction spectrum of gold nanorods," Chin. Phys. Lett. **25**, 4459–4462 (2008).

[26] C. Ungaro, S. K. Gray, and M. C. Gupta, "Black tungsten for solar power generation," Appl. Phys. Lett. **103**, 071105–071105–3 (2013).

[27] J. C. Fiala, "Reconstruct: a free editor for serial section microscopy," J. Microsc. **218**, 52–61 (2005).

[28] L. Hu and G. Chen, "Analysis of optical absorption in silicon nanowire arrays for photovoltaic applications." Nano Lett. **7**, 3249–3252 (2007).

[29] C. Schlemmer, J. Aschaber, V. Boerner, and J. Luther, "Thermal stability of microstructured selective tungsten emitters," AIP Conference Proceedings **653**, 164–173 (2003).

[30] J. Habainy and C. Nilsson, "Oxidation of pure tungsten in the temperature interval 400 to 900 C," (2013), Lund University, Sweden. Master's thesis.

Design of Emitter Structures Based on Resonant Perfect Absorption for Thermophotovoltaic Applications

Jonathan J. Foley IV[1,‡], Craig Ungaro[2,‡], Keye Sun[2], Mool C. Gupta[2,*], Stephen K. Gray[1,†]

[1] *Center for Nanoscale Materials, Argonne National Laboratory, 9700 South Cass Avenue, Argonne, IL, 60439, USA*

[2] *Department of Electrical & Computer Engineering, University of Virginia, Charlottesville, Virginia, 22901, USA*

[*] *mgupta@virginia.edu,* [†] *skgray@anl.gov*

Abstract:

We report a class of thermophotovoltaic emitter structures built upon planar films that support resonant modes, known as perfectly-absorbing modes, that facilitate an exceptional optical response for selective emission. These planar structures have several key advantages over previously-proposed designs for TPV applications: they are simple to fabricate, are stable across a range of temperatures and conditions, and are capable of achieving some of the highest spectral efficiencies reported of any class of emitter structure. Utilization of these emitters leads to exceptionally high device efficiencies under low operating temperature conditions, which should open new opportunities for waste heat management. We present a theoretical framework for understanding this performance, and show that this framework can be leveraged as a search algorithm for promising candidate structures. In addition to providing an efficient theoretical methodology for identifying high-performance emitter structures, our methodology provides new insight into underlying design principles and should pave way for future design of structures that are simple to fabricate, temperature stable, and possess exceptional optical properties.

OCIS codes: 350.6050, 350.4238, 310.4165, 310.6805

References and links

1. S. Fan, "Photovoltaics: An alternative 'sun' for solar cells," Nature Nanotechnology **9**, 92–93 (2014).
2. P. A. Davies and A. Luque, "Solar thermophotovoltaics: brief review and a new look," Solar Energy Materials and Solar Cells **33**, 11–22 (1994).
3. P. Bermel, M. Ghebrebrhan, W. Chan, Y. X. Yeng, M. Araghchini, R. Hamam, C. H. Marton, K. F. Jensen, M. Soljacic, J. D. Joannopoulos, S. G. Johnson, and I. Celanovic, "Design and global optimization of high-efficiency thermophotovoltaic systems," Opt. Express **18**, A314–A334 (2010).
4. C. Ungaro, S. K. Gray, and M. C. Gupta, "Black tungsten for solar power generation," Appl. Phys. Lett. **103**, 071105 (2013).
5. C. Ungaro, S. K. Gray, and M. C. Gupta, "Graded-index structures for high-efficiency solar thermophotovoltaic emitting surfaces," Opt. Lett. **18**, 5259–5262 (2014).
6. A. Lenert, D. M. Bierman, Y. Nam, W. R. Chan, I. Celanovic, M. Soljacic, and E. N. Wang, "A nanophotonic solar thermophotovoltaic device," Nature Nanotechnology **9**, 126–130 (2014).
7. H. Ye, H. Wang, and Q. Cai, "Two-dimensional vo2 photonic crystal selective emitter," Journal of Quantitative Spectroscopy and Radiative Transfer **158**, 119 – 126 (2015).

8. E. Rephaeli and S. Fan, "Absorber and emitter for solar thermophotovoltaic systems to achieve efficiency exceeding the schockley-queisser limit," Opt. Express **17**, 15145–15159 (2009).
9. L. M. Fraas, J. E. Avery, and H. X. Huang, "Thermophotovoltaic furnace-generator for the home using low bandgap GaSb cells," Semiconductor Science and Technology **18**, S247 (2003).
10. V. P. Khvostikov, S. V. Sorokina, O. A. Khvostikova, N. K. Timoshina, N. S. Potapovich, B. Y. Ber, D. Y. Kazantsev, and V. M. Andreev, "High-efficiency GaSb photocells," Physics of Semiconductor Devices **47**, 307–313 (2013).
11. M. W. Dashiell, J. F. Beausang, H. Ehsani, G. J. Nichols, D. M. Depoy, L. R. Danielson *et al.*, "Quaternary InGaAsSb thermophotovoltaic diodes," IEEE Transactions on Electron Devices **53**, 2879–2891 (2006).
12. C. A. Wang, H. K. Choi, S. L. Ransom, G. W. Charache, L. R. Danielson, and D. M. DePoy, "High-quantum-efficiency 0.5 eV GaInAsSb/GaSb thermophotovoltaic devices," Applied Physics Letters **75**, 1305–1307 (1999).
13. N. P. Sergeant, O. Pincon, M. Agrawal, and P. Peumans, "Design of wide-angle solar-selective absorbers using aperiodic metal-dielectric stacks," Opt. Express **17**, 22800–22812 (2009).
14. J. J. Foley. IV, H. Harutyunyan, D. Rosenmann, R. Divan, G. P. Wiederrecht, and S. K. Gray, "When are surface plasmon polaritons excited in the kretschmann-raether configuration?" Sci. Rep. **5**, 09929 (2015).
15. P. Yeh, *Optical waves in layered media* (Wiley, 2005).
16. J. A. Nelder and R. Mead, "A simplex method for function minimization," Comp. J. **7**, 308–313 (1965).
17. J. M. Montgomery and S. K. Gray, "Enhancing surface plasmon polariton propagation lengths via coupling to asymmetric waveguide structures," Phys. Rev. B **77**, 125407–125415 (2008).
18. E. D. Palik, *Handbook of optical constants of solids* (Academic Press, 1998).
19. P. B. Johnson and R. W. Christy, "Optical constants of noble metals," Phys. Rev. B **6**, 4370 (1972).
20. M. Shimizu, A. Kohiyama, and H. Y. Yugami, "High-efficiency solar-thermophotovoltaic system equipped with a monolithic planar selective absorber/emitter," J. Photon. Energy **5**, 053099–53107 (2015).
21. G. V. Naik, J. L. Schroeder, X. Ni, A. V. Kildishev, T. D. Sands, and A. Boltasseva, "Titanium nitride as a plasmonic material for visible and near-infrared wavelengths," Opt. Mater. Express **2**, 478–489 (2012).
22. W. Chan, R. Huang, C. Wang, J. Kassakian, J. Joannopoulos, and I. Celanovic, "Modeling low-bandgap thermophotovoltaic diodes for high-efficiency portable power generators," Solar Energy Materials and Solar Cells **94**, 509–514 (2010).
23. P. Nagpal, S. E. Han, A. Stein, and D. J. Norris, "Efficient low-temperature thermophotovoltaic emitters from metallic photonic crystals," Nano Lett. **8**, 3238–3243 (2008).
24. M. Lim, S. Jin, S. S. Lee, and B. J. Lee, "Graphene-assisted si-insb thermophotovoltaic system for low temperature applications," Opt. Express **23**, A240–A253 (2015).

---

1. Introduction

Solar energy conversion has been explored through direct sunlight to electric conversion via the photovoltaic (PV) effect, and sunlight to heat, which can be efficiently stored for later use and can be converted to electric power. Solar cells based on the PV effect have a theoretical maximum efficiency of about 32% due to the Shockley-Queisser limit. The reason for the low theoretical maximum conversion efficiency of PV cells is that a significant amount of solar light lies at energies outside of the solar cell bandgap. Solar energy in excess of the bandgap is wasted as heat, while solar photons with energies below the bandgap are transmitted rather than absorbed by the cell. In thermophotovoltaic (TPV) systems, incoming energy is used to heat an emitting surface to high temperatures, which results in a large amount of thermal emission from the surface. This thermal emission is then captured by a low-bandgap PV cell where it is turned into electrical energy. Traditional TPV systems use waste heat or a burning fuel to heat the emitter while solar thermophotovoltaic (STPV) systems use concentrated solar energy [1].

Using a STPV system allows broad-spectrum sunlight to be effectively absorbed and converted into heat and then to electrical energy. This allows for energy from the entire solar spectrum to be used, resulting in a theoretical maximum efficiency of 85.4% based on the Carnot cycle limit [2]. As a result, STPV systems have the potential to be far more efficient than PV cells. By controlling the optical properties of the STPV emitting surface, its thermal emission can be spectrally matched to a PV cell, resulting in high efficiency operation [3, 4, 5, 6]. Perhaps the most impressive emitters to date have exploited optical resonances resulting from patterned surfaces, including a VO_2-based photonic crystal with an optimal spectral efficiency (see Eq. 1) of 54% for InGaSb PV cells with a band gap of 0.62 eV [7], W-based graded index structure with an optimal efficiency of 59% for GaSb PV cells with a band gap of 0.73 eV [5], and W-based photonic crystals with an optimal efficiency of 63% for GaSb PV cells with a band gap of 0.73 eV [8]. However, these structures suffer from several key drawbacks: they typically rely on precise fabrication of sub-wavelength structures to tune their resonant properties, and they require high operating temperatures to achieve high spectral efficiencies. For example, the spectral efficiency of the VO_2 photonic crystal drops from 54% to 41% if the operating temperature is lowered from the optimal 1500 K to 1300 K [7]. The requisite high operating temperatures means these structures are susceptible to deformation during operating conditions, which can compromise their resonant properties and severely degrade their performance. Their low-efficiency at low temperatures precludes their application to a number of potential waste heat reclamation technologies.

In this work, we present a theoretical framework for a phenomenon known as resonant perfect absorption that can be leveraged for the design of simple planar emitter structures that have the highest reported spectral efficiencies to our knowledge. These planar structure have several key advantages over previously-proposed structures for TPV applications: they are simple to fabricate, are stable across a range of temperatures and conditions, and can be used to achieve high conversion efficiencies even at low operating temperatures. We also provide experimental validation for our designs by fabricating and characterizing an emitter structure based on this methodology. In addition to providing an efficient theoretical methodology for identifying high-performance emitter structures, our methodology provides new insight into underlying design principles and should pave way for future design of structures that are simple to fabricate, temperature stable, and possess exceptional optical properties. The exceptional performance of devices utilizing these emitter structures at low (1000 K) temperatures should open new opportunities for waste heat management.

2. Spectral Efficiency

Emitter structures are often characterized by their spectral efficiency (SE), which reports the fraction of the absorbed energy emitted by the selective emitter that a PV cell is able to use. The total available emitted spectral energy is found by multiplying the emittance by the blackbody thermal radiation spectrum. In this work, we consider the spectral efficiency of structures for two PV cells common in TPV systems: GaSb with a bandgap of 0.7326 eV ($\lambda_{bg} = 1707$ nm) and InGaAsSb with a bandgap of 0.550 eV ($\lambda_{bg} = 2254$ nm) [9, 10, 11, 12]. High (1750 K) and low (1000 K) temperature conditions are considered.

The spectral efficiency is given by [5]

$$SE = \frac{\int_0^{\lambda_{bg}} \frac{E_{bg}}{E_\lambda} B(\lambda,T)\, \varepsilon_S(\lambda)\, d\lambda}{\int_0^{\infty} B(\lambda,T)\, \varepsilon_S(\lambda)\, d\lambda} \tag{1}$$

where E_{bg} is the bandgap energy of the PV cell, E_λ is the energy of a photon with wavelength λ, $B(\lambda,T)$ is Planck's law for blackbody radiation, and $\varepsilon_S(\lambda)$ is the spectral emittance of the surface. High SE emitters tend to have negligible emittance at wavelengths longer than λ_{bg} and near-unity emittance at or just short of λ_{bg}. While a spectrally narrow emission is desired to reduce thermalization loss in the PV cell, some bandwidth is required to increase the power density of the emitted radiation. Systems with extremely narrow emission require a large emitter area, which results in a large PV cell area requirement and a greatly increased system cost [3, 4, 5, 6].

3. Resonant Perfect-Absorption in planar structures

If the emissivity of the emitter structure can be expressed simply in terms of its geometry and material parameters, then the spectral efficiency may be viewed as an objective function, and an optimization can be performed in terms of these variables. For example, this concept has been used to design planar structures for TPV absorbers and emitters, where the spectral efficiency objective function is optimized using derivative-less techniques like the Nelder-Mead method [13]. This approach can also be used to design more complicated structures, such as the 2-D photonic crystal described in reference [8], but analytical methods are no longer appropriate for computation of the emissivity to update the objective. In this case, the numerical optimization must also be coupled to numerical electrodynamics techniques, which increases the computational cost. An important drawback of this approach is that in all cases, it is unclear how to uncover design principles for promising structures without first identifying a concrete physical phenomenon that gives rise to high spectral efficiency.

We have recently developed a theoretical framework for a physical phenomenon in simple planar structures, known as resonant perfect absorption, that leads to the optical response requisite for high spectral efficiency [14]. Here we demonstrate that this theoretical framework provides predictive power for the design of high spectral efficiency emitter structures, and also provides insight that can guide their further improvement. Optimizing over spectral efficiency, which lacks clear necessary conditions for optimality, is replaced by locating zeros in the reflectance amplitude, which are well defined in terms of a complex wavevector values that define perfectly absorbing modes. We demonstrate this predictive power by using this framework to identify simple planar structures that show an exceptional spectral efficiency of nearly 70%. The simplicity of the structures designed by our methodology is amenable to simple fabrication processes, which allows us to easily validate our predictions experimentally.

Electromagnetic waves supported by a general L-layer structures must satisfy appropriate boundary conditions, which are written concisely in the matrix form introduced by Yeh [15],

$$\begin{pmatrix} E_1^+ \\ E_1^- \end{pmatrix} = \begin{pmatrix} M_{1,1} & M_{1,2} \\ M_{2,1} & M_{2,2} \end{pmatrix} \begin{pmatrix} E_L^+ \\ E_L^- \end{pmatrix}, \tag{2}$$

where the precise value of the matrix elements $M_{i,j}$ depend on the thickness and refractive index of each layer in the multi-layer structure, as well as the frequency, polarization, and (complex) wavevector of light, see Appendix for more details. Resonant perfect absorption in these structures can be understood in terms of modes in these structures, known as perfectly absorbing (PA) modes. PA modes are defined as solutions to the above matrix equation when E_1^- and E_L^+ are set to zero, which is satisfied when $M_{2,1} = 0$. [14] By definition of the Fresnel reflection amplitude, $r = M_{21}/M_{11}$, we see that the reflection on resonance with the PA mode is rigorously zero. In this work, we confine our attention to structures terminated by an optically-thick metal substrate, meaning transmission through these structures is also necessarily zero. Hence absorption, and emission at thermal equilibrium, are indeed perfect for the PA modes in these structures. Because they are resonant modes, they have the potential to impart selective spectral emission requisite for high efficiency TPV emitter structures.

Recalling that the matrix elements depend on the geometry as well as the wavevector, we formulate the modal equations as a search for $M_{2,1}(\omega, \alpha, \beta, \mathbf{d}) = 0$, where β and α denote the real and imaginary components of the optical wavevector, respectively. The vector $\mathbf{d}$ denotes the vector of thicknesses of each planar film, which completely defines the geometry of the structure so long as the composition of each layer is specified. The wavevector components β can be related to an angle of incidence that is resonant with the PA mode, specifically $\beta = n_i k_0 \sin(\theta_i)$, where k_0 is the free-space wavevector and n_i is the refractive index of the material through which light is incident, typically air. While a similar interpretation is possible for the imaginary wave-vector component, a more physically concrete interpretation is that it relates to the resonance line-width of the PA mode. In either interpretation, a smaller α magnitude is desirable for TPV applications because it indicates that the PA modes can be efficiently coupled into by light at real angles of incidence, and that the resonance line-width is relatively narrow, which are both desirable from the point of view of spectral efficiency. We also desire that β be close to zero so that normally-incident light can couple efficiently into the PA mode.

With this in mind, we can design a search routine using standard numerical methods to locate structures that support PA modes in the frequency range of our choice that also have magnitudes of β and α that are relatively small [16, 17, 14]. That is, for the InGaAsSb PV cells, we can search for 2- and 4-layer structures that support PA modes in the energy window slightly higher than 0.55 eV, and for GaSb PV cells, we search for 2- and 4-layer structures that support PA modes in the energy window slightly higher than 0.72 eV. Such a search can be used to hone in on structures that show considerable promise for TPV applications. Further refinement can be performed on these candidate structures by optimizing over the FOM defined by Eq. 1 where the emissivity is computed simply from the Fresnel equations and the Blackbody spectrum corresponds to the temperature of interest. While in this work, we will focus exclusively on planar structures, we note that resonant perfect absorption can occur in higher dimensional photonic crystals. The methodology we outline can therefore be generalized to these structures, though numerical electrodynamics techniques may be required to compute the photonic band structure.

4. Results

We follow the procedure outlined above to locate geometries of 2- and 4-layer planar structures. For 2-layer structures, layer 1 functions as a dielectric anti-reflective coating and layer 2 is an optically-thick absorbing layer. For 4-layer structures, layers 1 and 3 are dielectric layers, while layers 2 and 4 are absorbing layers. Layer 4 is again optically-thick, while layer 2 is a thin film (see Fig. 1 inset and Fig. 2c for a schematics). Silver and tungsten are considered for the absorbing layers, and yttria-stabilized zirconia (YSZ) is used for the dielectric layers. We assume a refractive index of 2.1 for YSZ and take the permittivity of W from reference [18] and the permittivity of Ag from reference [19].

We perform searches for PA modes as described in the previous section. For 4-layer structures, we allow d_1, d_2, and d_3 (the thicknesses of layers 1, 2, and 3, respectively) to vary, while for 2-layer structures, we allow only d_1 (dielectric over-layer) to vary. We first confine our attention to energy ranges between 0.73 and 0.85 eV (λ between 1450 and 1700 nm, or 3.69 to 4.33 μm^{-1}) to target emitters for GaSb cells. If we confine our search to ranges of the modal wavevector magnitude less than or equal to 1 μm^{-1}, we can consider our search as confined to a reciprocal volume of about 0.64 μm^{-3}. A particularly high density of PA modes can be found in this reciprocal volume for structures of the type YSZ/Ag/YSZ/W and YSZ/W/YSZ/W, while the density of PA modes in this reciprocal volume for YSZ/W/YSZ/W and YSZ/Ag/YSZ/Ag are considerably lower. Furthermore, we find no PA modes can be found within the light line for 2-layer structures of YSZ/W or YSZ/Ag. Of the two structures with a highest density of PA modes in the reciprocal volume of interest, we see that YSZ/Ag/YSZ/W has considerably more PA modes with $\beta < 0.1\mu m^{-1}$, indicating that normally incident light can couple very efficiently to these modes. In particular, we see from this modal search that structures with d_1 in the range 100-150 nm, d_2 in the range 10 to 20 nm, and d_3 in the range 250 to 300 nm can support PA modes with small β and α in the frequency range of interest.

This process is repeated to target structures for InGaAsSb cells, this time confining the search to energy ranges between 0.55 and 0.65 eV (λ between 1900 and 2254 nm). From this search, we see a high density of modes with small β and α when d_1 is in the range 130-170 nm, d_2 is in the range 16-30 nm, and d_3 is in the range 350-470 nm.

Table 1. Geometries, spectral efficiencies, and device efficiencies of structures optimized for $\lambda_{bg} = 2254$ nm and $\lambda_{bg} = 1707$ nm, for low- (1000 K) and high-temperature (1750 K) operation. We compare 4-layer structures to 2-layer structures. For 4-layer structures, d_1 is the thickness of a dielectric coating, d_2 is the thickness of a thin metal film, d_3 is the thickness of the dielectric spacer on top of an optically-thick tungsten substrate. For to 2-layer structures, d_3 is the thickness of a dielectric coating on top of optically-thick tungsten.

Structure	d_1 (nm)	d_2 (nm)	d_3 (nm)	Spec. Eff. (%)	Sys. Eff. (%)
$\lambda_{bg} = 2254$ nm at 1000 K					
Si_3N_4/Ag/Si_3N_4	167	14	456	45.7	9.7
YSZ/Ag/YSZ	148	15.5	393	47.8	10.0
Si_3N_4/W/Si_3N_4	169	48	369	42.2	9.5
YSZ/W/YSZ	148	52	314	43.7	9.8
Si_3N_4/Ta/Si_3N_4	178	24	440	35.2	7.7
YSZ/Ta/YSZ	154	22	345	39.5	8.6
Si_3N_4/W	0	0	167	39.7	7.1
YSZ/W	0	0	146	41.4	8.3
Bare W	0	0	0	31.1	3.6
$\lambda_{bg} = 1707$ nm at 1000 K					
Si_3N_4/Ag/Si_3N_4	129	13	335	34.4	5.7
YSZ/Ag/YSZ	115	14	288	36.2	5.9
Si_3N_4/W/Si_3N_4	132	60	16	24.6	5.4
YSZ/W/YSZ	113	60	16	25.6	5.6
Si_3N_4/Ta/Si_3N_4	137	24	316	20.9	4.7
YSZ/Ta/YSZ	118	25	266	22.2	5.2
Si_3N_4/W	0	0	133	24.8	4.7
YSZ/W	0	0	115	25.8	5.3
$\lambda_{bg} = 2254$ nm at 1750 K					
YSZ/Ag/YSZ	175	20	389	65.2	16.8
YSZ/Ta/YSZ	156	23	321	59.5	17.0
YSZ/W/YSZ	159	47	288	60.2	17.1
YSZ/W	0	0	160	58.3	16.9
$\lambda_{bg} = 1707$ nm at 1750 K					
YSZ/Ag/YSZ	126	19	283	68.0	20.8
YSZ/Ta/YSZ	107	27	244	56.2	19.8
YSZ/W/YSZ	105	60	16	57.0	20.2
YSZ/W	0	0	104	57.3	20.3

We further refine our structures by optimizing Eq. 1 over **d** for a given band-gap energy and temperature. We first fix the temperature at 1000 K for optimizations for InGaAsSb and GaSb cells. Indeed, the performance of YSZ/Ag/YSZ/W structures optimized for this low-temperature operation is quite impressive for low temperature conditions, giving SE of about 48% for InGaAsSb cells and 37% for GaSb cells (see Table I). This is particularly impressive considering that this structure's spectral efficiency at 1000 K is 13.5% higher than the that of the 2-D photonic crystal at 1300 K described in Ref. [7]. Maps of the emissivity of these

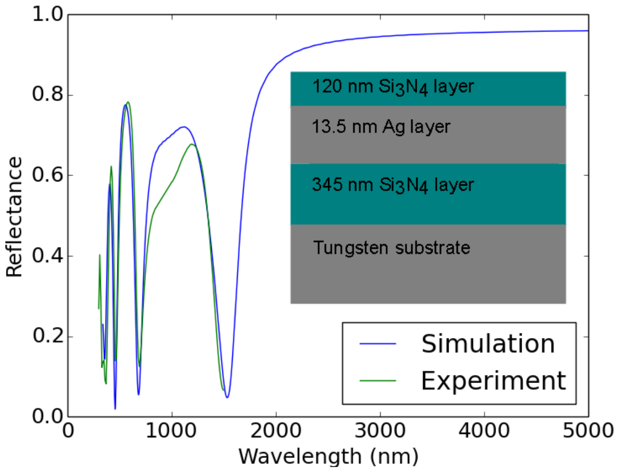

Fig. 1. Comparison of simulated and experimental results for the reflectance of a sample with a d_1 of 120 nm, a d_2 of 13.5 nm, and a d_3 of 345 nm. **Inset:** The fabricated structure.

structures as a function of wavelength and angle are given in Fig. 2, as well as a schematic of the structure geometry. An important feature of the optical response of these structures is that the frequency of the emissivity maxima is relatively angle-insensitive. This can again be related to features of the PA modes, in particular, their dispersion. In Fig. A2 in the Appendix we show the PA dispersion for several structures optimized for the InGaAsSb cells at 1000 K operation and see that the PA dispersions at around 0.55 eV are relatively flat, which accounts for the lack of strong angular dependence of the emissivity peak. Compared to the YSZ/Ag/YSZ/W structures, we find that optimized YSZ/W/YSZ/W structures, which were recently discussed by Shimizu, Kohiyama, and Yugami for higher (1650 K) operation [20], perform considerably worse, with spectral efficiencies that are lower by 11% and 29% for InGaAsSb and GaSb cells, respectively. In fact, the performance of tungsten with an optimized anti-reflective coating can essentially match the performance of the more complicated YSZ/W/YSZ/W structure seen in reference [20] (see Table I). The optical response of YSZ/W and YSZ/W/YSZ/W structures differs markedly from the YSZ/Ag/YSZ/W structure, as can be seen by the emissivity curves of the optimized structures (see Table I for optimal geometries). In Fig. 3a, we plot the emissivity of these structures optimized for InGaAsSb cells at 1000 K operation, and note the near perfect emissivity that is observed at $\lambda = 2\mu m$ in the YSZ/Ag/YSZ/W structure. Under these operation conditions, the various structures in fact give fairly similar spectral efficiencies despite having qualitatively different emissivities. However, the perfect absorption/emissivity feature of the YSZ/Ag/YSZ/W structure shows exceptional tunability (see Fig. 2), which allows this structure to be simply modified to give superior performance for a variety of PV materials and operating conditions. If we examine the PA modes for this YSZ/Ag/YSZ/W, we see indeed that β is nearly zero, indicating normally incident light can couple efficiently into this mode (see Fig. 3b). On the other hand, β is fairly large for PA modes in YSZ/W and YSZ/W/YSZ/W, indicating that normally incident light cannot couple efficiently to these modes (see Fig. A3 in the Appendix). We consider substituting tantalum for layer 2 in the base structure from the modal search, i.e. YSZ/Ta/YSZ/W, but find that performance is generally lower than structures with either W or Ag. The results are much less sensitive to substitution of the dielectric material. For example, using Si_3N_4, another common dielectric material for high-temperature applications, for layer

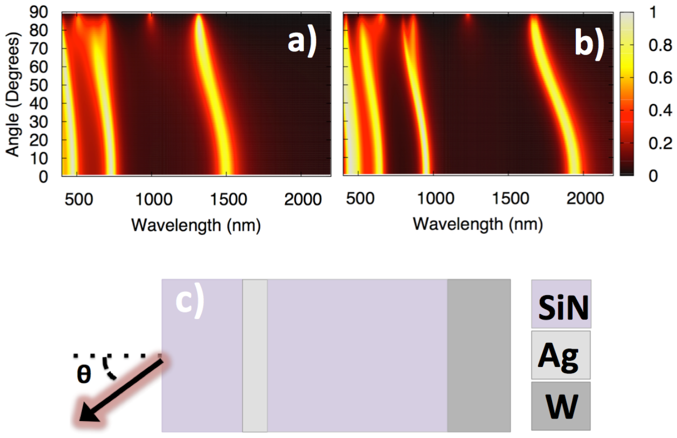

Fig. 2. Maps of Emissivity as a function of emission angle and wavelength. **a)** Emissivity map of thin-film structure optimized for PV material with $\lambda_{bg} = 1707$ nm with an operating temperature of 1000 K. **b)** Emissivity map of thin-film structure optimized for PV material with $\lambda_{bg} = 2254$ nm with an operating temperature of 1000 K. **c)** Schematic of emitter structure consisting of an optically-thick tungsten substrate with thin-film layers of Ag and Si_3N_4 to mediate selective absorption/emission.

1 and 3 yields results quite similar to those when YSZ is used. We find that structures can be optimized with Si_3N_4 to give nearly the same spectral efficiencies, although the dielectric layers are generally thicker to achieve comparable optical path lengths, as we take the refractive index of Si_3N_4 to be 1.8. These results suggest that the nature of the PA modes can be tuned dramatically by changing the properties the thin-film absorbing layer. Ideally, the wavevector of the mode should approach zero. A map of α and β as a function of permittivity for PA modes at an energy well matched to the GaSb cell suggests that thin-films that are good plasmonic materials are ideal for these applications (see Fig. A4 in the Appendix). Recent investigations on the plasmonic properties of temperature-stable ceramics like titanium nitride may therefore offer promising materials for constructing high-efficiency emitter structures based on resonant perfect absorption [21].

To further demonstrate the robust performance of the YSZ/Ag/YSZ/W structure, we optimize over **d** for both PV cells assuming an operating temperature of 1750 K, giving a spectral efficiency of 68% and 65% for GaSb and InGaAsSb cells, respectively (see Table I). Indeed, this exceeds what is, to our knowledge, the highest reported spectral efficiency for GaSb cells by more than 7% with a much simpler design [8]. Here, the YSZ/W/YSZ/W structures discussed in reference [20] have optimal spectral efficiencies that are 16% and 8% lower for GaSb and InGaAsSb cells, respectively. Interestingly again, the optimized 4-layer structure consisting of YSZ/W/YSZ/W performs comparably to a simple W substrate with an optimized YSZ anti-reflective coating (see Table I).

The reflectance of fabricated and simulated structures are compared in Fig. 1 for a sample with a d_1 of 120 nm, a d_2 of 13.5 nm, and a d_3 of 345 nm. The FOM of this structure is 0.56 at 1750 K. Excellent agreement is found between these results, which serves both to validate the theoretical predictions and demonstrate the feasibility of fabricating structures to within the specifications required to achieve high spectral efficiencies. The discrepancy between simulated and experimental results in the 800 to 1200 nm range is due to a lamp change in the spectrometer in this region.

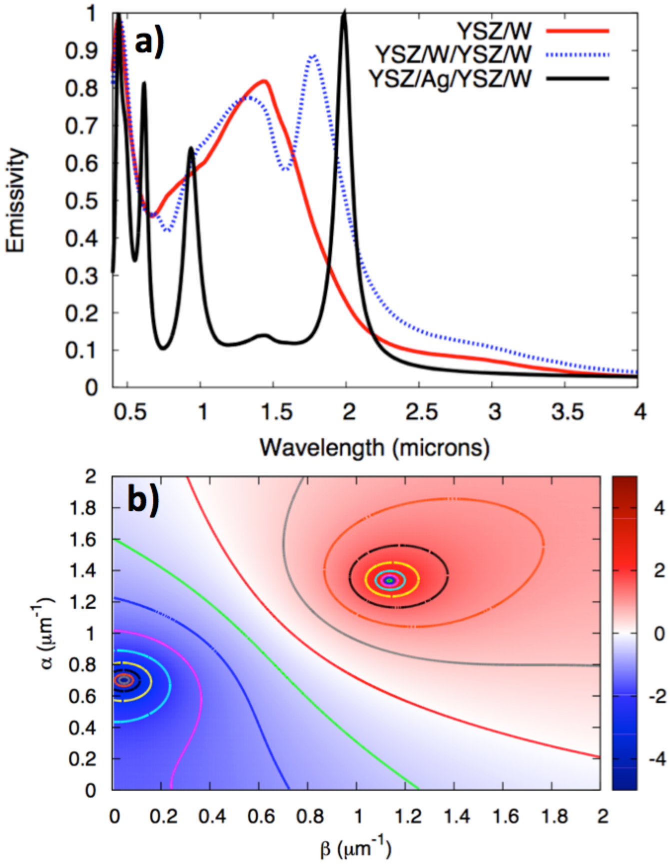

Fig. 3. **Top** Emissivity of various structures optimized for InGaAsSb cells. **Bottom** Reflectance in the complex β, α plane for optimized YSZ/Ag/YSZ/W structure at $\lambda = 2\mu m$. We see that the strong emissivity peak of the YSZ/Ag/YSZ/W structure corresponds to resonant perfect absorption.

The fabrication procedure is straightforward and easy to implement. Double-side polished tungsten (W) substrates were purchased from MTI Corporation. Substrates were cleaned by acetone and methanol sequentially. Stacks of silicon nitride (Si_3N_4) and silver (Ag) layers were deposited onto the W substrates. The structures is analogous to the schematic shown in Fig. 2. The Si_3N_4 layers were deposited by plasma-enhanced chemical vapor deposition (PECVD). The deposition temperature was kept at 100°C. The Ag layer was deposited by e-beam evaporation. The reflection of the coating was measured by a spectrometer (PerkinElmer, Lambda 950 UV/VIS).

The total power conversion efficiencies for cylindrical STPV systems utilizing the structures outlined in this paper are also shown in Table I. These were calculated assuming a blackbody (absorbance = 0.99) absorber, and solar concentration ratio of C = 1000 for the low (1000 K) temperature systems, and C = 2500 for the high (1750 K) temperature systems. GaSb PV cells with an E_{bg} of 0.72 eV, fill factor of 0.82, V_{oc} of .55, and EQE of 0.7 and InGaAsSb PV cells with an E_{bg} of 0.55 eV, fill factor of .74, V_{oc} of .4, and EQE of .56 were used in these simulations [6, 10, 22]. The simulations show that a high system efficiency can be obtained using the simple structures outlined in this paper. They also show that high efficiencies can be maintained at lower operating temperatures by changing the parameters of the coatings used in the emitting structures. Low temperature TPV structures are of great interest for waste-heat reclamation [23, 24].

We presented a theoretical framework for a phenomenon known as resonant perfect absorption that can be leveraged for the design of high spectral-efficiency emitter structures. This framework guided the design of a simple class of emitter structures built upon planar films that support perfectly absorbing (PA) modes. In particular, we found that structures composed of YSZ/Ag/YSZ/W support PA modes with particularly favorable characteristics for TPV applications. Importantly, this structure is robust to substitutions of the dielectric material, which we demonstrate by comparing the performance of Si_3N_4/Ag/Si_3N_4/W structures. Further refinement of the structure, taking into account key parameters like temperature, is possible using the spectral efficiency as an optimization objective. Following this procedure, we obtain structures that have exceptionally high spectral efficiencies across a range of operating temperatures. That these simple planar structure can achieve such high spectral efficiencies is advantageous from the point of view of fabrication feasibility and temperature stability. A further advantage of our approach is that it identifies a concrete physical phenomenon, resonant perfect absorption, that provides the basis for the exceptional performance of these emitter structures, as well as a predictive theoretical framework for identifying structures that support perfectly absorbing modes. Hence our methodology provides new insight into underlying design principles and should pave way for future engineering of structures that are simple to fabricate, temperature stable, and possess exceptional optical properties.

Acknowledgments

This work was performed at the Center for Nanoscale Materials, a U.S. Department of Energy, Office of Science, Office of Basic Energy Sciences User Facility under Contract No. DE-AC02-06CH11357. We would also like to thank the NASA Langley Professor and NSF IUCRC programs for their support of this project. ‡ JJF and CU contributed equally.

Appendix

Boundary Conditions of Electromagnetic Waves in planar structures

Consider an L-layer system, with Figure A1 depicting the L = 4 case. The optical response in each layer j arises from the (in general) frequency-dependent refractive index, $N_j(\omega) = n_j(\omega) + ik_j(\omega)$, where n_j and k_j are real numbers. The associated electrical permittivity is $\varepsilon_j = N_j^2$. Layers $j = 1$ and $j =$ L are semi-infinite, generally non-absorbing dielectric materials characterized by real, positive refractive indices, $N_1 = n_1 > 0$ and $N_L = n_L > 0$. The central layers 2,.., L-1 could include absorbing materials that are described by complex refractive indices. Metallic layers are absorbing but can also be such that $\mathrm{Re}(\varepsilon_j) = \mathrm{Re}(N_j^2) = n_j^2 - k_j^2 < 0$. Since the films, with our coordinate system choice (Fig. A1), are homogeneous in the y-direction, the relevant tangential electrical field component is taken to be the real part of the phasor $\exp(i(k_x x - \omega t))$ $E(z)$ with [1,2]

$$E(z) = \left\{ \begin{array}{cc} E_1^+ \exp(ik_{z1}z) + E_1^- \exp(-ik_{z1}z) & z < z_1 \equiv 0 \\ E_2^+ \exp(ik_{z2}(z-z_1)) + E_2^- \exp(-ik_{z2}(z-z_1)) & z_1 < z < z_2 \\ \cdots & \\ E_L^+ \exp(ik_{zL}(z-z_{L-1})) + E_L^- \exp(-ik_{zL}(z-z_{L-1})) & z > z_{L-1} \end{array} \right)$$

where the z-component of the wavevector in each layer satisfies

$$k_{zj} = \pm\sqrt{N_j^2 k_0^2 - k_x^2} \quad , \tag{3}$$

with $k_0 = \omega/c$. For p-polarized light $E(z) \equiv E_x(z)$, and for s-polarized light $E(z) \equiv E_y(z)$.

The boundary conditions for satisfying Maxwell's equations are that the tangential components of the magnetic (and electric) field be continuous across each interface, which leads to [1]:

$$\begin{pmatrix} E_1^+ \\ E_1^- \end{pmatrix} = D_1^{-1} D_2 \begin{pmatrix} E_2^+ \\ E_2^- \end{pmatrix}$$

and

$$\begin{pmatrix} E_l^+ \\ E_l^- \end{pmatrix} = P_l\, D_l^{-1}\, D_{l+1} \begin{pmatrix} E_{l+1}^+ \\ E_{l+1}^- \end{pmatrix}$$

for $l = 1, ..., L-1$. The matrix D_l is defined

$$D_l = \begin{pmatrix} \cos(\theta_l) & \cos(\theta_l) \\ N_l & -N_l \end{pmatrix}$$

for p-polarized light and

$$D_l = \begin{pmatrix} 1 & 1 \\ N_l \cos(\theta_l) & -N_l \cos(\theta_1) \end{pmatrix}$$

for s-polarized light. For the entire L-layer structure, we have

$$\begin{pmatrix} M_{11} & M_{12} \\ M_{21} & M_{22} \end{pmatrix} = D_1^{-1} \left(\prod_{l=2}^{L-1} D_l P_l D_l^{-1} \right) D_L,$$

where P_l is

$$P_l = \begin{pmatrix} \exp(-ik_{zl} d_l) & 0 \\ 0 & \exp(ik_{zl} d_l) \end{pmatrix}.$$

Supporting Figures for Perfectly Absorbing Modes

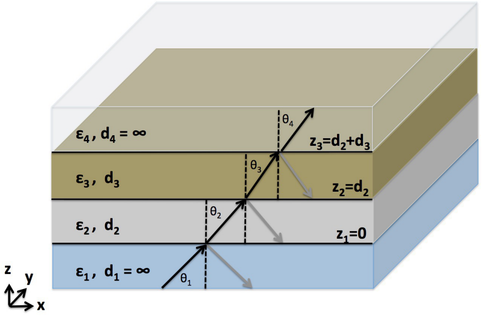

Fig. A1. Schematic of 4 layer system with finite thickness (d_2 and d_3) sandwiched by 2 semi-infinite dielectric layers illustrating coordinate system used for Fresnel equations.

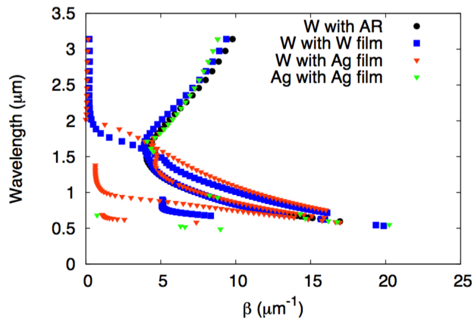

Fig. A2. Dispersion of perfectly absorbing modes in various structures. **W with AR** corresponds to a 2-layer YSZ/W structure. **W with W film** corresponds to a 4-layer YSZ/W/YSZ/W structure. **W with Ag film** corresponds to a 4-layer YSZ/Ag/YSZ/W structure. **Ag with Ag film** corresponds to a 4-layer YSZ/Ag/YSZ/Ag structure. At critical frequencies, the YSZ/Ag/YSZ/W structure supports perfectly absorbing modes with low β and α, indicating that normally-incident light couples efficiently into these modes.

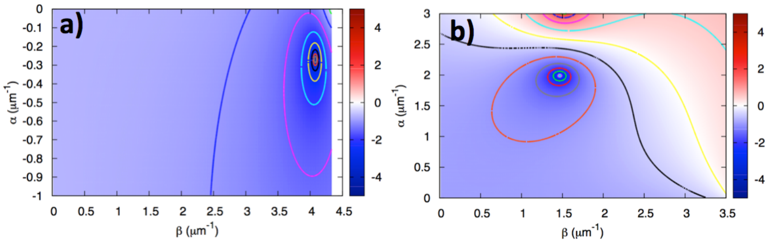

Fig. A3. Reflectance in the complex wavevector plane near perfectly absorbing resonances. Reflectance plane near PA resonance for **a)** YSZ/W structure and **b)** YSZ/W/YSZ/W structure optimized for InGaAsSb cells at 1000K operation, see Table I in the main text for geometries.

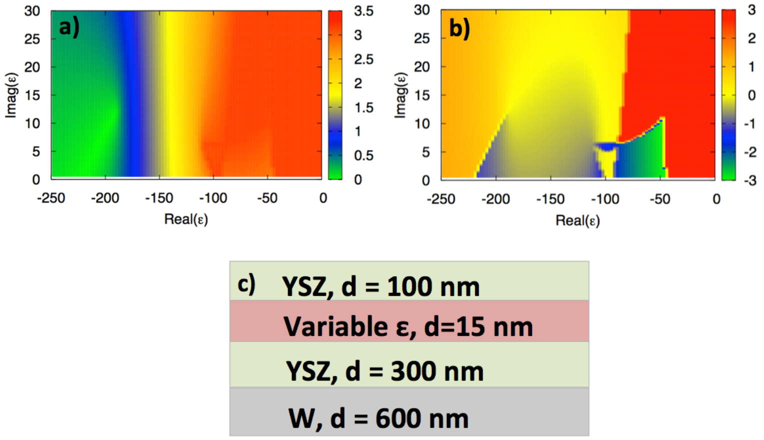

Fig. A4. Map of the β (panel **a)**) and α (panel **b)**) defining the PA modes in a hypothetical structure illustrated in panel **c)**. For this structure, we fix the geometries of all layers as illustrated. We use a permittivity value of 4.41 for layers 1 and 3 (corresponding to YSZ), and a permittivity value of -56.13 + 19.25i for layer 4 (corresponding to Tungsten at 2 μm). The modal equations are scanned for values of Re(ε) in the range of -250 to 0 and Im(ε) in the range 0.5 to 30 with k_0 fixed at 3.14μm, yielding a map of the β and α values, note that α can have both positive and negative values. This calculation reveals that in general, large negative values of Re(ε) and small values of Im(ε) give rise to PA modes in this structure with small β and α values, meaning that normally incident light can couple efficiently to these modes and that these modes have narrow resonance features.

A solar thermophotovoltaic system using nanostructures

Craig Ungaro[1], **Stephen K. Gray**[2], **and Mool C. Gupta**[1,*]

[1]*Department of Electrical & Computer Engineering, University of Virginia, Charlottesville, Virginia, 22901, USA*
[2]*Center for Nanoscale Materials, Argonne National Laboratory, 9700 South Cass Avenue, Argonne, IL, 60439, USA*
[*]*mgupta@virginia.edu*

Abstract: This paper presents results on a highly efficient experimental solar thermophotovoltaic (STPV) system using simulated solar energy. An overall power conversion efficiency of 6.2% was recorded under solar simulation. This was matched with a thermodynamic model, and the losses within the system, as well as a path forward to mitigate these losses, have been investigated. The system consists of a planar, tungsten absorbing/emitting structure with an anti-reflection layer coated laser-microtextured absorbing surface and single-layer dielectric coated emitting surface. A GaSb PV cell was used to capture the emitted radiation and convert it into electrical energy. This simple structure is both easy to fabricate and temperature stable, and contains no moving parts or heat exchange fluids.

OCIS codes: (230.0230) Optical Devices, (310.6628) Subwavelength structures, Nanostructures.

References and links

1. W. Shockley and H. J. Queisser, J. Appl. Phys **32**, 510–519 (1961).
2. D. L. Chubb, "Fundamentals of thermophotovoltaic energy conversion," Elsevier (2007).
3. M. A. Green, K. Emery, Y. Hishikawa, W. Warta, and E. D. Dunlop, "Solar cell efficiency tables (Version 45)," Progress in Photovoltaics: Research and Applications **23**, 1–9 (2014).
4. H. Yugami, H. Sai, K. Nakamura, H. Nakagawa, and H. Ohtsubo, "Solar thermophotovoltaic using $Al_2O_3/Er_3Al_5O_{12}$ eutectic composite selective emitter," IEEE Photovoltaic Specialists Conference **28**, 1214–1217 (2000).
5. A. Datas and C. Algora, "Development and experimental evaluation of a complete solar thermophotovoltaic system," Progress in Photovoltaics: Research and Applications **890**, 327–334 (2012).
6. A. S. Vlasov, V. P. Khvostikov, O. A. Khvostikova, P. Y. Gazaryan, S. V. Sorokina, and V. M. Andreev, "TPV systems with solar powered tungsten emitters," AIP Conference Proceedings **890**, 327–334 (2007).
7. A. Lenert, D. M. Bierman, Y. Nam, W. R. Chan, I. Celanovic, M. Soljacic, and E. N. Wang, "A nanophotonic solar thermophotovoltaic device," Nature Nanotechnology **9**, 126–130 (2014).
8. M. Shimizu, A. Kohiyama, and H. Yugami, "High-efficiency solar thermophotovoltaic system equipped with a monolithic planar selective absorber/emitter," Journal of Photonics for Energy **5**, 053099 (2015).
9. Y. Nam, Y. X. Yeng, A. Lenert, P. Bermel, I. Celanovic, M. Soljacic, and E. N. Wang, "Solar thermophotovoltaic energy conversion systems with two-dimensional tantalum photonic crystal absorbers and emitters," Solar Energy Materials and Solar Cells **122**, 287–296 (2014).
10. "Reference solar spectral irradiance: ASTM g-173," http://rredc.nrel.gov/solar/spectra/am1.5/ (2012). Accessed: 2015-06-10.
11. K. Ryu, J.-G. Rhee, K.-M. Park, and J. Kim, "Concept and design of modular Fresnel lenses for concentration solar PV system," Solar Energy **80**, 1580–1587 (2006).
12. L. G. Ferguson and L. M. Fraas, "Theoretical study of GaSv PV cell efficiency as a function of temperature," Solar Energy Materials and Solar Cells **39**, 11–18 (1995).

1. Introduction

Solar thermophotovoltaic (STPV) systems are energy conversion methods that are capable of overcoming the Shockley-Queisser efficiency limit of 32.1% for silicon photovoltaic (PV) cells [1]. In fact, the upper theoretical limit for the efficiency of STPV systems is 85.4% [2]. This is possible because in STPV systems the broadband solar spectrum is converted into a narrow spectrum tailored for use in a PV cell. This emission spectrum typically consists of photons with an energy just above the bandgap energy (E_{bg}) of the PV cell, resulting in greatly reduced thermalization and transmission losses in the cell.

Figures 1 a and b show two common system architectures in this field: planar and cylindrical systems. While the cylindrical architectures allow more control over the size of the emitting surface, they require large PV cell areas and are extremely difficult to achieve. Planar structures are much more simple and allow for a reduced PV cell area, making them ideal for this application. The key to realizing highly efficient STPV systems is precise control of the optical properties of the light absorbing and emitting surfaces. The absorbing surface must efficiently absorb solar energy, while simultaneously minimizing the emission of thermal energy, and the emitting surface must have high emission in a narrow band just above the E_{bg} of the PV cell used. This spectral control is typically achieved through the use of nanostructures or thin film coatings; this paper will consider a combination of both methods.

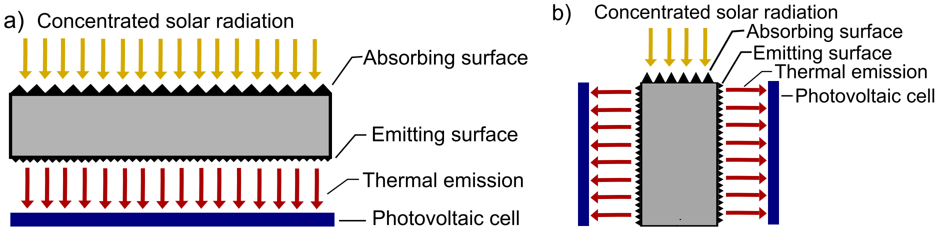

Fig. 1: Diagram of a) a flat STPV system and b) a cylindrical STPV system, both with solar absorber and thermal emitter.

The choice of PV cell in an STPV system is primarily determined by the operating temperature. The maximum efficiency for an STPV system occurs when the blackbody peak of the emitting surface is near the E_{bg} of the PV cell used [2]. This allows the PV cell to absorb a large portion of emitted thermal energy, increasing the efficiency of the system. Narrowing the emission spectrum by controlling the optical properties of the emitting surface will further increase the portion of emitted energy that is usable by the PV cell. The wavelength of peak emission of a blackbody at a certain temperature is given by Wien's displacement law. Due to these restrictions, PV cells commonly used in STPV systems include germanium (Ge), gallium antimonide (GaSb), and indium gallium arsenic antimonide (InGaAsSb) cells. Silicon (Si) cells would require an operating temperature of about 2600 K for efficient operation, making them a poor choice for most STPV systems. Ge and GaSb cells have high efficiencies at operating temperatures around 1600 K, while InGaAsSb cells operate efficiently at temperatures around 1250 K [3].

2. State of the Art

Despite the extremely high theoretical efficiency possible in STPV systems, experimental efficiencies remain low. Early STPV systems focused on cylindrical geometries, with large cavities for an absorbing surface and bulk tungsten or rare earth compounds as emitters [4, 5, 6]. Sunlight was concentrated onto these systems via Fresnel lens, raising their temperatures as high as 1680 K, and emitted radiation was collected by Ge or GaSb PV cells. These early designs all had $<1\%$ efficiency, with PV cell heating, temperature gradients along the cylinders, and a lack of efficient absorbing and emitting surfaces lowering the efficiency.

In 2014, a paper was published by A. Lenert et al. demonstrating an STPV system with 3.2% efficiency, sparking a renewed interest in the field [7]. This system used a planar geometry to simplify the architecture, reduce the required PV cell area, and remove the problem of a temperature gradient across the emitting surface. InGaAsSb PV cells with a 0.55 eV bandgap were used to allow the system to operate at lower temperatures (the 3.2% efficiency was recorded at 1,285 K), which afforded increased material stability and reduced the level of solar concentration required for operation. A multi-walled carbon nanotube blackbody absorber was used for the absorbing surface, and a Si/SiO_2 Bragg stack was used for the emitting surface. Experimental validation of this system was done using a xenon-arc light source and concentrating lens system to simulate the solar spectrum. Due to the fact that a blackbody absorber was used, spectral mismatch between solar energy and the xenon-arc light source used in the experiment would have a negligible effect on the results; however, solar concentrator systems have optical losses up to 50% that would not be present in this simulated setup. The low efficiency of this system is primarily due to the low operating temperature and low efficiency PV cells.

A recent 2015 paper by M. Shimizu et al. showed a ground-breaking experimental efficiency of 8% using a planar geometry and GaSb PV cells [8]. Due to the 0.75 eV E_{bg} of these cells, high operating temperatures were required for efficient operation, and the system was operated at a temperature of 1640 K. Both the absorbing and emitting surfaces consisted of a stack of a yttria-stabilized zirconia (YSZ) layer followed by a tungsten (W) layer, followed by an additional YSZ layer and a W substrate. This resulted in reduced thermal emission from the absorbing surface; however, the absorption band was narrow and a 20% reflection loss from the absorbing surface was reported. Again, a solar simulator was used to illuminate the setup, and potential solar concentrator losses were not taken into account.

Despite the large advances in STPV systems, further research is needed to improve system efficiencies to make them competitive with traditional PV systems. This article aims, through modeling and experimental studies, to examine the losses in an experimental system in detail to provide a path forward to a more efficient STPV system.

3. System Design Considerations and Simulation

The STPV system presented here consists of a solar concentration system, a vacuum chamber to reduce convective losses and ensure material stability, a tungsten absorbing/emitting structure with a laser-textured blackbody absorbing surface and dielectric-coated emitting surface, and a GaSb PV cell with a water-based cooling system. Tungsten is used as a substrate due to its high thermal stability and good intrinsic reflectance properties for this application [5].

For efficient operation, the absorbing and emitting surfaces of an STPV system must meet the following requirements: a) sunlight must be efficiently absorbed by the absorbing surface, b) the emission of thermal radiation by the absorbing surface must be minimized, c) a large amount of power must be emitted by the emitting surface, and d) the emitting surface must emit primarily in a narrow band just above the E_{bg} of the PV cell.

To maximize the solar absorption (α) of the absorbing surface, a laser-textured blackbody with an anti-reflective dielectric coating was used. Since blackbodies have high thermal emission as well as high solar absorption, the surface area of the absorbing portion of the top surface must be minimized to lower emission loss. In a planar STPV system, the surface area of the top and bottom surfaces must be equal; however, laser texturing allows only a small portion of the top surface to be textured. This small textured area, combined with the naturally low thermal emittance of tungsten in untextured areas, resulted in a low overall thermal emittance for the top surface of the STPV system while maintaining a very high solar α. Additionally, an IR reflecting mirror may be placed over the untextured portions of the top surface to further reduce thermal loss.

The emitting surface consisted of a single dielectric layer on the tungsten substrate of a thickness to minimize reflectance around a wavelength of 1400 nm. This simple structure maintains the high efficiency of more complex structures while being easy to fabricate and having a high thermal stability. Emission is spectrally matched via controlling the thickness of the dielectric layer on the tungsten. GaSb PV cells are used in this design due to their having high efficiency compared to cells with similar bandgaps, and the fact that their E_{bg} corresponds well with STPV system temperatures.

The STPV device was modeled as a thermodynamic system that can be broken down into a series of components with individual efficiencies that are multiplied together to obtain an overall efficiency [9]. While each loss is affected by the system temperature, losses can still be separated and examined as individual functions of temperature, not directly related to other losses. Incoming solar energy is simulated with an air-mass 1.5 (AM 1.5) solar spectrum with no diffuse energy component since it is not captured by solar concentrators [10].

The temperature of the STPV system rises until thermal equilibrium is reached, with the assumption that temperature is constant at every point on the absorbing/emitting structure. This is accurate for the thin planar systems examined here but may be less accurate for other system designs. Energy leaves this structure via heat conducted through the mechanical supports, convection, thermal energy radiated out of the top and sides, and thermal energy emitted from the emitter. The overall efficiency of the STPV system is given by the efficiency of the PV cell output compared to the input optical power into the system.

4. Experimental

Polished W substrates with dimensions 25x25x1 mm were purchased from the MTI Corporation and cleaned with acetone and then methanol. On one substrate, the top surface, a 0.6 cm^2 area was laser-textured to reduce reflectance, while on another substrate the entire top surface was microtextured. A nanosecond 1064 nm laser (IPG Photonics, GLP-10) operating with a pulse width of 50 ns, focused to a spot with an average power of 24 W and 30 kHz frequency was scanned across a 6.5 cm^2 tungsten substrate at a rate of 50 mm/s by means of a Galvo.

The top and bottom surfaces were then coated by a 160 nm thick Si_3N_4 protective layer. This layer was deposited by plasma-enhanced chemical vapor deposition (PECVD) at a temperature of 100°C. The diffuse reflectance of the laser-microtextured absorbing surface was measured using lasers with 405 nm, 532 nm, 633 nm, 790 nm, 980 nm, and 1064 nm wavelengths and a Labsphere RTC-060-SF integrating sphere with a Spectraflect barium sulfate reflecting surface. The reflection of the Si_3N_4 coated flat tungsten substrate was measured by a PerkinElmer Lambda 950 UV/VIS spectrometer.

Four GaSb PV cells were purchased from JX Crystals, with an active area of 1.48 cm^2 each. These cells have an E_{bg} of 0.67 eV, fill factor (FF) of 0.61, and an external quantum efficiency (EQE) of 0.72 at a wavelength of 1500 nm. The cells were soldered to copper substrates via reflow soldering and connected together in series. To simulate solar radiation under laboratory conditions, a 300 W continuous wave, 808 nm laser diode stack was purchased from Sino-Laser, inc. Although this laser emits radiation at a single wavelength, the absorbing surface used in this case is a blackbody across the visible and near IR spectra, making the wavelength of radiation irrelevant. The laser was focused onto the 0.6 cm^2 textured area on the absorbing surface, and the relative solar concentration was calculated assuming an incident solar power of $0.1\frac{W}{cm^2}$ and a concentration factor ranging from 1 to 2500. 2500 was chosen as the upper concentration limit due to its being achievable with Fresnel lens systems, and to avoid unrealistic solar tracking requirements [11].

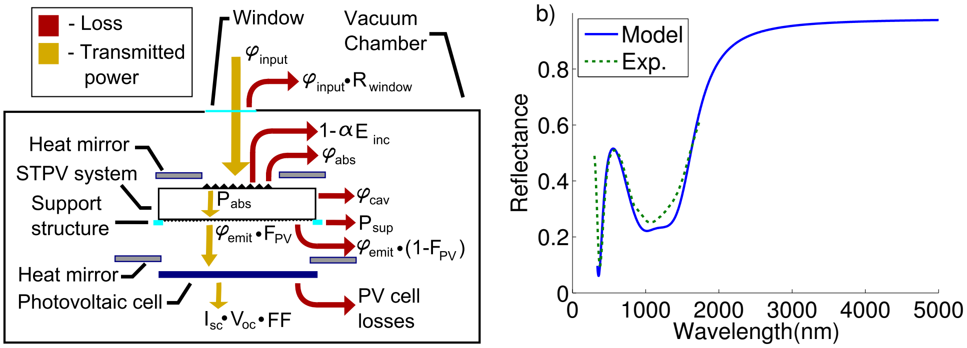

Fig. 2: a) The flow of power through an STPV system, showing each component and the power remaining after each loss. Total efficiency (η_{total}) is given by $I_{sc} \times V_{oc} \times FF$ divided by the input power, ϕ_{input}. Losses are quantified and described in Table 1. b) measured and simulated reflectance of an emitting surface made of a 160 nm thick Si_3N_4 coating on a W substrate.

The PV cells were placed inside a vacuum chamber on a water-cooled copper heat sink, with Arctic Silver 5 thermal compound used to reduce thermal resistance between the substrate and heat sink and prevent air pockets from forming. A thin aluminum cover plate was then placed over the heat sink and PV cell, with a hole cut out to allow radiation to reach the cell. This prevented excess radiation from the emitting surface from reaching the heat sink and PV cell frame. A glass slide was placed over this window to prevent convective heating of the PV cells by the substrate and to reduce the amount of long wavelength infrared (IR) radiation that reached the cell. Next, the W substrate was suspended above the cover plate on two 0.5 mm diameter fused silica rods. Thin fused silica rods were used due to their high melting point, low thermal conductivity, and optical clarity. Lastly, a reflective plate was positioned over the absorbing surface of the substrate with a small hole cut out of it over the textured portion of the absorbing surface to reflect back thermal radiation from the untextured portion of the top surface. This assembly was kept under a vacuum of 10 mTorr during the experiment. Figure 2a shows a diagram of this system and the flow of power through it.

Temperature measurements were taken with a type R thermocouple purchased from Nordic Sensors, inc. This thermocouple was bonded to the surface with a high-temperature thermally-conductive cement purchased from Sigma-Aldrich. Temperature measurements were reliably taken at temperatures up to 1200°C. The open circuit voltage (V_{oc}) and short circuit current (I_{sc}) of the PV cells were recorded with a multimeter.

5. Results and Conclusions

The α of the microtextured and coated portion of the absorbing surface was found to be 92%. The emittance of the emitting surface was measured and simulated via the Fresnel method, and can be seen in Figure 2a. This surface shows good spectral selectivity with increased emittance at photon energies just higher than the E_{bg} of the PV cell. The temperature and efficiency of the STPV system were recorded at various laser power levels. These measurements were then compared to simulated temperature and efficiency values. Figure 2b shows the flow of power through this system Good matching between simulated and experimental results was found, showing that the basic premise of the simulation is sound. The measured and simulated temperature and efficiency of the system under these conditions is shown in Figures 3 a and b. The temperature of the PV cell reached a maximum of 72°C during the experiment. A maximum efficiency of 6.2% was measured at a laser power of 149 W, corresponding to a solar concentration factor of 2483, and simulations show that this efficiency would rise to 7.5% if the PV

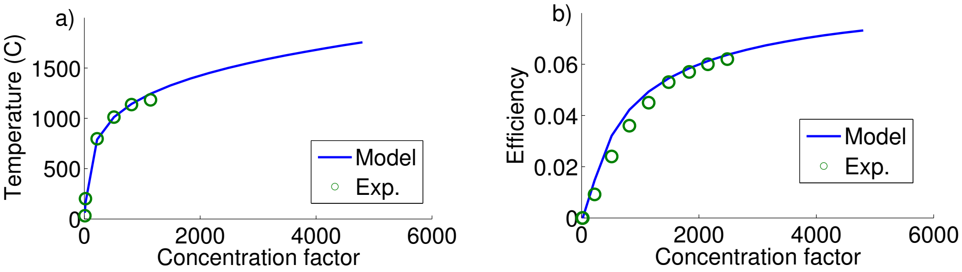

Fig. 3: Comparison of simulated and experimental values for a) system temperature and b) system efficiency with concentration factor.

cell was kept at room temperature during this measurement [12].

Table 1 shows the breakdown of how much energy is lost to each factor shown in Figure 2b. This shows that the quality of the absorbing and emitting surfaces are paramount to the operation of an efficient STPV system. It also shows that PV cell losses play a large role, and that the use of more advanced GaSb PV cells could greatly improve STPV system efficiency. Additionally, the use of a hot mirror with a 1.7 μm cutoff wavelength between the emitting surface and PV cell could both improve system efficiency by returning longer wavelength radiation to the emitting surface and help to keep the PV cell cooler, which in turn would increase the PV cell efficiency. In conclusion, this paper demonstrates a simple way to fabricate STPV system utilizing nanostructures that operates at high efficiencies. The system is studied under simulated solar conditions, and an experimental efficiency of 6.2% was recorded. This is the highest efficiency recorded for an STPV system using nanostructures, and this can be further improved. For example, our theoretical modeling results match the experimental results well and the losses in the system could be analyzed through this model. A path forward for increased STPV system efficiency is found by analyzing the simulated losses as well.

Table 1: List of losses in the simulated STPV system using a tungsten substrate at a concentration ratio of 2500 (losses shown in Figure 2b, where F_{PV} is the view-factor between the emitting surface and PV cell, and E_{inc} is the optical energy available to the absorbing surface.

Loss type	Designation in figure	Percent of input power
Reflection off of absorbing surface	$1-\alpha E_{inc}$	8.0%
Emittance from absorbing surface	ϕ_{abs}	26.4%
Emittance from sides of structure	ϕ_{cav}	1.1%
Thermal conductivity through supports	P_{sup}	0.17%
Convective losses	P_{conv}	3.5%
Radiation from emitter that doesn't reach PV cell	$\phi_{emit} \times (1-F_{PV})$	10.2%
Thermal emission below E_{bg}	PV cell loss	14.2%
Thermalization loss in PV cell	PV cell loss	7.8%
Loss due to PV cell efficiency	FF & EQE	19.9%
Power conversion efficiency	η_{total}	6.37%

Acknowledgments

We would like to thank the NASA Langley Professor and NSF IUCRC programs for their support of this project. This work was performed, in part, at the Center for Nanoscale Materials, a U.S. Department of Energy, Office of Science, Office of Basic Energy Sciences User Facility under Contract No. DE-AC02-06CH11357.

Optical Nanostructures Design, Fabrication, and Applications for Solar/Thermal Energy Conversion

Mool C. Gupta[1,*], **Craig Ungaro**[1], **Jonathan J. Foley IV**[2], **Stephen K. Gray**[2,†]

[2] *Department of Electrical & Computer Engineering, University of Virginia, Charlottesville, Virginia, 22901, USA*
[2] *Center for Nanoscale Materials, Argonne National Laboratory, 9700 South Cass Avenue, Argonne, IL, 60439, USA*
[*] *mgupta@virginia.edu,* [†] *skgray@anl.gov*

Abstract: Optical nanostructures can control the optical absorption and emission properties of surfaces and are therefore being investigated for solar thermophotovoltaics, thermophotovoltaics, solar thermal, infrared sensing, infrared sources, incandescent light sources, and thermal imaging applications, among many others. This review article describes various modeling methods available for design of optical nanostructures to control light absorption and emission properties of surfaces, as well as various methods available for the fabrication of large area nanostructured surfaces. Throughout the review, we provide examples of state of the art energy generation devices using such optical nanostructures. A discussion of outstanding obstacles for the achievement of high efficiency solar thermophotovoltaics systems is provided along with examples of systems showing exceptional promise.

OCIS codes: 220.0220, 230.0230, 240.0240, 240.0310, 350.6050, 310.6628

References and links

1. M. Thirugnanasambandam, S. Iniyan, and R. Goic, "A review of solar thermal technologies," Renewable and Sustainable Energy Reviews **14**, 312–322 (2010).
2. Y. Tian and C. Y. Zhao, "A review of solar collectors and thermal energy storage in solar thermal applications," Applied Energy **104**, 538–553 (2013).
3. T. Bauer, *Thermophotovoltaics: basic principles and critical aspects of system design* (2011).
4. P. Bermel, M. Ghebrebrhan, W. Chan, Y. X. Yeng, M. Araghchini, R. Hamam, C. H. Marton, K. F. Jensen, M. Soljacic, J. D. Joannopoulos, S. G. Johnson, and I. Celanovic, "Design and global optimization of high-efficiency thermophotovoltaic systems," Optics Express **18**, A314–334 (2010).
5. N. Harder and P. Wurfel, "Theoretical limits of thermophotovoltaic solar energy conversion," Semiconductor Science and Technology **18**, S151 (2003).
6. C. Ferrari, F. Melino, M. Pinelli, P. R. Spina, and M. Venturini, "Overview and status of thermophotovoltaic systems," Energy Procedia **45**, 1160–1169 (2014).
7. I. Celanovic, P. Bermel, and Marin, "Thermophotovoltaic power conversion systems: current performance and future potential," http://rredc.nrel.gov/solar/spectra/am1.5/ASTMG173/ASTMG173.html.
8. T. Inoue, M. Zoysa, T. Asano, and S. Noda, "Realization of narrowband thermal emission with optical nanostructures," Optica **2**, 27 (2015).
9. A. Lenert, D. M. Bierman, Y. Nam, W. R. Chan, I. Celanovic, M. Soljacic, and E. N. Wang, "A nanophotonic solar thermophotovoltaic device," Nature Nanotechnology **9**, 126–130 (2014).
10. E. Rephaeli and S. Fan, "Absorber and emitter for solar thermophotovoltaic systems to achieve efficiency exceeding the schockley-queisser limit," Opt. Express **17**, 15145–15159 (2009).

11. V. Rinnerbauer, A. Lenert, D. M. Bierman, Y. X. Yeng, W. R. Chan, R. D. Geil, J. J. Senkevich J. D. Joannopoulos, E. N. Wang, M. Soljacic, and I. Cleanovic, "Metallic photonic crystal absorber-emitter for efficient spectral control in high-temperature solar thermophotovoltaics," Advanced Energy Materials **4**, 1400334 (2014).
12. Y. Nam, Y. X. Yeng, A. Lenert, P. Bermel, I. Celanovic, M. Soljačić, and E. N. Wang, "Solar thermophotovoltaic energy conversion systems with two-dimensional tantalum photonic crystal absorbers and emitters," Sol. Energy Mat. Sol. C. **122**, 287 – 296 (2014).
13. V. Stelmakh, V. Rinnerbauer, W. R. Chan, J. J. Senkevich, J. D. Joannopoulos, M. Soljacic, and I. Celanovic, "Tantalum-tungsten alloy photonic crystals for high-temperature energy conversion systems," Proceedings of the SPIE - The International Society for Optical Engineering **9127**, 91270Q (2014).
14. I. Celanovic, N. Jovanovic, and J. Kassakian, "Two-dimensional tungsten photonic crystals as selective thermal emitters," Applied Physics Letters **92**, 193101 (2008).
15. H. Wang, V. P. Sivan, A. Mitchell, G. Rosengarten, P. Phelan, and L. Wan, "Highly efficient selective metamaterial absorber for high-temperature solar thermal energy harvesting," Solar Energy Materials and Solar Cells **137**, 235–242 (2015).
16. X. Liu, T. Tyler, T. Starr, A. Starr, N. Jokerst, and W. Padilla, "Taming the blackbody with infrared metamaterials as selective thermal emitters," Physical Review Letters **107**, 045901 (2011).
17. I. Khodasevvch, L. Wang, A. Mitchell, and G. Rosengarten, "Micro and nanostructured surfaces for selective solar absorption," Advanced Optical Materials **107**, 045901 (2015). doi: 10.1002/adom.201500063.
18. Y. Son, J. Yeo, C. Woo, H. Sukjoon, H. Seung, H. Ko, and D. Yang, "Fabrication of submicron-sized metal patterns on a flexible polymer substrate by femtosecond laser sintering of metal nanoparticles," International Journal of Nanomanufacturing **9**, 468–476 (2013).
19. E. P. B. Filho, O. S. H. Mendoza, C. L. L. Beicker, A. Menezes, and D. Wen, "Experimental investigation of a silver nanoparticle-based direct absorption solar thermal system," Energy Conversion and Management **84**, 261–267 (2014).
20. G. Katumba, L. Olumekor, A. Forbes, G. Makiwa, B. Mwakikunga, J. Lu, and E. Wackelgard, "Optical, thermal and structural characteristics of carbon nanoparticles embedded in zno and nio as selective solar absorbers," Solar Energy Materials and Solar Cells **92**, 1285–1292 (2008).
21. A. A. Shah and M. C. Gupta, "Spectral selective surfaces for concentrated solar power receivers by laser sintering of tungsten micro and nano particles," Solar Energy Materials and Solar Cells **117**, 489–493 (2013).
22. J. H. Schon, G. Binder, and E. Bucher, "Performance and stability of some new high-temperature selective absorber systems based on metal/dielectric multilayers," Solar Energy Materials and Solar Cells **33**, 403–416 (1994).
23. V. K. Narasimhan and Y. Cui, "Nanostructures for photon management in solar cells," Nanophotonics (2013). DOI 10.1515/nanoph-2013-0001.
24. M. C. Gupta, B. K. Nayak, V. Iyengar, and L.Wang, "Efficient light trapping by laser microtexturing of surfaces for photovoltaics," SPIE Newsroom (2012). DOI: 10.1117/2.1201208.004361.
25. M. C. Gupta and D. E. Carlson, "Laser processing for renewable energy materials," MRS Energy and Sustainability: A Review Journal (2015). DOI:10.1557/mre.2015.3.
26. V. V. Iyengar, B. K. Nayak, and M. C. Gupta, "Ultralow reflectance metal surfaces by ultrafast laser texturing," Applied Optics **49**, 5983–5988 (2010).
27. S. K. Gray, "Theory and modeling of plasmonic structures," J. Phys. Chem. C **117**, 1983–1994 (2013).
28. A. Taflove and S. C. Hagness, *Computational Electrodynamics: the finite-difference time-domain method* (Artech, 2000).
29. A. F. Oskooi, D. Roundy, M. Ibanescu, P. Bermel, J. D. Joannopoulos, and S. G. Johnson, "Meep: A flexible free-software package for electromagnetic simulations by the fdtd method," Comp. Phys. Comm. **181**, 687702 (2010).
30. C. F. Bohren and D. R. Huffman, *Absorption and Scattering of Light by Small Particles* (John Wiley and Sons, 1998).
31. P. Yeh, *Optical waves in layered media* (Wiley, 2005).
32. B. T. Draine and P. J. Flatau, "Discrete-dipole approximation for scattering calculations," J. Opt. Soc. Am. A **11**, 1491–1499 (1994).
33. J. M. McMahon, "Topics in theoretical and computational nanoscience: From controlling light at the nanoscale to calculating quantum effects with classical electrodynamics," Ph.D. thesis, Northwestern University (2011).
34. E. Rephaeli and S. Fan, "Tungsten black absorber for solar light with wide angular operation range," Applied Physics Letters **92**, 211107 (2008).
35. P. Bermel, M. Ghebrebrhan, W. Chan, Y. X. Yeng, M. Araghchini, R. Hamam, C. H. Marton, K. F. Jensen, M. Soljacic, J. D. Joannopoulos, S. G. Johnson, and I. Celanovic, "Design and global optimization of high-efficiency thermophotovoltaic systems," Opt. Express **18**, A314–A334 (2010).
36. J. R. Cole and N. J. Halas, "Optimized plasmonic nanoparticle distributions for solar spectrum harvesting," Appl. Phys. Lett. **89**, 153120 (2006).
37. S. M. Maier, *Plasmonics: Fundamentals and applications* (Springer, 2007).
38. H. A. Atwater and A. Polman, "Plasmonics for improved photovoltaic devices," Nature Mater. **9**, 205–213 (2010).

39. J. M. Geffrin, B. García-Cámara, R. Góomez-Medina, P. Albella, L. S. Froufe-Pérez, C. Eyraud, A. Litman, R. Vaillon, F. González, M. Nieto-Vesperinas, J. J. Sáenz, and F. Moreno, “Magnetic and electric coherence in forward- and back-scattered electromagnetic waves by a single dielectric subwavelength sphere,” Nat. Commun. **3**, 1171 (2012).
40. L. Wendler and R. Haupt, “An improved virtual mode theory of atr experiments of surface polaritons,” Phys. Stat. Sol. b **143**, 131–147 (1987).
41. L. Novotny and B. Hecht, *Principles of nano-optics* (Cambridge University Press, 2012), 2nd ed.
42. J. J. Foley IV, H. Harutyunyan, D. Rosenmann, R. Divan, G. P. Wiederrecht, and S. K. Gray, “When are surface plasmon polaritons excited in the kretschmann-raether configuration?” Sci. Rep. **5**, 09929 (2015).
43. E. F. C. Driessen and M. J. A. de Dood, “The perfect absorber,” Appl. Phys. Lett. **94**, 171109 (2009).
44. M. A. Kats, D. Sharma, J. Lin, P. Genevet, R. Blanchard, Z. Yang, M. M. Qazilbash, D. N. Basov, S. Ramanathan, and F. Capasso, “Ultra-thin perfect absorber employing a tunable phase change material,” App. Phys. Lett. **101**, 221101 (2012).
45. M. A. Kats, R. Blachard, P. Genevet, and F. Capasso, “Nanometre optical coatings based on strong interference effects in highly absorbing media,” Nat. Mat. **12**, 20–24 (2013).
46. M. Shimizu, A. Kohiyama, and H. Yugami, “High-efficiency solar thermophotovoltaic system equipped with a monolithic planar selective absorber/emitter,” Journal of Photonics for Energy **5**, 053099 (2015).
47. J. J. Foley IV, C. Ungaro, K. Sun, M. C. Gupta, and S. K. Gray, “Design of emitter structures based on resonant perfect absorption for thermophotovoltaic applications,” Opt. Exp. **Submitted** (2015).
48. K. Aydin, V. E. Ferry, R. M. Briggs, and H. A. Atwater, “Broadband polarization-independent resonant light absorption using ultrathin plasmonic super absorbers,” Nature Comm. **2**, 517 (2011).
49. C. Ungaro, S. K. Gray, and M. C. Gupta, “Black tungsten for solar power generation,” Applied Physics Letters **103**, 071105–071105–3 (2013).
50. C. Ungaro, S. K. Gray, and M. C. Gupta, “Graded-index structures for high-efficiency solar thermophotovoltaic emitting surfaces,” Optics Letters **39**, 5259–5262 (2014).
51. M. A. Yurkin, M. Min, and A. G. Hoekstra, “Applicaton of the discrete dipole approximation to very large refractive indices: Filtered doupled dipoles revived,” Phys. Rev. E **82**, 036703 (2010).
52. V. V. Iyengar, B. K. Nayak, and M. C. Gupta, “Optical characteristics of femtosecond laser micromachined periodic structures in Si 100,” Applied Optics **45**, 7137–7143 (2006).
53. M. C. Gupta and S. T. Peng, “Diffraction characteristics of surface-relief gratings,” Applied Optics **32**, 2911–2917 (1993).
54. C. Ungaro, A. Shah, I. Kravchenko, D. K. Hensley, S. K. Gray, and M. C. Gupta, “Optical and infrared properties of glancing angle deposited nanostructured tungsten films,” Optics Letters **40**, 506–509 (2015).
55. N. Selvakumar and H. Barshilia, “Review of physical vapor deposited (pvd) spectrally selective coatings for mid- and high-temperature solar thermal applications,” Solar Energy Materials and Solar Cells **98**, 1–23 (2012).
56. C. E. Kennedy, “Review of mid-to-high temperature solar selective absorber materials. Technical report NREL/TP-520-31267,” p. 58 (2002).
57. X. Li, Y. Chen, J. Miao, P. Zhou, Y. Zheng, and L. Chen, “High solar absorption of a multilayered thin film structure,” Optics Express **15**, 1907–1912 (2007).
58. N. P. Sergeant, O. Pincon, M. Agrawal, and P. Peumans, “Design of wide-angle solar-selective absorbers using aperiodic metal-dielectric stacks,” Optics Express **17**, 22800–22812 (2009).
59. N. P. Sergeant, M. Agrawal, and P. Peumans, “High performance solar-selective absorbers using coated sub-wavelength gratings,” Optics Express **18**, 5525–5540 (2010).
60. S. Esposito, A. Antonaia, M. Addonizio, and S. Aprea, “Fabrication and optimization of highly efficient cermet-based spectrally selective coatings for high operating temperature,” Thin Solid Films **517**, 6000–6006 (2009).
61. L. T. A. Berghaus, A. Djahanbakhsh, “Characterisation of cvd-tungstenalumina cermets for high-temperature selective absorbers,” Solar Energy Materials and Solar Cells **54**, 19–26 (1998).
62. M. Farooq and M. Hutchins, “Optical properties of higher and lower refractive index composites in solar selective coatings,” Solar Energy Materials and Solar Cells **71**, 73–83 (2002).
63. D. Xinkang, W. Cong, W. Tianmin, Z. Long, C. Buliang, and R. Ning, “Microstructure and spectral selectivity of Mo-Al_2O_3 solar selective absorbing coatings after annealing,” Thin Solid Films **516**, 3971–3977 (2008).
64. Q. Zhang, Y. Yin, and D. Mills, “High efficiency Mo-Al_2O_3 cermet selective surfaces for high-temperature applications,” Solar Energy Materials and Solar Cells **40**, 43–53 (1996).
65. Q. Zhang, “Recent progress in high-temperature solar selective coatings,” Solar Energy Materials and Solar Cells **62**, 63–74 (2000).
66. R. Schmidt and K. Park, “High-temperature space-stable selective solar absorber coatings,” Applied Optics **4**, 917–925 (1965).
67. K. A. Arpin, M. D. Losego, and P. V. Braun, “Electrodeposited 3D tungsten photonic crystals with enhanced thermal stability,” Chemistry of Materials **23**, 4783–4788 (2011).
68. C. Schlemmer, J. Aschaber, V. Boerner, and J. Luther, “Thermal stability of micro-structured selective tungsten emitters,” Thermophotovoltaic Generation of Electricity: 5th Conference, CP653 - American Institute of Physics (2003).

69. V. Rinnerbauer, S. Ndao, Y. X. Yeng, W. R. Chan, J. J. Senkevich, J. D. Joannopoulos, M. Soljacic, and I. Celanovic, "Recent developments in high-temperature photonic crystals for energy conversion," Energy and Environmental Science (2012).
70. H. Saia, H. Yugamia, Y. Kanamorib, and K. Hane, "Solar selective absorbers based on two-dimensional w surface gratings with submicron periods for high-temperature photothermal conversion," Solar Energy Materials and Solar Cells **79**, 35–49 (2003).
71. F. Ghmari, T. Ghbara, M. Laroche, R. Carminati, and J.-J. Greffet, "Influence of microroughness on emissivity," Journal of Applied Physics **96**, 2656–2664 (2004).
72. A. Lasagni, M. Nejati, R. Clasen, and F. Mucklich, "Periodical surface structuring of metals by laser interference metallurgy as a new fabrication method of textured solar selective absorbers," Advanced Engineering Materials **8**, 580–584 (2006).
73. A. Datas and C. Algora, "Global optimization of solar thermophotovoltaic systems," Progress in Photovoltaics: Research and Applications **21**, 1040–1055 (2013).
74. M. Saidi and R. H. Abardeh, "Air pressure dependence of natural-convection heat transfer," Proceedings of the World Congress on Engineering 2010 **II** (2010).
75. W. Shockley and H. J. Queisser, J. Appl. Phys **32**, 510–519 (1961).
76. J. Wang, B. Wei, Q. Wei, and D. Li, "Optical property and thermal stability of Mo/Mo-SiO_2/SiO_2 solar-selective coating prepared by magnetron sputtering," Physica Status Solidi A **208**, 664–667 (2011).
77. A. Lenert, D. M. Bierman, Y. Nam, W. R. Chan, I. Celanovic, M. Soljacic, and E. N. Wang, "A nanophotonic solar thermophotovoltaic device," Nature Nanotechnology **9**, 126–130 (2014).
78. A. S. Vlasov, V. P. Khvostikov, O. A. Khvostikova, P. Y. Gazaryan, S. V. Sorokina, and V. M. Andreev, "TPV systems with solar powered tungsten emitters," AIP Conference Proceedings **890**, 327–334 (2007).
79. H. Sai and H. Yugami, "Thermophotovoltaic generation with selective radiators based on tungsten surface gratings," Applied Physics Letters **85**, 3399–3401 (2004).
80. E. D. Palik, *Handbook of optical constants of solids* (Academic Press, 1998).
81. H. Yugami, H. Sai, K. Nakamura, H. Nakagawa, and H. Ohtsubo, "Solar thermophotovoltaic using $Al_2O_3/Er_3Al_5O_{12}$ eutectic composite selective emitter," IEEE Photovoltaic Specialists Conference **28**, 1214–1217 (2000).
82. A. Datas and C. Algora, "Development and experimental evaluation of a complete solar thermophotovoltaic system," Progress in Photovoltaics: Research and Applications **890**, 327–334 (2012).
83. C. Ungaro, "Control of optical properties of surfaces for improved solar thermophotovoltaic systems," Phd thesis, University of Virginia (2015).
84. Y. B. Chen and Z. M. Zhang, "Design of tungsten complex gratings for thermophotovoltaic radiators," Optics Communication **269**, 411–417 (2007).
85. Y. Xuan, X. Chen, and Y. Han, "Design and analysis of thermophotovoltaic systems," Renewable Energy **36**, 374–387 (2011).
86. H. Sai, Y. Kanamori, K. Hane, H. Yugami, and M. Yamaguchi, "Numerical study on tungsten selective radiators with various micro/nano structures," Photovoltaic Specialists Conference pp. 762–765 (2005).
87. S. Lin, J. Moreno, and J. G. Fleming, "Three-dimensional photonic-crystal emitter for thermal photovoltaic power generation," Applied Physics Letters **83**, 380–382 (2003).
88. C. Wu, B. N. III, J. John, A. Milder, B. Zollars, S. Savoy, and G. Shvets, "Metamaterial-based integrated plasmonic absorber/emitter for solar thermo-photovoltaic systems," Journal of Optics **14**, 24005–24008 (2012).
89. C. Ungaro, S. K. Gray, and M. C. Gupta, "A solar thermophotovoltaic system using nanostructures," Opt. Exp. **Submitted** (2015).
90. Y. Tian and C. Y. Zhao, "A review of solar collectors and thermal energy storage in solar thermal applications," Applied Energy **104**, 538–553 (2013).

---

1. Introduction

Many energy generation devices such as solar thermal (ST) [1, 2], solar thermophotovoltaic (STPV) [3, 4, 5] and thermophotovoltaic (TPV) [6, 7] systems require control of light absorption and emission from surfaces to achieve high efficiency. This spectral light control can be achieved by nanostructuring of surfaces, which can strongly modify their optical properties [8, 9, 10]. Recently, significant progress has been made in the modeling and fabrication of nanostructures to control optical absorption and emission properties of surfaces. A highly reflective surface can be made highly absorptive through the design and fabrication of nanostructures. Similarly, surfaces can be made to emit infrared radiation in a very narrow spectral range, providing spectrally selective surfaces. Figure 1 shows the change in emission spectra from a blackbody emitter to a selective emitter using optical nanostructures.

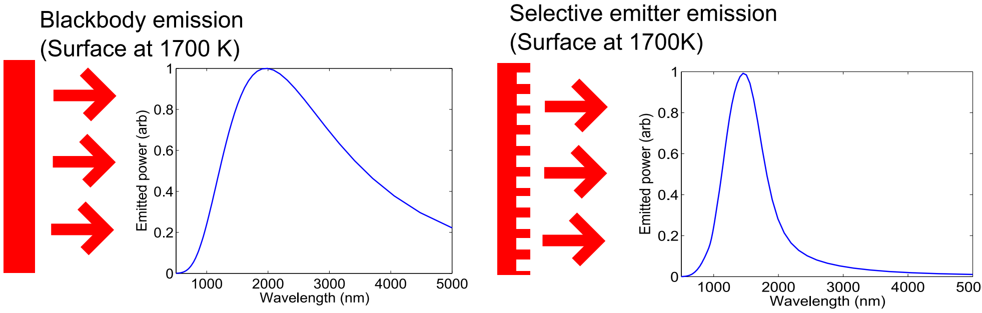

Fig. 1: Spectral emission of a blackbody vs a selective emitter.

Such control of light absorption and emission properties allows the design of high efficiency solar and thermal energy conversion devices. It also has applications in the development of high efficiency infrared sources, sensors, and incandescent light sources. Various approaches have been demonstrated for controlling light absorption and emission from surfaces such as the use of photonic crystals [11, 12, 13, 14], optical metamaterials [15, 16, 17], nanoparticles [18, 19, 20, 21], multilayer thin films [22, 10] and micro/nano textured structures [23, 24, 25, 26]. This review article describes various modeling methods available for design of optical nanostructures to control light absorption and emission properties of surfaces, the various methods available for the fabrication of large area nanostructured surfaces, and provides some examples of high-efficiency, state of the art, energy generation devices using such optical nanostructures. A path forward to more efficient solar and thermal energy generation devices using practical design methods and fabrication techniques is examined.

Fig. 2: Types of nanostructured absorbing and emitting surfaces: a) random nanotexture b) periodic nanotexture and c) dielectric/metal stack.

There are many examples in the literature of nanostructures being applied to make high efficiency systems. Wang *et al.* [15] have demonstrated a highly efficient selective metamaterial absorber for high-temperature solar thermal energy harvesting. Using nanostructured titanium gratings on an MgF_2 spacer deposited on W thin films was demonstrated with UV-near IR absorption of 0.9 and mid-IR emittance of 0.2. A solar to heat conversion efficiency of 80% at 400°C structure was modeled and fabricated to achieve high solar light absorption efficiency over broad spectral wavelength range and emission surfaces emitting in a narrow band of wavelengths.

Spectrally selective surfaces have also been achieved by coating nanoparticles on a substrate and modifying surface morphology. Shah *et al.* [21] investigated spectrally selective surfaces for concentrated solar power receivers by laser sintering of tungsten micro and nanoparticles. A solar absorptance of 83% and thermal emittance of 11.6% at room temperature was reported. The tungsten nanoparticles were laser sintered on stainless steel substrate. Multi-layer thin films of metal-dielectric coatings have also been shown to provide high broad wavelength solar absorption and low thermal emittance [22].

The use of theory and modeling has been critical to the design of these types of record-breaking structures, and will no doubt be critical moving forward as the community continues to push the limits of conversion efficiency, durability, aforadbility, etc. In the following section, we will try to illustrate how theoretical electrodynamics techniques can be brought to bear to design these types of structures, as well as what challenges exist.

2. Design Methodologies

2.1. Overview of the theoretical foundations of the optical properties of nanostructures

Understanding how a nanostructured surface or particle absorbs, scatters, and/or reflects incident light provides critical information enabling the design of systems for solar energy conversion. Calculating these quantities depends upon the ability to solve Maxwell's equations when light is incident upon nanostructures [27]. A wide variety of theoretical methodologies exist for solving Maxwell's equations either in the time-domain (see for example Refs. [28, 29]), or in the frequency domain (see for example Refs. [30, 31, 32, 33]). Time-dependent approaches to solving Maxwell's equations typically start from the first-order time-dependant electric and magnetic field equations, whereas frequency domain methods usually take the second-order frequency-dependant wave equation, supplemented by appropriate boundary condisions, as their starting point.

In a few cases, Maxwell's equations can be solved analytically; indeed, under some often reasonable approximations, the analytical solutions can even be written simply, which greatly aids intuition about the behavior of a nanostructure. Two important analytical examples we will consider include the interaction of light with spherical nanostructures, solvable by Mie theory, and the interaction of light with planar nanostructures, solvable by the Transfer Matrix method. For more general structures, numerical techniques must be employed, and several approaches have been put to considerable use. Here we will discuss the finite-difference time-domain (FDTD) method and the discrete dipole approximation (DDA); the former solves Maxwell's equations in the time-domain, while the latter solves them in the frequency-domain. (The finite element method, or FEM, is a more generally applicable frequency-domain approach for electrodynamics problems [33]. The vectorial nature of Maxwell's equations make implementations of FEM significantly more sophisticated than DDA.) We will also give several examples of applications of nanostructures for solar energy conversion, focusing on which of the above methodologies are most appropriate, and how they would be utilized for designing these nanostructures.

2.2. Mie theory for spherical nanostructures

Mie theory provides an analytical solution for Maxwell's equations when light is incident upon a spherical particle. A key idea behind Mie theory is to write the field components, including the scattered and internal (inside the particle) components, as an expansion in a spherical multipole basis, allowing Eq. (3) to be replaced with a scalar wave equation [30, 37]. Using Maxwell's equations as conditions on the fields in this expansion leads to closed-form expressions for the expansion coefficients. Quantities like the absorption, scattering, and extinction cross section of the particle can be easily computed in terms of these coefficients [30],

$$C_{scat} = \frac{2\pi}{k^2} \sum_{n=1}^{\infty} (2n+1) \left(|a_n|^2 + |b_n|^2\right) \tag{1}$$

$$C_{ext} = \frac{2\pi}{k^2} \sum_{n=1}^{\infty} (2n+1) \, \mathrm{Re}\left(a_n + b_n\right) \tag{2}$$

$$C_{abs} = C_{ext} - C_{scat}, \tag{3}$$

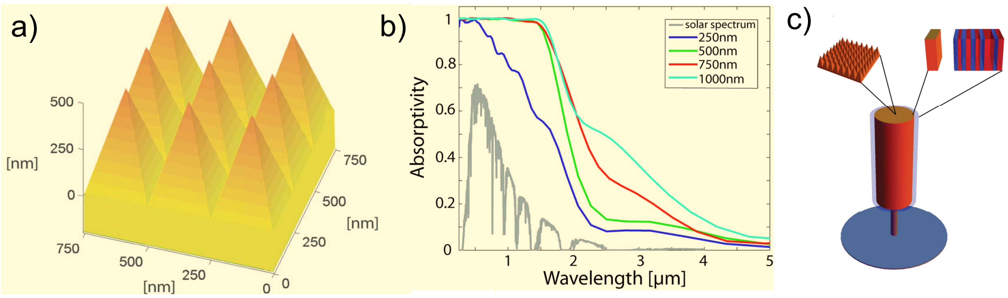

Fig. 3: Illustration of a STPV system with multiple components designed electrodynamics calculations. A textured absorber structure composed of tungsten pyramids on a tungsten substrate is illustrated in **(a)**. The absorptivity of this textured structure is plotted in **(b)** for a variety of pyramid heights with the period of the pyramids fixed at 250 nm. The finite-difference time-domain (FDTD) method (see Section *2.6*) was used to compute the absorptivity shown in **(b)**. An integrated STPV system with the textured absorber and a 1D photonic crystal emitter is shown in **(c)**. The photonic crystal emitter can be optimized using the Transfer Matrix Method (see Section *2.4*). Figures reproduced from Ref. [34, 10] with permission.

where k denotes the wavevector of incident light, and a_n and b_n are the expansion coefficients, which depend on particle size, composition, and frequency. The computational effort scales linearly with the number of terms in the expansion, which can be reasonably truncated. An excellent discussion of Mie theory, as well as practical source code, can be found in Ref. [30].

For particles that are very small compared to the incident wavelength of light ($d << \lambda$), this expansion can usually be truncated after the dipolar term, which yields a particularly simple form for the absorption and scattering cross sections [30], namely

$$C_{abs} = 4\pi\sqrt{\varepsilon_m}\frac{\omega}{c}r^3\,\mathrm{Im}\left(\frac{\varepsilon_p(\omega)-\varepsilon_m}{\varepsilon_p(\omega)+2\varepsilon_m}\right) \tag{4}$$

$$C_{scat} = \frac{8\pi\varepsilon_m^2\omega^4 r^6}{3c^4}\left|\frac{\varepsilon_p(\omega)-\varepsilon_m}{\varepsilon_p(\omega)+2\varepsilon_m}\right|^2. \tag{5}$$

Hhere $\varepsilon_p(\omega)$ denotes the permittivity of the particle (which we have allowed to be frequency dependent and complex), while ε_m denotes the permittivity of the surrounding medium (which we assume to be static and real). This expression predicts particularly large scattering and absorption cross sections at frequencies where $\mathrm{Re}(\varepsilon_p(\omega)) = -2\varepsilon_m$. This equality is satisfied by many metallic nanostructures at visible frequencies, and is the condition for a localized surface plasmon resonance, collective electronic oscillations that concentrate optical energy near the surface of nanostructure.

2.3. Design of nanostructures for enhancing solar energy conversion using Mie theory

The relative simplicity of the theoretical framework describing scattering and absorption of spherical nanostructures affords the ability to design systems utilizing spherical nanoparticles for a variety of solar conversion applications. The scattering properties of spherical nanoparticles can be leveraged to concentrate and trap incident light into thin-film photovoltaic (PV) materials to increase their conversion efficiency. This strategy is particularly effective if the light scattering can occur only in the forward direction, increasing the flux of optical energy

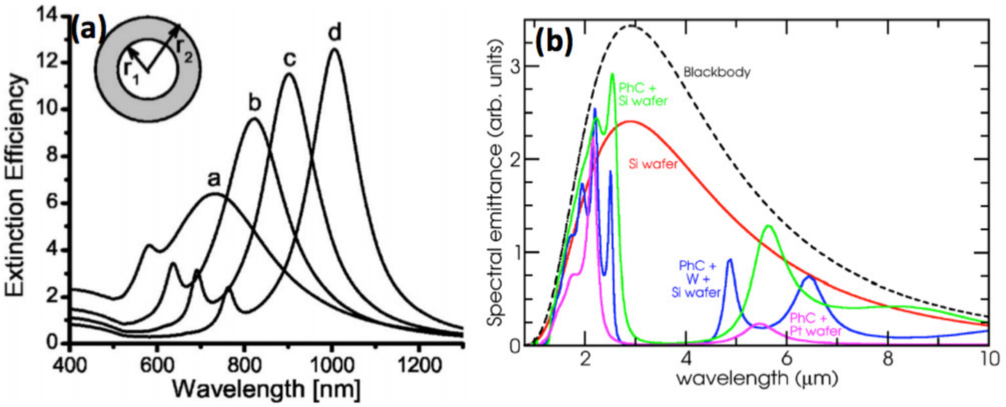

Fig. 4: Illustration of radiation control using engineered spherical core-shell nanoparticles **(a)** and multi-layer planar film structures **(b)**. The absorption, scattering, and extinction cross sections of the core-shell particles can be tuned across the solar spectrum by changing the ratio of the shell thickness (r_2) to the core radius (r_1), and these quantities can be computed using Mie theory (see Section *2.2*) for isolated particles, or the DDA method (see Section *2.8*) for assemblies of particles. In **(a)**, the radius of a silica core is fixed at 60 nm, and the thickness of a gold shell is taken to be 80 nm for curve **a**, 70 nm for curve **b**, 67 nm for curve **c**, and 65 nm for curev **d**. The emittance of several multi-layer structures plotted in **(b)** can be simply computed using the Transfer Matrix Method (see Section *2.4*); however, more sophisticated global device efficiency considerations were used to identify a photonic crystal on a platinum substrate (violet curve in **(b)** as the optimal emitter structure for an integrated STPV system [35]. Figures reproduced from Refs. [36] and [35] with permission.

into an active PV material, for example [38]. Mie theory leads to the prediction of this particularly extreme form of anisotropy where the particles scatter light only in the forward direction when the coefficients for the electric and magnetic dipolar terms (a_1 and b_1, respectively) are identical, which is often called the first Kerker condition [39]. Physically, this can be understood as an interference between electric and magnetic dipolar resonances. Because this is a resonant effect, a given particle geometry will support such scattering behavior only at certain frequencies. Nevertheless, Mie theory computes these coefficients directly, and it is straightforward to develop a design protocol for spherical particles embedded in a medium with known optical properties (e.g. corresponding to the PV material, or a compatible substrate) that support these resonances at a desired frequency. The exceptionally large extinction cross sections of metal nanoparticles, due to their ability to support surface plasmons, can also be exploited to efficiently trap light across the solar spectrum. For example, the optical response of spherical dielectric-core metal-shell nanoparticles is highly tunable, and can be computed exactly with a generalization of Mie theory. Halas and co-workers have employed Mie theory to design optimal distributions of core-shell nanoparticles to enhance absorption over the AM 1.5 solar spectrum [36]. Using a distribution of simple silica core/gold shell particles with modest coverage allowed absorption of 84% of incident solar power across the AM 1.5 spectrum [36]. Figure 4 shows the extinction efficiency computed by Mie theory for various core-shell particle structures.

2.4. *Transfer Matrix methods for planar structures*

For multi-layer planar structures, the fields can be written piece-wise as plane waves, and closed-form expressions for the wavevectors and amplitudes of the fields in each layer can be determined from considerations of Maxwell's equations and appropriate boundary conditions. The boundary conditions can be expressed conveniently as matrix equations, and the amplitudes can be computed by straightforward matrix multiplication, which forms the basis of what is called the Transfer Matrix Method [31]. The general Transfer Matrix equations for an L-layer system can be written as

$$\begin{pmatrix} E_1^+ \\ E_1^- \end{pmatrix} = \begin{pmatrix} M_{1,1} & M_{1,2} \\ M_{2,1} & M_{2,2} \end{pmatrix} \begin{pmatrix} E_L^+ \\ E_L^- \end{pmatrix}, \tag{6}$$

where the elements $M_{i,j}$ depend on the material properties (the refractive index, n) and geometry of each layer, as well as the frequency and polarization of incident light. The precise form of these elements can be found in the excellent treatment by Yeh [31]. We interpret E_1^+ and E_1^- as incoming and outgoing wave amplitudes on the incident side, respectively; similarly, E_L^- and E_L^+ are incoming and outgoing wave amplitudes, respectively, on the terminal side of the structure. With the access to the field amplitudes and wavevectors, a number of useful quantities may be computed. For example, the Fresnel reflection and transmission amplitudes may be computed as $r = E_1^-/E_1^+ = M_{2,1}/M_{1,1}$ and $t = E_L^+/E_1^+ = 1/M_{1,1}$, respectively. The reflection can then be calculated as $R = |r|^2$, the transmission as $T = |t|^2\, n_L cos(\theta_L)/(n_1 cos(\theta_1))$, where n_i and θ_i denote the refractive index of the material of layer i and the incident/refraction angle in layer i, respectively. For computing the Fresnel equations, the field amplitude E_L^- is set to zero and the amplitude E_1^+ is set to 1 by convention. The absorption can simply be computed as $A = 1 - T - R$. The computational effort of the Transfer Matrix Method is minimal as it primarily involves the computation of the matrix elements $M_{i,j}$, which can be accomplished in a number of arithmetic operations that scales linearly with the number of layers in the structure. The Transfer Matrix Equations can also be used to compute the dispersion for resonant modes in multi-layer structures. Two resonant modes of particular interest for multi-layer structures with one or more absorbing layers include surface plasmon polariton (SPP) modes [40, 37, 41, 38, 42], and perfectly absorbing (PA) modes [43, 44, 45, 42]; the former occurs when $r \to \infty$ and $T = 0$, while the latter occurs when $r \to 0$ and $T = 0$. SPPs involve collective electronic oscillations coupled to a propagating electromagnetic wave, and they allow light to be guided along the 2-dimensional interface between a metal and a dielectric layer. Perfectly absorbing modes can allow perfect absorption of incident light by thin absorbing layers. Unlike SPPs, PA Modes are non-propagating [42] .

2.5. *Design of selective emitters for thermophotovoltaic applications using Transfer Matrix methods*

The resonant properties of multi-layer planar structures can be exploited for designing highly-selective emitter structures for use in thermophotovoltaic (TPV) and STPV devices. In TPV devices, thermal energy is transfered to a spectrally-selective emitter structure. The radiation of the emitter should be well matched to a PV cell so that it's thermal emission can be efficiently converted to electrical current. TPV systems can harvest thermal energy as waste heat from engines or other sources. An STPV system is simply a TPV system that harvests thermal energy from solar radiation, and involves a good solar absorber as one of its components. The design of both absorbers and emitter structures has been the focus of considerable theory and modeling effort. Fig. 3 illustrates an STPV system whose emitter can be designed using Transfer Matrix Methods [10].

One approach for the design of emitter structure involves defining a figure of merit in terms of the emissivity of the structure, the band-gap of the PV cell, and the target temperature of operation (see Eq. 13 in section *4.2*). The emissivity can be computed from the reflectance and transmission using the Transfer Matrix Method, enabling efficient computation of the figure of merit. The design problem can then be formulated as a maximization of the figure of merit in terms of the geometry and material properties of the emitter structure. This approach has been employed to design 1D photonic crystals involving tungsten and dielectric layers with spectral efficiencies of about 53% [46] (see Table 2). Similarly, the Transfer Matrix Method can be used to design broad-band absorbers, and has allowed to absorption efficiencies of 74% in 1D photonic crystals made of tungsten and dielectric layers [46] (see Table 1).

A different Transfer Matrix Method-based approach for the design of STPV components, recently introduced by us, leverages the observation that structures that support perfectly absorbing modes with certain characteristics can perform as exceptional selective emitters. These characteristics, described in detail in Ref. [47], can be encoded directly into a search routine that allows for the identification of structure geometries that support these modes. The optimization over the figure of merit is therefore replaced with a search for a zero in T and R, which is equivalent to finding a zero in the transfer matrix element $M_{2,1}$ under the condition that the transmission is also zero, which can be easily satisfied. This approach has predicted structures with spectral efficiencies of 68% at operating temperatures of 1750 K when coupled with common PV materials [47].

2.6. Finite-difference time-domain method

For the optical behavior of more general structures, numerical approaches must be employed to solve Maxwell's equations. Perhaps the most conceptually simple approach is known as the finite-difference time-domain (FDTD) method. Here the time evolution of the fields is computed using the curl equations, Eq. (1) and (2), where the spatial and temporal variables are discretized on a rectangular grid, and centered finite-differences are used for the derivatives in terms of these variables [28]. The **E**and **H** fields are spatially staggered on the computational grid, which enforces Gauss' law. Quantities such as absorption, scattering, reflection, and transmission can be defined in terms of fluxes of electromagnetic fields. Electric field distributions and other quantities may be obtained in the frequency domain by the appropriate Fourier transform of the time-domain fields. The permittivity of metals and semiconductors can have strong frequency dependence across the UV/Vis/IR spectrum, and this frequency dependence requires some consideration for time-domain simulations like FDTD. Material dispersion leads to time-dependence of the material susceptibility and causes that the polarization density to depend on field values at all previous times. This is commonly handled by fitting the permittivity to an analytical function of frequency, commonly a sum of Drude and Lorentz oscillator functions, so that the convolution can be easily computed. A practical drawback is that it can be difficult to obtain a good fit for these functions across a broad spectrum for highly-dispersive materials.

The computational effort of FDTD scales with the 4^{th} power of the computational domain for simulations with 3 spatial and 1 temporal dimension. Considerations for size of the spatial and temporal domain include the requisite resolution for the smallest feature size and the lifetime of the optical response(s) modeled. For example, typically the spatial grid size should be on the order $d/10$ or smaller, where d is the dimension of the smallest feature to be resolved in the simulation. The time-step is usually defined relative to the spatial grid size by the Courant factor [28]. This tends to make simulations of structures with several disparate length-scales challenging, as a small grid size is required for the smallest feature, while many grid elements are required to span the physical structure. However, FDTD implementations can utilize multi-resolution grids to reduce the computational effort in these cases. Furthermore, FDTD simulations can exploit symmetry, periodicity, and can be massively parallelized, all of which has enabled their application to a variety of complex systems.

2.7. Design of patterned structures for absorption enhancement for solar energy applications using the FDTD method

Extensions of the previously-discussed multi-layer planar structures involve introducing geometric features in the lateral dimension(s). These types of structures include 2D and 3D photonic crystals, metasurfaces, metamaterials, and random-textured materials. FDTD can be a powerful tool for designing these types of structures, and can be particularly efficient when symmetry and/or periodicity can be exploited. Often, these sorts of patterned materials are desired to enhance the absorption of visible light, for example, to design a perfect absorber across the solar spectrum for solar thermophotovoltaic applications. For such an application, the transmission, reflection, and absorption can be computed across the spectrum as features of the surface are varied. This procedure is illustrated in Fig. 3a) and b), where the absorptivity of a tungsten surface patterned with pyramidal structures is computed by the FDTD method [34]. Similarly, Atwater and co-workers have employed FDTD simulation to design ultra-thin patterened surfaces that behave as broad-band "super absorbers" capable of enhancing conversion efficiency in thin-film PV materials [48]. Several of the current authors have utilized FDTD simulations to study and design tungsten absorber surfaces patterned with nanocones with absorption efficiencies of 80% [49] (see Table 1), as well as tungsten blazed grating emitter surfaces with spectral efficiencies of 59% [50] (see Table 2).

Many codes like Lumerical, a commercial-grade FDTD simulator, and Meep [29], an open-source FDTD code, have scripting capabilities and other built-in tools to perform sweeps and optimizations over system variables, including material constants and geometric parameters. These sorts of scripting interfaces also allow the computation of more sophisticated quantities; for example, the phase profile or the momentum distribution of scattered fields may be desired, and can be computed by Fourier transforms of the time-domain fields.

2.8. Discrete Dipole Approximation

Several computational methodologies for solving Maxwell's equations in the frequency domain are also available, and here we focus on the Discrete Dipole Approximation (DDA), which is particularlly useful for problems involving scattering and light absorption from particles. The idea behind DDA is to represent scattering structures by an array of N dipoles. The polarizability of each dipole, α_j, is determined from the permittivity of the material being modeled [32]. The electric field at the position j of a given dipole is expanded as

$$\mathbf{E}_j = \mathbf{E}_{inc,j} - \sum_{k \neq j}^{N} \mathbf{A}_{j,k} \mathbf{P}_k. \tag{7}$$

Here the incident field, $\mathbf{E}_{inc,j}$, has the form of a monochromatic plane wave, $\mathbf{P}_j$ is the polarization of dipole j, and the product $-\mathbf{A}_{j,k}\mathbf{P}_k$ gives the electric field at point j due to the polarization at point k; hence, the matrix $\mathbf{A}$ carries information about the geometry and polarizability of the array that couples the response of the dipoles together. Quantities such as the absorption and extinction cross sections are written directly in terms of $\mathbf{P}$ [32]:

$$C_{ext} = \frac{4\pi k}{|\mathbf{E}_0|^2} \sum_{j=1}^{N} \mathrm{Im}\left(\mathbf{E}_{inc,j}^{*} \cdot \mathbf{P}_j\right) \tag{8}$$

$$C_{abs} = \frac{4\pi k}{|\mathbf{E}_0|^2} \sum_{j=1}^{N} \left(\mathrm{Im}\left(\mathbf{P}_j \cdot \left(\alpha_j^{-1}\right)^{*} \mathbf{P}_j^{*}\right) - \frac{2}{3} k^3 |\mathbf{P}_j|^2 \right). \tag{9}$$

The polarization is found by solving the system of linear equations given by $\sum_{k=1}^{N} \mathbf{A}_{j,k} \mathbf{P}_k = \mathbf{E}_{inc,j}$, and the size of this linear system grows quadratically with the number of dipoles used.

However, iterative methods are used to solve the equations, and convergence is often achieved in a number of iterations that scales linearly with the number of dipoles, which leads to overall quadratic scaling of the computational effort with the number of dipoles [32]. In general, high resolution can be obtained for small structures with a relatively small number of dipoles, and so DDA can be extremely efficient for modeling the optical properties of nanoparticles. DDAs formulation in the frequency domain also makes it more convenient than FDTD for modeling materials whose permittivity depends strongly on frequency since the permittivity as a function of frequency can be fed directly into the simulation. While scattering is solved for one frequency at a time, DDA can be run in parallel over the desired frequency range. One considerable drawback is that convergence of the DDA method, both in terms of the number of iterations for solving the linear equations and in terms of the accuracy of the polarization with respect to the number of dipoles, can be quite challenging for materials with large real or imaginary components of refractive index [51]. Silver is a classic material for which DDA modeling presents a particular challenge at visible frequencies.

2.9. *Design of nanostructures for near-field enhancement of solar energy conversion using the DDA method*

Concentration of incident optical energy into the near-field of localized surface plasmons supported by nanostructures can also be leveraged to enhance solar conversion efficiency in PV materials. This approach is complementary to the one discussed with anisotropic scattering because it exploits the absorption of the nanostructure(s) rather than the scattering. The optical energy concentrated in the near-field of the plasmon can directly excite particle-hole pairs in a PV material with high efficiency if the absorption rate of the PV material is larger than the plasmon damping rate (equivalently, the inverse lifetime of the plasmon excitation) [38]. Therefore, nanoparticle systems with high nearfield intensities and long plasmon lifetimes are ideal for these applications. The large cross sections of plasmonic particles can also be leveraged to increase absorption efficiency in absorber structures in STPV applications. DDA methods can efficiently compute near-field distributions, absorption cross sections, etc, for multiple particles with complex geometries and sharp asperities that are separated by small-gaps, which are structures that typically give rise to exceptional near-field enhancement and large absorption cross sections. Plasmon lifetime information can be obtained from a Fourier transform over the absorption spectrum that is generated directly by DDA simulations run over a desired frequency range. Because the DDA method captures the fully coupled optical response of assemblies of nanostructures, it could be used to obtain an exact description of the absorption efficiency of the distribution of core-shell nanoparticles leveraged by Halas and co-workers for absorption enhancement[36] (see Figure 4).

2.10. *Summary and Outlook for Theoretical Design Methodologies*

We have described a number of powerful theoretical methodologies that can be put to use to understand, predict, and even taylor the optical response of systems of simple or complex nanostructures. The use of these methods, along with the ingenuity of many researchers, has allowed the design of many novel and useful systems for radiative control. However, as will be discussed in more detail in the remaining sections, overall conversion efficiencies of TPV/STPV systems often fall around 1%, well short of the theoretical limit of 85%. A significant challenge remains in integrating various theoretical methodologies to model and optimize global device performance [35, 9]. Certainly one challenge is that an integrated TPV/STPV system must couple together various optical modalities for absorption and emission. Usually, this requires abandoning exact analytical approaches in favor of approximate (e.g. perturbative) analytical approaches like coupled-mode theory. Alternatively, researchers must rely on the use of the numerical methodologies described above, though this may prove daunting from a computational point of view due to the multi-scale nature of these systems. Global system optimization must also include considerations like thermal management along with electrodynamics, as the requisite operating temperatures can lead to oxidation or deformation of the constituent structures and degradation of the device performance. Consideration of these various system parameters creates a highly heterogeneous optimization problem and presents significant challenges for global optimization. However, several authors including Celanovic and co-workers [35] as well as Wang and co-workers [9] have taken on the challenge of designing systems with optimal device consideration, which have led to device efficiencies approaching 3% and 10%, respectively. Figure 4(b) illustrates the emittance spectra of various structures designed by the global device optimization approach described by Celanovic, resulting in considerable advances in overall device efficiencies [35].

3. Large area fabrication of optical nanostructures

3.1. Direct laser writing and laser interference lithography

A high power laser beam focused to submicron dimensions allows direct ablation of surface material, as shown in Figure 5a, to form periodic or non-periodic structures. Alternatively, selective exposure of a photoresist can create feature sizes of about 0.5 microns [52].

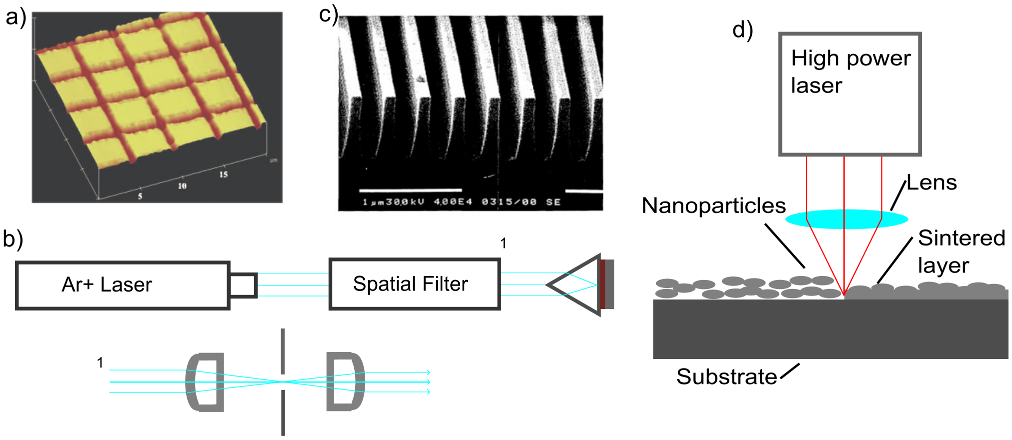

Fig. 5: a) AFM photograph of a micromachined double periodic structure with line-widths less than a micron [52] (reproduced with permission), b) Experimental setup for laser interference lithography, c) SEM image of gratings fabricated by laser interference lithography and etched into quartz [53] (reproduced with permission), and d) experimental setup for laser sintering of nanoparticles.

To obtain feature sizes of few hundred nanometers over a large area, laser interference lithography is ideal [53]. In interference lithography, a laser beam is split into two components, which can be recombined to form an interference pattern, as shown in Figure 5b.

The period, d, of the grating is determined by $d = \frac{\lambda}{2n\sin(\theta)}$ where λ is the wavelength of the laser light, n is the refractive index of the medium and θ is the angle between two beams. For a wavelength of 442 nm, a surrounding medium index of 1.5, and an angle between the two beams of 60 degrees, line-widths of about 200 nm will be generated. Figure 5c shows a scanning electron microscope image (SEM) of the periodic pattern obtained with a He-Cd laser. This technique can allow the fabrication of large area patterns on various substrates. An exposed photoresist mask is used to etch the pattern on the substrate materials.

This method will be well suited for the fabrication of spectral selective surfaces as needed for solar thermophotovoltaics and thermophotovoltaics systems. The selective spectral emission wavelength and the efficiency of the emission can be controlled by the period, height and spacing between lines.

3.2. Laser sintering of nanoparticles

To achieve nanoscale roughness, nanoparticles dispersed in a liquid can be coated on a substrate. A laser sintering process is then used to fuse the nanoparticles together by the high temperature generated by laser light absorption. In this process, the nanoparticles also get bonded to the substrate. The laser sintering process is shown in Figure 5d. By controlling laser processing parameters such as optical power, scan speed, and beam overlap, different surface morphologies can be achieved. This fabrication method is well suited for solar thermal applications where high solar absorptance and low thermal emission is required.

3.3. Glancing angle deposition (GLAD)

Highly light-absorbing surfaces can be generated by micro-scale roughness as multiple reflections within the surface layer effectively trap incident light. Thin films of various materials, when deposited at large angles of incidence to the substrate and under vacuum conditions, give rise to cone like structures as shown in Figure 6a. The deposited films look black to the naked eye because of their extremely high optical absorption. The absorption efficiency of these structures can be controlled by the height of, and spacing between, the pillars. The glancing angle deposition method can be used to enhance solar light absorption and for the fabrication of spectral selective surfaces

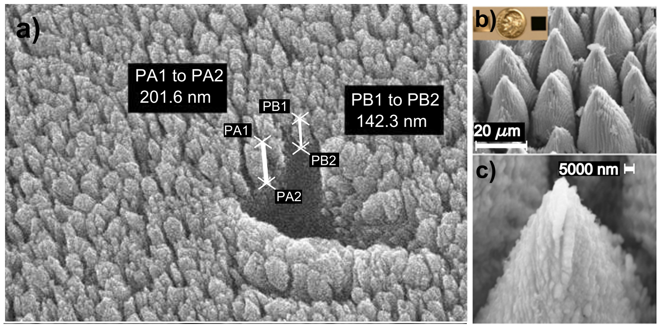

Fig. 6: a) SEM image of GLAD structures (reprinted with permission) [54] and b) and c) SEM images of a laser micro/nano textured Ti surface (reprinted with permission) [26].

3.4. Laser micro/nano textures

Micro- and nano-textured surfaces can be obtained when a high power laser beam is focused on a substrate and laser processing is carried out in a certain power and scan speed range [26]. The details of the texture, including height and spacing, can be controlled by laser processing parameters. The properties of the textured surface allow control over the absorption efficiency of the surface. Figure 6b and 6c show SEM images of a laser microtextured Ti surface.

Multi-layer thin films composed of metal dielectric layers can also be designed such that high optical absorption can be achieved. Reciprocally, the emissivity of multi-layer structures can be tuned over a narrow spectral range. Figure 2c shows an example of thin film structure to control the emission properties.

The high solar radiation absorption can be achieved by fabrication techniques such as metal-dielectric multi-layer structures, surface microtexturing and by the use semiconductor-metal layer structures. The spectral selective emittance can be achieved by fabrication of photonic crystal structures using standard optical or e-beam lithography method or by the use of periodic/non-periodic submicron surface textures. The microtexture fabrication method is suited to achieve black surface with extremely high (>95%) light absorption over broad wavelength and incidence angular range.

4. Solar energy conversion applications

4.1. Solar thermal

Solar thermal (ST) systems are solar powered devices that generate energy via a heat engine. Incoming solar energy is concentrated on an absorbing surface, which is heated to high temperatures. A heat exchange fluid is then used to draw energy from the absorbing surface to the heat engine. Since heat engines can be more efficient at higher operating temperatures, ST systems operate at high temperatures, up to 1000°C.

Operating at such high temperatures means that there will be a large amount of thermal emission from the absorbing surface, resulting in a loss of energy. To reduce this loss, the thermal emittance of the absorbing surface must be minimized. Here, we will define ϵ_{abs} as the thermal emittance of an absorbing surface held at a specific temperature relative to the thermal emittance of a blackbody held at the same temperature. This means that an absorbing surface with an ϵ_{abs} of 0.5 at 1000°C would have half the thermal emission of a blackbody at 1000°C. Note that the ϵ_{abs} of a surface can change drastically with temperature if its reflectivity and absorbance change for different wavelengths of light. This is because the spectral composition of blackbody radiation changes with temperature. At the same time, the solar absorptance (α_{sol}) of the surface must be maximized to ensure a high power input into the device.

For a surface to have high α_{sol} and low ϵ_{abs}, it must have a low reflectance and high absorbance in visible wavelengths (where most solar light is located), and a high reflectance in the near infra-red (NIR) region (where most thermal emission is located). This is a type of spectrally selective surface. These surfaces must also remain stable under the high operating temperatures found in ST systems. The relative importance of high α_{sol} and low ϵ_{abs} can change due to changes in system parameters. For example, higher operating temperatures increase thermal emission and place more importance on achieving a low ϵ_{abs}, while higher solar concentrations result in achieving a high α_{sol} being more important.

Spectrally selective surfaces are a focus in ST research because they are a key to high efficiency systems. While coatings for lower (<500°C) temperatures have been extensively studied, they are generally not suitable for high temperature operation due to a lack of thermal stability [55]. Some research has attempted to use silicon or germanium based absorbers, but their high solar reflectance necessitates the use of broadband anti-reflective coatings which results in high ϵ_{abs}, and their performance degrades at high temperatures due to oxidation [56].

Stacks of layered dielectric and metallic films can be used to control the reflectance of structures via multiple reflections and interference effects [57]. Many different materials have been investigated for this purpose, including stacks using tungsten, molybdenum, titanium oxide, and magnesium fluoride that had an $\epsilon_{abs}<7\%$ and $\alpha_{sol}>94\%$ [58, 59, 56]. Unfortunately, fabrication of these surfaces requires vacuum deposition of multiple layers with precise thickness, which can be difficult.

Ceramic-metal composites (cermets) consist of metallic particles in a dielectric host that are often used as spectrally selective surfaces in ST applications. The metallic particles in the cermet layer result in high α_{sol} due to multiple reflections, and they are typically used on metallic substrates with high IR reflectance, resulting in low ϵ_{abs} [56, 60, 61, 62, 63, 64, 65, 66]. The disadvantages of cermets include sensitivity to oxygen at high temperatures and the requirement for vacuum fabrication methods.

Nanotextured surfaces can be temperature stable when they are formed from high melting point metals such as tungsten and tantalum and are coated with a protective oxide [67]. They also lend themselves to fabrication using the methods described in this report. Because these methods take advantage of surface geometry, they do not require multiple materials, resulting in a high thermal stability. Indeed, nanostructures of tungsten coated with a protective hafnium coating have been shown to be stable to temperatures of 1100 °C in air [67, 68]. Tantalum photonic crystals have also been reported to be stable at temperatures of over 1000°C [69].

Periodic sub-wavelength gratings on tungsten substrates have been fabricated with an α_{sol} of 82% and ϵ_{abs} of 5.6% at 770°C and were experimentally verified to be temperature stable up to 900 °C [70]. These structures cause standing wave resonances that can be tuned for solar absorption.

Sub-wavelength roughness on metallic substrates can also increase solar absorbance due to the surface acting as a graded index medium [70, 71]. The ϵ_{abs} of these surfaces can be kept low because NIR wavelengths are much longer than the dimensions of the roughness, so the surface appears smooth [72]. An advantage of these types of structures is that they do not require periodicity, and randomness can in fact be an advantage [49]. Simulations have shown pseudo-random nanocones on a tungsten substrate to have an α_{sol} of 97% and ϵ_{abs} of 16% at 1400 °C [49]. Experimental data on surface roughness created by laser-sintering of nanoparticles have shown an α_{sol} of 83% and ϵ_{abs} of 11.6% [21].

4.2. *Solar thermophotovoltaics*

Typical STPV systems consist of an absorbing/emitting structure that is held under vacuum to reduce convective losses and increase thermal stability [73, 74]. Then, sunlight is focused on the absorbing surface of the structure, where it is absorbed and converted into thermal energy. This results in the absorbing/emitting structure becoming very hot, with temperatures up to 1750 K common in these systems. As the system temperature rises, it begins to emit a large amount of thermal radiation. The portion of thermal energy that is emitted by the emitting surface can then be collected by a PV cell and converted into electrical energy. An additional advantage of STPV systems is their ability to store absorbed energy as heat, which is more efficient than battery storage with traditional PV cells. STPV technology can also be easily adapted to thermophotovoltaic (TPV) systems, which operate similarly to STPV devices but use a burning fuel or waste heat as a thermal source instead of the sun. By transforming the incoming solar radiation from a broadband source to a more narrow-band one, STPV systems can operate at efficiencies exceeding the Shockley-Queisser limit of 32.1% for silicon PV cells [75]. In fact, the upper *theoretical* limit for STPV system efficiency is 85.4% [56].

The absorbing surfaces for STPV devices are similar to those used in ST systems, although higher operating temperatures (up to around 1750 K) make thermal stability a more prominent concern, and high levels of solar concentration (>4000) make a high α_{sol} of paramount concern. This means that nanotextured absorbing surfaces are a very good match for these systems. Most experimental STPV systems to date have utilized blackbody absorbing surfaces [81, 82, 78, 77], leaving room for much improvement by using selective absorbing surfaces. A yttria-stabilized zirconia and tungsten stack was used as a selective absorber in an experimental system, but while it's thermal emission was low, its performance was hindered by a low α_{sol} of 80%. Simulations of various surfaces have shown large gains in system efficiency from the use of nanotextured selective absorbing surfaces, such as pseudo-random nanocones with an α_{sol}

Table 1: Efficiency, relative solar absorption, and relative thermal emission at a temperature of 1700 K of selected absorbing surfaces.

Absorber type	Absorber efficiency	α_{sol}	ϵ_{abs}
Ideal solar absorber	0.83	0.87	0.04
Pseudo random nano-cones in W	0.80	0.97	0.16 [49]
W pyramidal nanostructures	0.79	0.92	0.13 [34]
Mo-SiO$_2$ cermet	0.77	0.93	0.16 [76]
Carbon nanotubes	0.74	0.99	0.95 [77]
1-D photonic crystal on W	0.74	0.80	0.06 [46]
Blackbody absorber	0.73	1.00	1.00
Anti-reflection coating on W	0.67	0.73	0.05 [46]
W cavities	0.59	0.74	0.15 [78]
Surface-relief grating on W	0.49	0.53	0.05 [79]
Bare W	0.41	0.44	0.04 [80]

of 97% and ϵ_{abs} of 16% [49], or pyramidal nanostructures in tungsten with an α_{sol} of 92% and ϵ_{abs} of 13% [34] but none have been experimentally demonstrated in a working STPV system to date [67, 79].

Various methods of evaluating STPV system performance exist, but in this work we will focus on the relative efficiencies of the individual surfaces of an STPV device. This allows us to directly compare different methods of making selective absorbing and emitting surfaces. Many parameters in STPV systems can effect the performance of these surfaces, so an operating temperature of 1450°C, a solar concentration of 2500, and a GaSb solar cell are assumed here due to their prevalence in STPV systems [81, 82, 78, 49, 50, 10]. This provides for a good relative comparison of different surfaces, although it is not a measure of overall device efficiency.

Table 1 shows the α_{sol} and ϵ_{abs} of some absorbing surfaces, as well as a calculated surface efficiency (η_{abs} given by:

$$\eta_{abs}(T) = \frac{\int_0^\infty \{E_{inc}(\lambda)\alpha(\lambda) - \varepsilon(\lambda)B(\lambda,T)\}\,d\lambda}{\int_0^\infty E_{inc}(\lambda)d\lambda} \tag{10}$$

$$E_{inc}(\lambda) = C\eta_{conc}E_{sun}(\lambda) \tag{11}$$

where, $\alpha(\lambda)$ is the spectral absorption of the surface, $\varepsilon(\lambda)$ is the spectral emittance of the surface, C is the concentration ratio of incoming sunlight, η_{conc} is the solar concentration efficiency, $E_{sun}(\lambda)$ is the spectral irradiance of the sun at the earth's surface, $B(\lambda,T)$ is Planck's law for blackbody radiation, and $E_{inc}(\lambda)$ is the spectral energy incident on the absorbing surface.

For emitting surfaces, a similar approach to absorbing surfaces can be taken, but with a focus on low reflectance in a narrow peak near a specific wavelength (which depends on the bandgap energy of the PV cell used), as opposed to a broad low reflectance band in the visible region. To accurately compare emitting surfaces, their spectral efficiency is used.

The spectral efficiency is given by [50]:

$$SE = \frac{\int_0^{\lambda_{bg}} \frac{E_{bg}}{E_\lambda} B(\lambda,T)\,\varepsilon_S(\lambda)\,d\lambda}{\int_0^\infty B(\lambda,T)\,\varepsilon_S(\lambda)\,d\lambda} \tag{12}$$

where E_{bg} is the bandgap energy of the PV cell, E_λ is the energy of a photon with wavelength λ, and $\varepsilon_S(\lambda)$ is the spectral emissivity of the emitting surface, approximated as the surface's absorptivity. This gives the relative efficiency of the emitting surface, but does not represent an overall system efficiency.

Two structures work particularly well for this purpose: dielectric-metal stacks and 2-D or 3-D photonic crystals. A yttria-stabilized zirconia (YSZ) and tungsten stack was able to achieve highly selective emission and experimentally demonstrated to be stable at temperatures up to 1350 °C [46].

Table 2: Optical efficiency of selected emitting surfaces at 1700 K [83].

Emitter type	η_{emit}
Ideal emitting surface	0.84
Periodic hole array on W	0.64 (simulated)
Blazed grating on W	0.59 [50]
Anti-reflection coating on W	0.59 (simulated)
Complex square grating on W	0.53 [84]
1-D photonic crystal on W	0.53 [46]
Micro-cavity in W	0.51 [85]
$Al_2O_3/Er_3Al_5O_{12}$ eutectic composite	0.41 [81]
Blackbody emitter	0.29

Many nanotextured emitting structures have been simulated to be extremely efficient [86]. These include blazed gratings on tungsten [50], complex square gratings on tungsten [84], micro-cavities in tungsten [85], tungsten surface gratings [79], 3-D photonic crystals [87], and metamaterials [88]. Table 2 shows the spectral efficiencies of some of these surfaces. This shows a large increase in efficiency for selective emitters over blackbody emitters. While experimental systems using these structures have not yet been realized, they promise large efficiency gains for the future. Table 3 shows the electrical efficiencies of some simulated and experimental STPV systems. This shows the large increase in efficiency that can be achieved by using nanostructures to close the gap between experimental and theoretical devices. The simulation and fabrication methods outlined in this paper show that this is possible.

Thermophotovoltaic (TPV) systems are another important area for harvesting waste heat energy. The reported efficiency of TPV systems is low at around few percent. However, as demonstrated by Bermel et al. [4] by using spectral selective surfaces the calculated efficiency can be very high (26.2%). The calculation was based on operating temperature of 1200 K. Similarly, Foley et al. [47] has shown in the paper as part of this special issue that by using metal (Ag)-dielectric (Si_3N_4) structure the calculated efficiency of 10% can be achieved at low operating temperature of 1000 K. It can also be further enhanced by using selective filters and operating at 1200 K.

5. Conclusions

We have discussed a variety of modeling and fabrication techniques associated with controlling the light absorption and emission by nanostructures. Such control is relevant to a variety of solar and thermal energy conversion devices including traditional photovoltaic (PV), solar thermal (ST), and solar thermophotovoltaic (STPV) devices. The use of thermal energy conversion in some manner, in particular, circumvents some efficiency limitations on standard PV cells, and we believe significant improvements in efficiency can be achieved in this area by building on the techniques discussed here. For example, while ST systems are already achieving high efficiencies in commercial use [90], experimental TPV and STPV efficiencies remain low. The

Table 3: Efficiency of selected STPV systems.

Absorbing surface	Emitting surface	PV cell	Temp. (K)	Efficiency (%)
Experimental systems				
Laser-textured W with Si_3N_4 coating	W with Si_3N_4 coating	GaSb	1777	6.2 [89] (2015)
YSZ and W stack	YSZ and W stack	GaSb	1640	8 [46] (2015)
Carbon nanotubes	Si/SiO_2 stack	InGaAsSb	1285	3.2 [77] (2014)
Graphite	W with HfO_2 coating	Ge	$\sim$1700	0.8 [82] (2012)
Tungsten cavity	Thin W film	GaSb	$\sim$2000	1 [78] (2007)
Graphite	$AL_2O_3/Er_3Al_5O_{12}$ composite	GaSb	Unmeasured	0.02 [81] (2000)
Simulated systems				
Pyramidal W nanostructures	Si/SiO_2 stack	GaSb	6000	49 [10]
Blackbody absorber	Monochromatic emitter	Ideal cell	2872	45.3 [73]
Selective absorber	W surface grating with Si/SiO_2 filter	GaSb	1920	23.4 [85]
Periodic hole array on W	Pseudo-random cones on W	GaSb	1700	14.4 [83]
2D Ta photonic crystal	2D Ta photonic crystal	InGaAsSb	1400	10 [12]

primary cause of lowered device efficiency is lack of control over the spectral emissivity of the absorbing and emitting surfaces. The nanostructures, simulation, and fabrication methods highlighted in this paper can be used to greatly increase efficiencies in all three of these systems. Simulations of nanostructured devices show that extremely high efficiencies exceeding the Shockley-Queisser limit are achievable. Additional efficiency increases can be achieved by using ST systems in tandem with STPV systems to capture waste heat from the STPV device.

Acknowledgments

We would like to thank the NASA Langley Professor and NSF IUCRC programs for their support of this project. Part of this work was performed at the Center for Nanoscale Materials, a U.S. Department of Energy, Office of Science, Office of Basic Energy Sciences User Facility under Contract No. DE-AC02-06CH11357.